CRANFIELD UNIVERSITY

MARCO CASTELLI

ADVANCES IN OPTICAL SURFACE FIGURING BY REACTIVE ATOM PLASMA (RAP)

SCHOOL OF APPLIED SCIENCES
Precision Engineering

PhD Thesis
Academic Year: 2011-12

Supervisors: Professor Paul Shore and Mr Paul Morantz
October 2012

CRANFIELD UNIVERSITY

SCHOOL OF APPLIED SCIENCES
Precision Engineering

PhD Thesis

Academic Year 2011-12

MARCO CASTELLI

ADVANCES IN OPTICAL SURFACE FIGURING BY REACTIVE
ATOM PLASMA (RAP)

Supervisor: Professor Paul Shore and Mr Paul Morantz
October 2012

This thesis is submitted in partial fulfilment of the requirements for
the degree of Doctor of Philosophy

ABSTRACT

In this thesis, the research and development of a novel rapid figuring procedure for large ultra-precise optics by Reactive Atom Plasma technology is reported. The hypothesis proved in this research is that a metre scale surface with a form accuracy of ~1 µm PV can be figure corrected to 20 – 30 nm RMS in ten hours. This reduces the processing time by a factor ten with respect to state-of-the-art techniques like Ion Beam Figuring.

The need for large scale ultra-precise optics has seen enormous growth in the last decade due to large scale international research programmes. A bottleneck in production is seen in the final figure correction stage. State-of-the-art processes capable of compliance with requisites of form accuracy of one part in 10^8 (CNC polishing, Magneto-Rheological Finishing and Ion Beam Figuring) have failed to meet the time and cost frame targets of the new optics market.

Reactive Atom Plasma (RAP) is a means of plasma chemical etching that makes use of a Radio Frequency Inductively Coupled Plasma (ICP) torch operating at atmospheric pressure. It constitutes an ideal figuring alternative, combining the advantages of a non-contact tool with very high material removal rates and nanometre level repeatability. Despite the rapid figuring potential of this process, research preceding the work presented in this manuscript had made little progress towards design and implementation of a procedure for metre-class optics.

The experimental work performed in this PhD project was conducted on Helios 1200, a unique large-scale RAP figuring facility at Cranfield University. Characterisation experiments were carried out on ULE and fused silica surfaces to determine optimum process parameters. Here, the influence of power, surface distance, tool speed and surface temperature was investigated. Subsequently, raster-scanning tests were performed to build an understanding on spaced multiple passes.

Drawing on the acquired knowledge, modified dwell-time calculations and a dedicated tool motion path were devised. In combination with an iterative

figuring method, these techniques were expected to deliver rapid convergence towards the required form accuracy. Such methodology constitutes the new reactive plasma figuring procedure.

This procedure allowed achieving first figuring results on 100 and 150 mm diameter fused silica surfaces, with residual errors down to 16 nm RMS. These were attained within three iterations of less than seven minutes each. To prove the rapid large scale figuring capability, a ULE part with a 405 mm diameter polished clear aperture was processed. For repeatability purposes, two surfaces were figure corrected and final figure errors of 45 and 31 nm RMS were achieved. The mean processing time of 50 minutes per iteration proves the hypothesis that, within two iterations, a metre scale surface can be figure corrected in ten hours.

ACKNOWLEDGEMENTS

"If you find a path with no obstacles, it probably doesn't lead anywhere."
(F. H. Clark)

TABLE OF CONTENTS

LIST OF FIGURES

xiii

LIST OF TABLES

LIST OF ABBREVIATIONS

APPP	Atmospheric Pressure Plasma Processing
ATLAST	Advanced Technology Large Aperture Space Telescope
CCD	Charge Coupled Device
CCP	Capacitive Coupled Plasma
CMM	Coordinate Measuring Machine
CNC	Computer Numerically Controlled
CTE	Coefficient of Thermal Expansion
CU	Cranfield University
CVM	Chemical Vapor Machining
E-ELT	European Extremely Large Telescope
ELT	Extremely Large Telescope
EUV	Extreme Ultra-Violet
FEA, FEM	Finite Element Analysis, Finite Element Method
FWHM	Full Width at Half Maximum
GMT	Giant Magellan Telescope
HiPER	High Power laser Energy Research
HST	Hubble Space Telescope
IBF	Ion Beam Figuring
ICP	Inductively Coupled Plasma
ISO	International Organization for Standardization
IOM	Institut für Oberflächenmodifizierung
JWST	James-Webb Space Telescope
LAPP	Laser Assisted Plasma Processing
LLNL	Lawrence Livermore National Labs
LMJ	Laser Mega Joule
MRF	Magnetorheological Finishing
MRR	Material Removal Rates
NIF	National Ignition Facility
OWL	Overwhelmingly Large telescope
PJM	Plasma Jet Machining
PSD	Power Spectral Density

PV (or p-v)   Peak-to-Valley

RAP   Reactive Atom Plasma

RF   Radio Frequency

RMS   Root Mean Square

ROC   Radius Of Curvature

SLM   Standard Litre per Minute

SSD   Subsurface Damage

TMT   Thirty Meters Telescope

ULE   Ultra-Low Expansion (glass)

UPS   Ultra Precision Surfaces

UPS^2 Ultra Precision and Structured Surfaces

VLT   Very Large Telescope

LIST OF PUBLICATIONS

Journal:

Castelli, M., Jourdain, R., Morantz, P., Shore, P. (2012), "Rapid Optical Surface Figuring Using Reactive Atom Plasma", *Precision Engineering*, vol. 36, no. 3, pp. 467 - 476.

Conference (reviewed):

Castelli, M., Jourdain, R., McMeeking, G., Morantz, P., Shore, P., Proscia, D. and Subrahmanyan, P. (2010), "Initial strategies for 3D RAP Processing of Optical Surfaces Based on a Temperature Adaptation Approach", in: *Proc. of the 36th MATADOR Conference*, 14 – 16 July 2010, Manchester (UK), section 18, pp. 569 - 572.

Jourdain, R., **Castelli, M.**, Shore, P., Subrahmanyan, P. (2010), "Process characterisation and key tasks for cost-effective 3D figuring of specular surfaces using RAP", *In: Proc. of the International Conference of the European Society for Precision Engineering and Nanotechnology*, vol. 2, 31 May – 4 June 2010, Delft (NL), EUSPEN, Cranfield, pp. 185 - 188.

Castelli, M., Jourdain, R., Morantz, P., Shore, P. (2012), "Reactive Atom Plasma for rapid figure correction of optical surfaces", *In: 6th International Congress on Precision Machining (ICPM2011), Key Engineering Materials,* vol. 496, 13 – 15 September 2011, Liverpool (UK), Trans Tech Publications, Zürich (CH), pp. 182 – 187.

Jourdain, R., **Castelli, M.**, Shore, P., Morantz, P. (2011), "Fast 3D Figuring of Large Optical Surfaces Using Reactive Atom Plasma (RAP) Processing", *In: Proc. of the International Conference of the European Society for Precision Engineering and Nanotechnology*, vol. 2, 23 – 27 May 2011, Como (I), EUSPEN, Cranfield, pp. 406 – 408.

Castelli, M., Jourdain, R. Morantz, P., Shore, P. (2012), "Fast Figure Correction of 400 mm Diameter ULE Mirror by Reactive Atom Plasma", in: *Proc. of the*

International Conference of the European Society for Precision Engineering and Nanotechnology, vol. 2, 4 – 8 June 2012, Stockholm (SE), EUSPEN, Cranfield, pp. 387 – 390.

Jourdain, R., **Castelli, M.**, Morantz, P., Shore, P. (2012), "Plasma surface figuring of large optical components", in: *Optical Micro- and Nanometrology IV, Proc. of SPIE*, vol. 8430, 16 – 18 April 2012, Brussels (BE), SPIE, Bellingham WA, art. no. 843011.

Castelli, M., Jourdain, R. Morantz, P., Shore, P. (2012), "Fast Figuring of Large Optics by Reactive Atom Plasma", in: *Astronomical Telescopes + Instrumentation, Proc. of SPIE*, 1 - 6 July 2012, Amsterdam (NL), SPIE, Bellingham WA, vol. 8450, art. no. 845034-845034-8.

Shore, P., Jourdain, R., **Castelli, M.**, Morantz, P. (2012), "UK Developments Towards Rapid Process Chains for Metre Scale Optics", in: *Optical Fabrication and Testing*, *OSA Technical Digest (online)*, paper no. OW3D.1.

1 INTRODUCTION

In the past decade, new ambitious research aims were set by several major international science programmes such as the National Ignition Facility (NIF), Laser Megajoule (LMJ), the High Power laser Energy Research facility (HiPER), X-EUV (lithography wafer steppers) and a number of astronomical projects (e.g. E-ELT, TMT) for the construction of very large telescopes. Main components for these projects are metre-sized optical surfaces with extremely demanding finishing requirements. Therefore, an escalating request for large scale Ultra Precision Surfaces (UPS) has been taking place [1].

At present, primary segmented mirrors of existing large telescopes measure about 10 m diameter with 1 – 1.8 m sized segments. The need for higher resolution and lower radiation intensity acquisition lead to concepts and designs of segmented mirrors up to ~39 m diameter (E-ELT) and more. This means a jump in fabrication from ~ 50 segments to thousands of segments requiring <20 nm RMS form accuracy and better than 1 nm RMS roughness [2]. Citing Hallock et al. [3], "*Future mirrors will require larger apertures to be made faster and less expensively than can be done today. ... Consequently, conventional methods will not meet the future required costs and schedule goals*".

In sight of such challenging requests, a new production chain for metre-class optics had been proposed (UPS and UPS[2] Projects). This novel manufacturing sequence would consist of processing steps of less than 10 hours duration each. Currently, the bottleneck stage preventing a more rapid production of high specification optics is the final figuring process. Only three assessed technologies currently seem to have the requisites to (partially) respond to the present UPS demand: "Precessions" Polishing by Zeeko, Magnetorheological Finishing (MRF) by QED and Ion Beam Figuring (IBF). However, significant limitations affect even these state-of-the-art techniques.

Polishing and MRF are more traditional contact processes and are, therefore, subject to edge effects and induced substrate stress. Also, residual figure error cannot be excluded, particularly when working on aspheric optics [3]. Finally,

despite recent progress, the two techniques haven't been able to meet the 10 hours target, being up to hundred hours or more ([4] and confidential communication with OpTIC Technium).

IBF is a process based on surface ion bombardment. It is capable of achieving very high form accuracy and, as a non-contact process, avoids the mentioned disadvantages of micro-cracks and chamfer problems. However, expensive high vacuum chambers are required to enable ions to reach the substrate. Moreover, poor material removal rates are reported (e.g., [5], [6], [7]), making IBF a very slow figuring method.

Reactive Atom Plasma (RAP) technology made its appearance in this context as a promising, yet embryonic, process emerging from the Lawrence Livermore National Labs (LLNL). Patented by RAPT Industries [8], [9], the method is based on an RF Inductively Coupled Plasma (ICP) torch where argon gas is ignited to form plasma and maintained through magnetic induction. A reactive species containing fluorine or chlorine compounds is injected in the plasma and atomised. Reactive gases utilised so far include CF_4, NF_3 and SF_6. Acting like a shield, argon plasma allows for fluorine (or chlorine) radicals to reach the point of interest (substrate) without interacting with the surrounding medium (air). In this way the process can be operated at atmospheric pressure.

RAP can etch optical materials like Ultra Low Expansion (ULE - Corning) glass, Fused Silica, BK7 (Schott) and Silicon at room temperature, while glass-ceramics like SiC and Zerodur (Schott) need to be heated up to ~200 ^{o}C (see, e.g., [10], [11], [12]). High removal rates, comparable to those of mechanical finishing processes, are reported on these kinds of substrates. Together with proven nanometre level repeatability, the absence of subsurface damage and potentially low roughness deterioration, these properties make RAP a possible ideal alternative for the figure correction of large optical surfaces.

In the RAP process, the plasma plume etching the surface leaves a characteristic near-Gaussian footprint. Its depth and width can vary depending on parameters like input power, substrate material, fluorine concentration, standoff distance from the surface, dwell time and temperature. Optimisation

2

and control of these parameters by appropriate characterisation and tool-path algorithms should enable the realisation of a large optics figuring capability using Reactive Atom Plasma. In this way, the RAP process will become an integral part of the ultra-precise optical fabrication chain.

Research on RAP has been progressed at Cranfield University since 2004. Experimentations were carried out on a first prototype machine, RAP300, within a Joint Research Councils Basic Technologies project entitled "*Ultra-Precision Surfaces; a New Paradigm*". This was undertaken in cooperation with EPRSC's Innovative Manufacturing Research Centre (IMRC) at Cranfield and the UPS^2 Integrated Knowledge Centre (IKC). Thanks to these pioneering investigations, better understanding of the process was delivered by first results, such as footprint characteristics and effects of multiple passes (trenches and neutral removal, see [11] and [13]). Moreover, as part of a previous PhD project, advanced studies of plasma thermal aspects of the RAP torch were performed [13]. This research was carried out to develop a first stage of understanding of heat effects in the RAP process. In fact, in accordance with an Arrhenius-type trend, the temperature is reckoned to enhance the rate of chemical reaction between fluorinated plasma and substrate. While improving the etching rates, the described heat effect makes material removal less predictable, thus worsening RAP figuring effectiveness. Novel techniques and understanding were therefore required in order to attain a convergent figure correction procedure.

A new stage of research aimed at realising the actual figuring potential of the Reactive Atom Plasma method began with the development of the new facility Helios 1200 at Cranfield in 2008. Designed for the figure correction of optical parts up to 1.2 m diameter, its performance has been studied and tested during the three years project reported in this manuscript [14], [15], [16], [17], [18].

The research goal pursued in this work was to demonstrate that, using the RAP process, a metre scale optical surface with a form accuracy of ~1 μm PV can be figure corrected to 10 – 30 nm RMS in ten hours, with minor roughness

deterioration (~7 nm RMS). To achieve this aim, the research has the following major objectives:

I. Tool-footprint characterisation – Assessment of the etching footprint performance and identification of its suitability to figuring and any need for optimisation.

II. Tool-path algorithm – Design of process dedicated tool motion path and development of dwell-time calculations to determine the demanded too velocity.

III. Investigation of surface temperature effects on the etching rates and of surface temperature gradients – Consideration of an in-process adaptation to temperature variations.

IV. Development of a converging figuring procedure, based on the outcomes of the previous three objectives – Small scale proof of concept with particular focus on processing times, form accuracy and finish roughness.

V. Scaling up of the process – Demonstration of the research aim achievement.

In this thesis, the research and development of the first RAP figuring procedure is described. Within the three years of this PhD project, major progress was made which allowed RAP to become a cost-effective figuring technique, potentially replacing current state-of-the-art technologies. Firstly, in Chapter 2, the scientific and commercial context in which this plasma figuring technique was invented and developed is illustrated. Subsequently, in Chapter 3, the theoretical background of the figuring procedure is introduced. Here, a description of how the appropriate surface figure correction techniques were devised is given. Such techniques constitute the essential means to enable the RAP figuring capability. In particular, in this chapter, a dedicated tool-path algorithm, designed to reduce heat gradients and compensate for etching irregularities, is described together with the derivation of the torch velocity maps from purposely adapted dwell-time calculations.

The experimental work started with the assessment of the ICP torch performance and took place on the basis of trenches and neutral removal [14]. This part of the work is described in Chapter 4. Trench etching constituted the characterisation of the removal rates. Conversely, neutral removal tests were aimed at proving the capability of removing constant amounts of material over fixed areas, as this is considered pivotal to figuring. Following the outcomes of these experiments, a more detailed characterisation of the torch-tool parameters was seen as necessary and a systematic investigation was carried out. This delivered an optimised etching footprint performance. Further, the investigation of neutral removal schemes served the design of the new tool-path introduced in Chapter 3.

The figure correction results are discussed in Chapter 5. First, the validity of the non-linear theory was verified through a preliminary test (sinusoidal trench). Finally, heat effects on the removal rates were compensated empirically through an iterative type of figuring procedure. By means of the described approach, repeatable figuring results down to ~16 nm RMS were achieved on fused silica surfaces over areas of 100 and 150 mm diameter. These processes were completed within three iterations of typically less than seven minutes duration each.

The procedure was subsequently scaled up to 400 mm diameter surfaces. For this purpose, a substrate made of ULE was utilized, which presented a spherical surface geometry of 3 m radius of curvature. In this way, the free form figuring capability of the process was also proved. This part of the work was supported by an interferometric setup suitable for large scale metrology. Residual errors of 45 and 31 nm RMS were achieved within three and two iterations respectively. The mean processing time of 50 minutes per iteration allows predicting about ten hours duration for the figuring of a metre-scale surface in two iterations. This result demonstrates that the figure correction procedure devised in the course of the presented work is functional for the processing of large optics and will allow for official introduction of Reactive Atom Plasma into the large optics manufacturing chain.

Further, in Chapter 6, critical assessment and discussion of the achieved results is presented and possible improvements are suggested. In particular, process convergence, residual waviness and edge effects are analysed. In Chapter 7, methods for making the process adaptive to surface temperature variations are briefly introduced and discussed. Also, a future implementation of such methods into the figuring procedure is proposed. Finally, the work presented in this thesis is summarised and discussed in Chapter 8 where some economic aspects of the process are also considered. In Chapter 9, the conclusions are drawn and the contributions to knowledge highlighted. In Chapter 10, the perspectives for forthcoming work are discussed and suggestions based on the achieved results are made. In particular, the figure correction of a metre-class surface, and ultimately also of an E-ELT type segment, are highly emphasised.

2 LITERATURE REVIEW

2.1 The need for ultra-precision optics

In the majority of research sectors the use of instrumentation based on precise optics is an inescapable need. In several scientific branches the required quality of a finished optical part becomes a limitation for the achievement of research purposes. It is therefore natural that a continuous request of improvements has historically affected progress in optics production, leading to *ultra-precision* optical fabrication. Thus, for decades, established processes such as grinding, lapping and polishing have constituted the production flow of optics and been able to comply even with the tightest specifications [3].

Recently, however, the exploration of pioneering frontiers of knowledge and technology by several international scientific programmes has set a radically new standard for the demand of high accuracy optical components. In fact, current and proposed major projects in the areas of laser fusion energy production, astronomy and Extreme Ultraviolet (EUV) lithography require not only optics with the highest specifications achievable nowadays, but also larger apertures and impressive production rates [3].

An example of laser fusion establishment is the National Ignition Facility (NIF) [19]. Located at Lawrence Livermore National Labs, it makes use of 192 laser beams. Each laser set-up needs 36-38 large scale ultra-precise optical elements that constitute the light conveying and focussing system. In total, this means 7360 optics whose combined surface area covers nearly 3600 m^2 [20], [21], [22]. Another major laser fusion facility is the Laser Mega Joule (LMJ), situated at Cesta in the south-west of France [23]. Developed on the basis of the results obtained on LIL (Ligne d'Integration Laser), the LMJ predecessor, it will consist of 240 laser beams, capable of delivering 1.8 megajoule of energy onto a conic Deuterium-Tritium target [24] (**Figure 2-2**). Like the NIF, its construction has both scientific and military purposes and it will be operational in 2014.

Conversely, the concept of the European **Hi**gh **P**ower laser **E**nergy **R**esearch facility (HiPER, **Figure 2-3**) [25] will include a 48 laser beams focussed on a fuel target by means of arrays of fused silica lenses with a size 75x75 cm^2 [26].
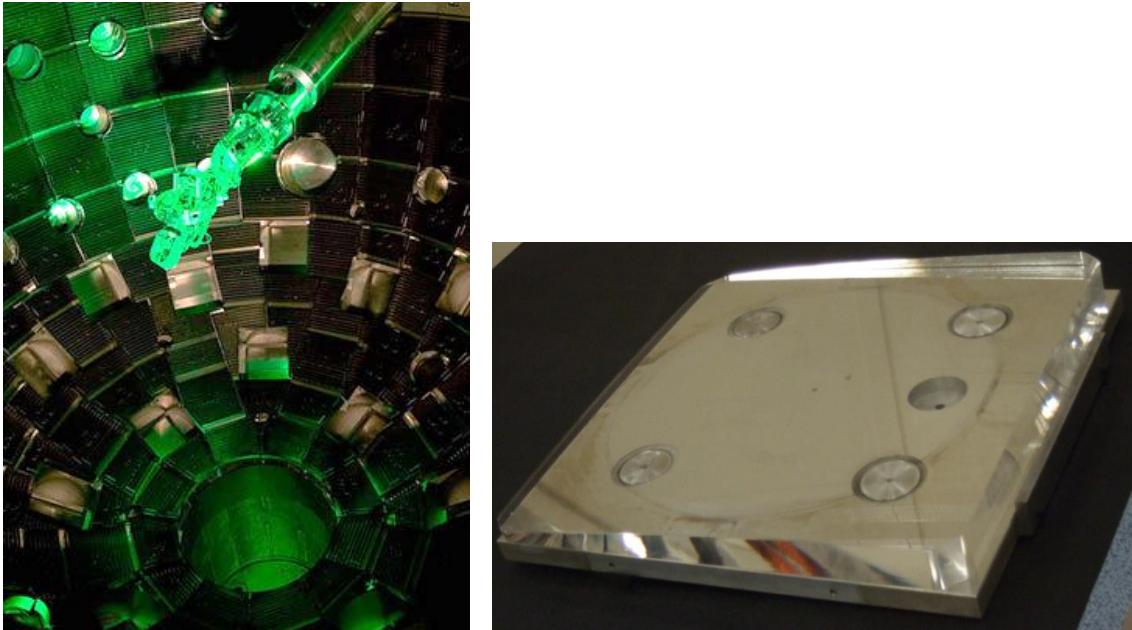
Figure 2-1 *left:* **NIF target chamber with lasers optics (source: [19]);** *right*: **one of the wedge optics (fused silica) utilised in the NIF focussing systems.**
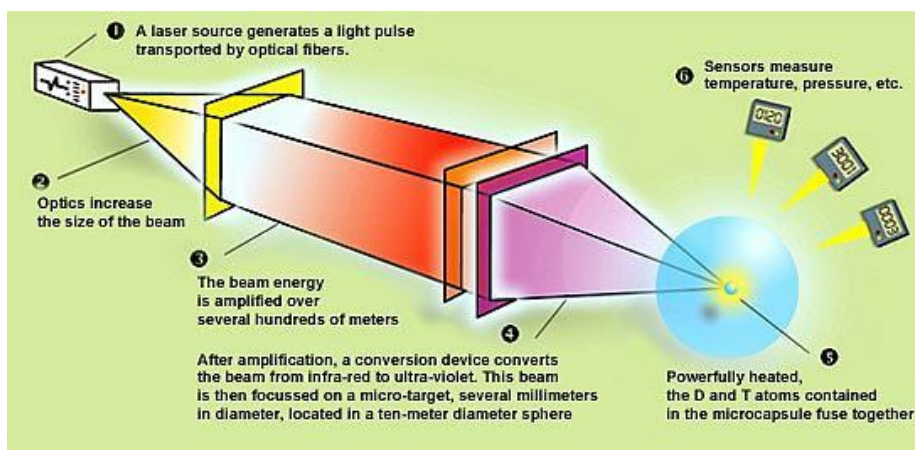
Figure 2-2 Laser amplifying and focussing system in the LMJ facility (source: [23]).
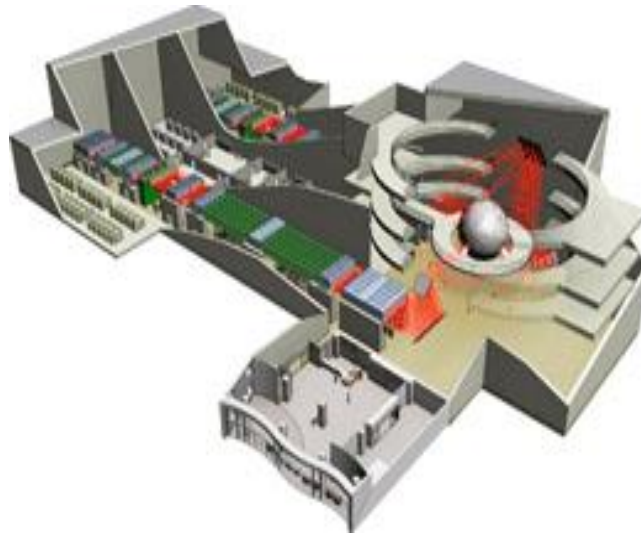
Figure 2-3 Vision of the HiPER project (artist's impression, source: [25]).

In astronomy, large space and ground based telescopes represent the next generation instrumentation capable of delivering answers to many of the intriguing cosmological and planetary questions "nagging" astrophysicists today [27]. The main issue is represented by the construction of their primary segmented mirrors. These will need to be composed of several hundred of segments of 1-2 m size, having shape accuracy of ~20-30 nm RMS and roughness RMS of ~1 nm [2], [27], [28], [29], [30], [31].
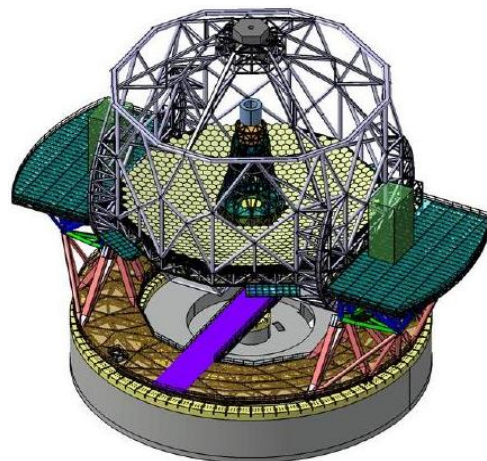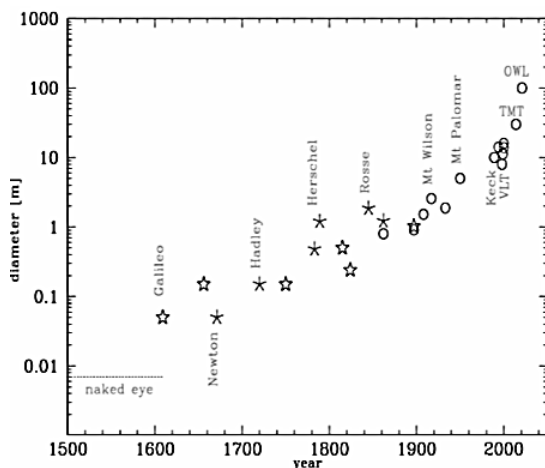
Figure 2-4 *left*: tendency in diameter increase of telescopes primary mirror (source: [31]); *right:* representation of the E-ELT telescope (source: [32]).

Increases in telescope primary mirror diameter have been showing a consistent trend since the invention of reflectors. In **Figure 2-4** (*left*) the history of this

9

growth is shown: the size of the primary mirror nearly doubled every 50 years, with a slight acceleration from the 20th century (see also [31]). Operational large telescopes reach today 8-10 m primary diameter (e.g., Keck-Twin telescopes, VLT, Gemini [33]). In the last few years, however, so-called giant telescopes with primary mirrors ranging from about 20 to 100 m width have been proposed ([2], [31]), thus trying to break the *growth law* (**Figure 2-4** *left*). The scientific reasons for these audacious concepts are linked both to the most recent astrophysical challenges and to the fact that no other instrumentation improvement is possible. Citing Gilmozzi (2004)*, "Now that detectors are at efficiencies close to 100%, large improvements can be obtained only through large increases in diameter."* Moreover, the progresses made by Adaptive Optics (AO) in their Multi-Conjugated form (MCAO) enable near instrumental resolution limit, making large terrestrial telescopes an attractive alternative to risky and expensive space-based solutions. Another valid explanation has an economical background. Extremely large telescopes can be built only within projects based on international cooperation, thus granting wider funds in support for a very long term scientific endeavours.

Examples of such telescopes (proposed or under construction) are E-ELT (European Extremely Large Telescope, ~42m) [32], [34], TMT (Thirty Meters Telescope) [35], [36], GMT (Giant Magellan Telescope) [37], [38] and the OWL (Over-Whelming Large) telescope (~100m) [39].

Besides terrestrial giant optical ensembles, a parallel request of medium-to-large-sized light optics with similar specifications concerns the sector of space based systems. These are relevant for military purposes, environmental monitoring and, above all, astronomy [30]. Significant examples are the James-Webb Space Telescope (JWST) [40], the Advanced Technology Large Aperture Space Telescope (ATLAST) [41], as well as a series of gravity science missions [30], [42].

Another area of interest for the large optics market is Extreme Ultra-Violet (EUV) lithography. This technology is part of so-called Next Generation Lithography (NGL) and is currently a subject of intense academic and company

research (e.g., LLNL, Carl Zeiss, Nikon and IBM). The plan to exploit wavelengths ranging from about 11 to 14 nm will represent a major progress for the industrial production of integrated circuits with respect to current state-of-the-art EUV lithography at 193 nm. The use of such short wavelengths should allow for patterning of structures as small as 20-30 nm width and below, thus going beyond the current 45 nm node [41].

Because of the high resolution required to imprint nanometre sized features, EUV lithography probably constitutes the most complex challenge in terms of optics manufacturing. Optical elements employed so far are 100 – 400 mm lenses requiring form accuracy of 2-10 nm RMS ([2], [44]) and roughness of better than 1 nm RMS. However, radiation at ~13.5 nm would be absorbed by any refractive system. Thus, future EUV optics (XEUV) will be silicon mirrors provided with high-reflectance coatings (Mo/Si). For these revolutionary optical components, even higher specifications in the order of magnitude of few Angstroms are claimed by Carl Zeiss [45].

Figure 2-5 Extreme Ultraviolet lithography: the 193 nm lithography system Starlith1700 (left) and the next generation EUV mirror (right). Source: [45].

2.2 Materials of optical interest

Before describing the different machining methods for the production of ultra-precise optics, an introduction of substrate materials of interest is appropriate. Generally, optical components are made of glasses and glass-ceramics having particular optical properties. In optics, a type of material is principally chosen on the basis of properties like refractive index, transmittance and dispersion (Abbe

number). However, in order to obtain a high quality optical component, certain "secondary" properties become fundamental for the manufacturing phases and the secular stability of the part. These are homogeneity, absence of bubbles, striae or contaminants, chemical resistance, workability (ductility/fragility), stiffness, coefficient of thermal expansion and birefringence. Chemical resistance and workability are very important for processes like grinding and polishing, as they determine the machining parameters and times and the finishing quality.

Most commonly used materials for large optics fabrications were developed with the highly requested property of having low Coefficient of Thermal Expansion (CTE). The reason is easy to understand by considering a simple example of standard optical glass (BK7, CTE = $8 \cdot 10^{-6}$). Here, a temperature variation of $1^{\circ}C$ over 25 mm length already causes ~200 nm deformation which can significantly influence the surface figure.

Pure SiO_2 glass has a naturally small thermal expansion coefficient. For example, the CTE of Lithosil (synthetic fused silica) by Schott is reported as $0.5 \cdot 10^{-6}$/K in the range 25 – 100 $^{\circ}C$ [46]. Further optimisation of the thermal expansion properties could be achieved only by artificially developed glass-ceramics. These are based on a common principle of thermal expansion compensation. Within such materials, silica molecules find themselves in a micro-crystalline phase, with particles of 30 to 50 nm in size embedded in a glassy phase. When heated, the glass expansion is compensated by the micro-crystals contraction thanks to appropriate choice of concentration and dimensions. This mechanism results into expansion coefficients up to two orders of magnitude smaller than the one of standard optical glass.

One of the most common glass-ceramics used in optical applications is Zerodur. Manufactured by Schott Optik, it is well known for being a virtually *zero expansion glass ceramic* [46]. Variation of its Coefficient of Thermal Expansion (CTE) are reported as ~ $0.02 – 0.1 \cdot 10^{-6}$/K in the range 0 – 50 $^{\circ}C$ [46]. It is mainly composed of SiO_2 (50-80%) and Al_2O_3 (20-50%) with traces of oxides of titanium, zirconium, lithium, magnesium and phosphorus. Although its

workability in terms of grinding or polishing is better than other low expansion optical glasses, its production is quite slow and expensive (~1 year [46]). For years, Zerodur optics have dominated the market. It has already been widely used for telescopes optics and hundreds of segments for large astronomical mirrors were produced (Keck, HET, GTC [47]). Thanks to its high performances and low weight it was also chosen for several space applications (Meteosat, Rosat). Particularly for space applications, a "lightening" operation is usually achieved by machining a so-called honeycomb structure on the backside of the bulk. Very similar in terms of chemical composition, two further material types are available to optical engineers: Astrositall by LZOS and CLEARCERAM-Z by Ohara Corporation [48].

Another popular low thermal expansion material is Ultra Low Expansion (ULE) glass by Corning [49]. It is made of 92.5% SiO_2 and 7.5% TiO_2. Its excellent CTE is about 0.03×10^{-6}/K in the range $5 - 35\ ^{\circ}$C. Lighter than Zerodur (2.21 versus 2.53 g/cm^3), it is harder and therefore more difficult to machine by mechanical processes[1]. Its current applications are rather in the field of space optics (Hubble), but telescope mirrors for Gemini and DCT (Discovery Channel Telescope) were also produced. It is also considered a candidate material for the new generation ELTs [50]. An improved ULE version is as well in competition with fused silica for meeting EUV lithography needs [49].

SiC is an alternative substrate material, considered particularly suitable for mirror optics. Although heavier than Zerodur or ULE, it has often been preferred because of its exceptional mechanical properties, like much higher specific stiffness and hardness. However, these same properties worsen the workability of silicon carbide substrates by conventional machining processes, inducing poor removal rates compared to ULE and Zerodur (see, e.g., [51]). Furthermore, its coefficient of thermal expansion can be as high as $2.5{\cdot}10^{-6}$/K. The very high thermal conductivity and temperature resistance (~130 – 280 W/mK), though, support its good dimensional stability. Generally, SiC

---

[1] On ULE, Reactive Atom Plasma has shown the highest material removal rates achieved so far.

substrates are porous and need coatings for practical applications. Constituted of a purely crystalline structure, different arrangements of Si and C atoms are possible (polytypes). There is a variety of methods to produce SiC, with different outcomes. The two most common production techniques are sintering from powders and Chemical Vapour Deposition of SiC. The second one delivers higher levels of purity and absence of porosity, but consists of a slow and expensive procedure. A more detailed description of silicon carbide production is given in [51].

Table 2-1 Properties of optical materials.

Material	ULE	Lithosil	Zerodur	CLEARCERAM	Sintered SiC	CVD SiC	Silicon
Density ρ [g/cm^3]	2.21	2.2	2.53	2.55	2.89	3.212	2.329
Young Modulus E [GPa]	67.6	72.1	90	90	391	466	150
Hardness [Kg/mm^2]	460	522	620	600 – 640	___	2463	1150
CTE α [10^{-6}/K]	0.03 (0–35 ^{o}C)	0.5 (0–200 ^{o}C)	0.02 − 0.1	0.02 – 0.1	2.4	2.2	2.6
Thermal conductivity K [W/(m ^{o}C)]	1.31	1.31	1.46	1.51 – 1.52	155	280	130
Thermal Diffusivity D [cm^2/s]	0.0079	0.0075	0.0072	0.00762− 0.00775	~0.5	~0.4	0.8
Specific Heat c_p [J/(Kg ^{o}C)]	767	770	800	773 − 777	114	___	700

Other less employed materials for optical substrates are Beryllium (e.g., James Webb Telescope primary mirror), BK7 by Corning and Silicon (EUV lithography). In **Table 2-1**, some relevant properties of optical materials are summarized.

2.3 Optical fabrication processes

The quality of optical elements for any type of high level application is evaluated on the basis of physical properties linked to the material, but also to the fabrication process. Thus, from composition and cut of the initial stock, passing through all roughing and re-roughing phases (e.g., grinding) until the final "touch-up", processes involved in optics manufacture need to be able to comply with the finest requirements set by service applications. Properties like stiffness, internal structure or refractive index are chosen to qualify a certain material for a specific application and need to be preserved during machining.

Particular features for the finished component necessitate to be added by the production techniques and consist of reduced surface roughness, minimized subsurface damage and, above all, surface form accuracy. This last term describes how precisely the requested end-form was approximated by the processing methods. Following MacEwen [29], "*Surface figure, also called accuracy, is a measure of the large-scale deviation of the mirror's surface from the specification*".

In practical evaluations of form accuracy, the difference between wished and achieved shape is computed and a *figure error map* is derived. This is characterized over low and medium spatial frequencies, depending on the characteristic (cut-off) length over which the inaccuracy is considered. Two parameters are usually defined to describe form accuracy: root-mean-square (RMS) and peak-to-valley (PV) deviation. The first corresponds to the standard deviation of the figure error over a predefined area, while the second is the absolute value of the difference between maximal and minimal surface deviation. ISO Standards classify these and other surface form tolerance parameters and link them to optical metrology and design [52], [53]. Such

classification occurs based on mathematical representations of surface optical aberrations by means of so-called Zernike polynomials (see, e.g., [54]). Recently, a new parameter called *PVr* has been introduced by Zygo [55], [56]. The PVr (*r*: robust) redefines the peak-to-valley of a surface topography map based on high order (36th) Zernike fits. Its purpose is to moderate the influence of localized spikes or pits when reporting the overall surface height.

Although the required surface form accuracy of an optic generally depends on customer specifications, a rule of thumb for meter-class optics is that this should be kept within ~ 30 nm RMS ($\lambda/20$, $\lambda = 633$ nm) residual *wavefront error* [29]. Wavefront error is the actual deviation of light wavefronts, after reflection (or transmission) by the optical surface, from an ideal front-shape. This concept is often considered more rigorous because it includes the fact that the performance of the optical surface figure is wavelength dependent. When the wavefront error is specified, though, its relation to the figure error must be also indicated. For reflection optics, generally the figure error is taken as the wavefront error divided by two.

The other surface qualifier, surface texture (micro-roughness), is usually identified by RMS values (R_q or S_q), but several other parameters are of common use as standard surface topography qualifiers. Typically, roughness assessments are performed by means of profilometres or white-light interferometers (see Appendix D), which deliver R-parameters or areal S-parameters, respectively. For a long time, ISO standards have been available for profile roughness measurements only [57]. In 2012, ISO 25718 Part 2 and 3 for areal parameters standardisation were finally approved [58], [59]. The general roughness requirement for large optics (section 2.1) is ~1 nm RMS, although more stringent specifications apply to EUV lithography at 13 nm wavelength.

For the assessment of optical surfaces topographies (form and roughness), a popular mathematical tool are Power Spectral Density (PSD) plots [60]. In the Fourier domain, PSDs allow identifying fine features and patterns as a function of the spatial frequency, thus permitting to investigate the residual errors

frequency components (e.g., mid-spatial frequencies) or infer the influence of a machine tool shape [60], [61], [63]. In some cases, the required surface finish specifications can also be expressed in terms of the PSD magnitude over the spatial frequency (e.g., NIF optics [64]).

Finally, subsurface damage is identified by the size and number of micro-cracks and residual stress, principally induced by first stage machining processes like grinding or milling (see, e.g., [65] and [66]).

In general, successful compliance with the manufacturing specifications of new generation optical surfaces ultimately requires the use of ultraprecision machine tools. These are designed based on the concept of determinism and following key principles to assure highest performances in terms of process accuracy, repeatability and resolution. Several authors (Bryan, McKeown, etc.), over the years, have reported and described the aforementioned approach to machine tool design and discussions on this matter can be found, e.g., in [67] or [68].

In particular, the ultra-precision production chain for optical fabrication generally consists of a first rough cut by rigid-tool grinding, followed by a re-roughing procedure to reduce machining marks (lapping). Finally, advanced polishing techniques are needed to achieve figuring and smoothing of the surface down to nanometre level. As mentioned in the introduction, this last step has recently been the object of fervent research because it builds a "bottleneck" for the production of ultra-precision optical surfaces. The majority of contact polishing processes result in rapid material removal and roughness reduction, but can show unpredictable behaviours of the tool and consequent slower convergence. In contrast, non-contact alternatives like IBF are capable of higher accuracy, but at the cost of time-consuming and expensive process conditions.

Certainly, the quality of metrology equipment and its integration in the optical manufacturing chain are as important as the development of the fabrication technologies. In fact, "*To achieve the optical specification in a reasonable time requires measurements with an unprecedented combination of accuracy, stability and speed.*" (Peggs et al., 2004, [69]). Therefore, the development of a novel UPS fabrication chain capable of complying with the challenges of the

large optics market necessitates a parallel implementation of existing and growing measurement technologies. Companies like Taylor-Hobson [70], Zygo [55], 4D-Technology [71] or ESDI [72] have been researching solutions for contact and non-contact metrology applications. Their main efforts were concentrated on the elimination of environmental influences (vibrations, air turbulence, thermal effects, etc.) and of dimensional and temporal limitations, as well as on the development of free-form (aspheric) surface measuring capability. Cooperation between metrology and optics manufacturers is today strongly encouraged and coupling of optical testing and fabrication facilities is, in many cases, already an existing reality (Zygo [55], QED [73], Sagem [74], [75], Zeeko [76]).

A review paper listing the precision technologies employed in large optics manufacturing, as well as the currently associated optical testing techniques has been recently published by Shore et al. [42]. In the next sections, the principal manufacturing technologies constituting the state-of-the-art for the optical fabrication chain are described.

2.3.1 Grinding

The first step of the production flow of medium and large sized optical components is the grinding process. A detailed description of high precision grinding process and machine tools for large optics manufacturing can be found in [77] and [78]. Grinding is a fully deterministic, position controlled process. It is usually based on an iterative procedure where different types of grits on grinding wheels allow going from a rough to a series of semi-finish and finishing cuts by means of finer abrasives. Grinding machining can be performed by fixed tool or in loose mode and material removal can take place in ductile or brittle mode. Less damage is caused to a substrate by ductile grinding because of the small depth of cut (~50 nm), although this results in lower removal rates. Grinding is seen, mainly, as a mechanical removal process, with a negligible effect of chemical reactions between abrasives and substrate.

Different kinds of machines are available for grinding modes. This can depend, for example, on whether they have fixed or rotating work-piece table. Also, the

position of the substrate with respect to the tool determines the characteristics of the process parameters. In **Figure 2-1 (b),** two grinding modes are showed for cup-wheel grinding: in one case (right sketch) the substrate is kept horizontal, while the wheel is tilted by an angle. Pitch and cutting depth are controlled in the directions identified as z_c and z_t respectively. In the other case, the inclination angle is given by the tilted workpiece with the wheel moving along z_c and z_t.

The principal grinding process parameters are depth of cut, grinding wheel speed, work-piece speed, feed per revolution. The choice of such parameters determines the process speed, but also the level of the resulting machining accuracy, texture and subsurface damage. Key to an accurate and rapid grinding process is also the *machine loop stiffness* (static and dynamic) which determines the quality of tool motion and ductile material removal [79]. From a point of view the energetic process assessment, a grinding process is often evaluated based on the *grinding power* and the *specific grinding energy* (see, e.g., [77]).

Fundamental for the performance of the process are the wheel specifications. For *plunge grinding* the tool is larger than the workpiece, while for more classical *traverse grinding* a sub-aperture sized wheel is used.
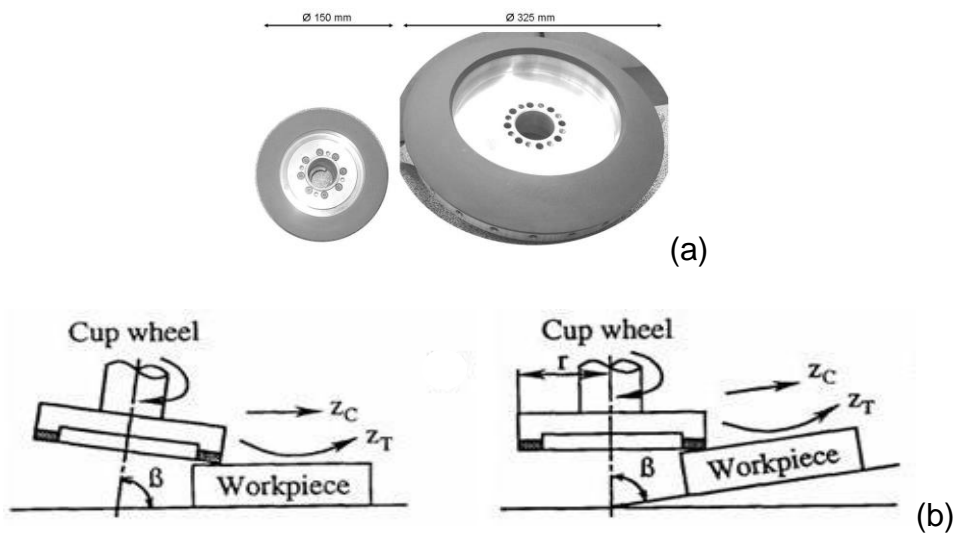
Figure 2-6 (a) resin bonded diamond grinding wheels; (b) two grinding modes (source: [77]).

A grinding wheel can have different shapes[2], bond materials (metal, resins, polyimides) and abrasive grits (Al_2O_3, diamond grains, SiC). For the shaping of optical elements made of glass or ceramics, diamond abrasives are usually employed. In Europe, the sizes of the grains are defined according to FEPA (Federation of European Producers of Abrasives) [80].

The size of the abrasives, together with the cut depth, distinguishes the iteration cutting stages. Successful grinding cannot take place without a dedicated coolant system. Here, a water or oil based liquid helps reducing friction, wear and, above all, heat effects on tool and substrate. Coolant also removes chips and swarfs produced by the machining.

Prior to grinding, an important step is *conditioning* of the grinding wheel. This consists of two processes: *truing* (or *forming*) and *dressing* [77]. The first can be accomplished, e.g., by means of a so-called diamond *truing tool* and the purpose is to restore the wheel's surface to a perfectly straight, flat, smooth shape. Dressing is a procedure where the bond material is removed to make the abrasive grains protrude, thus increasing wheel sharpness and reducing unwanted friction.

For loose abrasive processes, the volumetric material removal rate (MRR) is usually calculated from Preston's equation:

$$MRR = \frac{\Delta V}{\Delta t} = K \cdot P \cdot v \cdot A \qquad \text{(2-1)}$$

with K: material constant, P: contact pressure, v:velocity, A: contact area. For fixed tool grinding, instead, MRR are inferred from the process parameters:

$$MRR = a_e \cdot f_r \cdot v_w \qquad \text{(2-2)}$$

where a_e is the depth of cut, f_r is the feed per revolution and v_w the surface speed [77]. It is reported [77] that ductile regimes enable higher removal rate in parallel grinding than in cross grinding.

---

[2] Grinding wheels shapes are identified by ISO 6104.

Figure 2-7 *left*: **The Kodak OAGM 2500 built by Cranfield Precision (source:** *http://cranfield-precision.blogspot.co.uk/2011/10/kodak-oagm-2500-off-axis-grinding.html*)**;** *right* **The BoX machine at Cranfield University (source: [79]).**

Grinding machining enables very high material removal rates, suitable for the initial shaping of the surface. Examples of removal rates between 1-5 mm^3/s are reported for the Off-Axis Grinding Machine (Kodak OAGM 2500, **Figure 2-7**, *left*). The BoX machine (Cranfield University Precision Engineering, **Figure 2-7**, *right*), designed for rapid achievement of high form accuracy, can remove up to 200 mm^3/s [77]. The final residual surface error that can be obtained with these machines is 2-5 μm PV respectively [77].
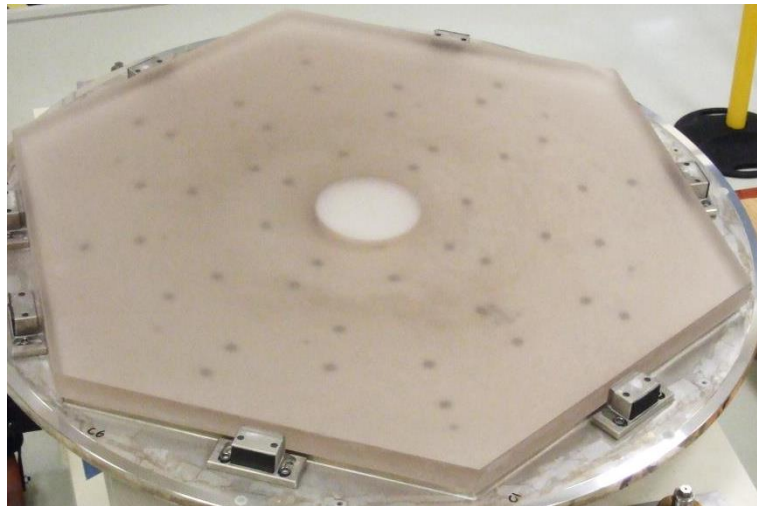
Figure 2-8 ULE hexagonal segment ground on the BoX machine.

2.3.1.1 Subsurface damage (SSD)

Grinding processes are known to cause micro-cracks and related subsurface damage (SSD). One reason is connected to vibrations that provoke a jerky motion of the wheel at the point of contact with the workpiece. Good dynamic loop stiffness between tool and workpiece is therefore required to minimize this issue.

In **Figure 2-9**, the generation of a micro-fracture is illustrated. At first, the indentation causes a plastic deformation. A deeper indentation, then, leads to the formation of a *median crack* that will split with increased force. When the load is released, the main cut closes, but the fracture walls structures result in mismatching. Therefore, stress builds up within the first layers of the bulk and, from the main cut, a series of lateral and radial cracks initiate through an intermediate plastic zone. The size of these damaging structures can vary from < 1 µm to several hundred micrometres. They also cause additional residual stress in the very first substrate layers. A number of non-contact and destructive investigation techniques to analyse SSD exist today (HF etching, wedge method and ultrasonic Rayleigh wave measurement[3]).
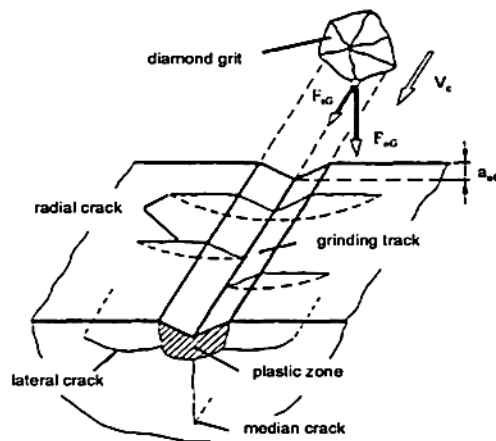
Figure 2-9 Cracks initiation along grinding track (source: [77]).

A more detailed description of subsurface damage and inspection methods can be found in [77], [81], [82] and [83]. Here, results concerning the amount of

---

[3] Less common due to the low spatial resolution.

subsurface damage in ground substrates made of materials of optical interest (ULE, fused silica, Zerodur) are reported.

Traditionally, polishing techniques are known to minimize or even eliminate SSD. However, recent developments saw plasma etching techniques (e.g., RAP) as a rapid method to reduce surface stress and facilitate the removal of micro-cracks from ground or milled surfaces by means of lapping tools [60].

2.3.2 Polishing

Polishing is probably one of the oldest finishing techniques in manufacturing of optical glass. For decades, hand-polishing has been an "art" performed by skilled and experienced craftspeople. Only recently, a certain extent of determinism was introduced with the advent of CNC polishing machines.

Polishing is a chemical-mechanical (*tribochemical*) removal process. The removal mechanism is reckoned to take place by brittle fracture, chemical attack and plastic flow. A number of studies have been carried out in order to investigate the fundamentals of the material removal processes involved [84]. Some of these have shown that a complex overlapping of chemical reactions take place between glass surface, slurry/water and polishing pad material (e.g., cotton). Moreover, the abrasive crystals tend to break and chips from substrate and powders undergo chemical reactions catalysed by particle lattice defects [84] (**Figure 2-10**). Also, abrasion causes heat that enhances the chemistry and transports the diluted chips containing solution. A review of such model mechanisms can be found, e.g., in [85]. However, despite such protracted research, the basic physics and chemistry of polishing processes are still scarcely understood. Therefore, polishing needs to be performed in iterative manner to compensate for the process unpredictability that derives from such unknowns.
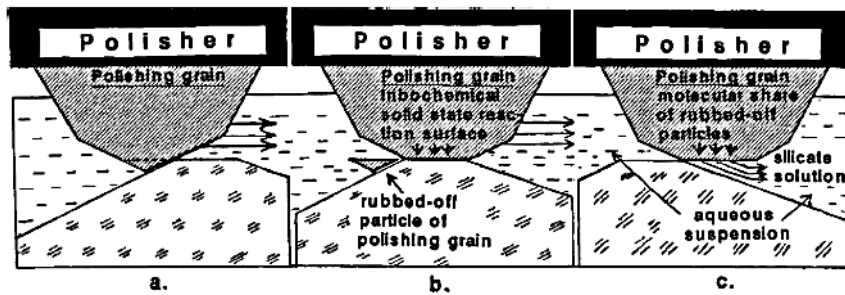
Figure 2-10 Illustration of the polishing mechanism (source: [84]).

In a classical polishing process, the substrate is sprinkled with slurry to which hard abrasive particles are added. Water based emulsions are commonly[4] used slurries. *Abrasive powders* containing crystalline particles like Al_2O_3, CeO_2, Fe_2O_3, SiC or diamond are added to the fluid. Their size can vary from several micrometres down to few tens nanometres, depending on the polishing stage. A loaded *pad* mounted on a dynamic (rotating) polishing head provides "stirring" of the suspension and ensures a friction motion of the particles against the substrate. In conventional precision polishing, a common fluid used to cover the pad is pitch (*pitch polishing lap*). The quality of the finishing, then, depends not only on slurry and abrasives, but also on the effects of the pitch preparation and conditioning [86]. More recently, pitch laps have been replaced by polyurethane pads that achieve higher material removal rates [87].

Modern polishing machines are provided with CNC motion systems to achieve a more deterministic figure correction. Equipment for ultra-precision figuring makes use of sub-aperture laps that produce a characteristic imprint called *influence function* (see section 3.1). This acts like a spatial filter on the surface figure error and the actual figuring process is therefore driven by numerical algorithms based on dwell-time methods (see also section 3.1). Downsides of traditional polishing are mainly due to a certain amount of unpredictability of the tool behaviour. Parameters like temperature and quality of compound affect pitch lap, pad and slurry in different ways. In fact, temperature variations cause deformation of the head and change in response of the emulsion because of

---

[4]"Recipes" for slurry and polishing agents' mixtures are usually companies' ownership.

alteration of viscosity, density or elasticity. Thus, the load pressure distribution can fluctuate in a non-repeatable manner and provoke residual figure error. Additionally, tool-to-tool stability is not assured. Furthermore, the pad tends to undergo unavoidable warping and even slip at the edges of the part, so that chamfers of several millimetres are often left unprocessed.

The advent of CNC controlled polishing allowed for partial real-time compensation of these inaccuracies, but, at present, more extensive research is still needed to achieve full deterministic control [3].

A well-known problem of polishing heads is the misfit between tool shape and surface geometry. While this issue can be easily sorted for flat and spherical surfaces, aspheres and free-form surfaces needed the introduction of compliant or small-tool solutions, as well as dedicated tool motion paths (see, e.g., [88]). An example of classical sub-aperture polishing facility provided with compliant pitch-tool is the Super-Smooth Polisher by Canon (CSSP). This facility has 6 DOF and the figuring capability is based on a complex tool-path algorithm. Machining of parts up to 500 mm diameter is possible on Canon's CSSP and figure error corrections down to 60-80 nm PV, with 0.15-0.18 nm RMS roughness have been reported. However, very long processing times have to be accounted for due to the low level of deterministic control on the process [89].

A further example is the Stressed-Lap Polishing facility at the Steward Observatory, at the University of Arizona (US) [90]. Principally designed for the polishing of very large monolithic mirrors, this technology is based on a 1.2 m wide aluminium lap-plate, mounted on actuators that allow for the tool to deform according to the local surface curvature. A detailed description of this technique can be found in [91]. Currently, this technology is being mainly employed for the final polishing of the Giant Magellan Telescope mirror segments [37]. The first of six off-axes near-parabolic segments (8.4 m diameter each) was recently figured down to 390 nm RMS [92], [93] (**Figure 2-11**).
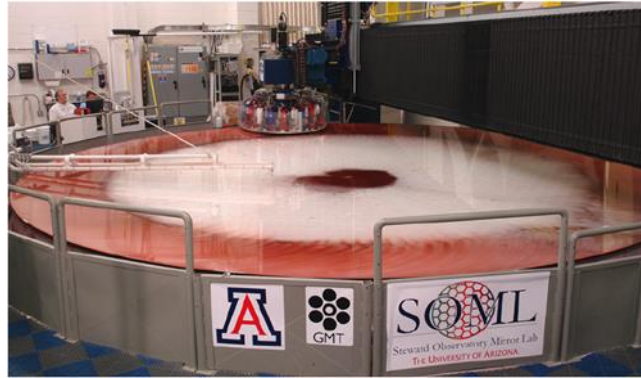
Figure 2-11 First Giant Magellan Telescope segment being polished with a 1.2 m stressed lap (source: [92]).

Conversely, a revolutionary type of small-tool polishing technology is Zeeko's "precessions" polishing [76], [94]. In this process, 7-axis CNC machines host a particularly shaped tool called *bonnet* (**Figure 2-12 *left***).

The bonnet consists of a spherical inflated membrane covered with a non-pitch flexible polishing surface. The advantage of this membrane is that it always maintains the same contact with the substrate by independently varying the polishing pressure and the spot size. In this way, a deterministic behaviour of the tool is accomplished.

In precession polishing, the rotating head tool is brought into contact with the surface at an angle (**Figure 2-12**). On the contrary, a static, pole-down spinning tool would exhibit zero surface-speed, hence zero removal, at the centre.

The surface is polished with the inclined bonnet by precessing it in four directions perpendicular to each other. This allows smoothing the rotation marks that would otherwise be left by each single precession position. The removal rates follow a version of Preston's equation formulated for a radial dependence of material removal [94]:

$$D(r) = k \cdot P(r) \cdot S(r) \tag{2-3}$$
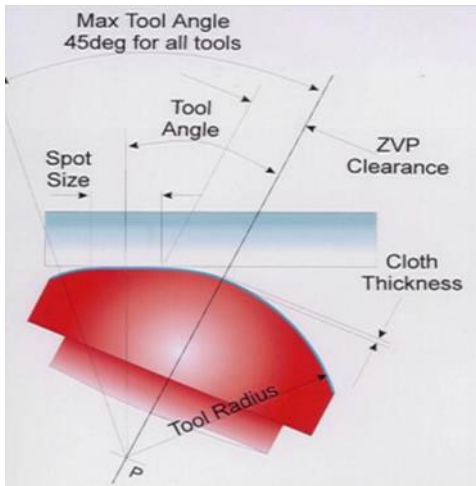
Figure 2-12 Zeeko's Precession polishing: bonnet schematic (*left*, source: [94]) and IRP1200 figuring facility (*right*, source: [76]).

with P and S as pressure and angular speed distributions, and k as material related constant. An example of material removal depth versus rotation speed performed with CeO_2 slurry is shown for BK7 in **Figure 2-13**.
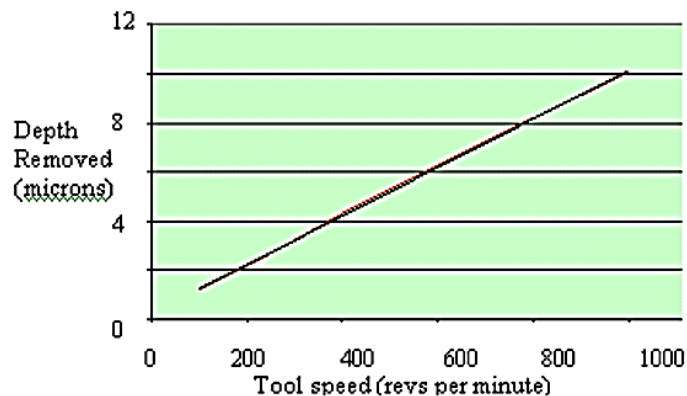
Figure 2-13 Removal depth versus tool-speed for BK7 with CeO_2 polishing fluid (source: [94]).

Depending on substrate and abrasive types, volumetric removal rates are reported in a range going from ~0.03 mm^3/min to more than 200 mm^3/min [2]. Precession polishing machines can also be implemented with a hybrid process tool called *grolishing* ("grinding" + "polishing") bonnet: this is provided with hard pellets that enable to achieve the highest removal rates for the precession process and is mainly employed as post-grinding procedure to remove grinding marks [95].

In terms of figure correction capability, various examples can be found on Zeeko's website [76]. One of the most recent achievements concerns the finishing of an 84 m radius of curvature master sphere (1.7 meters across corners). This is necessary for the calibration of an optical test tower setup that will be used for the metrology of E-ELT segments.
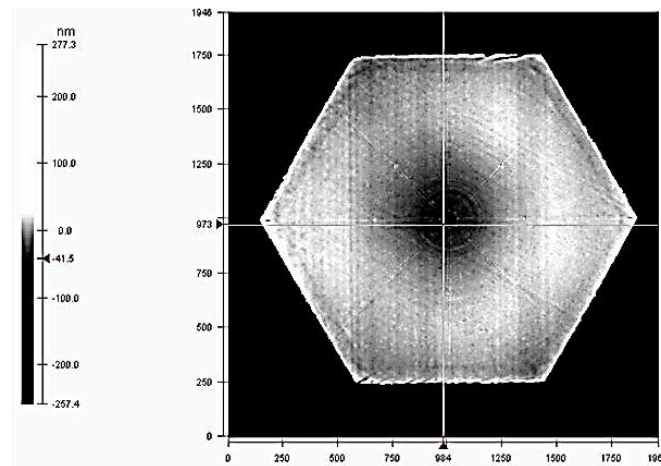
Figure 2-14 Residual figure error map of the 84 m ROC master sphere after processing with Zeeko's precession polishing (courtesy of OpTIC Technium).

The part, originally ground in Cranfield on the BoX machine, was processed on an IR1600 Zeeko machine where residual figure error of ~17 nm RMS, ~88 nm PV, was achieved after ~300 hours polishing (confidential communication from OpTIC Technium, St. Asaph, North Wales, UK).

2.3.3 Magnetorheological Finishing (MRF)

An innovative kind of figuring and smoothing technology is Magnetorheological Finishing (MRF). The principle of MRF was discovered in Belarus at the end of the eighties and later transferred to the Centre for Optics Manufacturing (COM) and optimized. In 1997-98 MRF was commercialized by QED Technologies [73], [89], [96]. In **Figure 2-15** *(left)*, the principle of the process is sketched. A magnetorheological (MR) fluid containing non-magnetic abrasives (e.g., CeO_2) and carbonyl iron particles in aqueous solution is pumped through a nozzle onto the processing wheel. Here, a magnetic field of the order 10^4 Gauss is generated by an electromagnet.
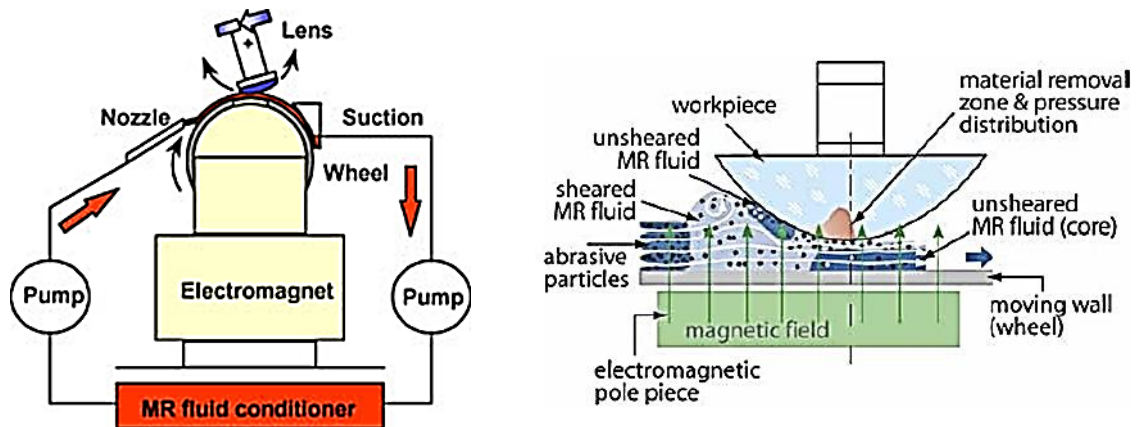
Figure 2-15 (*left*) schematic of an MRF machine (source: [89]); (*right*) model of the contact zone (source: [73]).

The MR fluid becomes stiff, thus creating a polishing-like lap. In the sketch, the work-piece, mounted on a spindle, is finally brought into contact with the hardened fluid that steadily conforms to the contact surface shape. After leaving the contact spot, the MR liquid is depleted into a suction system and re-cycled.
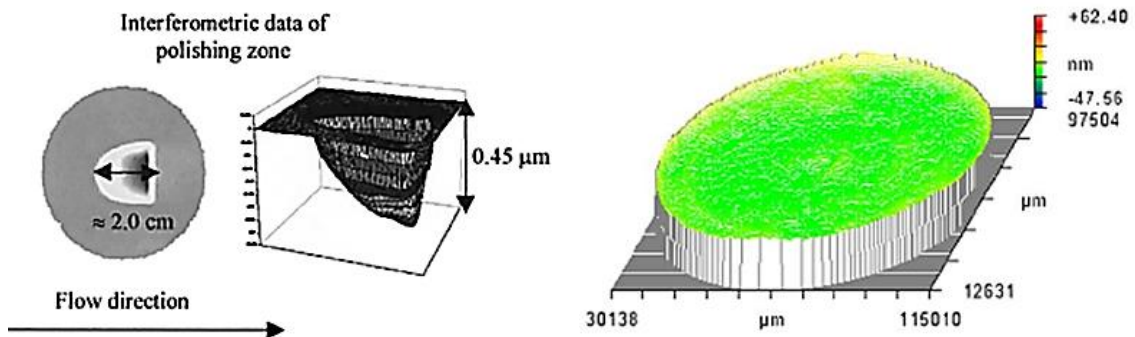
Figure 2-16 *left*: MRF removal spot (source: [85]); *right*: figure error correction result on small optic (100 mm Ø) with edges control– 30 nm PV (source: [97]).

The material removal mechanism of MRF is showed in **Figure 2-15 *(right)*.** According to a model proposed by Kordonski [85], regions of sheared and unsheared material form in the MR fluid. The unsheared cores cause a shear stress gradient by preferentially reducing the gap between wheel and surface towards the draining zone of the flow. This mechanism generates an oblique spot footprint with highly deterministic behaviour (**Figure 2-16, *left***). Such

consistency is mainly assured by the secular stability of the rheological fluid. In fact, the fluid properties are maintained by the continuous reconditioning system that guarantees repeatability of removal within a few percents for machining durations up to 200 hours [4].

The main control parameters of MRF are wheel speed, magnetic field intensity and type of abrasive particles. However, like many polishing processes, interactions of multiple factors can affect the removal rates. Their complexity was object of a study by DeGroote et al. [98]. In this article, Preston's equation was upgraded by considering surface mechanical properties, abrasive size and concentration, glass chemical durability and surface energy. This model showed good agreement with experimental data.
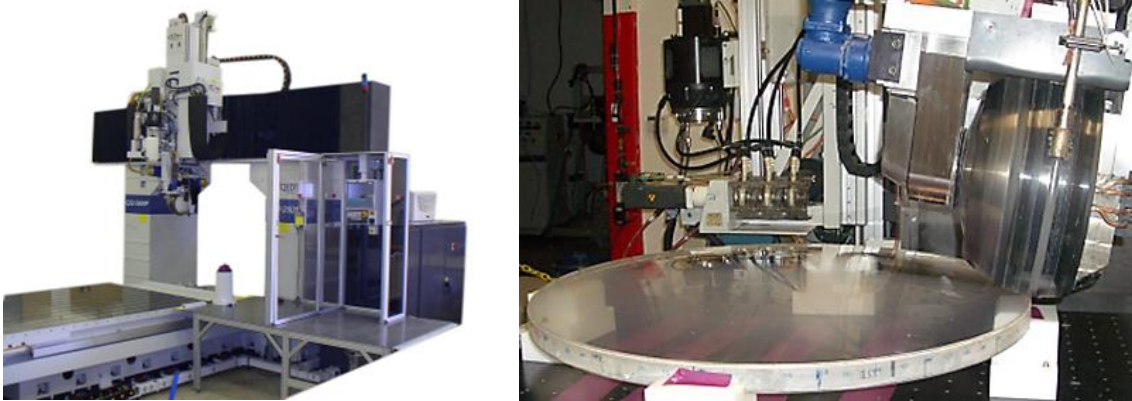
Figure 2-17 *left:* **the Q22-2000F MRF figuring machine (source: [73]);** *right:* **processing of 1.3 m diameter fused silica mirror on the Q22-950F machine (source: [4]).**

From this same paper and from [85], MRF removal rates on different types of optical glass can be deduced as being in the range 0.5 – 20 μm/min. For a 20 mm wide spot (**Figure 2-16 (***left***)**) volumetric removal rates can be estimated as 0.3 – 13 mm^3/min.

Early works by QED using MRF were performed on small-to-medium sized (~10 – 400 mm) optics due to the originally non-dynamic nature of the tool. Excellent results were achieved with residual figure error of only few nanometres RMS and roughness < 1 nm RMS. Recently, QED have directed their interests towards the large optics market with a range of new machines provided with a

dynamic, face-down MRF tool (**Figure 2-17, *right***). For instance, the Q22-2000F (**Figure 2-17, *left***) is currently the largest existing MRF machine with a 2 m diameter figuring capability. A noteworthy achievement was the figure correction of a 1.1 m diameter mirror from 84nm (λ/7) to 9nm (λ/70) RMS in two iterations, for a total machining time of 20 hours (see [73]).

QED also envisages MRF as potential technology capable of taking charge of all the main post-grinding phases, including removal of SSD and tool marks. The manufacture of two 840 mm diameter fused silica mirrors is an example of such implementation (**Figure 2-17, *right***). In that application, ~7 µm PV figure error were removed on a Q22-950F machine and the target specification (0.14 µm RMS) was met after 256 hour machining time [4]. The example indicates that even this deterministic process is still far from meeting the ten hours target for large optics figuring.

2.3.4 Edge effects

Contact abrasive processes suffer from well-understood limitations whenever the tool overhangs the workpiece edge. In these cases, warping of the tool head will occur while the pressure over the tool portion still in contact with the surface is redistributed, with consequent variation of the tool influence function [97]. A simple, but somewhat impractical solution is the use of wasters. These are extensions of the workpiece edges made of sacrificial bits of the same material that are glued adjacent to the part boundaries. To avoid the application of wasters, the minimisation of edge misfigure (roll-off) requires particular approaches like the use of different tool-sizes, pressure control near the boundaries or compensation by complex modelling [62], [97], [99], [100]. In **Figure 2-18**, a model for a circular tool overhanging the workpiece edge is represented. In this theoretical analysis, the tool overhanging ratio S_{tool} is defined (see **Figure 2-18**) and the effects of overhang distance on the pressure over the substrate are studied [97].

As a consequence of roll-off effects, many optics have a clear aperture that is reduced by several millimetres to the part outer edge. Some even tighter requirements are specified for the segments used for the mirror assembly of

extremely large telescopes [34]. The reason is linked to diffraction effects caused by segmentation that could be enhanced by turned down/up edges [101].
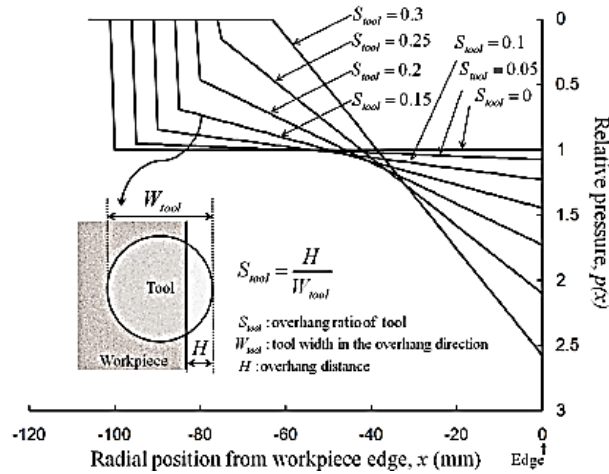
Figure 2-18 Dependence of the overhanging ratio S_{tool} on pressure and distance from workpiece edge (source: [97]).

Non-contact processes like Ion Beam Figuring and Reactive Atom Plasma present an effective means to reduce edge roll-off concerns. In fact, energy beams can be slickly carried across substrate edges with minimum effects on the footprint performance. In section 6.3, the figure error edges after RAP processing are discussed.

2.3.5 Ion Beam Figuring (IBF)

Ion Beam Figuring (IBF) is a prime example of a non-contact figure correction technology for ultra-precise optics. Initiated in the seventies (Belarus), the processing method is based on simple sputtering of substrate atoms by accelerated ions. The typically used source is an ion gun of Kaufman-type [102]. This consists of an ionization chamber where a thermionic cathode filament provides electrons. These are magnetically confined to favour collisions with a noble gas, like Ar or Xe. In this way, the gas is ionized and can be accelerated by an electric field (acceleration chamber) to be expelled with high kinetic energy towards the substrate. Before hitting the target, ions are usually

32

neutralized by an additional electron beam in order to avoid electrostatic charging of the substrate.

IBF needs to be operated in high vacuum chambers at pressures of ~10^{-6} mBar to avoid energy losses by collisions with atmospheric particles. The ion source is operated at energies below 2 keV and the resulting distribution of atoms impacting the surface produces a near-Gaussian footprint. The material removal depends on parameters like pressure, size of the ion beam (typically a few centimetres) and the substrate material. Typical removal rates are in the order of magnitude of few tens of nanometres per minute (see, e.g., [5] and [7]). The use of higher energy sources would improve this aspect, but also induce more heat onto the substrate. A way to increase the rate of volumetric material removal by means of low energies is to use broader beams, but at the cost of losing the figuring resolution.

Early applications of IBF as an optical figuring technique were reported by Wilson et al. in 1988 [103]. In this work, figure correction of 30 cm diameter optical flats of fused silica, Zerodur and copper was carried out and residual error as good as 171 nm PV was reported. Investigations of roughness were also carried out and degradation was evidenced, in particular, for polycrystalline materials.

Following Wilson's demonstrations, Eastman Kodak developed the 5-axis Ion Figuring System (IFS, **Figure 2-19**), capable of hosting 2.5m x 2.5m x 0.6m optics [104]. Significant achievements by the Kodak team are reported in [104] and [105] and concern the figure correction of 0.5 m diameter ULE mirror and of an off-axis ULE petal (1.3 m across corners).

The work done on the 0.5 m mirror achieved a residual figure error of 10 nm RMS. During the process, temperatures were measured on the back of the substrate by means of thermocouples. The purpose was to monitor temperature changes that might be dangerous for the structure of the optic. The conclusion was that no significant thermal effect had been taking place. The ULE substrate of petal geometry was figure corrected to a final form accuracy of 9.5 nm RMS in four iterations, for a total processing time of nearly 100 hours [105]. Finally,

over a four years period, the IFS was used for the figure correction of 84 hexagonal 1.8 m segments for the 10 m diameter Keck telescope primary mirror [106]. The segments had several micrometres departure from specification (PV and RMS), and were figure corrected down to ~60 nm RMS.
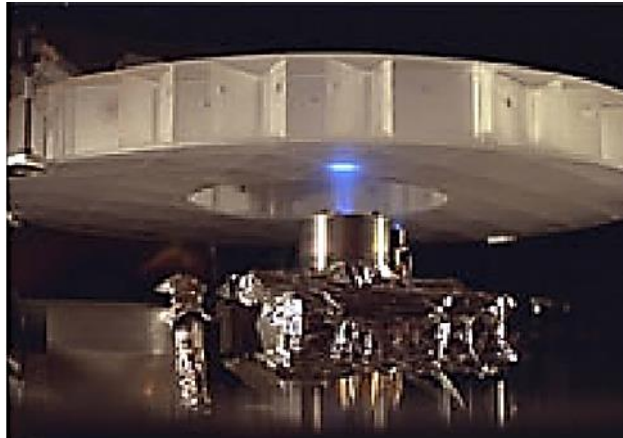
Figure 2-19 Internal view of the IFS Kodak (ITT) ion beam figuring facility (source: [42]).

During the same period, CLS (Centre Spatial de Liège) built a 1.5 m^3 ion beam figuring facility. Here, optics up to 20 cm diameter can be processed. An interesting investigation on thermal effects was carried out by Gailly et al. at CLS [6]. By means of an infrared camera, temperature measurements were carried out on small BK7 and Zerodur disks (105 mm diameter, 12 mm thickness). During IBF processing of these substrates, temperature values up to 140–150 ^{o}C were detected on the surface being scanned. On BK7, comparison of the surface measured before and after IBF showed distortion of the etched figure and stress due to local heat (spot test). If such distortions were permanent this would mean additional figure error to be accounted for at the end of a processing cycle. On the contrary, the same test performed on Zerodur didn't give any measurable evidence of thermal deformation. This investigation should be taken as a lesson for any energy beam process, including RAP. In fact, even if borosilicate glasses like BK7 can be promptly machined the same way as lower thermal expansion materials, control of the work-piece form will be an issue in case of non-elastic deformations.

Another renowned centre working in the area of optical surface finishing is the *Leibniz Institut für Oberflächen Modifizierung* (IOM – Leibniz Institute for Surface Modification) [107], founded in 1992 in cooperation with the University of Leipzig (Germany). An IBF facility, UPFA-1, was developed by IOM in cooperation with NTGL and OPTEG and can host optics up to 700 mm diameter. High figuring performances of better than 1 nm RMS over small substrates (up to 100 mm diameter) were achieved on UPFA-1 by means of advanced tool-path algorithms [5]. On this facility, several footprint sizes can be obtained by adapting the ion beam through a shaping diaphragm. In this way, a wider spectrum of spatial frequencies correction capability can be covered with the same tool. Alternatively, the same purpose can be achieved with the use of semitransparent masks or shutter-masks that enable the modulation of the ion beam for the creation of thinner footprints [108].

Although ion figuring methods are known to slightly degrade surface roughness, two particular IOM variations of the technique, called *ion beam direct smoothing* and *ion beam planarization*, allow for improvements of the surface texture. The first exploits surface relaxation mechanisms to dominate the topography evolution and obtain ultra-smooth conditions. Conversely, the working principle of planarization is based on a sacrificial layer used to coat the surface which is subsequently bombarded at a specific angle. This angle is chosen so that the removal rate of the sacrificial layer matches the one of the surface. Micro-roughness results by both methods can be better than 0.5 nm RMS (R_q) [109], but applications are limited by the type of substrate and the complexity of the procedures. More details on ion smoothing techniques at IOM can be found in [110].

Besides classical IBF, IOM implemented two further techniques for optical surface processing: Reactive Ion Beam Etching (RIBE) and Plasma Jet Machining (PJM). These are chemistry based material removal processes that closely resemble the Reactive Atom Plasma technology (more in the next sections). A review paper describing ion figuring and smoothing capabilities at IOM has been recently published by Arnold et al. (2010) [109].
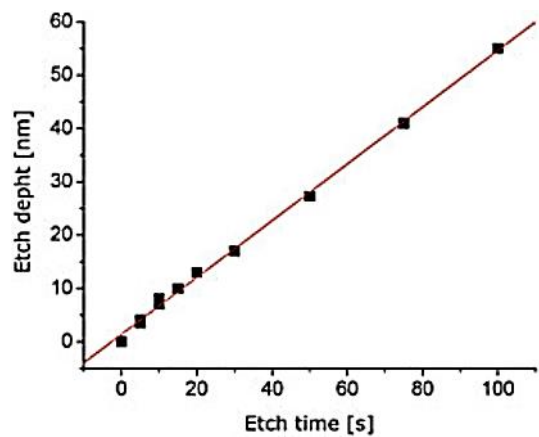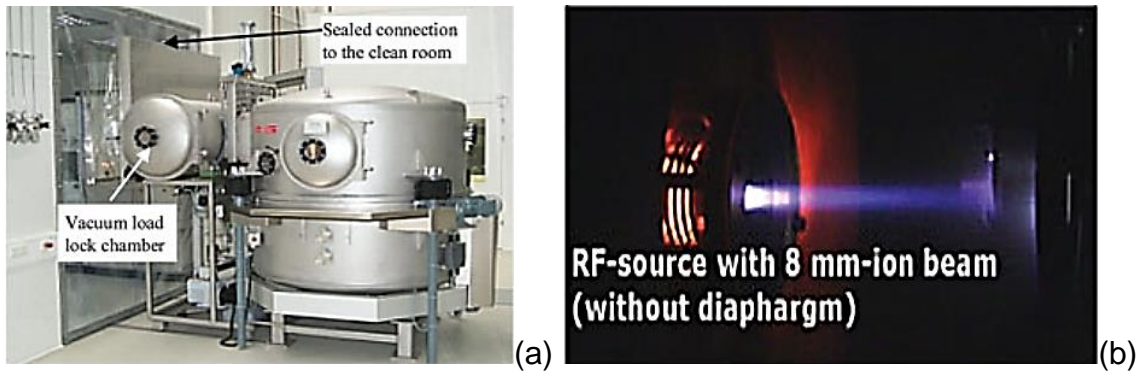
Figure 2-20 UPFA-1 IBF facility at IOM (a) and its ion gun (b); (c) Removal rates of a 0.5 mm FWHM ion beam (source: [5]).

2.3.6 Alternative techniques

In this section a number of alternative finishing processes are briefly presented. Some hybrid techniques, as well as surface smoothing methods are covered. These were mainly implemented as surface processing techniques to compensate for some of the disadvantages of the methods discussed so far.

Reactive Ion Beam Etching (RIBE): In this technique chemically reactive gases like CF_4 or SF_6 are added to a classical IBF ions beam. In this way, besides atomic sputtering, chemical etching takes place under ionic enhancement. The method was, once again, proposed by IOM for a more rapid finishing of small optics. In fact, higher material removal rates are achieved with respect to IBF. For example in [88] it is reported that 23 μm were removed from a 25 mm wide fused silica at a rate of 140 nm/min. However, RIBE is still operated in vacuum and system complexity doesn't contribute to process stability [2].

Plasma Jet Chemical Etching (PJCE): This process was developed by IOM in cooperation with Carl Zeiss as low-vacuum rapid etching alternative to IBF [111]. This makes use of a microwave driven reactive plasma jet, operated at 10-600 mBar pressure [112]. An inert (Ar, He) and reactive (CF_4, SF_6) gas mixture is used. Removal rates up to 10-50 mm^3/min have been recently achieved [108], [112]. Figuring capabilities are in a development phase. PJCE shows plenty of similarities to RAP and has acted as precursor process to an atmospheric plasma machining technique at IOM (see [108], [109], [111], [112] and section 2.3.10).

Gas Cluster Ion Beam (GCIB): This processing method is used for roughness reduction on pre-figured substrates. Operated in vacuum, the surface is bombarded with inert or active ions clusters (~2000 atoms); when the cluster hits the substrate it breaks, distributing its kinetic energy among its individual components. Spiky features are preferentially attacked by lateral sputtering which results in surface smoothing. This technique can be applied to improve ISO standard flats; however the need for complex additional etching steps makes it unsuitable for large optics [88].

Fluid Jet Polishing (FJP): Invented at Delft University of Technology [113], this hybrid method makes use of a jet of polishing fluid propelled towards the optical surface at low pressure. The footprint is near-Gaussian and it is suitable for working on edges and marks by previous processes. A version of Fluid Jet Polishing has been successfully implemented by Zeeko for the smoothing of diamond turning incisions [76].

Magnetorheological Jet: For the surface finishing of strongly concave parts, QED developed and patented a jet polishing technology performed with magnetorheological fluids [114]. Similarly to classical MRF, an axial magnetic field is applied to the jet, transforming a squirting fluid into a highly stable, "rod-like" stiff polishing tool. This is suitable for polishing of aerospace and military components (e.g., missile domes), as well as for other unique geometries that would otherwise be prohibitive for classical finishing tools [115].

Elastic Emission Machining (EEM): For the ultimate ultra-precise polishing of optical surfaces, Osaka University proposed this non-contact machining method at the end of the eighties [116]. The process is capable of atomic level material removal by chemical interaction of fine (0.1 µm size) powder particles with the substrate material. These particles are in a pure water solution which is stirred by a polyurethane rotating sphere. A fluid film of ~1 µm is kept between the sphere and the surface and its flow promotes the removal of material. In spite of the low removal rates (~0.001 mm^3/h [117]), this process is capable of achieving impressive form accuracies down to ~1 nm PV and is utilised for the finishing of X-rays optics, often in combination with plasma CVM (section 2.3.10) [118]. Reactive Atom Plasma Etching

2.3.7 Plasmas & plasma etching

A plasma is commonly defined as any ensemble of particles that manifest response to electromagnetic fields due to a sufficient number of free charged elements. Its properties differ from those of solids, liquids and gases and it is therefore called the fourth state of matter. Ionized gases are a classical example of plasmas. Plasma is also the most common state of matter in the universe: stars, nebulae and interstellar gas are always ionized to a certain degree, thus exhibiting plasma behaviour.

Plasmas already have high electric conductivity at low ionization degree. For example, on the Sun only 0.01% of atomic Hydrogen is ionized, but the conductivity can be considered infinite for most applications. Plasmas are considered *quasi-neutral*, which means that, averaged over a minimum volume $\Delta V \sim \lambda_D{}^3$, the electromagnetic influence of positive and negative charges cancels out. λ_D is called the *Debye length* and is defined as:

$$\lambda_D = \sqrt{\frac{\varepsilon_0 k T_e}{n_e e^2}} \qquad \textbf{(2-4)}$$

with T_e: electron temperature, k: Boltzmann's constant, ε_0: permittivity of vacuum, n_e: electron density, e: unit charge.

Considering a plasma volume large compared to λ_D and a charge dislocation within it, an electric field will result from the inhomogeneity. Consequently, a backlash force will act on electrons as to rebalance charge inequality. Thus, an oscillatory motion is started that propagates with frequency:

$$\omega_{pe} = \sqrt{\frac{n_e e^2}{\varepsilon_0 m_e}} \tag{2-5}$$

On the same basis, incident electromagnetic radiation will interact with the plasma. In particular, waves of lower frequency than ω_{pe} will be damped by a factor e over a distance called the *skin depth* δ_{pe}:

$$\delta_{pe} = \sqrt{\frac{2}{\sigma_{el} \mu_0 \mu_r \omega_{EM}}} \tag{2-6}$$

with σ_{el}: plasma electric conductivity, μ_0 & μ_r: magnetic permeability of vacuum and relative permeability, ω_{EM}: frequency of incident EM radiation.

Besides natural plasmas, DC and AC discharges are used in several industrial applications for different types of material processing and coating. One of the most common ways to initiate a plasma discharge is using parallel plate electrodes connected to high DC voltage. The power necessary for the break-down to occur will depend on pressure. Also AC currents can be used in the range of radio frequency or microwaves. Classification upon pressure defines low and atmospheric pressure plasma processes. Examples of low pressure techniques are glow discharges (fluorescent light tubes) and Capacitive Coupled Plasmas (CCP). Conversely, the most common type of atmospheric pressure processes are plasma torches like DC plasma torches (welding), RF Inductively Coupled Plasma (ICP) torches and microwave torches. Currently, their principal applications are in the areas of coating, plasma spraying, plasma chemical synthesis, plasma waste treatment [119] and plasma chemical etching. This last example includes a variety of methods developed for research and industrial applications during the second half of the last century [120]. RAP technology is a recent example of plasma etching by Inductively Coupled

Plasma torch (see section 2.3.8). An extensive review of atmospheric pressure plasmas can also be found in [121].

In this context, an introduction to plasma etching and related chemistry seems appropriate. Plasma or *dry* etching was developed at the beginning of the seventies as a cheaper alternative to complicated and indirect *wet* processes. It offered the advantages of unique processing sequences, substitution of safer gases for corrosive liquids, easy waste elimination and, above all, high vertical (anisotropic) removal rates. Nowadays, a variety of processes is gathered (legitimately or not [120]) under the definition of *plasma etching*, but two main categories can be distinguished on the basis of the etching mechanism: *sputtering* and *chemical etching*. For example, Ion Beam Figuring is a pure atomic sputtering process, while RAP belongs to the family of chemical etching processes. The transition from a purely mechanical material removal nature to a chemical one is related to the processing pressure, as illustrated in **Figure 2-21**.
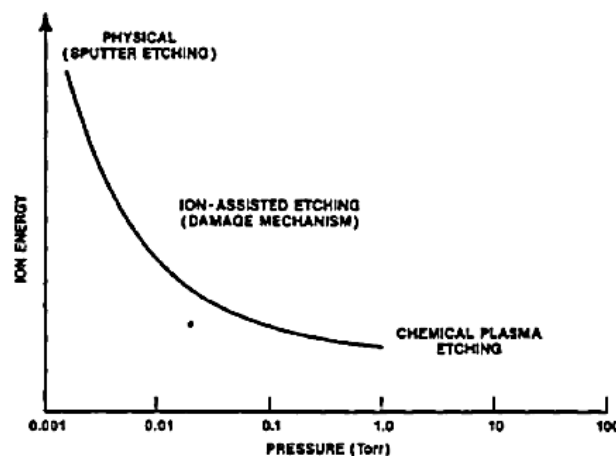
Figure 2-21 Qualitative effect of pressure on ion energy and the etching mechanism (source: [123]).

Optical surfaces of silicon based materials are preferably processed in fluorine or chlorine containing discharges. Some fluorinated plasmas typically adopted in plasma processing of silica are F_2, CF_4, C_2F_6, SF_6, NF_3, ClF_3, XeF_2, XeF_6 and CHF_3. Molecular fluorine is usually considered too dangerous for practical applications, so compounds like NF_3, CF_4 or SF_6 are preferred. It is reported by Manos and Flamm ([120]), however, that CF_4 and SF_6 tend to form polymeric

films as residues on processed surfaces (CO_xF_y, SO_xF_y, SiO_x). Therefore, O_2 is sometimes used as an additive to help produce gaseous CO_2, SO_2 or other by-products and raise the rate of reaction (etchant-unsaturate model). Extensive descriptions of the behaviour of CF_4 and SF_6 plasma discharges and the use of additive O_2 can be found in [123], [124] and [125].

The chemical mechanisms behind silicate etching by fluorinated plasmas are complex and rather unexplored at high pressure. In **Figure 2-22** a simplified illustration is shown.

The reaction can take place following the two depicted branches and can be summarized in following 3-steps reaction:

$F + F{-}Si{-} \rightarrow SiF_2$ (g - **Figure 2-22 Ia**)**,** (bound - **Figure 2-22 Ib**)

$SiF_2 + F\ (F_2) \rightarrow SiF_3^{\,*}\ (+F)$

(**Figure 2-22 II**)

(2-7)

$SiF_3^{\,*} \rightarrow SiF_3 +$ photon

$SiF_3 + F \rightarrow SiF_4$ (g - **Figure 2-22 III**)   (ΔH: −711 kJ/mol)[5]

---
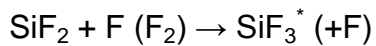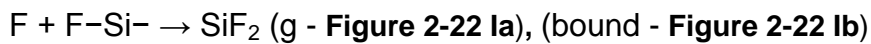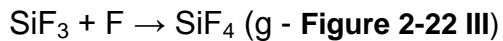
[5] ΔH : standard enthalpy of reaction.
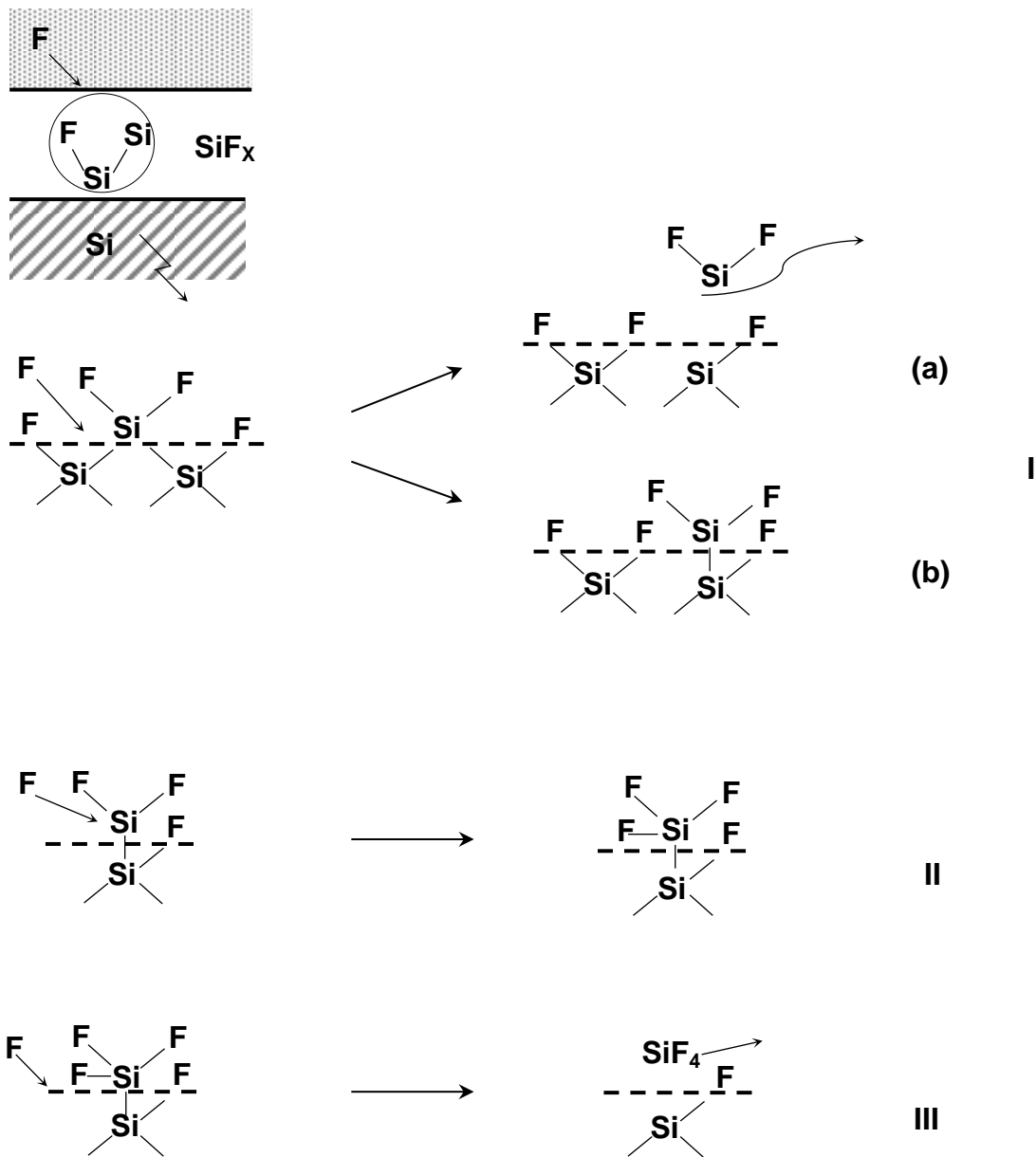
Figure 2-22 Mechanism of silicon etching by fluorine. Simplified depiction of a two-channel concerted reaction between F atoms and the fluorinated layer. Reaction results in the formation of gaseous SiF2 (Ia) and bound fluorosilicon radicals (Ib) that are fluorinated further to form higher SiF$_x$ products. Kinetics indicates that (Ia) and (Ib) are branches of a single, rate-limiting reaction that may involve a common, vibrationally-excited intermediate (source: [123]).

The reactive species used for the work described in this manuscript is SF_6. The first order reaction expected for plasma etching of SiO_2 based substrates is then [9]:

$$3SiO_2 + 2SF_6 \rightarrow 3SiF_4 \text{ (g)} + 2SO_2 \text{ (g)} + O_2 \text{ (g)} \qquad (\Delta H: -309.82 \text{ kJ/mol})$$

or **(2-8)**

$$3SiO_2 + 2SF_6 \rightarrow 3SiF_4 \text{ (g)} + 2SO_3 \text{ (g)} \qquad (\Delta H: -511.74 \text{ kJ/mol})$$
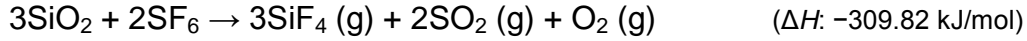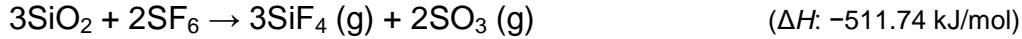
It is a fundamental requirement that the products of the chemical reactions in equations (2-7) and (2-8) are of volatile form: this allows waste gases to leave the surface during plasma processing. It is also worth noting that the standard enthalpy values of the involved chemical reactions are negative which underlines their exothermic nature. This allows for a rapid progress of the material removal which is enhanced through energy transfer provided by the plasma. In fact, the rate of chemical reaction is known to be temperature dependent and to follow an Arrhenius-type law:

$$r(T) = A(T) \cdot e^{-\frac{E_A}{RT}} \qquad \textbf{(2-9)}$$

with E_A: reaction activation energy and R: gas constant. The pre-exponential factor is usually considered to be a "weak" function of temperature. However, Manos and Flamm report that, for fluorine etching of SiO_2, a form for A(T) seems to be in agreement with the following expression [120]:

$$A(T) = C n_F T^{\frac{1}{2}} \qquad \textbf{(2-10)}$$

whereas n_F: concentration of fluorine, C: experimental proportionality constant.

The RAP process certainly presents a large raise in etching rates due to the plasma heat input onto the substrate. Recent work carried out in Cranfield has been directed towards characterisation and FEA modelling of the energy flux onto the surface [15], as well as investigation of the etching rates dependence on surface temperature [14]. Further investigations concerning the thermal aspects of the process are described in section 4.2.3. This research lays the foundations for the development of an in-process adaptation which would

enable adaptive torch travelling velocity according to substrate surface temperature variations.

2.3.8 Inductively Coupled Plasma (ICP) torches

The Reactive Atom Plasma system is based on plasma generation by electromagnetic induction at atmospheric pressure. An Inductively Coupled Plasma (ICP) torch constitutes the processing tool through which fluorine radicals chemically etch a substrate. Argon gas becomes the activating plasma and a reactive species is atomized, shielded and transported within it. A first precursor reactive gas for RAP was CF_4, then replaced by NF_3 [11] because of its greater dissociation enthalpy (-925 kJ/mol [122] versus -131.5 kJ/mol [126]). Currently SF_6 is preferred because of its non-toxicity, higher quality of processed surfaces and cost.

ICP torches have been used for decades in industrial processes, as well as in spectro-chemical analysis [127]. The atmospheric pressure induction arc was discovered by Babat in 1942 in the form of ring (electrodeless) discharges. The invention of the first ICP torch, instead, is attributed to Reed in 1961 [119], [128] (**Figure 2-23**). In principle, an ICP torch can be considered a high frequency transformer: AC-current flows through copper coils around quartz tubes, thus constituting a primary solenoid, whereas the plasma discharge acts like a secondary. RF excitation frequencies (0.2–40 MHz) are commonly used for induction arcs. The choice of the correct operational frequency depends not only on the plasma frequency, but also on the ratio between the skin depth (2-6) and the external tube radius. This ratio is called coupling coefficient and its optimum value is reported to be ~1.75 (see, e.g., [129]).

ICP torch ignition takes place when electrons from the argon gas are captured and accelerated by the magnetic field generated by the coils. Collisions with the gas atoms initiate a cascade reaction: the inductively coupled plasma discharge. The generation of free electrons can occur by means of carbon (or tungsten) ignition rods, sparking by a Tesla coil [127], [128], [129] or relying on natural ionization by cosmic radiation.

44
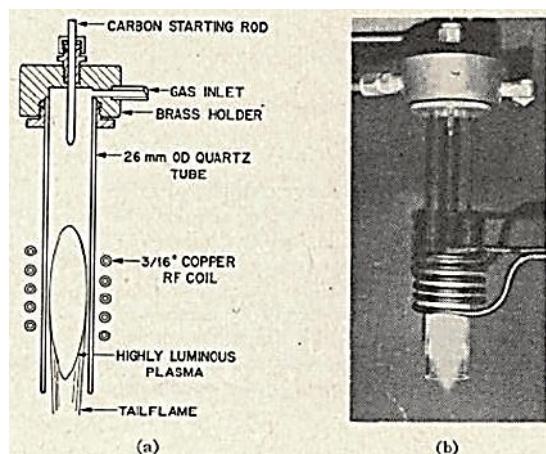
Figure 2-23 Reed's induction torch (source: [128]).

The first type of ignition mechanisms was originally exploited by Reed (**Figure 2-23**), who managed to break down the gas with 100 V at 1 torr pressure [128]. Conversely, the Tesla coil mechanism is the one used for the RAP300 facility, while natural ionization ignition applies for Helios 1200.

The fundamental structure of an ICP torch is illustrated in **Figure 2-24**. It consists of three concentric tubes, typically made of quartz. Around the external cylinder few turns of a conductive coil, usually made of copper, are wound up. Argon gas is passed between the outer and middle tubes at flow rates of several litres per minute where it forms a stream tangential to the main tube walls. This is called the *coolant flow*, as it prevents the plasma from annihilating the external quartz tube. A second gas flow, the *auxiliary* gas, passes between the middle tube and the central one at ~1 L/min. It is used to tune the height of the base of the plasma relative to the tube and protect the inlet of the reactive species. The third tube, also called *injector*, after plasma ignition introduces the reactive species. This needs to be pumped in at the right speed in order to be decomposed instead of just flowing through.

The coupling power is supplied by an RF generator and three main frequencies are usually chosen, 13.56, 27 and 40 MHz. However, the selection of operational frequency and minimum plasma sustaining power are not independent. In **Figure 2-25**, the plots illustrate the dependence of plasma discharges minimum sustaining power on frequency and pressure.
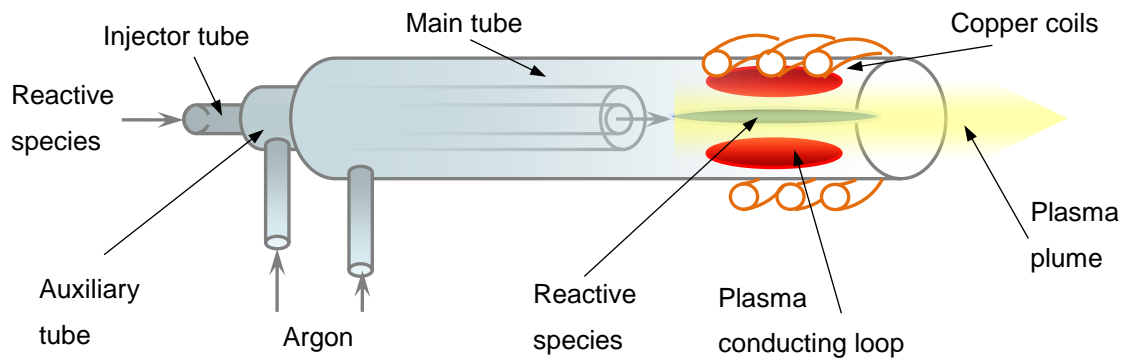
Figure 2-24 Sketch of an ICP torch.

It is easy to infer that, at atmospheric pressure, Ar plasma maintenance is more conveniently achieved at several tens MHz. For instance, the generator available on Helios 1200 supplies energy at 40 MHz. The transfer of energy to the plasma via inductive coupling is typically indirect and relatively inefficient. This has to take place over a matching network composed of capacitances to adjust the overall impedance since the plasma will usually constitute a non-constant load [127].
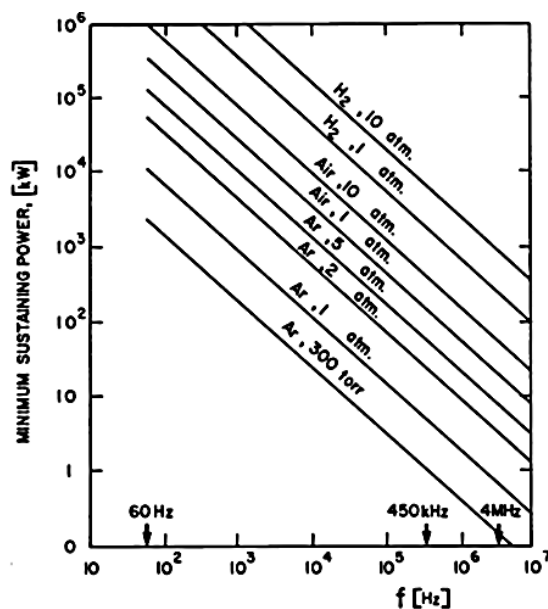
Figure 2-25 Operational frequency versus minimum sustaining power for induction plasmas (source: [119]).

Typically, two capacitors are available: one is connected in parallel with the coil, the other in series. This allows for finer tuning of the impedance. In the majority of practical applications concerning ICP systems, due to the matching networks, only about 20-40% of the energy is effectively transferred to the plasma [127].

2.3.9 Reactive Atom Plasma and Helios 1200

Plasma Assisted Chemical Etching (PACE) had already been applied by Bollinger et al. for the figuring of optical surfaces in 1990 [130]. The system configuration consisted of a DC plasma source ("puck") and an experimental arrangement suitable for small areas only (100 mm diameter). Conversely, the principles of an ICP torch were applied for the first time for the etching of optical substrates at Lawrence Livermore National Labs with the purpose of removing subsurface damage. Later, the process was made commercial with the formation of RAPT Industries in 2001. Afterwards, studies aimed at optimising the process and scaling it up for metre-size substrates were initiated by Shore et al. at Cranfield University. A first research facility, RAP 300, was acquired by Cranfield University Precision Engineering in 2003. By means of this machine, assessments on material removal capabilities, footprint properties and torch performances were carried out. In particular, the process was proven to be effective on optical materials like ULE, silicon and SiC, while the etching capability on Zerodur remains questionable. Also, spectrometric thermal analysis of the plasma was the subject of previous work. Details on these investigations can be found in [11] and [13].

Through this early research RAP was proven to be repeatable at nanometre level (within ~7 nm) and to achieve removal rates up to tens of mm^3/min. At the same time, the process and the torch could be modified to obtain just few nanometres depth per pass. The RAP etching footprint has a characteristic near-Gaussian shape. Depending on standoff distance from the substrate and aperture of the torch nozzle, Gaussian profiles of different width can be imprinted onto a surface. In terms of Full Width at Half Maximum (FWHM), sizes ranging from ~10 to 18 mm have been reported [11], [14]. A novel research

stage started with the establishment of the new facility Helios 1200, the apparatus used for this project. This can be observed in **Figure 2-26**.

(a)

(b)
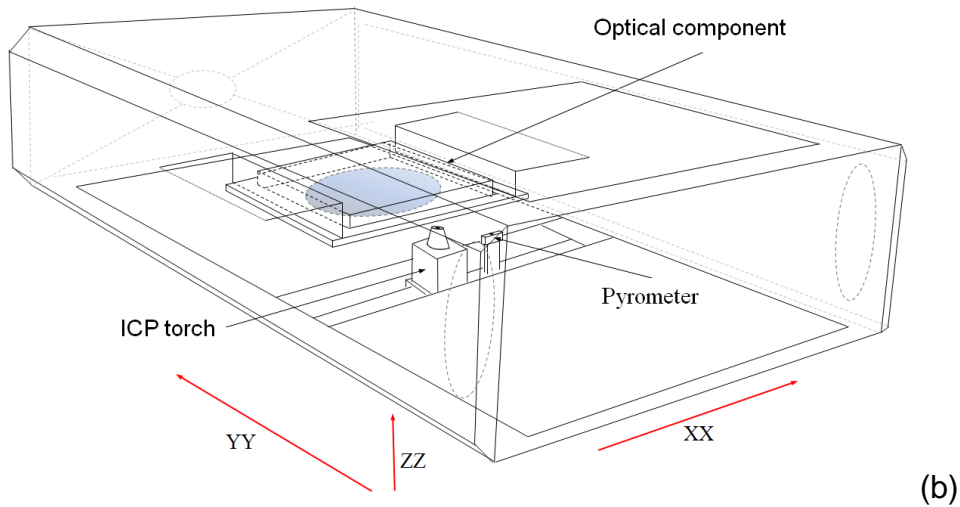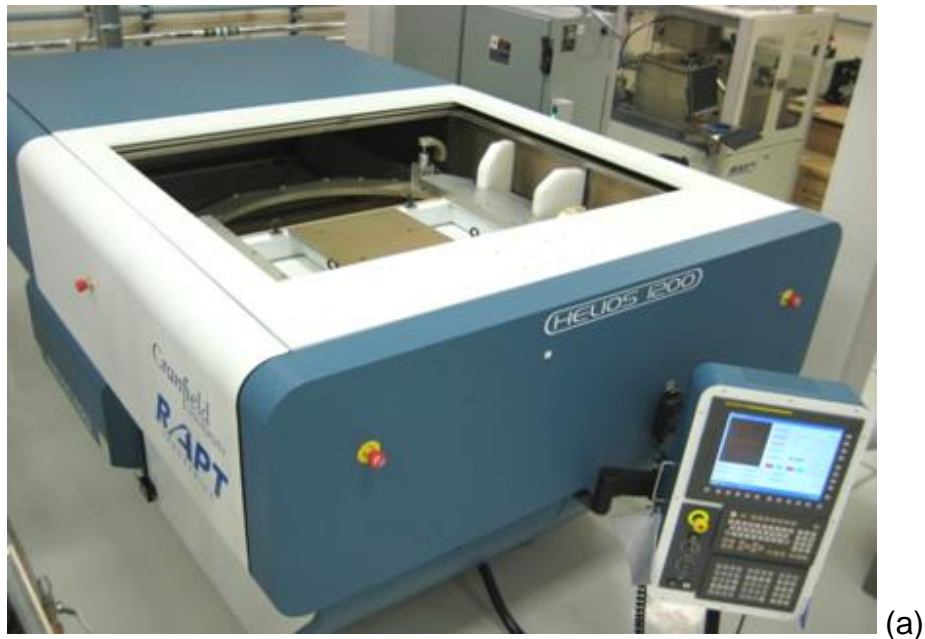
Figure 2-26 The RAP facility Helios 1200 in the Loxham laboratory of Cranfield Precision Engineering Institite (a) and a sketch of its motion configuration and internal structure (b).

Installed in the Loxham lab of Cranfield University Precision Engineering, the machine is conceived for the figuring of optics up to 1.2 m diameter. Its micrometre resolution motion is ensured by a computer numerical control system (Fanuc 30i series). It integrates dedicated software and a double skin

structure to increase machine safety. As shown in **Figure 2-26 (b)**, three axes form the motion configuration. The component moves face-down along the YY direction, while scanned by the plasma torch travelling in the XZ plane. Technical details on the machine specifications can be found in [131] and [132].
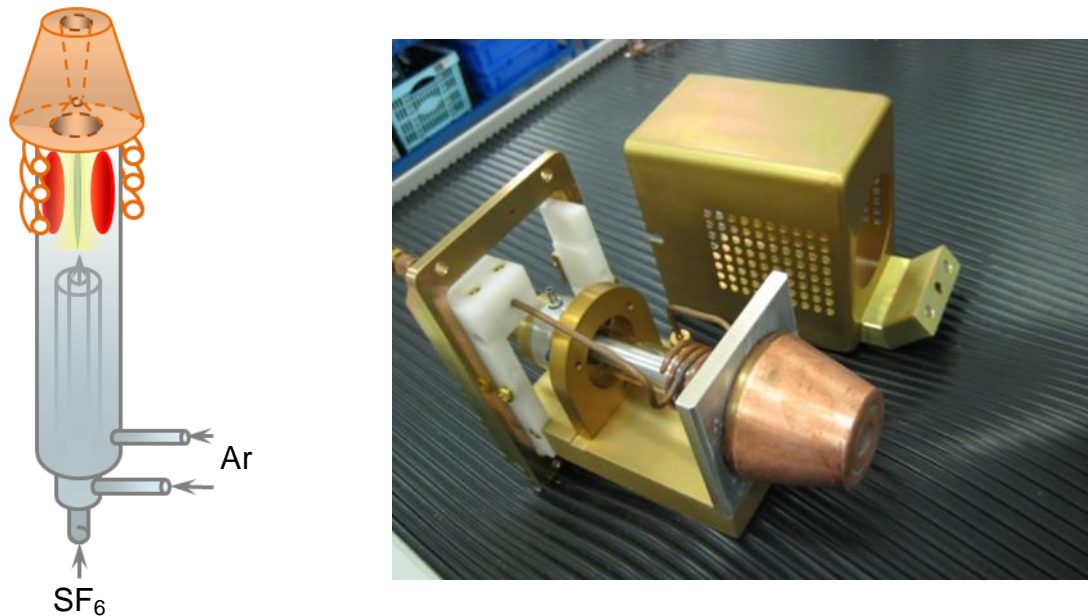
Figure 2-27 Sketch (*left*) and photograph (*right*) of the ICP torch currently in use for Helios 1200.

The ICP torch in use for Helios 1200 is shown in **Figure 2-27** (sketch and photo). As visible in the sketch (*left*), it matches a classical ICP torch design in its main structure. The auxiliary tube consists of an aluminium trumpet that confers solidity to the torch assembly. The flow of gases in the coaxial tubes is controlled by mass flow control units. The respective fluxes are: 20 slm of Argon for the main, 0.2 slm of Argon for the auxiliary and 0.8 slm of SF_6/Ar mixture for the injector. A conic brass nozzle is added to cool down the plasma jet and control its flow distribution through a De-Laval internal configuration (convergent-divergent nozzle type). Both nozzle and coils are prevented from overheating by internal water flow.

On the right-hand side of the torch, a pyrometer is mounted ~16 cm far from the nozzle centre. This distance was made necessary by electromagnetic reciprocal disturbances between this instrument and the ICP torch. Also, the pyrometer is shielded from the plasma jet by argon flowing within the sensor head case.

However, such protection had revealed itself insufficient in closer proximity to the nozzle (sensor head disruption). This instrument was used for some of the surface temperature assessment carried out in this project.

2.3.10 Competing technologies

The advantages of atmospheric plasma enhanced chemical etching have been originally envisaged not only by RAPT Industries, but also by two further research centres: IOM and Osaka University. More recently, the Harbin Institute of Technology (China) followed with Atmospheric Pressure Plasma Processing (APPP) [133].
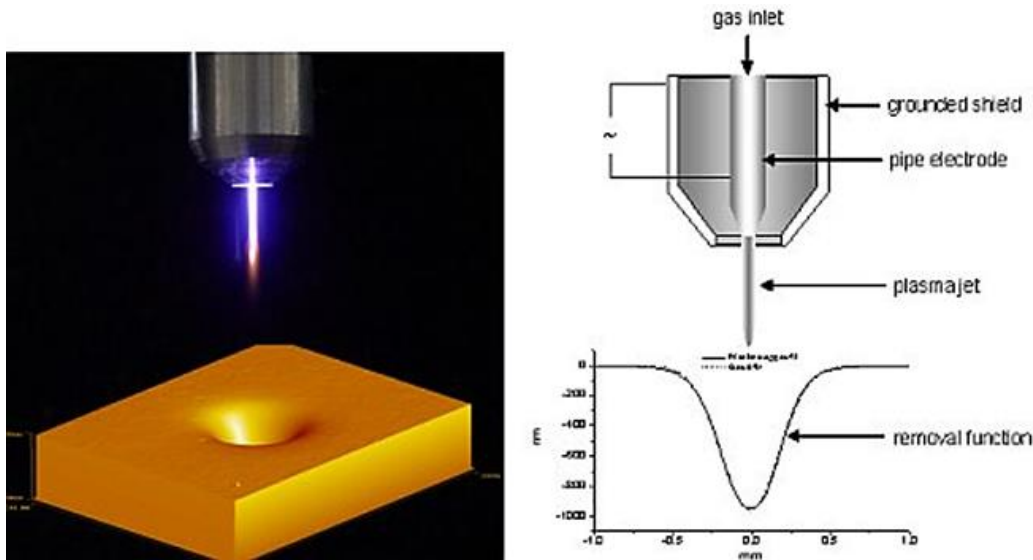
Figure 2-28 (*left*) chemically reactive plasma jet with Gaussian tool function; (*right*) Schematic of a plasma jet source and cross section of a removal profile (source: [107]).

As mentioned in section 2.3.6, IOM developed a low pressure plasma assisted etching technique, followed in 2001 by Plasma Jet Machining (PJM). This is an atmospheric pressure process with several similarities to Reactive Atom Plasma [109], [111]. A schematic of PJM is shown in **Figure 2-28**. The process is based on RF plasma excitation at ~13 MHz and 60 W. The torch design (**Figure 2-28**, *right*) is similar to that of an *Atmospheric Pressure Plasma Jet* (*APPJ*) [121] and is based on two coaxial electrodes where the RF field is applied to the inner one. The same reactive species as for RAP are used in a mixture with oxygen

which is reported to enhance the removal rates. A near-Gaussian footprint is etched by the beam (**Figure 2-28**, *left*) and several sizes are available (FWHM 0.3 – 12 mm). Removal rates are reported in the range $5 \cdot 10^{-5}$ – 50 mm^3/min. As for RAP, the heat transferred from the beam to the substrate increases the chemical etching rate. The approach chosen by IOM researchers in order to control temperature effects consists of in-depth investigations on heat transfer phenomena (see section 2.6). Assessments of surface temperatures during PJM were brought in connection with the etching rate to enable the creation of a numerical simulation of the process. The dwell-time calculation for tool-path algorithms generation is then derived from this theoretical model [135].

Examples of PJM performances are reported in [109], [111] and [136]. In one case, three SiC mirrors of 10 mm diameter clear aperture and ~50 mm radius of curvature were needed for the GAIA satellite mission. Figure correction from ~20 µm PV to ~32 nm PV took place over four iterations, alternated by polishing cycles. In another example, a SiC parabolic surface of 10 mm diameter was figured from 4.7 µm down to 89 nm PV in seven iterations. As noticeable from these cases, Plasma Jet Machining has been mainly applied for processing of small surfaces with several micrometres figure error. On small scale substrates, heat transfer phenomena dominate the figure correction performance, which explains the need for accurate simulations in PJM.
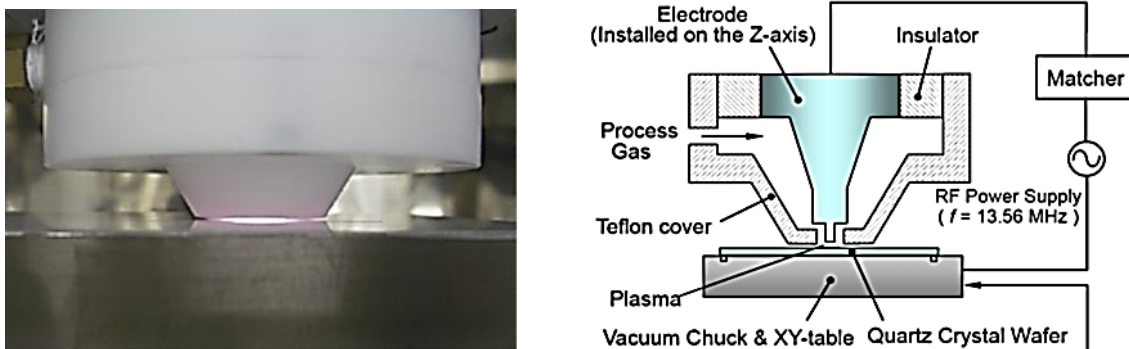
Figure 2-29 (*left*) CVM operating tool; (*right*) schematic diagram of the NC-plasma CVM system (source: [137]).

Differently, Reactive Atom Plasma was ultimately conceived for metre-scale optical surface with figure errors of the order of ~1 – 2 μm and requires therefore a dissimilar approach (see chapters 3 and 5).

Another plasma based figuring technology was developed at the beginning of the nineties by Osaka University, in cooperation with Nikon Company. Patented by Mori et al. [138], the new RF plasma method, illustrated in **Figure 2-29**, was called plasma Chemical Vaporization Machining (CVM).

Similar to RAP and PJM, plasma CVM differs from them in the use of a central electrode, driven by RF current at 13.56 MHz and about 150 W. Different electrode types are available, like a rotary or a pipe electrode, and their presence prevents the process from having the classical Gaussian shaped footprint, producing a ring or a hollow form instead. The shielding gas is Helium, while the etching species are usual CF_4, NF_3 or SF_6. The removal rates are comparable to those of the other atmospheric plasma processes (e.g., ~13 mm^3/min on fused silica [138]). The tool is held at ~200-400 μm from the surface and leaves a 5 to 10 mm wide footprint. In the process, substrates are usually pre-heated to ~80 ^{o}C to reduce heat transfer within the bulk and increase the removal rates. The tool-path algorithm used for CVM figuring is based on a stepwise constant feedrate method and not on dwell-time calculations where one would incur in the typical non-linear nature of the etching depth [139], [140]. More details on this and other tool-paths are given in section 2.5.2.

Achievements by CVM include the figure correction of a 160 mm SiO_2 asphere, where 130 nm PV residual error was attained after three iterations [88]. In the case of CVM, upscale of the technology for the processing of metre-class surfaces hasn't taken place so far. Instead, very recent research by Takino et al. saw the development of a millimetre-sized pipe-electrode tool for the figuring of small lenses [140], [141].

Finally, Harbin Institute of Technology has been performing studies based on a more classical atmospheric pressure plasma jet (APPJ) torch design [121]. This research, so far, has been concentrated on characterising the thermal,

spectroscopic and material removal properties of the plasma tool in use (see also [134]).
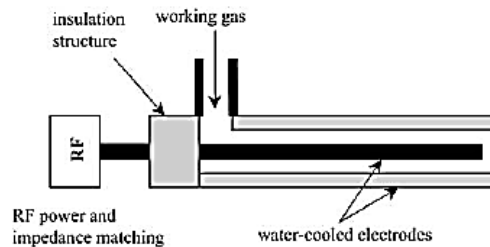
Figure 2-30 Schematic of the torch in use at Harbin Institute of Technology (source: [133]).

2.4 Review of fabrication technologies for large optics

In **Table 2-2**, a summary of the performances of the processes utilised in for large optics fabrication is presented. Included are all technologies described in section 2.3. Data are extracted from the mentioned publications and/or online sources. Also, a graphical representation of removal rates versus roughness is shown in **Figure 2-31**.

In **Figure 2-32**, a comparison is shown between the current production chain for ultra-precision optics and a proposed new one including RAP. The main advantage of the novel manufacturing procedure would be to achieve the same finishing quality within a much shorter period of time. In fact, smoothing and figuring performed by polishing and IBF currently take more than 100 hours, making, for example, extremely large telescopes impossible to build. In the proposed fabrication chain, the polishing (or MRF) stage would be performed mainly for roughness and subsurface damage reduction. This would leave the figuring step to RAP which could accomplish it within ~10 hours (see also Chapters 5 and 8).

Table 2-2 Overview of material removal processes (Reasonable estimates are given for not directly available data).

Process	Removal rates [mm³/min]	Residual figure error [nm]		Roughness RMS [nm]
		PV	RMS	
Precision Grinding	2 – 200	1000 – 5000	1000 – 2000	10 – 50
Stressed Lap Polishing*	5 – 150	50 – 100	10 – 20	1 – 2
Sub-aperture Polishing	0.03 – 280	50 – 500	10 – 100	0.15 – 2
MRF	~0.3 – 13	10 – 200	2 – 10	< 1
IBF	~0.01	10 – 100	~2	< 1 – 2
RIBE	0.3	10 – 100	~2	~1
Plasma Enhanced Chemical Etching (PJCE, PJM, RAP)	0.1 – 50	~50 – 200	~10 – 30	~1 – 10

*: Data are referred to the 1.2 m stressed lap used for the GMT segments figuring (courtesy of Dr. D.W. Kim, University of Arizona).
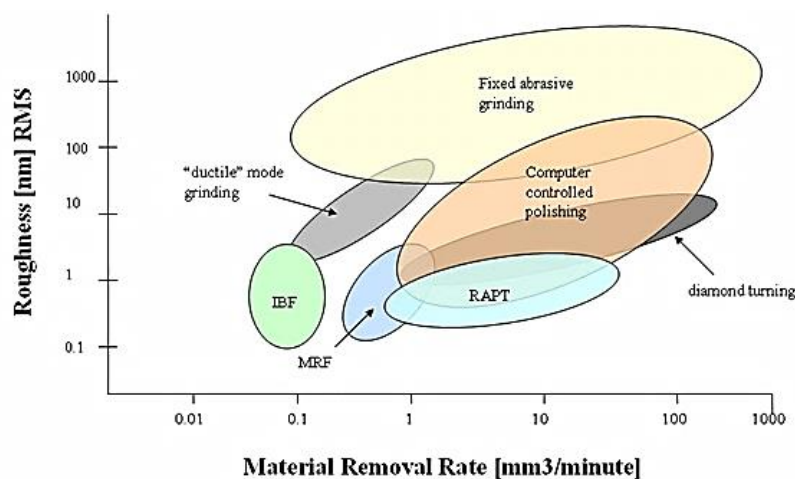
Figure 2-31 Volumetric removal rates versus roughness for several processes (*source*: [79]).
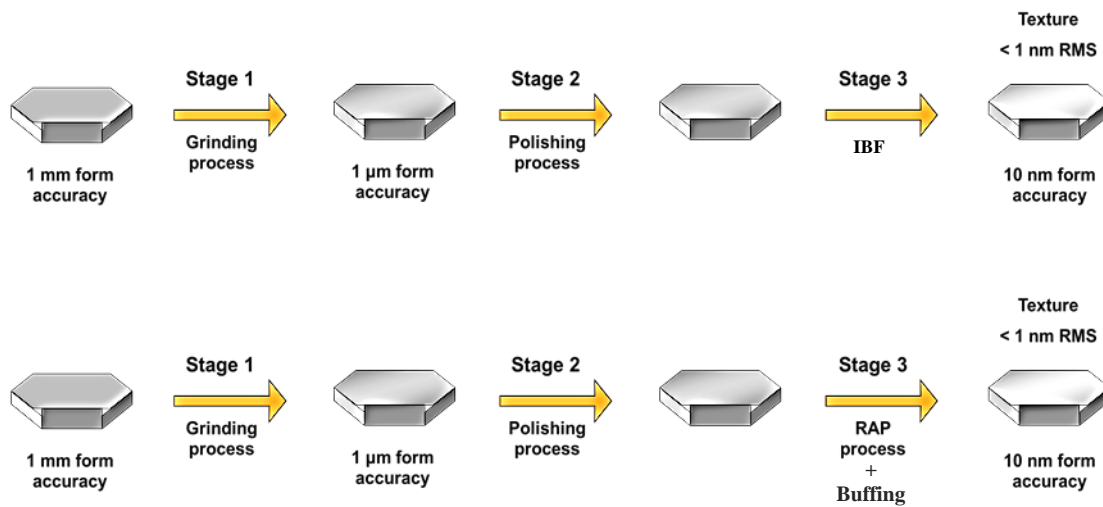
Figure 2-32 Representation of current ultra-precision optics production chain (upper picture) and the proposed new one including RAP (picture below).

2.5 Surface figuring and tool-path algorithms

All figuring techniques described so far make use of sub-aperture tool footprints with different sizes and shapes, depending on process type and spatial frequencies to correct. A common way to design tool-path algorithms for non-trivial footprints is based on mathematical deconvolution. Deconvolution methods owe their origin to works in the fields of image reconstruction and spectra recovery for astronomy and other applications. In surface finishing, the idea is to derive the optimum dwell time needed at every point in space for the footprint to "fill" the volume of material corresponding to the figure error. This dwell time can be subsequently translated into tool scanning speeds. Although Gaussian etching shapes are the most familiar among figuring processes (e.g., IBF), deconvolution generally applies for any kind of footprint.

In the next sections, deconvolution methods are introduced and explored, particularly focussing on the technique selected for the purpose of the project. As for several other energy beam technologies [5], the programming language utilised in this thesis for the development of tool-path algorithms is MATLAB. Although not the most rapid in terms of programs execution, this programming

language probably offers the widest set of pre-organized mathematical-numerical tool applications. An image and a curve fitting toolbox were also used for data processing.

2.5.1 Mathematical principles

Deconvolution techniques for surface figuring were first applied for IBF by Wilson et al. in 1988 [103]. To describe the removal of a defined amount of material (figure error) over a given area, the following *convolution integral* can be used:

$$r(x,y) = \iint_{-\infty}^{\infty} B(x - x', y - y')t(x'y') \, dx' \, dy' = B(x,y) \otimes t(x,y) \qquad \textbf{(2-11)}$$

r(x,y) is called *removal function.* Its unit is nanometres and represent the heights in the figure error map. B(x,y) is the footprint or *influence function* (sometimes also *beam function*). It is measured in nm/s and it is the characteristic depth removal rate as a function of radial distance from the plasma beam centre. The *dwell time map* t(x,y) describes the temporal interval needed by the etching process to remove a certain amount of material and its unit is time per unit area. A description of the conversion of dwell-time maps into velocity maps is given by Drueding et al. [142] (Cartesian strip velocity method). For instance, if a raster-type tool motion path is chosen, equation (2-11) must be written in a partially discretised form in which the surface texture is "broken" into strips:

$$r(x,y) = \sum_{i=0} \int_{-\infty}^{\infty} B(x - x', y - y_i')t(x', y_i') \, dx' \Delta y' \qquad \textbf{(2-12)}$$

Δy represents the characteristic width of a strip and corresponds to the stepping pitch of consequent passes. Multiplication with the dwell time of the corresponding strip leads to *rastering velocities*, controlling which a figuring process can be achieved.

$$V(x) \cong \frac{1}{t(x, y_i) \cdot \Delta y} \qquad \textbf{(2-13)}$$

A similar form can be derived for curved tool-paths like spirals [142].

For the derivation of the dwell time map, a direct solution of equation (2-11) from the convolution theorem of Fourier analysis will rarely deliver successful results. This is due to numerical divergence that can be caused by singularities or pseudo-zero points in the surface map, as well as to the nature of the influence function (e.g., Gaussian) [142]. Also, corrective solutions like threshold inverse filtering or Wiener filters tend to deliver coarse approximations or windowing effects. Therefore, in all recent figuring works, more complex solutions have been sought. In the majority of cases, iterative techniques are preferred because of their relative simplicity and computational and applicative effectiveness (see for example [4] and [143]). In few other cases, more "exotic" solutions have been attempted with discrete results [7], [142].

In this work, the more diffused iterative methods are chosen for the derivation of the dwell-time maps. In the codes developed during the course of this PhD project, the methods by Lucy-Richardson [143], [144], [145], [146] and by Van Cittert are available [144]. The mathematical derivation of the methods is outlined in Appendix B.

<u>Notes</u>:

- For 3-axes machine configurations, and on high gradient surfaces, the influence function shape will depend on the angle of incidence. Solutions of equation (2-11) that account for sloped surfaces exist (see, e.g., [147], [148], [149]). These code modifications haven't been implemented for the work presented in this manuscript, as machining of strongly curves surfaces was not intended within this PhD project (see also Appendix F). Also, the dynamics of the plasma jet flow on slopes is expected to change significantly, with possible loss of the etching footprint shape. A better solution consists of 5-axis machine systems.

- The finite acceleration capability of any CNC motion system could introduce realization errors due to a variation of the actual tool velocity and that demanded along the tool travelling direction. Compensation methods involving dwell-time "smoothing" calculations have been developed to minimise this problem [143], [150]. For RAP though, temperature effects on material removal rates are expected to dominate with respect to minor velocity variations. Consequently, such velocity corrections are not relevant for a successful figuring using the RAP process.

2.5.2 Types of tool-paths

In the development of figure correction processes, dedicated trajectories are designed to take into account the characteristics of the tool influence function, as well as the geometry and the properties of the substrate.
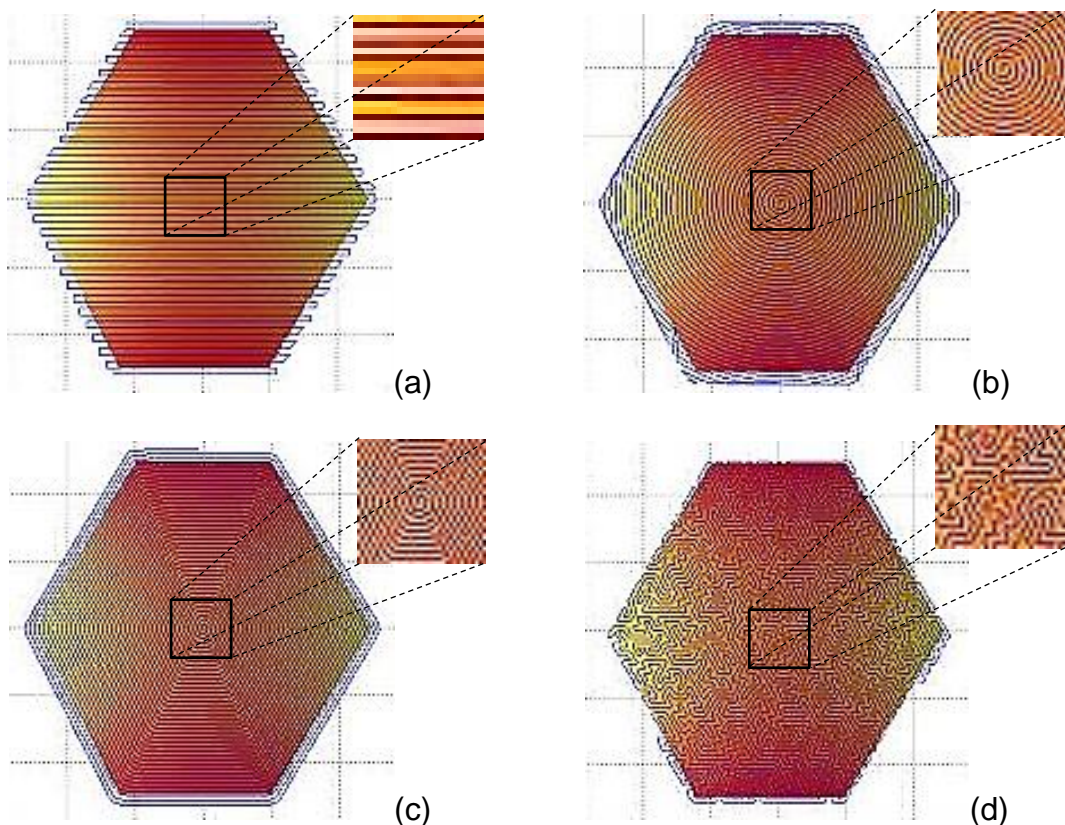
Figure 2-33 The tool motion paths used for the precession polishing: raster-pattern (a), spiral path (b), adaptive spiral (c) and randomised tool-path (c) (source: [76]).

Also, as discussed in section 6.3, modifications of such trajectories are typically applied in the proximity of parts edges to minimise roll-off.

In **Figure 2-33**, the tool-paths in use for the precession polishing process (section 2.3.2) are shown as an example. They all represent *unicursal* paths, where the tool follows tracks that never cross [151]. Together with the classical meander-type motion (raster-scan), spiral tool-paths are quite common for figuring techniques. Whilst more suitable for circular workpiece geometries, spiral paths present a disadvantage at the centre of the working areas due to the finite size of the tool heads. A variant, called adaptive spiral tool-path, is designed to follow specific perimeter geometries (e.g., hexagonal, petal, etc.). Finally, more recent developments have seen the introduction of randomised tool-paths. The purpose of random paths is to minimise the well-known residual waviness corresponding to a scanning pattern print-through. PSD analyses are typically used to reveal the spatial frequencies affected by such patterns (see also section 6.2). Also, for the production of optics, customised specifications concerning the waviness can be expressed in terms of RMS over a spatial interval according to ISO 10110 (see also [152])

Randomised tool-paths have proved to be efficient at reducing the presence of raster tracks on polished surfaces [151]. However, due to their complexity and limited applicability in machines motion systems, new solutions have been recently investigated [153], [154]. In these studies, part-randomised paths were introduced through an in-process variation of the scanning pitch with successful reduction of the scanning patterns.

Surface figuring by plasma chemical processes usually requires different adaptations of classical tool-path algorithms. In particular, the variability of the influence function due to the heat affecting the rate of material removal calls for compensation techniques. These can involve recalculation of the dwell times based on heat transfer simulations, or design of adaptive "smart" trajectories to minimise the influence of localised energy transfer.

59
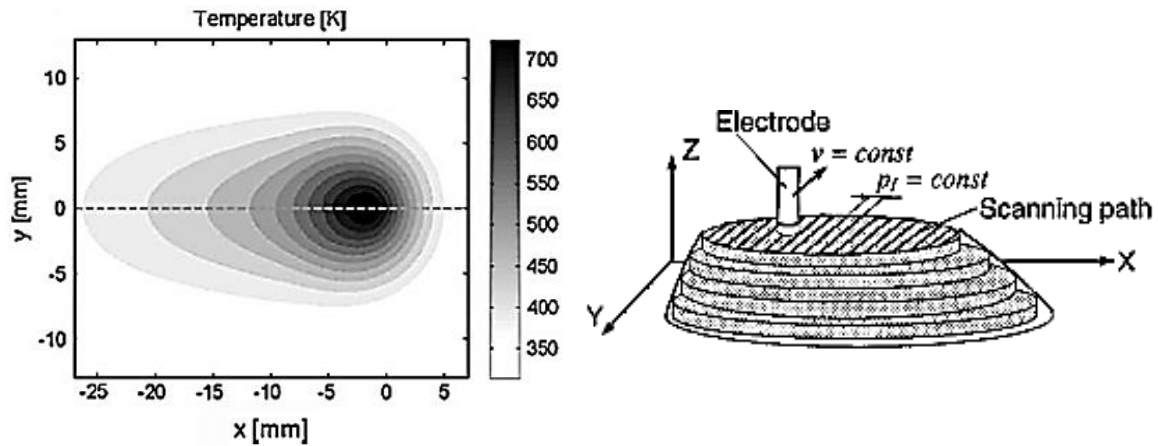
Figure 2-34 *left*: **Simulation of PJM moving thermal footprint (source: [135]);** *right*: **concept of the shaping method used for CVM (source: [140]).**

The first method was successfully applied by IOM for Plasma Jet Machining (**Figure 2-34**, *left*, see also section 2.6). Although quite accurate, this approach requires very long computational times [135] and its applicability to large surfaces is therefore disputable. Conversely, in the CVM process, the figure error is corrected by a raster-scan motion path that removes the required shape layer by layer, leaving a residual corresponding to the layer thickness (**Figure 2-34,** *right*). This method, though, necessitates rapid dynamic control of tool motion and power to account for discontinuities on error maps.

The tool-path algorithm developed during this PhD work is an adapted meander-type motion path and is described in section 3.2. This tool-path was designed to suit the energy input of the plasma beam onto the surface. Also, a strategy for waviness reduction was implemented in the later part of the work.

2.6 Heat transfer

In this section, an introductory description of heat transfer phenomena in solid bodies is given. In particular, the case of moving heat sources is evidenced, with an obvious reference to plasma jets on optical substrates. A detailed discussion, though, including the analysis of plasma convective heat transfer, or an exhaustive description of modelling techniques is beyond the scope of this manuscript. Extensive studies on these topics are available in the literature and

the aim of this section is to give an insight into the physical background that may be utilised in future work (see Chapter 7).

Thermal transfer in solids is classically described by Fourier's equation of heat conduction:

$$\vec{\nabla} \cdot (k(T)\vec{\nabla}T(\vec{r}, t)) - \rho c_p(T)\frac{\partial T}{\partial t}(\vec{r}, t) = -Q(\vec{r}, t) \tag{2-14}$$

In equation (2-14), T is the temperature at time t and position $\vec{r} = (x, y, z)$, while Q represents the heat flux. The material properties, density ρ, specific heat capacity at constant pressure c_p and thermal conductivity k, are considered for the case of a homogeneous medium. The explicit temperature dependence of c_p and k is relevant and can have significant impact on the solution of the heat equation[6]. In some cases, it is convenient to simplify (2-14) by applying a transformation (see, e.g., [155] and [156]):

$$T' = \frac{1}{k_0}\int_{T_0}^{T} k(T)\,dT \ \Rightarrow\ k_0\vec{\nabla}\,T'(T) = k\vec{\nabla}T \tag{2-15}$$

where k_0 is the thermal conductivity at T_0 (starting temperature). Through (2-15), equation (2-14) becomes:

$$\Delta T'(\vec{r}, t) - \frac{\rho c_p}{k_0}\frac{\partial T'}{\partial t}(\vec{r}, t) = -\frac{Q(\vec{r}, t)}{k_0} \tag{2-16}$$

Any solution of equation (2-16) is also a solution of (2-14), whereas the actual temperature T must be derived by inverting transformation (2-15). For this purpose, a function for k_0 can be inferred from tabulated data (see, e.g., [157]).

The characterisation of the heat flux Q is a crucial task that has both theoretical and experimental implications. In the context of this work, Q is a function that depicts the energy input (in watts per unit area) of a plasma plume onto a surface. Two possible approaches are discussed.

---

[6] The variation of density ρ due to temperature is negligible for the low thermal expansion materials considered in this work.
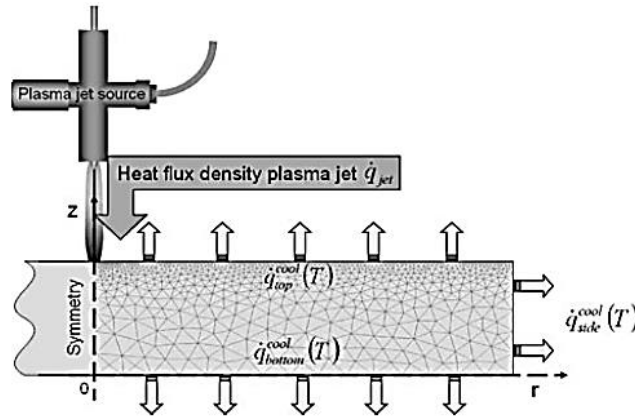
Figure 2-35 Schematic of the heat transfer model for PJM (source: [135]).

In each case, assumptions need to be made about the form in which the heat impinges and leaves the surface (boundary conditions); such hypotheses will then determine the type of experiments used for the heat flux characterisation. Meister and Arnold (2011) [135] developed a model for PJM based on forced convection. In **Figure 2-35**, schematic shows the principle and the boundary conditions adopted for the Finite Element Modelling (FEM) carried out in that work. In this model, the heat flux reads:

$$Q_{jet}\left(\vec{r}, T_{top}(\vec{r})\right) = \alpha_{jet}(|\vec{r} - \vec{r}_{jc}|) \cdot \left(T_{jet}(|\vec{r} - \vec{r}_{jc}|) - T_{top}(\vec{r})\right) \tag{2-17}$$

where the energy flux received by the surface results proportional to the plasma jet temperature and to a heat transfer function α. In this way, for the characterisation of the heat flux, determination of the plasma temperature distribution, as well as of the empirical function α is necessary. Such an experimental characterisation was indeed performed and is described in [135].

It should be noted, though, that a direct measurement of T_{jet} is generally unfeasible as thermal probes tend to fail in plasma environments. An alternative method is based on plasma spectroscopy and has been previously applied by O'Brien [13]. However, when convective heat transfer onto a substrate is considered, the actual temperature of interest ought to be taken in the closest proximity to the surface, within the so-called boundary layer. Here, the reliability of measurements, though, is difficult to achieve. Therefore, the heat flux is

usually characterised by indirect inference from acquisitions of the surface temperature distribution, through which both T_{jet} and α can be determined [135].

Following an analogous concept, a different type of model can be considered, in which the heat flux is fitted directly to a measured surface temperature distribution. This model is based on radiative heat transfer simulations, where the heat flux happens to be an intensity beam over a definite area (laser-like model, see, e.g., [158] and [159]). For instance, following the previous study of a RAP torch plasma heat distribution [13], it would appear reasonable to represent the heat flux of a RAP torch as a Gaussian:

$$Q(x,y,z,t) = P \frac{exp\left[-\frac{[(x-vt)^2 + y^2]}{2R^2}\right]}{2\pi R^2} \frac{h(z)}{\delta} \qquad \textbf{(2-18)}$$

In equation (2-18), a Gaussian beam of power P, distributed over a spot of radius R, moves at velocity v in x-direction; $h(z)/\delta$ defines the penetration of the heat flux normal to the surface (z-direction). The characterisation of the heat flux, then, can be based on the derivation of P and R from measured surface temperature distributions. Note, though, that in this form Q represents an *equivalent* heat flux, which incorporates all forms of energy (plasma enthalpies) and physical conditions present in the plasma torch environment.

At this point, equation (2-14) can be solved by FEM software (Ansys, Comsol, or Simulink). This approach was successfully attempted during an early stage work of the project and results are reported in [15]. However, due to the lengthy computational times of numerical simulations, an analytical solution has also been explored in the course of this work. Following, e.g., Cline and Anthony (1977) [159], the substrate can be represented by a semi-infinite plane and a solution of equation (2-14) is achievable by the method of Green-functions. In this approximation, the resulting temperature is given by an integral formula that can be quickly solved numerically (see [159]). An additional correction may be needed when accounting for the cooling rate in a moving medium. Equation (2-16) then becomes:

$$\Delta T'(\vec{r},t) - \frac{\rho c_p}{k_0}\left(\frac{\partial T'}{\partial t}(\vec{r},t) - \vec{v}\cdot\vec{\nabla}T'\right) = -\frac{Q(\vec{r},t)}{k_0} \qquad \textbf{(2-19)}$$

where the term $\vec{v}\cdot\vec{\nabla}T'$ represents a convective temperature variation (cooling).

The semi-analytical method described above is, in several instances, limited due to the needed approximations. In particular, edges and other geometry influences cannot be accounted for, and radiative heat losses are not included. However, the rapid execution times are considered a promising initial attempt for a heat source travelling on a large surface.

2.7 Conclusions of literature review

In this chapter, the increased demand of meter-scale ultra-precise surfaces has been highlighted. The related need for a novel rapid and cost-effective optical manufacturing chain has been reviewed, with particular emphasis on state-of-the-art figuring techniques. These constitute the finishing stage of optical fabrication chains and are still a limiting factor for mass production of large optical surfaces. Low removal rates, the need for expensive process conditions (vacuum chambers) and slow convergence called for the introduction of an alternative technology that would combine the advantages of a non-contact process like IBF with high material removal capabilities.

In this context, rapid plasma processes at atmospheric pressure have become an attractive solution to speed up the surface figuring at nanometre level. Technologies like PJM and CVM have already been proved to be efficient on surfaces of small and medium scale. The Reactive Atom Plasma process was proposed for the figuring of large optics in a cooperative work between RAPT Industries and Cranfield University. In this thesis, the research is focussed on the development of a RAP figure correction procedure for large optics. Like for other plasma etching processes, the energy input from the plasma plume onto the surface is consistent and is known to affect the removal rates. This, in turn, can make the process behaviour less predictable, thus potentially influencing its convergence. Therefore, compensation methods needed to be devised and researched in order to obtain a fast convergent figuring methodology for

Reactive Atom Plasma. This part of the research is described in the next chapters, together with the key achievements of this work.

3 TOOL-PATH ALGORITHM AND DE-CONVOLUTION FOR NON-LINEAR DWELL-TIME DEPENDENCES

3.1 Derivation of velocity maps

MATHEMATICAL DESCRIPTION

Similarly to ion beam techniques, the RAP figuring process follows from a convolution of the footprint with the dwell time. If a raster-type tool motion path is chosen, from the time-dwell function one can determine the velocities of the tool scanning the substrate. This was described in section 2.5.1. The convolution integral describing a figure correction process can be then formulated as in equation (2-11). This equation relies on a linear dependence of the removal rates on the dwell time. In general, however, the linearity condition is not satisfied for a plasma assisted chemical etching process. In fact, such removal process is a function of the quantity of reactants as well as of the heat affecting the rate of chemical reaction. Both variables are naturally bound to be dependent on the dwell time and therefore on the scanning speed. Hence, an overall non-linear time dependence of the etching depths is to be expected. This can be formulated as follows:

$$r(x,y) = \iint\limits_{\infty}^{\infty} f\big(t(x',y')\big)B(x-x',y-y')dx'dy' \tag{3-1}$$

As described in section 2.5.1, several de-convolution methods are available in order to solve the convolution integral for the dwell-time. For the work presented in this thesis, the Lucy-Richardson algorithm as implemented in a MATLAB routine was used. The solution of equation (3-1) was accomplished by assuming a near-Gaussian etching footprint of ~11 mm FWHM (see section 4.2). Such a calculation would then deliver $f(t(x,y))$ (pseudo dwell-time). Assuming an expression of type $a \cdot t^b$ for $f(t(x,y))$, the actual dwell-time can be easily computed. The characterisation of the removal rates is pivotal to the described mathematical method, as it depicts the non-linear behaviour of the influence function. For the RAP process, this is typically achieved by etching trenches on the substrate material at various speeds (see also [14]). This kind

of characterisation is considered more suitable for the RAP process. In fact, it is reckoned to be representative of heat transfer dynamics when adopting a raster-type tool-path like the one used for the purposes of this work (see section 3.2).

From the footprint characterisation, the beam residence-time can be derived by converting the measured trench into a series of virtual spots, each corresponding to an extremely short dwell time. Single virtual spots from trenches at different speeds will finally deliver the required trend of depths versus time. An example is given in **Figure 3-1**.
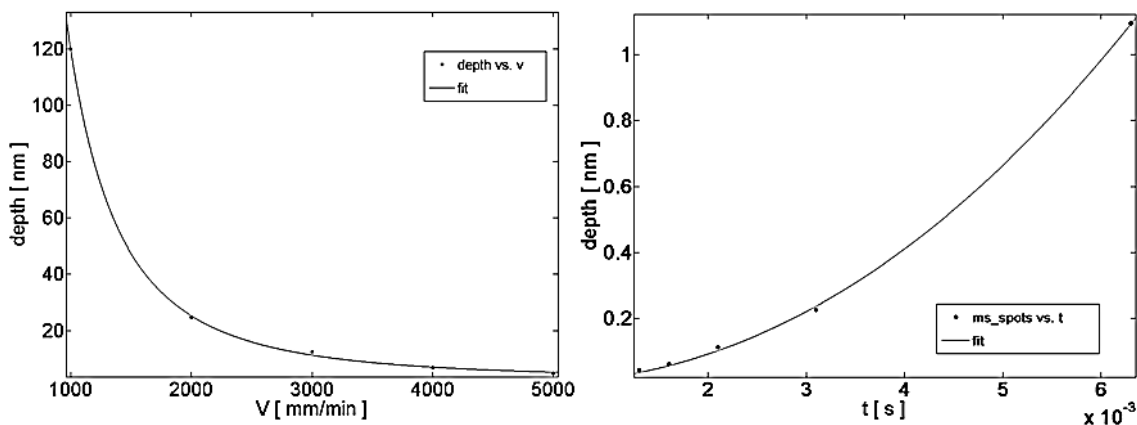
Figure 3-1 *left*: **Removal depths as a function of the torch velocity for fused silica;** *right*: **corresponding virtual spots.**

A verification for the method described in this section could consist of a single-pass figuring experiment. Such test was successfully carried out by etching a sinusoidal shaped trench on fused silica and ULE substrates. The outcomes are discussed in section 5.1.

METROLOGY DATA

The creation of a tool-path algorithm for figure correction is only as effective as the metrology data describing the surface error. Therefore, interferometer measurements must be free from artefacts and major noise. In **Figure 3-2**, an example of data treatment before codes generation is shown. The presence of noise is reduced by median filtering, while the data size is cropped to the dimension of the field of view.

Also, measurement repeatability should be assured. In order to do so, each map is taken by averaging multiple interferometric acquisitions. This procedure is then repeated (typically two or three times) and the respective measurement results are averaged in turn. In this way, long term repeatability down to few nanometres is assured. In Appendix D, more detailed descriptions of surface data generation and analysis are given.
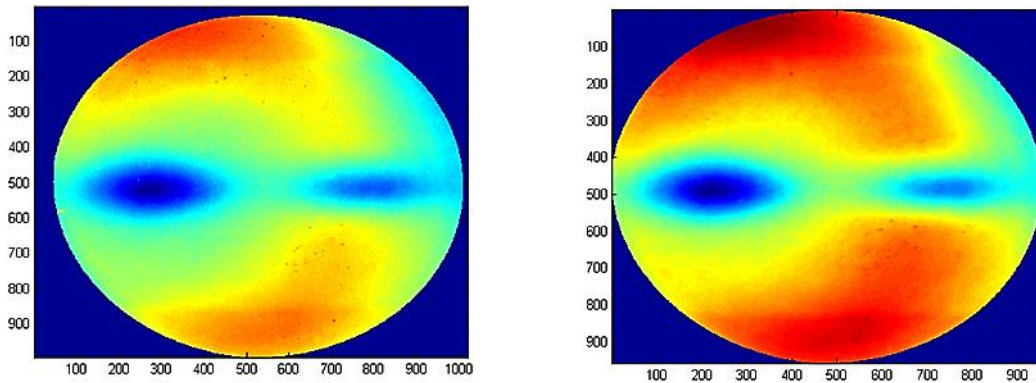
Figure 3-2 Comparison of data acquired with the 100 mm Ø collimator of a Twyman-Green interferometer by Fisba, before (left) and after (right) data pre-processing.

FIGURE ERROR MAP AND EDGES EXTENSION

Once measurement data are prepared, the removal function (or *figure error map*) can be computed by subtracting the surface topography map from the desired final shape. Since material can be only removed by the process, a necessary condition is the positivity of the removal function. Therefore, all values need to be offset so that the minimum of the function is zero. However, this operation is usually not sufficient: the measurement area is generally circular, which makes part of the rectangular data array have non-defined values. This causes sharp steps at the edges of the measured region and harmfully influences the convergence of de-convolution algorithms. Phenomena like ringing effect [144] are typical consequences of edge discontinuities. For this reason, edge tapering (or extension) algorithms were developed in order to cope with this issue (see, e.g., [7] and [143]). Following Jiao et al. (2009) [143], a similar boundary manipulation was applied for the scope of the figure

68

correction work presented in this report. In **Figure 3-3**, an illustration of the edge extension principle is given.

Pixels values *f* beyond the boundary of the measurement area (grey zone in **Figure 3-3**) can be expressed as:

$$E(f) = E(p)e^{-\left(l^2/2\sigma^2\right)}$$

(3-2)

Such extension function is chosen because de-convolution by a Gaussian influence function is expected to be more compatible with a Gaussian edge.
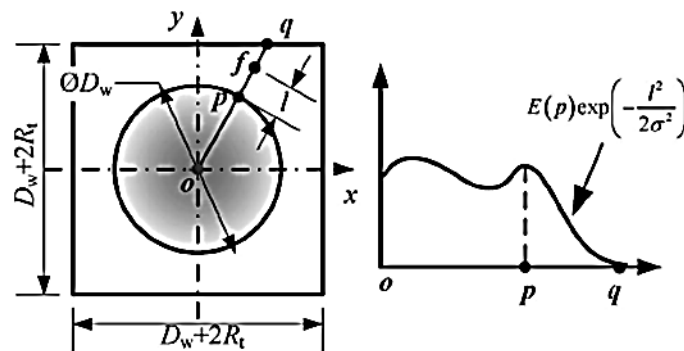
Figure 3-3 Principle of the edges extension (source: [143]).

The σ-parameter of the tapering function is taken equal or greater than the one of the beam footprint in order for the edge to match the figuring authority of the beam function. The rectangular figure error matrix results expanded in both directions by the width of the beam function radius (R_t).
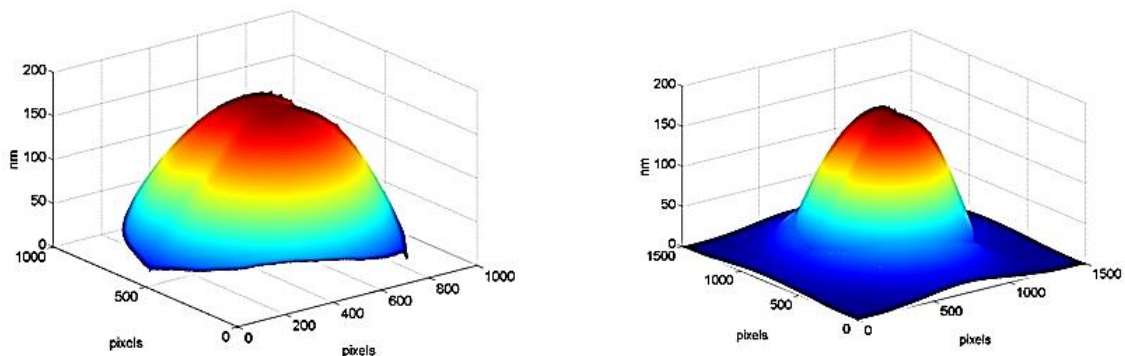
Figure 3-4 Figure error map before (left) and after (right) edges extension.

Taper data will fall outside the metrology area and this has the additional advantage of allowing for the actual figuring process to be smoothly carried

across boundary points. An example of the creation of an edge-extended figure error map is given in **Figure 3-4**.

VELOCITY MAPS

From the edge-tapered removal function, it is finally possible to derive the dwell-time map by solving equation (3-1). Subsequently, this needs to be converted into a chart of the tool scanning velocities for the use in a raster-type tool-path algorithm, as described in section 2.5.1. Key-parameter for this operation is the width of a strip, or re-positioning pitch: this determines the rastering resolution and the speed values will be inversely proportional to it (equation (2-13)). The pitch is usually taken few millimetres broad, although the choice of its best value is typically established on experimental basis (see sections 4.2.2 and 5.2). In **Figure 3-5**, an example of figure error map with the corresponding velocity chart is shown.
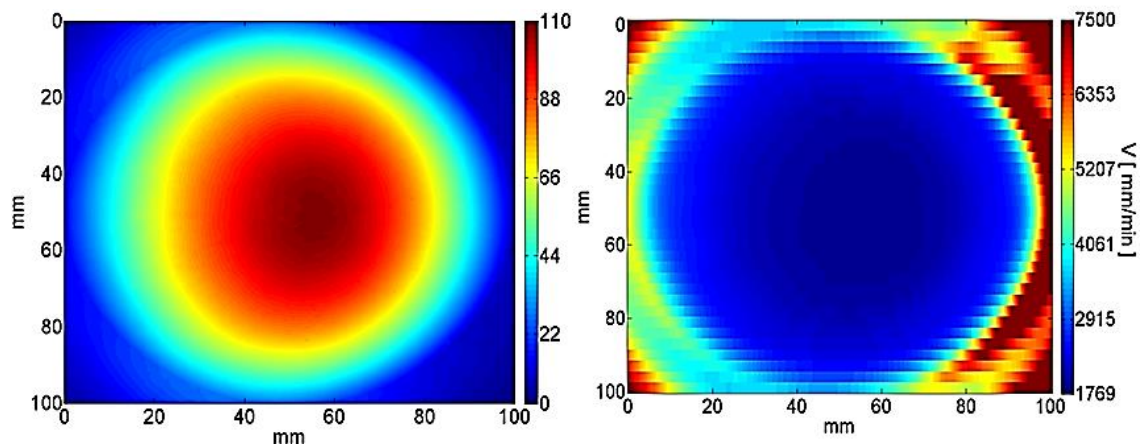
Figure 3-5 *left*: **example of error map;** *right*: **corresponding velocity map. The horizontal and vertical axes correspond, respectively, to the scanning and the pitch directions. The discretization of the velocity map across the vertical axis is due to the width of the pitch (3 mm) for the raster-scanning tool-path.**

It must be noted that the presented discussion doesn't take into account the progressive heating of the substrate during the RAP process. This has a considerable effect on the removal rates and compensation techniques are required in order to prevent divergence of the actual figuring process. For the work described in this manuscript, a thermal compensation coefficient method

was systematically applied. After completion of the edge extension, only a percentage of the total figure error depth is considered for the velocity map computation. Implemented in an iterative figuring procedure, this strategy was expected to show rapid convergence, while restricting the effects of heat on the figuring process. The choice of the targeted percentage of material removal followed from an empirical approach. Figure correction results down to ~16 nm RMS were achieved by combining this method with the tool-path described in section 3.2. In Chapter 5, details about the coefficient choice are given and the convergence procedure is discussed.

IMPORTANT NOTE: The non-linear behaviour shown in **Figure 3-1** can vary significantly depending on the considered dwell-time range. This, in turn, is determined by the resolution of the data sampling (e.g., CCD x-y grid for interferometer data). For a correct computation of the dwell-time/velocity maps, this influence must be taken into account when the conversion from trenches depths to virtual spots is performed.

3.2 Tool-path algorithm and CNC-code

The tool-path algorithm adopted for the work described in this manuscript is a *reversed staggered rastering*. The first two loops of the tool-path are visible in **Figure 3-6**. Different from a classical meander raster-scanning (section 2.5.2), this tool-path follows a larger staggering step in Y-direction until the whole substrate area is covered. The same pattern is then alternately reversed, each time shifting the path by a chosen sub-pitch until all foreseen passes are completed. The quotient of staggering step over pitch yields the number of reversals.

This tool-path, in combination with an even number of rastering sequence reversals, is reckoned to introduce a symmetry effect along the pitch direction (Y-axis) which would otherwise be affected by in-homogeneity of thermal distribution and material removal. This, in turn, reduces temperature gradient effects. Additionally, possible etching in-homogeneities are "smoothed" by the flattening effect of the tool-path (see Chapter 4). The choice of this algorithm follows from results on neutral removal tests. In fact, this tool-path enabled the

user to achieve neutral removal down to ~30 nm peak-to-valley over 70 mm length (section 4.2.2). The actual Computer Numerically Controlled (CNC) figuring process is finally realized by dedicated programs, specifically tailored to the machine motion configuration (3-axes). Every CNC-code consists of a point-by-point translation of the velocity map into expressions dictating axes motion in machinery language (G-codes & Fanuc 30i series - Macro-B). Such conversion is performed for every work-piece and each iteration step by a CNC-code generator, purposely created by the author for the scope of this work. The program "reads" the values of the velocity map along the predetermined scanning direction, following a re-positioning sequence dictated by the chosen tool-path (**Figure 3-6**).
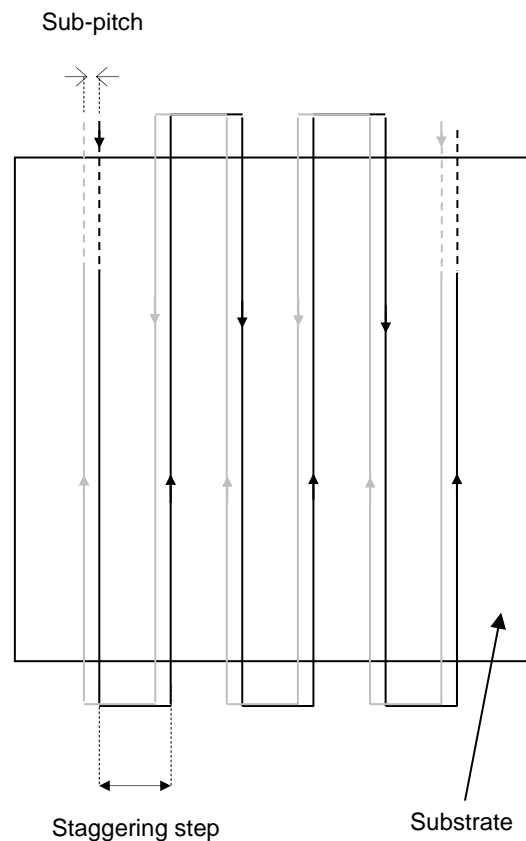
Figure 3-6 Schematic of reversed staggered tool-path algorithm: first two loops.
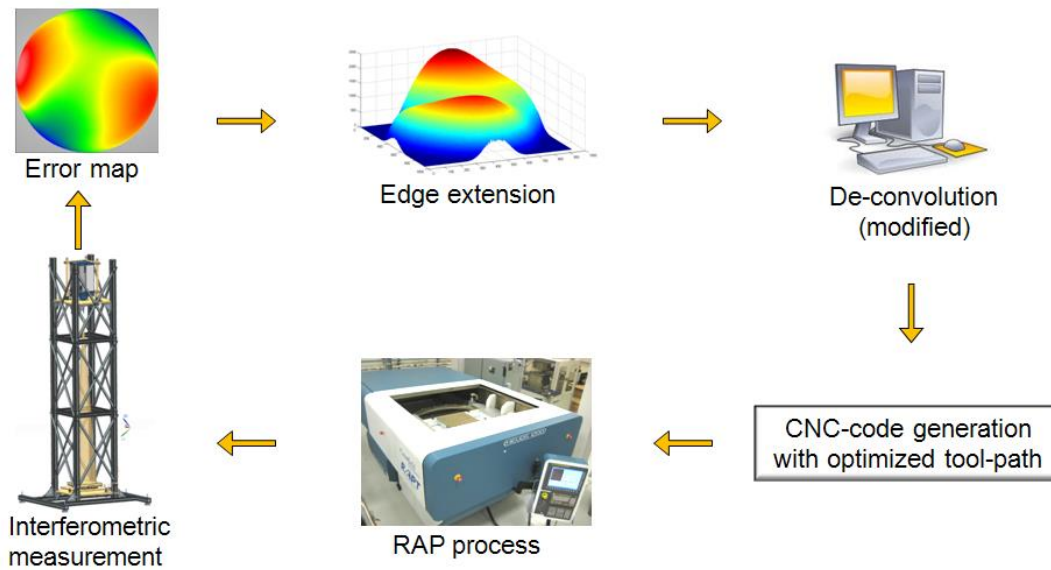
Figure 3-7 The iterative figuring procedure designed for the scope of this work.

The overall iterative figuring procedure is indicated in **Figure 3-7**.

4 EXPERIMENTAL DESIGN AND METHODOLOGY

In this chapter, the experimental investigation of the key parameters characterising the Reactive Atom Plasma process is presented and discussed. All results were accomplished using the Helios 1200 figuring facility. An extensive characterisation of the etching footprint was carried out in order to assess and optimise the properties of the influence function. Additionally, these investigations enabled the causes of etching inhomogeneities observed during earlier tests [14] to be identified and minimizing practices to be established. The design of the tool-path algorithm described in section 3.2 is based on the experimental observation of the behaviour of the optimised tool-footprint. Two types of substrate material were utilised in the course of this experimentation: Lithosil (synthetic fused silica) by Schott and ULE by Corning.

For every experiment carried out in the course of this project, after a RAP process was performed, the surface was hand-buffed for about 5 to 10 minutes by means of a polishing emulsion containing Al_2O_3 particles (mean particle size: 50 or 300 nm). This operation was introduced for the reduction of roughness and possible contamination (see also section 5.2.3); no measureable influence on the surface form was ever detected (surface measured before and after buffing). Only for the 400 mm diameter surface (section 5.2.6), the buffing time was about 20 minutes due to the size of the area.

Drawing on the knowledge acquired in this experimental work, the figure correction procedure was developed. The achieved results are discussed in Chapter 5.

NOTE: The trench tests carried out for the process characterisations were not repeated due to lengthy preparation and metrology times. To evaluate the uncertainties of trench depth and width, these parameters were assessed over a number of trench cross-sections and the standard deviations were calculated. Details are reported in Appendix C. This method estimates the characteristic etch profiles fluctuations within single passes. Such an estimate is considered appropriate, based on the proven repeatability of the RAP process [11].

4.1 Metrology equipment and methodology

For the experimental work carried out in this PhD, ultra-precision surface metrology equipment was utilised. This included monochromatic interferometers (He-Ne laser, λ=632.8 nm), as well as a white-light interferometer. Also, as mentioned in section 2.3.9, a pyrometer was available for non-contact surface temperature assessments. Differently, for the thermal footprint characterisation, thermocouples were utilised. Technical details about this instrumentation, as well as about the measurement procedures are given in Appendix D.

At the beginning of the project, only a phase-shifting interferometer of Twyman-Green type was available (FST10 by Fisba Optik). This was provided with a 100 mm diameter collimator, which limited assessments for process characterisation and first figure correction results to this small area (sections 4.2, 5.1, 5.2.1). A data acquisition method was devised in order to assure repeatability of the instrument down to few nanometres RMS (Appendix D.1). This is of particular importance when evaluating the trench and neutral removal data presented in the next sections. In those cases, subtraction of interferograms before and after the process is needed and the level of residual noise should be less than ten nanometres to allow assessing also the shallowest grooves (Appendix C).

At a later stage of the project, and for a limited period (April-May 2011), a vibration insensitive interferometer of Fizeau type was available on loan (Intellium H2000 by ESDI). This was provided with a 150 mm diameter beam expander and allowed a first upscale of the figuring procedure (section 5.2.2). Also for this instrument, a measurement methodology had to be optimised to assure repeatability and overcome artefacts issues (Appendix D.2).

Finally, for the metrology of large scale surfaces, a different vibration insensitive Fizeau interferometer was purchased (Zygo *DynaFiz*). Provided with a 4" f/3 transmission sphere, this instrument was utilised for the measurement of a 405 mm diameter area to prove the large scale application of the process. The Precision Engineering Institute at Cranfield designed and built an optical test-tower that would host the interferometer on its top. The interferometer was tested in this setup and, also in this case, a procedure was optimised to achieve

repeatability. More details on this method, as well as on the used technology can be found in Appendix D.3.

The surface roughness assessments were carried out by means of a white-light interferometer (CCI6000 by Taylor Hobson). The measurement field of view was 366μm x 366μm with a 50X magnification lens. Repeatability over this small area was assumed to comply with the manufacturer specifications (3 pm RMS). A discussion about white light interferometry, as well as the data acquisition and manipulation modes can be found in Appendix D.4.

For the work performed in this PhD project, samples made of fused silica and ULE were utilised. In particular, four 200mm x 200mm x 27mm fused silica substrates and four 200mm x 200mm x 25mm ULE samples were available (**Figure 4-1**). For all these samples, the two 200mm x 200mm surfaces were periodically polished with a tween-polisher by an external supplier, as no polishing facility for this size was present at Cranfield. The required surface quality was typically < 1 μm PV and the roughness < 2 nm S_q. As visible in **Figure 4-1**, a blue polyamide film tape was systematically used to cover one of the surfaces: this was done to prevent reflection from the back face when measuring the front surface with the interferometer.

Ultra-Low Expansion (ULE) glass
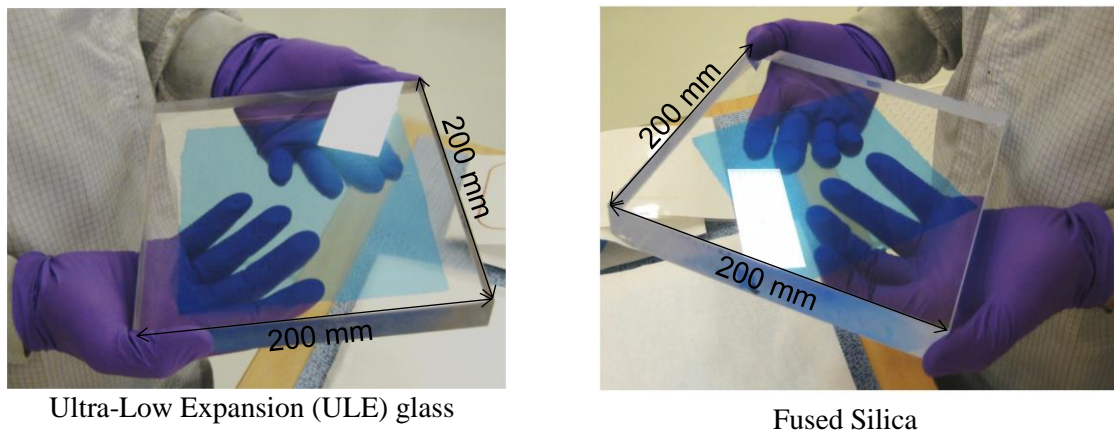
Fused Silica

Figure 4-1 *left*: **one of the 200mm x 200mm x 25 mm ULE samples;** *right*: **one of the 200mm x 200mm x 25 mm fused silica samples**

These samples were utilised for the process characterisation (section 4.2). The re-polished fused silica samples were then used for the small scale figuring

tests (sections 5.2.1and 5.2.2). The use of surfaces larger than the metrology field of view had the advantage of emulating heat transfer conditions of a large area process.
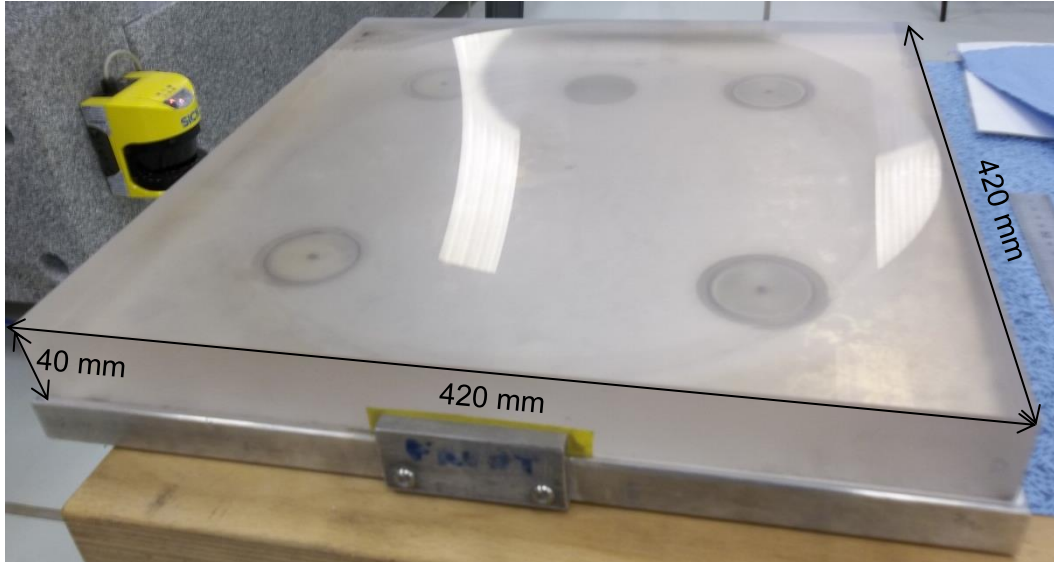
Figure 4-2 The 420mm x 420mm x 40mm ULE substrate with the concave spherical geometry machined on the large square face.

For the large scale experiments, only one 420mm x 420mm x 40 mm ULE substrate was available. This was due to the blank costs (6000 $), as well as to the preparation times (grinding and polishing). Therefore, the large scale figure correction test was performed twice on this same sample that was re-polished in-between. A concave spherical clear aperture of 405 mm diameter and 3 m radius of curvature was machined on one of the 420mm x 420mm surfaces. Its form accuracy after polishing was measured with the DynaFiz interferometer as ~2.4 μm PV. More details are given in section 5.2.6.

Finally, for the thermal footprint assessment, one circular silicon-wafer of 200 mm diameter and 0.73 mm thickness was utilised. The processed surface was polished to a roughness of 0.5 nm RMS.

As mentioned in section 2.3.9, in the machine the process surface faces downwards. Samples are therefore sustained by metallic fingers protruding by just 1 – 2 mm and 2 – 3 mm thick. Such thickness can be relevant to avoid bending due to the plasma heat. The fingers keep the samples process surface

aligned with the holder bottom face. In **Figure 4-3 (a)** and **(b)**, the samples holders for the 200mm x 200mm and 420mm x 420mm substrates are shown.

Finger sustaining the substrate

200 mm

200 mm

(a)

Copper finger sustaining the substrate

420 mm

420 mm

Holder seen from below

(b)
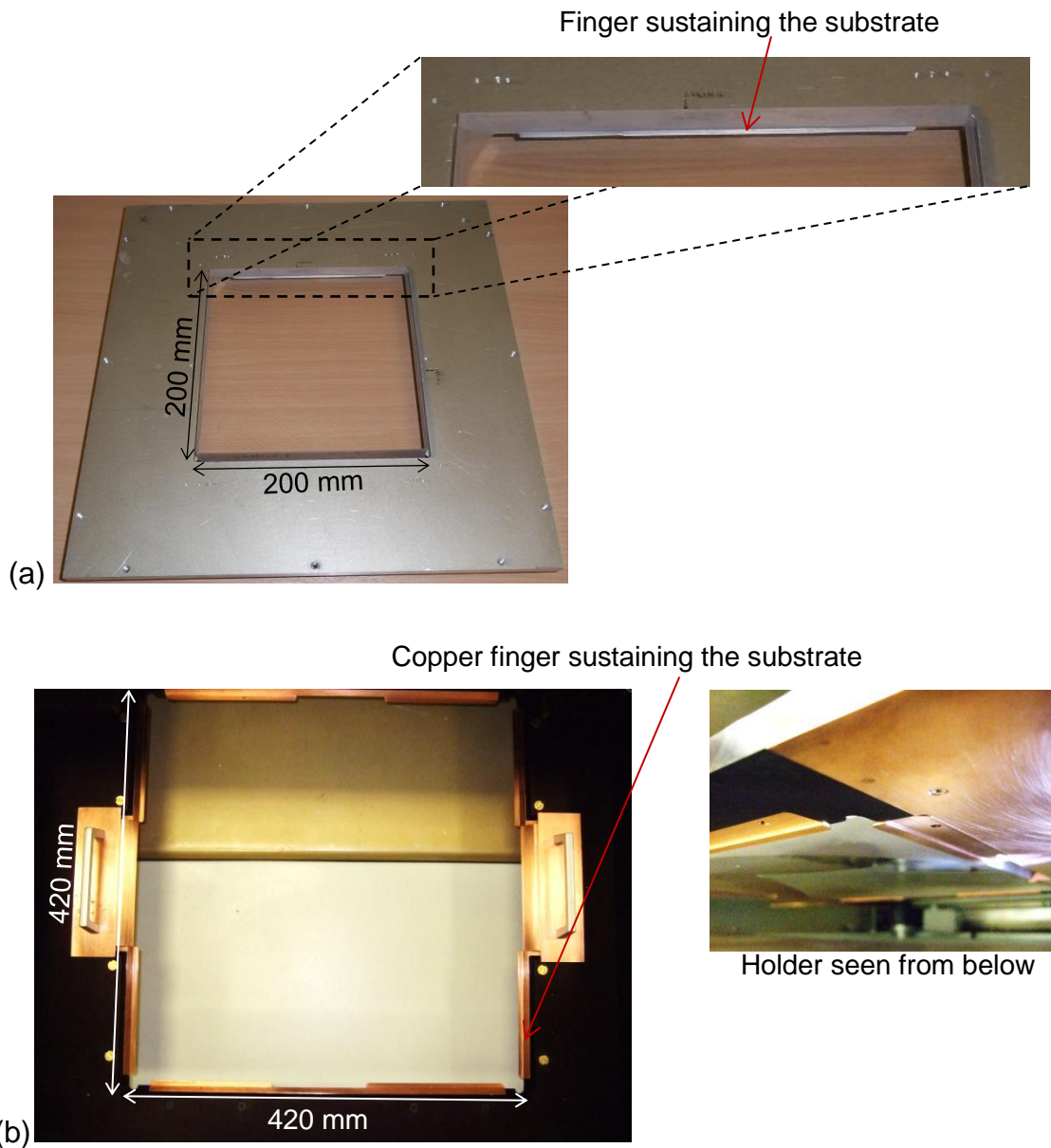
Figure 4-3 (a) Aluminium holder for 200mm x 200mm samples; (b) aluminium holder with copper fingers for the 420mm x 420mm substrate.

As shown in **Figure 4-3 (b)**, in the later part of the work a new holder was utilised for the 420mm x 420mm part. The side exposed to the plasma was provided with fingers and plates made of copper, as the aluminium had been observed to deteriorate under the action of the fluorinated plasma.
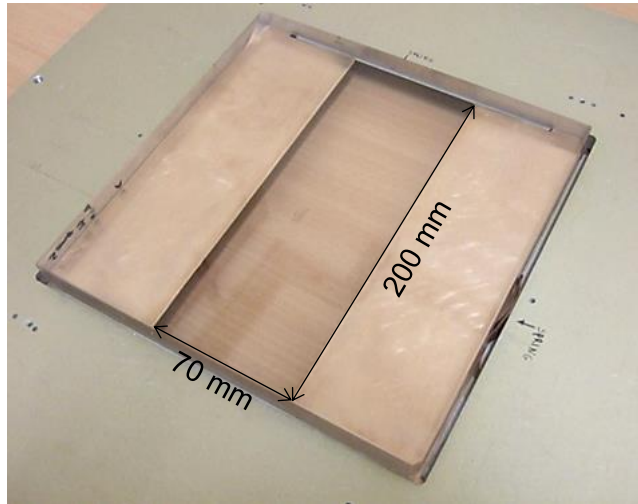
Figure 4-4 sample mounted onto the aluminium holder, with the brass mask defining the 200mm x 70mm area.

For trenches and neutral removal tests (section 4.2), a mask composed of two brass plates of ~3 mm thickness was added to the holder setup to cover the side areas of the sample surface, thus creating a non-etched reference zone. The process area was then ~70mm x 200mm (**Figure 4-3 (b)**).

4.2 Process characterisation

The etching footprint of the RAP process can be approximated by a Gaussian shape. For a given torch travel speed, the depth and width of the influence function depend on etchant concentration, power and stand-off distance between nozzle and substrate. The substrate composition will also affect the chemistry, hence the removal rates need characterising for each different material.

During early tests [14], it had been observed that an unwise choice of certain parameters can cause the appearance of irregular features which constitute a drawback for the control of the process. For illustration, the mean removal cross-section obtained by raster-scanning a 70mm x 200mm fused silica area is shown in **Figure 4-5**. The utilised setup is shown in **Figure 4-3 (b)** and the tool-path in **Figure 4-5** (*right*).
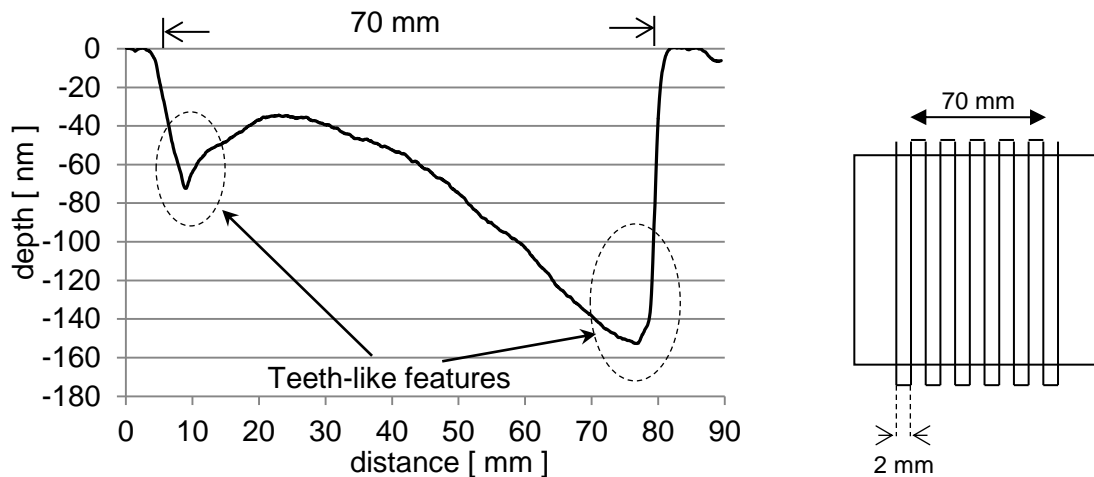
Figure 4-5 *left*: **mean cross-section profile resulting from a raster-scanning of fused silica substrate with the above reported processing parameters;** *right*: **utilised tool-path.**

For this example, the experimental setup is the one shown in **Figure 4-3 (b)** and the processing parameters were:

- 1000 W forwarded power;
- 0.8 slm of a 10% SF_6/Ar mixture;
- 7.5 mm nozzle-to-surface stand-off distance.

The steep hollows evidenced on the graph are the consequence of non-optimised process parameters. This point is investigated in sections 4.2.1, where the effect of two processing parameters on the etching footprint is explored. After optimisation of such process variables, in section 4.2.2, the process performance is assessed for surface raster-scanning patterns.

4.2.1 Tool-footprint characterisation and material removal rates

In this section, the etching footprint performance is investigated with respect to following process parameters: the power forwarded by the RF generator to the ICP torch and the stand-off distance between torch nozzle and surface. The process response for factors like SF_6 concentration and tool velocity was not expected to affect the ratio between a primary etch zone and the observed irregular features (see discussion as follows).

This part of the work was done in conjunction with Dr R. Jourdain.
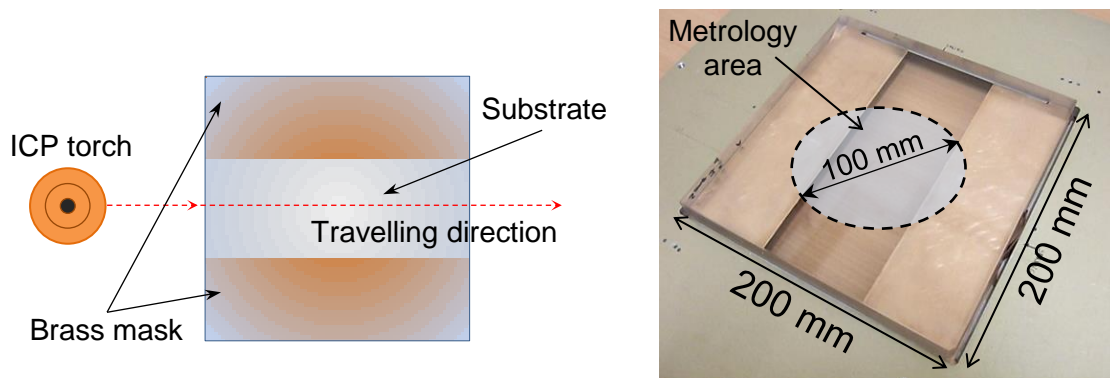
Figure 4-6 Process arrangement for trenches and neutral removal tests with brass mask: sketch (left) and photo (right).

In **Figure 4-6**, a sketch of the experimental arrangement is shown. A brass mask was used to create two reference zones indicating the zero depth (non-processed area)[7], while the surface was etched in single pass mode at constant speed. On each surface, the same 100 mm diameter area was measured before and after a test by means of the Twyman-Green interferometer (Fisba). Subtraction of these measurements delivered the result. The samples utilised in this work were the 200mm x 200mm x 27mm fused silica substrates.
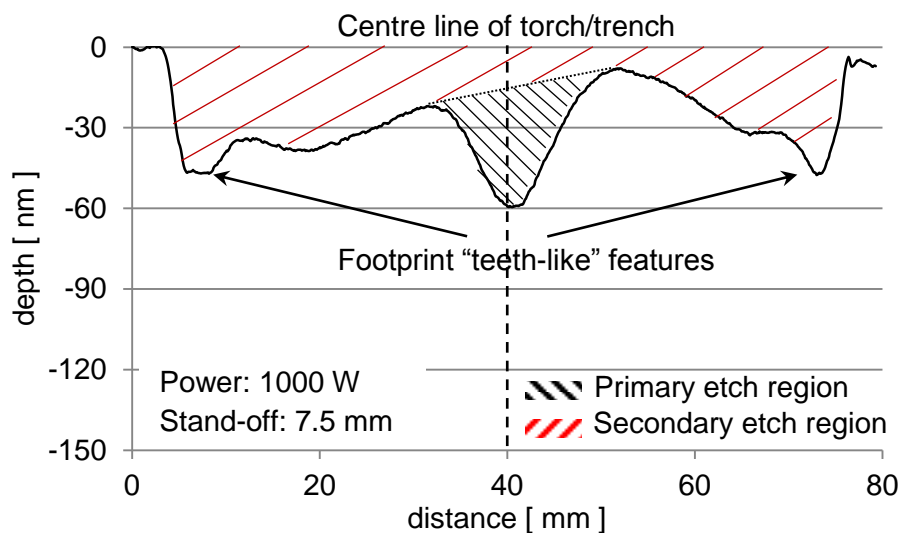
Figure 4-7 Trench etched at 1000 mm/min, 7.5 mm stand-off, 1 kW forwarded power.

---

[7] The presence of the mask is not considered influent for the etching depth assessment.

First, a qualitative assessment was carried out and this revealed the origin of the "teeth-like" features (see **Figure 4-5**, *left*). In **Figure 4-7**, the mean profile of a trench etched at a speed of 1 m/min is shown. As in the example of **Figure 4-5**, the stand-off between nozzle and surface was 7.5 mm, the forwarded power 1 kW and 0.8 slm SF_6/Ar mixture. Clearly, under these processing conditions, non-localized etching anomalies appear as integrated part of the footprint.

A reason for the presence of "teeth-like" features, or secondary etch regions, can be identified in a lack of heat enhanced etching anisotropy in the central area of the surface portion exposed to the plasma plume. Such anisotropy could be mainly improved by increasing the forwarded power. Also, reducing the distance to the surface was expected to increase the energy input by exploiting the heat from the hotter zone of the plasma plume.
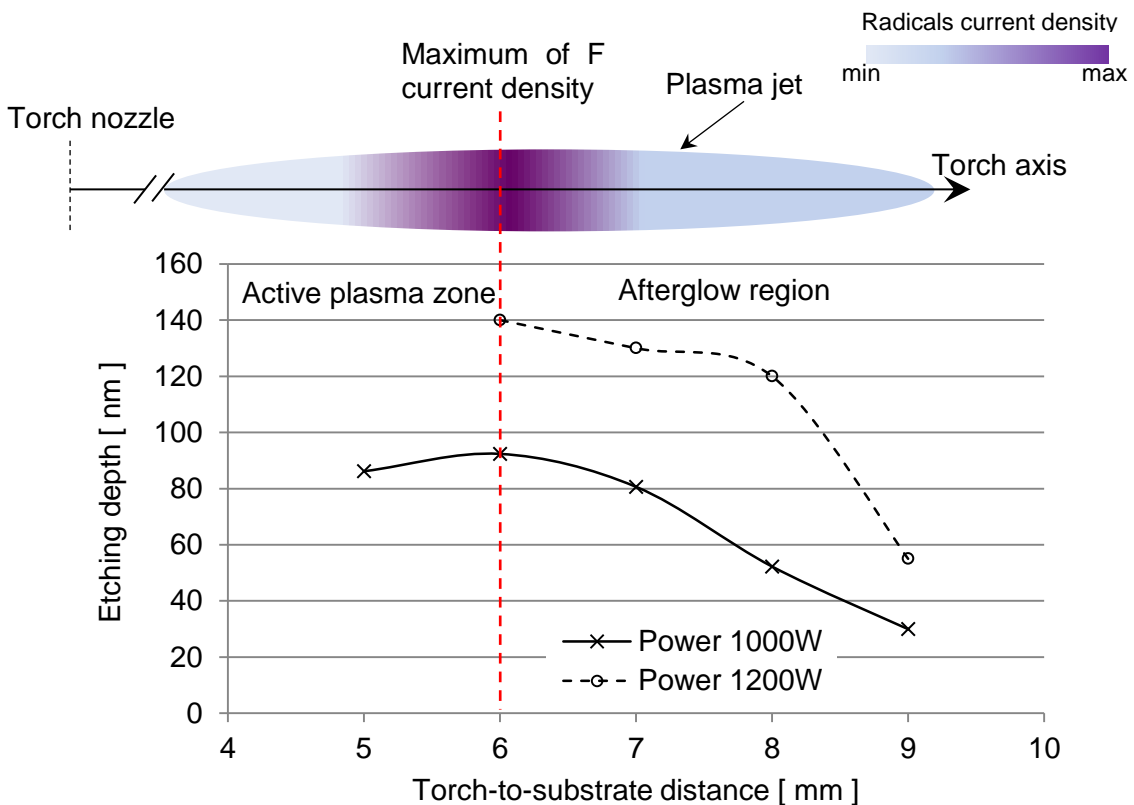
Figure 4-8 *upper sketch*: depiction of radicals current density as a function of the stand-off distance; *lower graph*: Characterisation etching depth versus of stand-off distance for two values of forwarded power – torch travel speed: 1000 mm/min.

When variations of the distance along the plasma jet axis are involved, a contiguous phenomenon linked to the evolution of SF_6 chemistry must also be considered. In 2008, Arnold and Schindler reported that the dissociation of the parent molecule SF_6 into F-radicals follows a temporal and spatial configuration along the torch axis [125]. In particular, in this study, mass spectrometry investigations confirmed that the fluorine current density distribution grows up to a maximum for a given distance along the jet axis and then drops again due to recombination into SF_x radicals.

When etching a surface, the removal rate is logically expected to increase up to the point of maximum fluorine density (active plasma zone). Beyond this limit (afterglow region), recombination reactions and the reduced heat input on the surface will produce a shallower primary etch with a more pronounced secondary etch region[8].
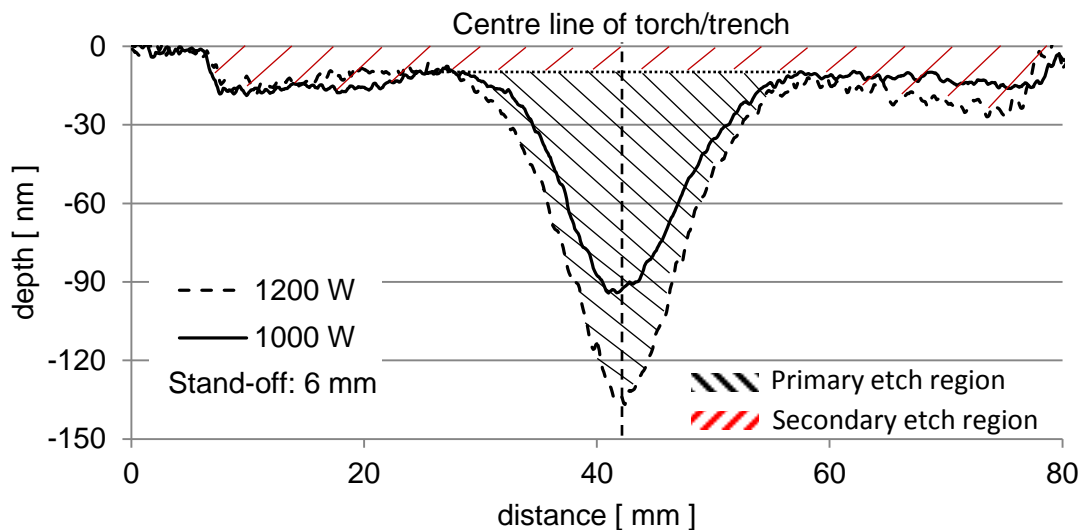
Figure 4-9 Mean profiles of trench etched at 1000 mm/min under the optimum processing conditions derived from the design of experiment (stand-off: 6 mm).

In **Figure 4-8**, the sketch of a plasma jet and the graph of illustrate the evolution of radicals current density in relation to maximum etching depths for the RAP

---

[8] According to Arnold and Schindler [125], the presence of oxygen plays also an important role for the width of the etching profile.

torch. Here, to confirm the described hypothesis, the effect of various stand-off distances was investigated at two levels of forwarded power. The torch travel speed was 1000 mm/min.

From these experiments, the optimum conditions were established (constant 10% SF_6/Ar mixture at 0.8 slm). In the graph of **Figure 4-8**, the trends of the plasma footprint etching depth are shown in relation to the stand-off distance for a forwarded power of 1000 and 1200 W. In both curves, the maximum occurs at **6 mm** stand-off[9]. Interestingly, this maximum of efficiency corresponds to a major improvement in the distribution of the secondary etch region. This appears obvious when comparing **Figure 4-7** and **Figure 4-9**. As mentioned before, the phenomenon is linked to the increase in etching anisotropy promoted by a larger energy input from the hotter plasma region along the torch axis. However, the influence of gas flow dynamics should also be considered, as these are responsible for radicals conveyance over the substrate surface.

Further, from **Figure 4-9**, it can be deduced that the higher level of forwarded power mainly improves the Gaussian depth and can be chosen to attain a better ratio of primary to secondary etch regions.

In conclusion, the most favourable etching parameters were identified through the presented characterisation and were adopted for the whole course of the subsequent experimental work. Such parameters are:

- **1200 W** forwarded power;

- 0.8 slm of a 10% SF_6/Ar mixture;

- **6 mm** nozzle-to-surface stand-off distance.

Finally, adopting optimum parameters, the etching depth as a function of the torch travel speed was assessed on two substrate materials: fused silica (Lithosil [46]) and ULE (**Figure 4-10**). These are the same materials utilised for the figuring work described in this thesis. The reader may note that trenches on

---

[9] It wasn't possible perform tests with a stand-off of 5 mm, at 1200 W forwarded power. The reason lies with the high gas pressure in the gap that impedes the plasma survival.

ULE result circa twice as deep as on Lithosil, which is probably linked to the different chemical composition (Ti content in ULE). The trends displayed in **Figure 4-10** constitute the basic dwell-time characterisation of the influence function and were exploited for the de-convolution computational method described in section 3.1.
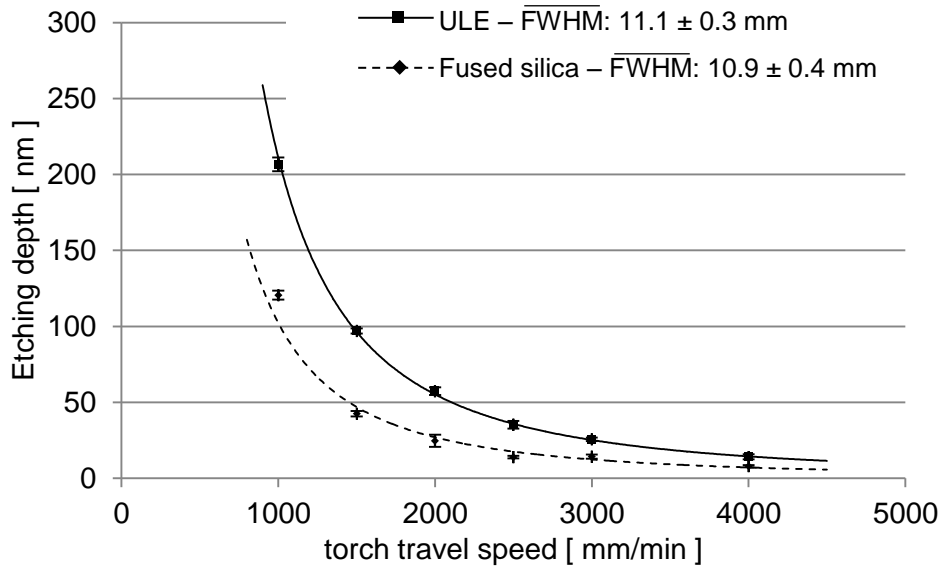
Figure 4-10 Removal depths versus torch travel velocity for ULE (solid line) and fused silica (dash line); error bars represent the standard deviation of trenches depth.

As a remark, the values of etching depth plotted on the graph (**Figure 4-10**) are the actual *Gaussian depths*, excluding secondary etch region depth. In fact, as noticeable in **Figure 4-9**, even under optimum conditions, lateral material removal isn't completely avoidable. However, this has minor relevance and compensation will occur during the actual figuring process. Indeed, later investigations showed that the secondary etch region depth becomes negligible at higher surface temperatures. This is discussed in section 4.2.2. Also, the design of the tool-path algorithm includes a form of compensation by uniformly distributing possible secondary region etching. This is described in section 4.2.2.

NOTE: attempts to achieve further improvements of the etching footprint performance were made by increasing the reactants concentration and the

power. While the first factor (0.9 slm reactive gas) didn't show any significant impact (saturation?), the heat generated by higher forwarded power (1300 W) caused damage to the torch main quartz tube.

As recognisable from the legend of **Figure 4-10**, fluctuations of the trenches width were observed. In [135], a correlation between FWHM and speed is reported and is explained as a result of heat flux dynamics varying with change of the torch velocity. Such a relationship couldn't be confirmed from the investigations carried out in the course of this characterisation work, as the width uncertainties appeared uncorrelated (see also Appendix C). It is, however, to be noted that the range of speeds considered by Meister and Arnold (2010) [135] is typically much lower than the one needed for the purpose of the figuring work described in this thesis. It is, therefore, conceivable that effects on the width become negligible at higher speed (> 1000 mm/min). However, since the trench width defines the figuring authority (see also Chapter 3), a test was required to check the assumption of a near-constant FWHM. The sinusoidal trench described in section 5.1 constitutes such an experiment.

4.2.2 Neutral removal and investigation of raster-scanning patterns

In order to achieve removal of a constant amount of material over a defined area, the effects of pitch variations of raster-scanning tool-paths were tested. Five different pitch values were investigated. The processing parameters are reported below, together with a sketch of the used tool-path (**Figure 4-12**):

- Stand-off distance between torch nozzle and substrate: 6 mm;

- Forwarded power: 1200 W;

- 0.8 slm SF_6;

- Brass mask used to define 70 mm areas;

- Speed: 3 m/min;

- Pitches: 2, 3, 5, 10, 14 mm (variable parameter).

Fixed parameters

The results are displayed in **Figure 4-12**. It can be seen that the meander paths with larger pitches produce more even removal trends. This seems to be a combined effect of more even secondary removal and more even heat gradient affecting the etching rate. The meander path with 14 mm pitch shows the waviness due to the Gaussian footprint, while this effect becomes less evident for shorter pitches.

Figure 4-11 Sketch of the experimental setup for raster-scanning patterns.

Linear slopes can be (partially) compensated by reversing the staggering sequence. One way of doing this is to take a larger main step as a multiple of a smaller pitch and then turn this raster-pattern around after shifting it by the length of such secondary pitch. Also, if the quotient of staggering step over pitch is even, homogeneity of removal can be expected. This is the basic principle of the *reversed-staggered rastering* tool-path introduced in section 3.2.

An applicative example of this tool-path algorithm is shown in **Figure 4-13**. Homogeneous etching down to ~30 nm PV was achieved over a 70mm x 100mm fused silica surface area. Based on the results shown in **Figure 4-12 (b)**,

87

the main pitch was compromised to 12 mm, with a secondary pitch of 3 mm for a total of four reversals.
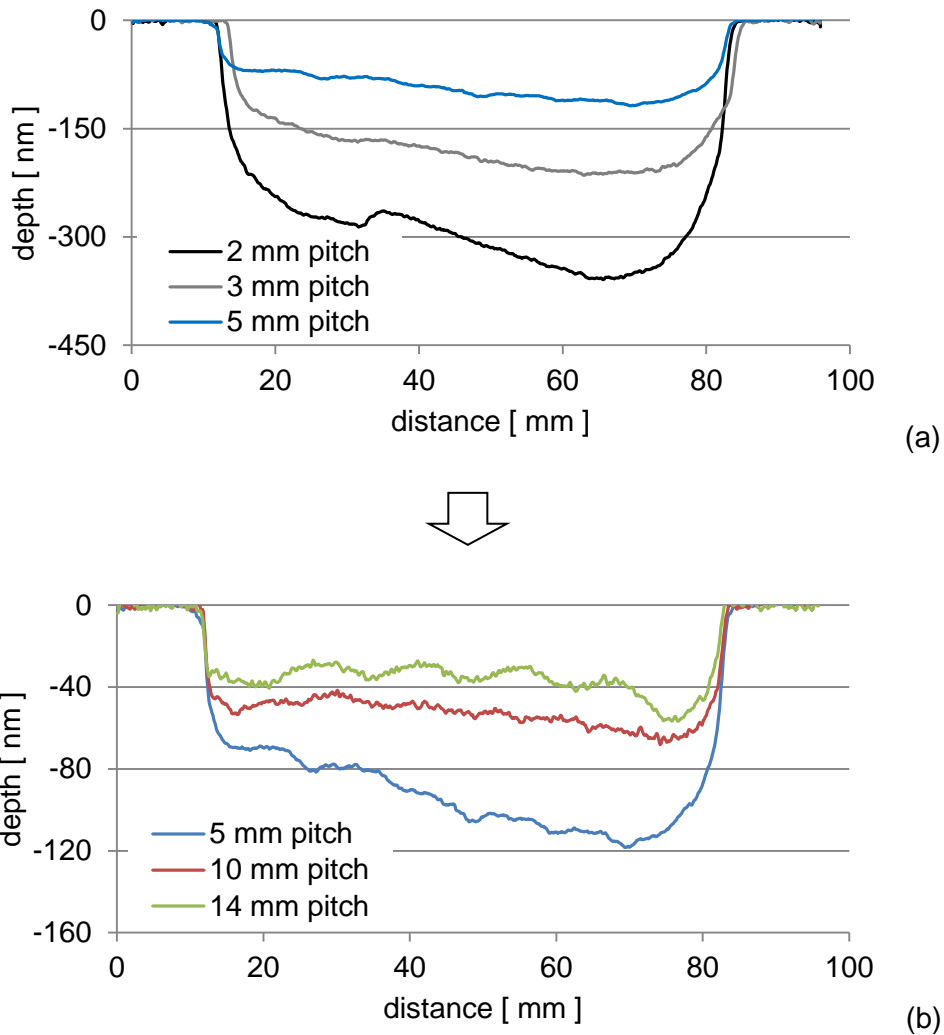
Figure 4-12 Raster-scanning of 70 mm wide areas: from small pitch (a) to large pitch (b); the profile at 5 mm pitch is displayed on both plots for comparative purposes.

The improvement achieved by means of the new tool-path is highlighted when comparing **Figure 4-13** with **Figure 4-12 (a)**. In **Figure 4-12**, the grey line represents an etching profile attained by a classical raster-scanning with 3 mm pitch and shows a deviation from flatness of about 100 nm PV. In comparison, the deviation value for the reversed staggered rastering is <30 nm.
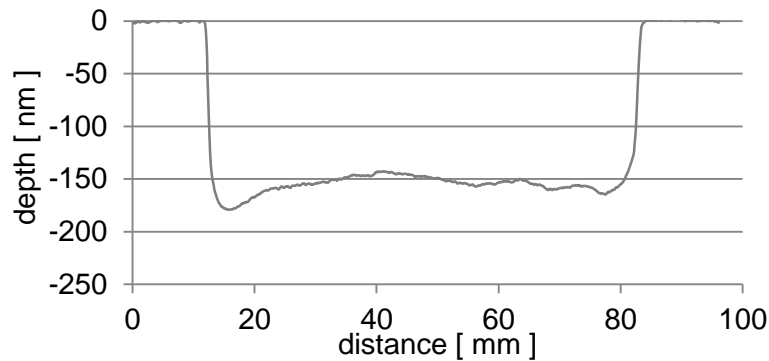
Figure 4-13 Average cross-section profile for a neutral removal over a 70 mm area achieved using the reversed staggered rastering. Raster speed: 3 m/min; staggering step: 12 mm; pitch: 3 mm.

4.2.3 Thermal assessments

<u>RELATION BETWEEN ETCHING DEPTHS AND TEMPERATURES</u>

The material removal rate of the RAP process is reckoned to increase with temperature, following an Arrhenius-type trend [10], [11], [14]. Therefore, the progressive heating of the substrate due to the plasma plume will quickly make the etching depths be significantly larger than at room-temperature (**Figure 4-10**). Such an effect prevents the process from being fully deterministic without temperature adaption, thus increasing the number of required figuring iterations. As demonstrated in Chapter 5, the empirical compensation method described in Chapter 3 is proven to be successful at delivering high quality results. However, further improvements are still expected by implementing an optimum use of the input energy. The aim of this part of the work is to lay the path for an in-process adaptation which shall enable to re-tune the torch travelling velocity according to surface temperature variations (see also [14]).

The strategy pursued within this project envisages an in-flight measurement of the surface temperature by means of the pyrometer (see section 2.3.9 and Appendix D.5). This instrument is located ~16 cm on the right of the ICP torch

(**Figure 2-26 (b)**) and temperature acquisitions can be logged by the machine logic system. The Arrhenius-plots depend on the processing parameters in use, as well as on the etched material.

In a first series of experiments, substrates were pre-heated on a hot-plate while the temperature rise was being monitored by means of three thermocouples attached on different locations of the surface that wouldn't be exposed to the plasma plume. Subsequently, a single-pass groove was etched at constant speed after recording the surface temperature value (**Figure 4-14**). The temperatures acquired with pyrometer and contact sensors were in agreement within better than 5 $^{\circ}$C, which shows homogeneous heating of the substrate for the utilised setup. Early results for this kind of investigations are reported in [14]. All experiments presented in this section were performed on fused silica substrates, but the same principles can be transferred on other materials like ULE.
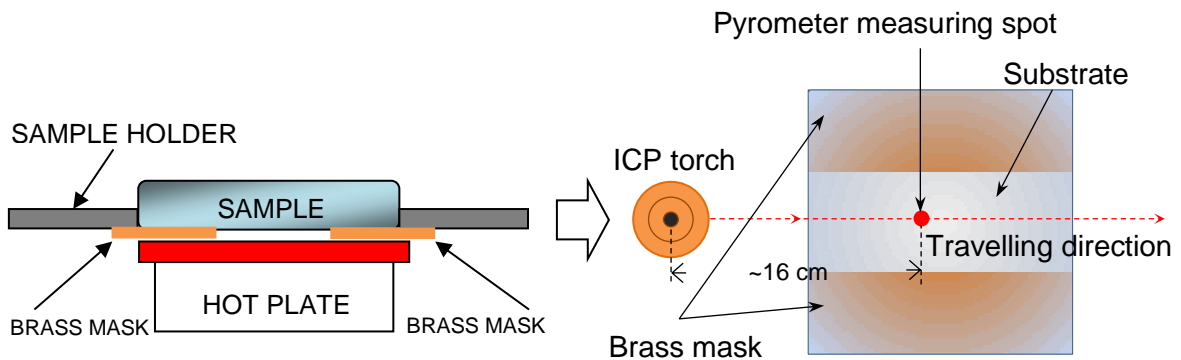
Figure 4-14 Experimental arrangements for hot trenches tests.

The results of this investigation are shown in **Figure 4-15** and **Figure 4-16**. In **Figure 4-15**, a comparison between the profiles of hot trenches and the same trenches at room temperature is shown for two values of torch velocity. From a first observation, one can infer that the secondary etch regions seem to disappear at high temperature ($\gtrsim$ 50 $^{\circ}$C). As a possible reason, a link between surface activation energy and etching selectivity is suspected. However, an ultimate explanation is still sought.
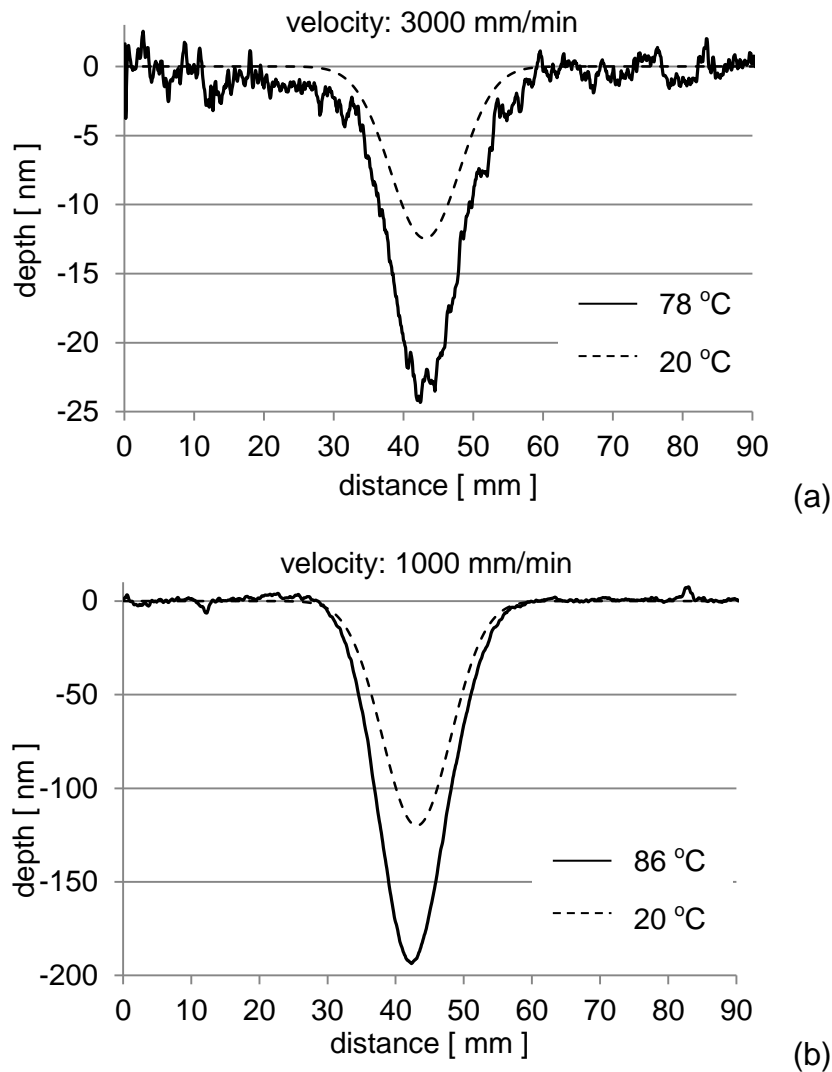
Figure 4-15 Mean profiles of hot trenches. (a) trench etched at 3000 mm/min, 78 $^\circ$C; (b) trench etched at 1000 mm/min, 86 $^\circ$C (profiles at 20 $^\circ$C are illustrated without secondary etch region for comparison purposes only).

In the upper plots of **Figure 4-16** (**(a)** and **(b)**), the trends of removal depth versus surface temperature are shown for two values of travel speed. **Figure 4-16 (c)** illustrates the comparison between the two trends in terms of relative etching depth percentage. Here, the values are normalized over the depth at 20 $^\circ$C.

Although both curves proceed near-linearly up to around 80 $^\circ$C, divergence could take place for higher values of temperature. To further assess this issue a different investigation was performed and is reported in section 5.2.4.
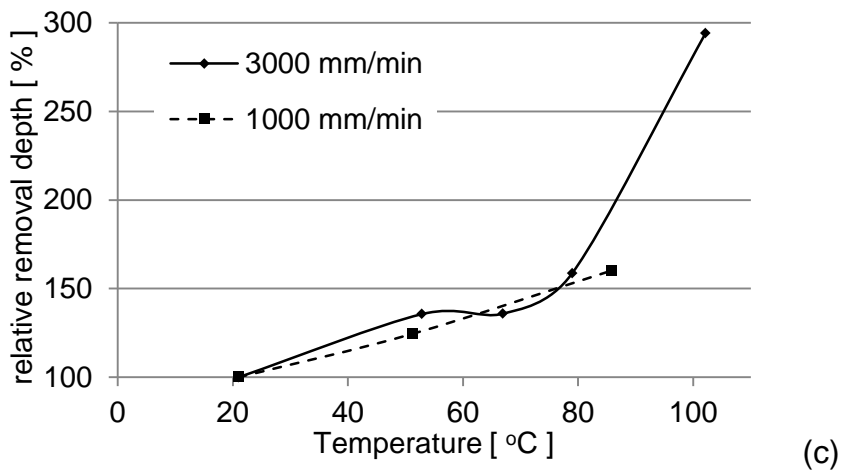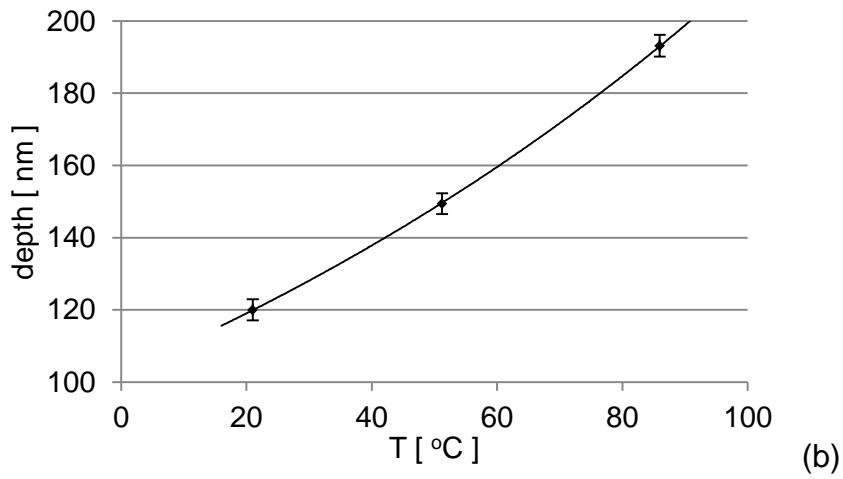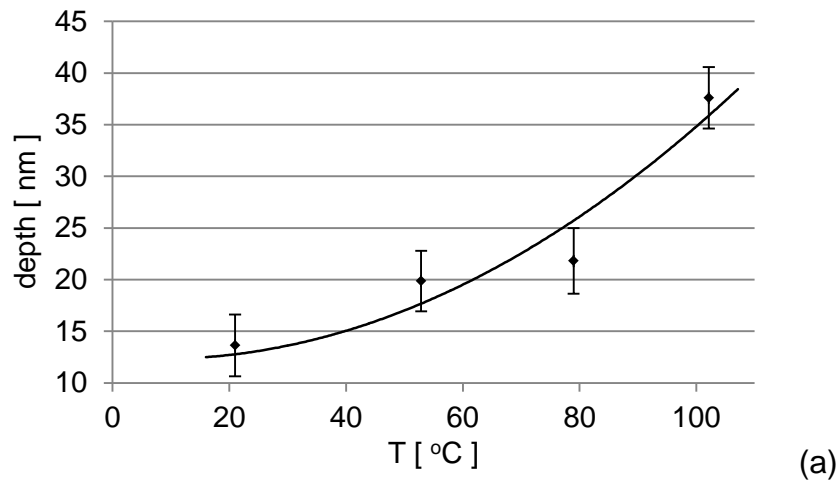
Figure 4-16 "Hot trends". (a): Removal depths vs. surface temperature for trenches at 3000 mm/min. (b): Removal depths vs. surface temperature for trenches at 1000 mm/min. (c): Percentages of removal depths increase vs. temperature for the two values of scanning speeds (1000 and 3000 mm/min).

From these investigations, it is not directly possible to relate the graphs in **Figure 4-16** to equation (2-9) as the actual etching temperature is unknown.

THERMAL INVESTIGATION OF A RASTER-SCANNING PROCESS

In this part of the work, the idea of a temperature-adapted surface processing was implemented for the case of neutral removal. The reversed-staggered raster tool-path (section 3.2) was upgraded in order to host in-flight temperature acquisitions by means of the pyrometer.
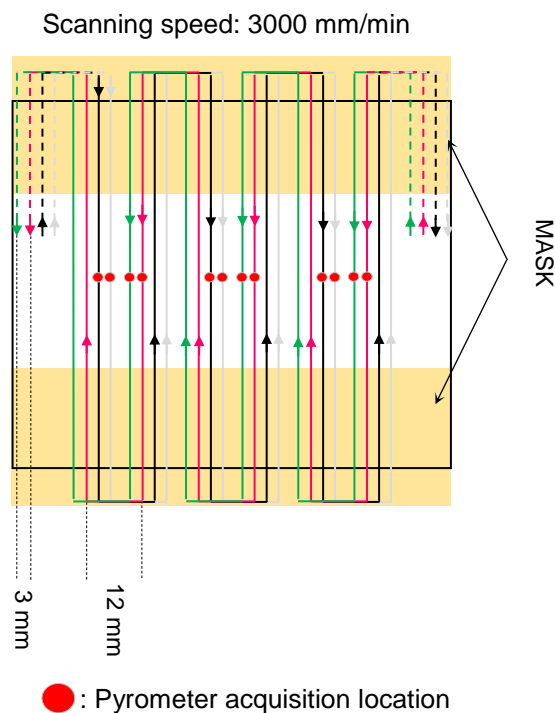
Figure 4-17 Sketch of reversed-staggered rastering with in-flight temperature acquisition.

In **Figure 4-17**, process set-up and tool-path parameters are shown. The reference mask was positioned perpendicularly to the torch travelling direction in order to allow for pyrometer acquisitions along the whole sample length. Temperature measurements were possible only every second pass due to the presence of one single sensor. The results of this test are displayed in **Figure 4-19 (a)**. For comparison, in **Figure 4-18 (b)**, the same principle was applied for a classical surface rastering with 3 mm pitch. The raster-scanning were first run at

a speed of 3000 mm/min without temperature monitoring. For the temperature adapted etching, the initial speed was the same, but the trend of **Figure 4-16 (a)** was exploited as feedback correction function to progressively increase the velocity values.

(a)

(b)
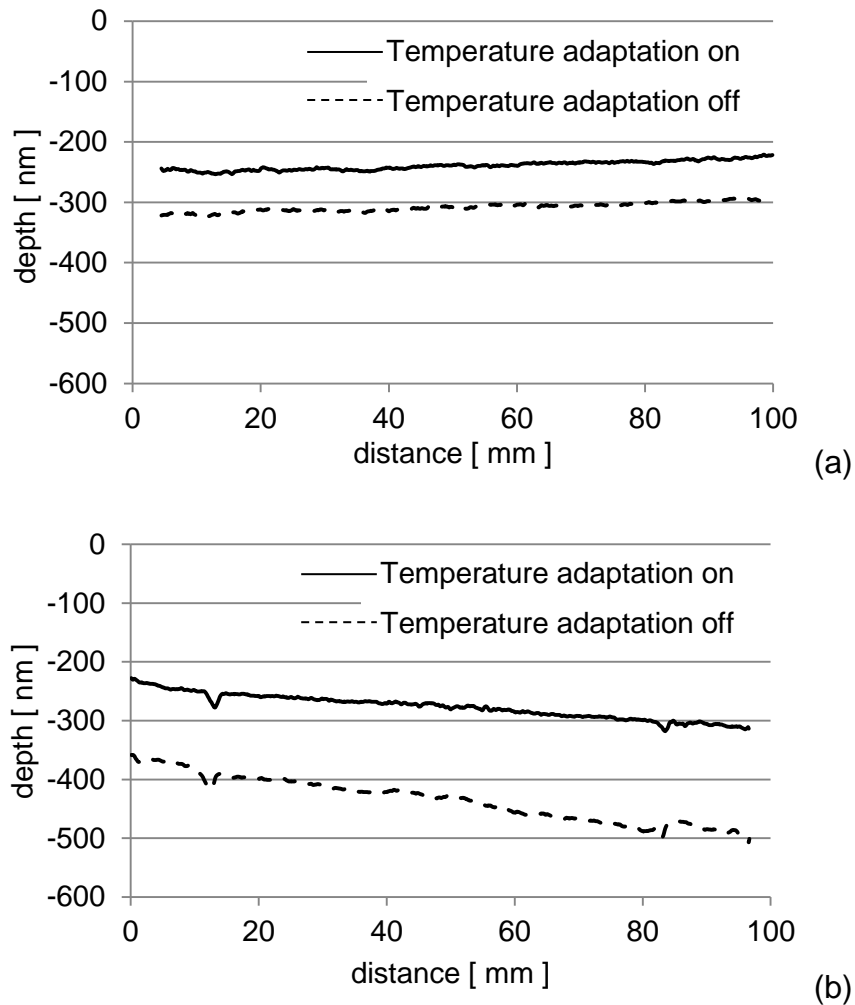
Figure 4-18 Mean profiles resulting from reversed-staggered rastering (a) and classical raster-scanning with 3 mm pitch (b). The solid lines represent the temperature adapted etching process.

This method bases on the implicit assumption that the same adjustment function applies for speed values larger than 3000 mm/min. As discussed in section 5.2.4, this supposition isn't necessarily valid for arbitrary ranges of speed.

In **Figure 4-19**, the comparison between the four kind of neutral removals is shown. Clearly, reduction of the etching depth is, in all cases, promptly achieved by the temperature adapted method. A comparative prediction, though, was not feasible within this work, as this would require a more detailed knowledge of the wings behaviour at temperatures above 20 ^{o}C. The improvements delivered by the reversed staggered tool-path are, once again, evident from the two graphs in **Figure 4-18 (a)** and **(b)**. In particular, from the plots the reader can appreciate the magnitude of the slope effect for a classical raster sequence.
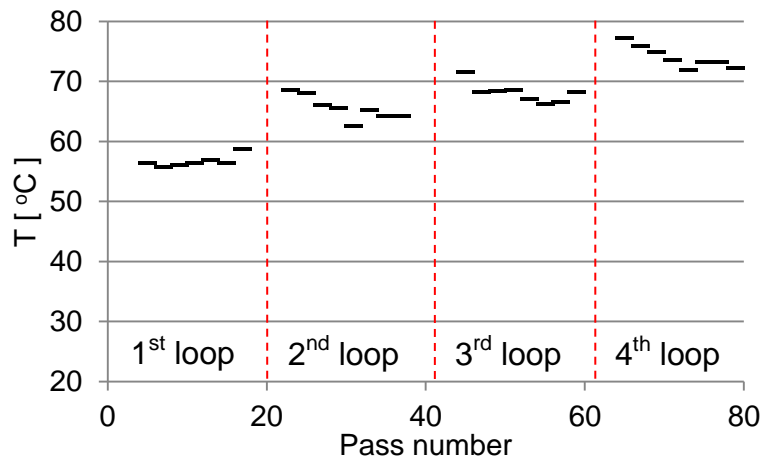
Figure 4-19 Values of temperature measured in-flight for every second pass.

In **Figure 4-19**, the graph illustrates the values of the sample front face temperature acquired during the process with the temperature adapted reversed staggered rastering (**Figure 4-18**). The plot is subdivided into consequent tool-path loops. Within single reversing-loops, the pyrometer acquisitions values confirm a very homogeneous temperature distribution (variation < 8 ^{o}C). As expected, a stepwise thermal increase from loop to loop occurs during the process.

This temperature measurements result confirms the capability of the reversed staggered tool-path algorithm to minimise heat gradients across the scanning direction throughout a process.

4.3 Summary of process characterisation tests

In this Chapter, the performance of the RAP ICP torch mounted on Helios 1200 has been characterised. It has been shown that two processing variables, stand-off distance from the surface and forwarded power, are the key parameters to optimise the etching footprint. In particular, the optimum values have been identified as 6 mm stand-off and 1200 W forwarded power. Under these processing conditions, maximum efficiency in material removal depth is achieved and the presence of anisotropic etching is minimised. These parameters have been subsequently adopted for the course of the entire experimental work. On this basis, the etching depths were assessed as a function of the torch travel speed for fused silica and ULE, the materials utilised for the figure correction work reported in Chapter 5. The inverse of these functions can be exploited for the dwell-time calculations.

Following the work on footprint optimisation, raster-scanning patterns have been investigated and the influence of the pitch size assessed. The introduction of larger pitches produces near-linear etching slopes, which are considered to be a combined effect of surface temperature increase and secondary etch regions. Based on these observations, the tool-path sequence described in section 3.2 has been designed. This compensates for the slopes by reversing the pitch increment direction an even number of times, thus achieving neutral removal over a defined area. Also, surface heat gradients were expected to show a homogeneous distribution thanks to the spreading action of the tool-path.

In a third characterisation session, a preliminary assessment of the surface temperature effects on the etching rates was carried out. Here, trenches were etched at constant speed on preheated fused silica samples. The experiments demonstrated that the material removal depth can linearly increase by as much as ~150% for temperatures up to 80 ^{o}C. However, some evidence is given that non-linearity may occur for higher temperatures and that velocity dependence could be involved. A further investigation on this point is reported in section 5.2.4. Finally, a first attempt of in-process adaptation to surface temperature

increase has been implemented for neutral removal. The test was based on in-flight pyrometer acquisitions of the front surface temperature prior to plasma plume traverse. The characterisation by "hot trenches" was utilised to generate a feedback mode algorithm which promptly showed a qualitative reduction of the etching depth (**Figure 4-17**). A quantitative evaluation of the effects was difficult because of the poor knowledge concerning the secondary etch evolution. For comparative purposes, the same test was carried out utilising a classical small pitch raster pattern. This assessment confirmed the superiority of the tool-path developed within this project. Also, for the same tool-path, the loop-by-loop logged surface temperature values validate the hypothesis of reduced temperature gradients along the pitch direction. A qualitative assessment of surface temperature gradients along the torch travelling direction is discussed in section 5.2.4.

5 FIGURE CORRECTION OF OPTICAL SURFACES

In this chapter, the principal results of the work presented in this manuscript are described and discussed. First, the dwell-time calculation method introduced in section 3.1 was tested on the basis of a single-pass figuring experiment (section 5.1). Subsequently, the actual figuring process was successfully attempted on flat fused silica areas of 100 and 150 mm diameter (sections 5.2.1 and 5.2.2). Results with residual figure error down to ~16 nm RMS (λ/40) were achieved. Surface error maps over 100 mm diameter areas were measured with the same Twyman-Green interferometer utilised during the characterisation work (Chapter 4). For the 150 mm regions, a vibration insensitive Fizeau interferometer, temporary in use at Cranfield, was employed (see Appendix D).

This experimental series allowed not only testing the capability of the figure correction procedure, but also determining the best choice of tool-path parameters. Also, the empirical choice of the thermal compensation coefficient could be fine-tuned. An upgrade of the figuring procedure involved an alternated use of the tool-path pitch parameters (section 5.2.4). This was first tested on a 100 mm diameter area with the aim of applying it to the large scale figuring.

For the upscale of the figure correction methodology, a 420mm x 420mm x 40mm mm ULE substrate hosting a 405 mm diameter spherical mirror was processed. In this last stage of the work, the relevance of the angle of incidence of the plasma plume on the surface was tested prior to figuring. Also, the three-dimensional tool-path motion was implemented. The same mirror was figured twice to show repeatability, with a rapid polishing between first and second procedure. The resulting topography maps presented a residual error of 45 and 31 nm RMS respectively.

5.1 Preliminary assessment: sinusoidal trenches

In order to experimentally verify the validity of the non-linear de-convolution method described in section 3.1, a test was carried out where a sinusoidal shape was etched onto fused silica and ULE substrates. First, a sinusoidal pattern of about 100 nm depth over 100 mm length was modelled.
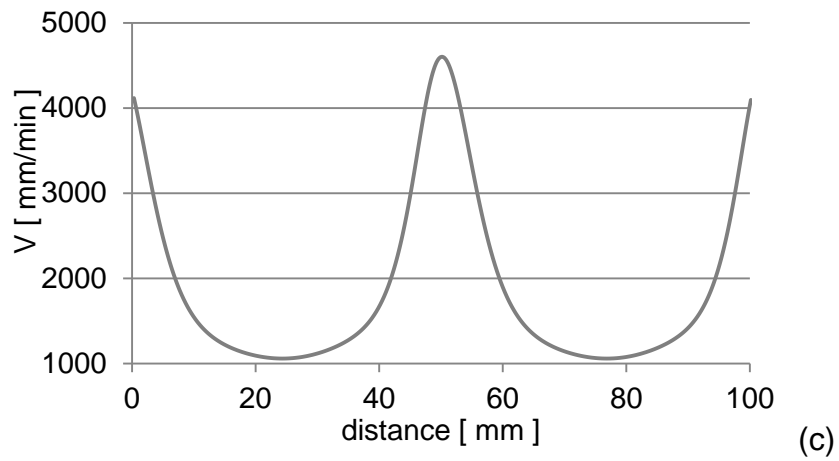
Figure 5-1 Calculated velocities along torch travelling direction.
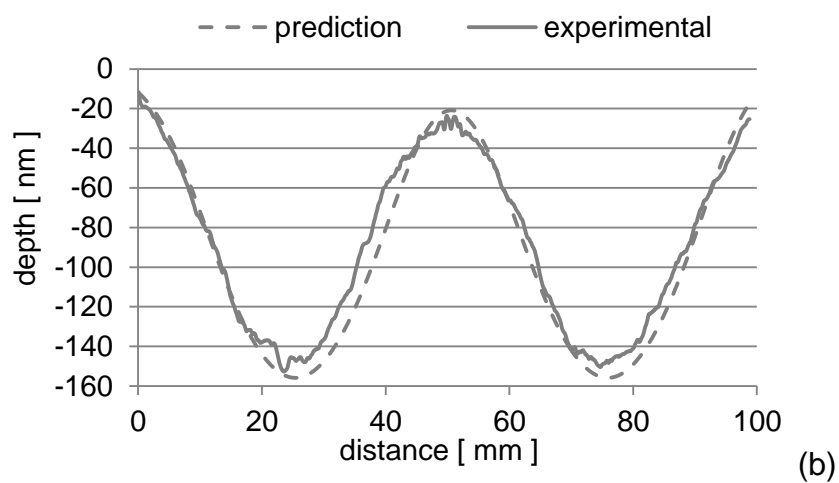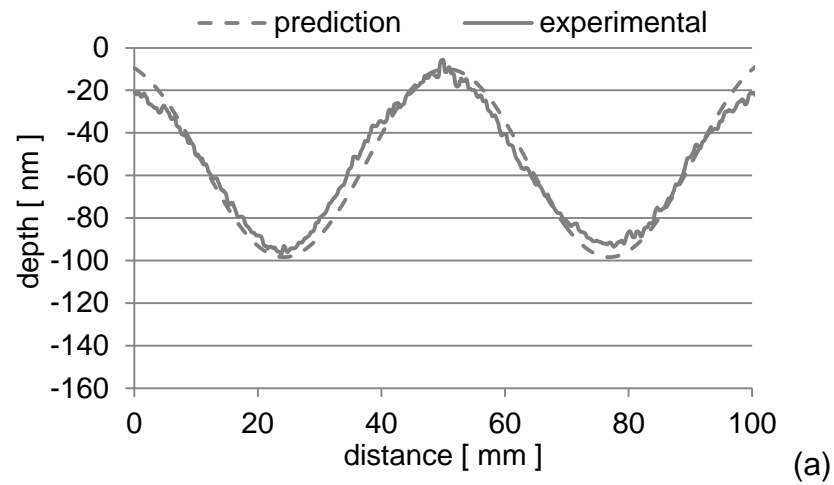
Figure 5-2 Predicted (dash-line) and experimental (solid line) central cross-section profiles of the sinusoidal trench etched on fused silica (a) and ULE (b).

99

The corresponding velocity profile was derived from the removal depths characterization through the calculation described in section 3.1 (**Figure 5-1**). The test was then performed in single-pass mode, by tuning the velocity of the torch travelling along the substrate surface. In **Figure 5-2**, the agreement between theoretical and experimental sinusoidal profiles is shown. Both tests were carried out twice for reproducibility purposes and the same outcome was observed. In **Figure 5-3**, three-dimensional illustrations of the sinusoidal trenches on fused silica **(a)** and ULE **(b)** are shown.
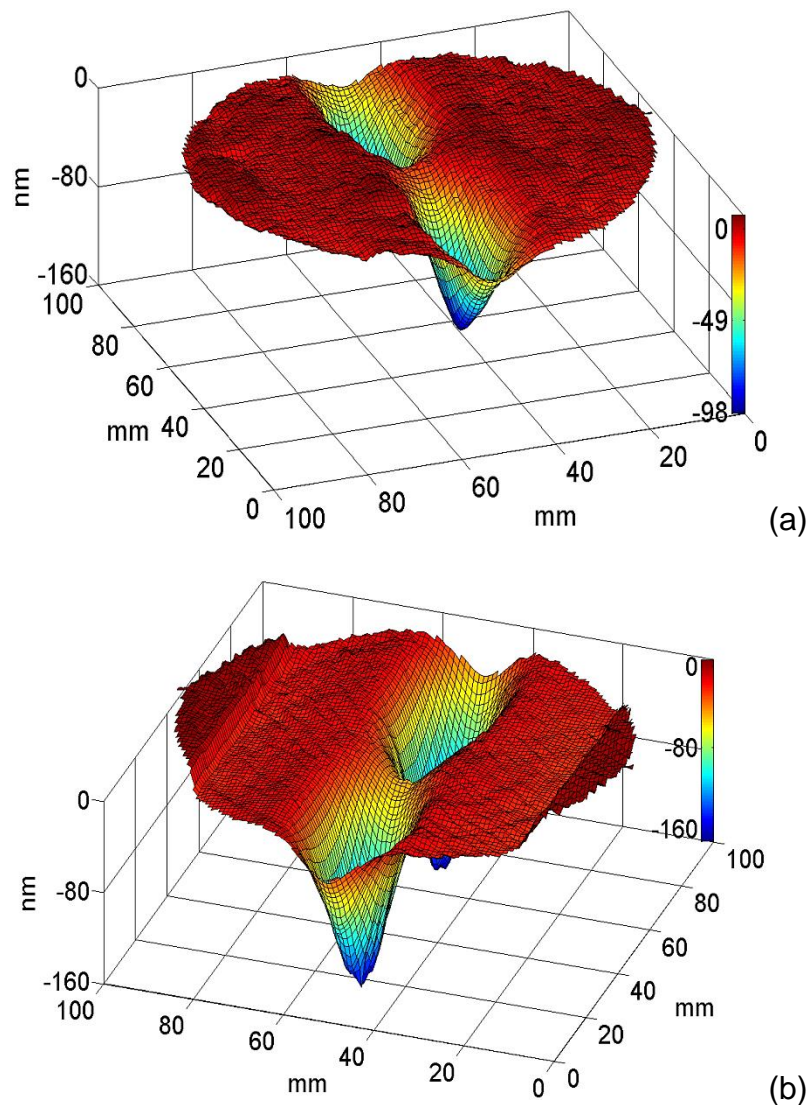
Figure 5-3 Three-dimensional illustration of the sinusoidal trenches on fused silica (a) and ULE (b).

These results demonstrate the suitability of the developed calculation to the figuring process. In particular, they show the capability to tackle the figure error over low spatial frequencies which are typical of polished surfaces. The limit of this figuring authority is defined by the FWHM of the etching footprint (~ 11 mm), as discussed, e.g., in [10].

5.2 Figure correction results

A series of figure correction tests was carried out on the central areas of fused silica samples. The substrates size was, also in this case, 200x200x27 mm. First, the figuring performance was tested over 100 mm diameter regions and the influence of the tool-path staggering step and pitch was investigated. Repeatability was proven and the figure correction was successful down to ~16 nm RMS. Subsequently, the figuring area was extended to 150 mm diameter. At the same time, an upgrade of the tool-path parameter and a third iteration were introduced in order to improve the residual waviness and edge finishing.

In the presented work, the main pre-processing operations consisted of measurement and computational stages. The metrology set-ups available for the small scale experiments required about thirty minutes for a complete form assessment, while circa twenty minutes were employed for the generation of the adapted tool-path algorithms. For the large scale tests, the use of a state-of-the-art interferometer and of an optical test tower significantly improved the measurement times (see Appendix D). Also, prior to process initiation, a torch start-up time of three minutes was typically introduced to reach tool stability.
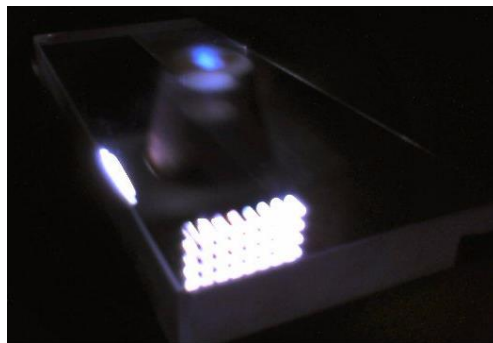
Figure 5-4 Inside view of Helios 1200 chamber: RAP torch raster-scanning the substrate.

5.2.1 Figuring of 100 mm diameter areas

In this part of the work, figuring of a 0.5 µm deep spherical hollow was attempted. The main staggering step for the tool-path algorithm was taken 12 mm broad. Two kinds of tests were carried out. During the first type of experiment a 3 mm wide sub-pitch was chosen. This yields four reversals in the tool-path. For the second set of figure correction experiments, the pitch was reduced to 2 mm. This option generates six reversals and a larger total number of passes which might induce more heat onto the substrate. However, more symmetry in the figure correction results was observed along the pitch direction. As discussed in section 3.1, the experiments were performed following an iterative procedure. A spherical hollow of 500 nm maximum depth was modelled over an area of 100 mm diameter (**Figure 5-5**). Each surface shape was assessed before every iteration step and the figure error was computed. The velocity maps were derived according to the method described in section 3.1. Two iteration steps were carried out for every single figuring attempt. In **Table 5-1**, details concerning the lasting times of the different operational stages, the levels of convergence and the RMS for each phase of the figuring process are reported. It is noteworthy that, for the two sets of experiments, residual figure errors of, respectively, 31 and 16 nm RMS ($\lambda/20$ and $\lambda/40$) were achieved.
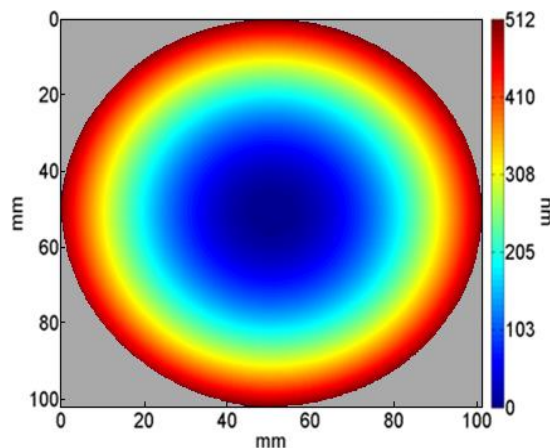
Figure 5-5 Modelled spherical hollow.

The results of the figuring process are shown in **Figure 5-6** and **Figure 5-7**. For each set of tests, the two pseudo-spherical shapes are compared with the theoretical one. The residual figure error is reported as 31 nm RMS ($\lambda/20$) for

the raster-scan with a 3 mm wide pitch. When reducing the same pitch to 2 mm, the deviation from sphere results into 16 nm RMS ($\lambda/40$). The improvement is attributed to enhanced symmetry, and hence a more uniform surface heating occurring. In particular, for the processes run with larger pitch, a residual sloped edge effect is evident (**Figure 5-6 (c)** and **(d)**). Conversely, choosing 2 mm delivers a far more homogeneous figure correction and both RMS and PV are improved by a factor two (**Figure 5-7 (c)** and **(d)**). A minor residual around the borders is also still present.
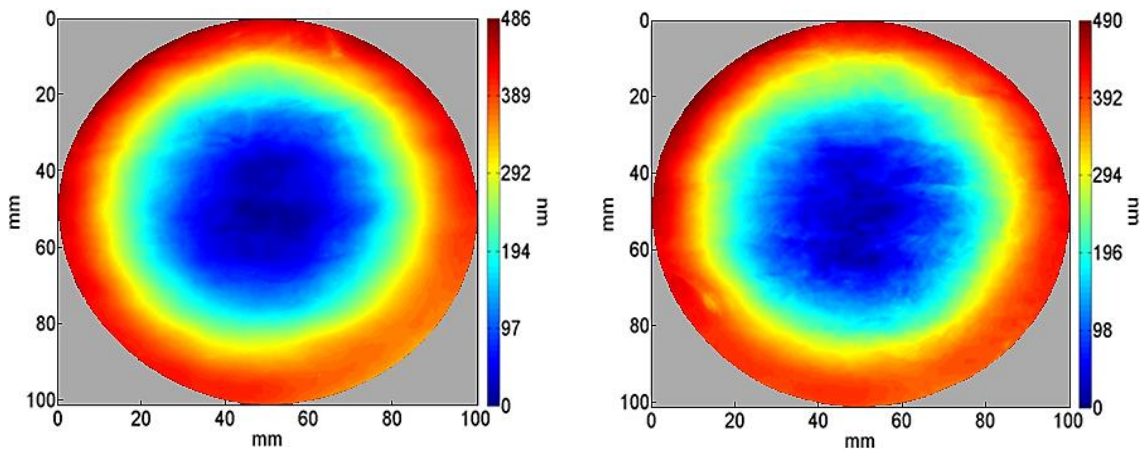
(a) Result of spherical figuring for test 1.   (b) Result of spherical figuring the repeat.
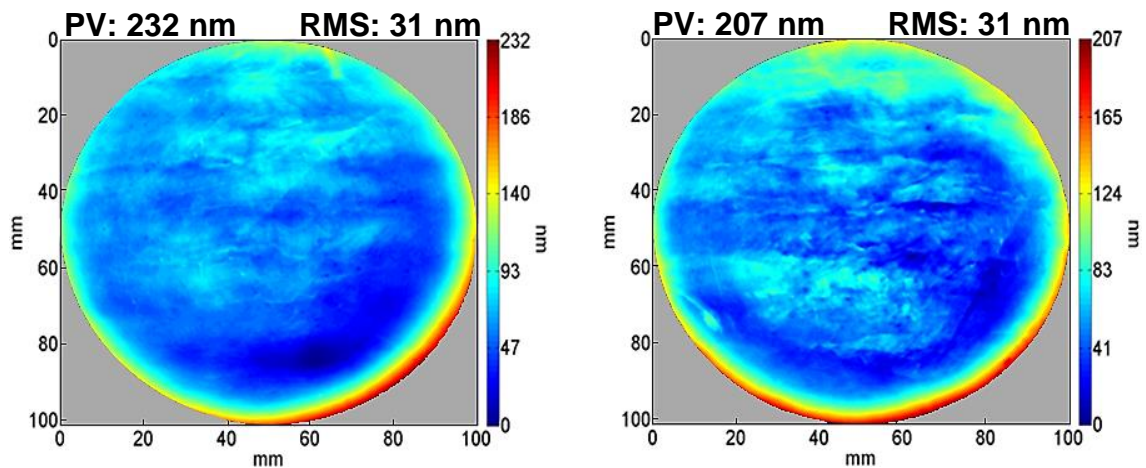
(c) Residual figure error for test 1.   (d) Residual figure error for the repeat.

Figure 5-6 Results and residual error of spherical figuring with 3 mm sub-pitch after 2nd iteration.

The two iteration steps carried out for each surface figuring lasted ~6 min actual etching time, for a total processing time of ~12 min. Overall convergences

ranging from 78 to 89 % were achieved. Again, a smaller pitch delivered the better convergence performance, making it the preferable option (**Table 5-1**).

The presence of "rolled up" edges can be attributed to two main factors. In one case, there is an influence of the edge extension algorithm that determines the run-in/run-out speed across the boundaries of the metrology area. In fact, as explained in section 3.1, a Gaussian function is applied on the figure edges to provide continuity.

(a) Result of spherical figuring for test 1. (b) Result of spherical figuring the repeat.

(c) Residual figure error for test 1. (d) Residual figure error for the repeat.
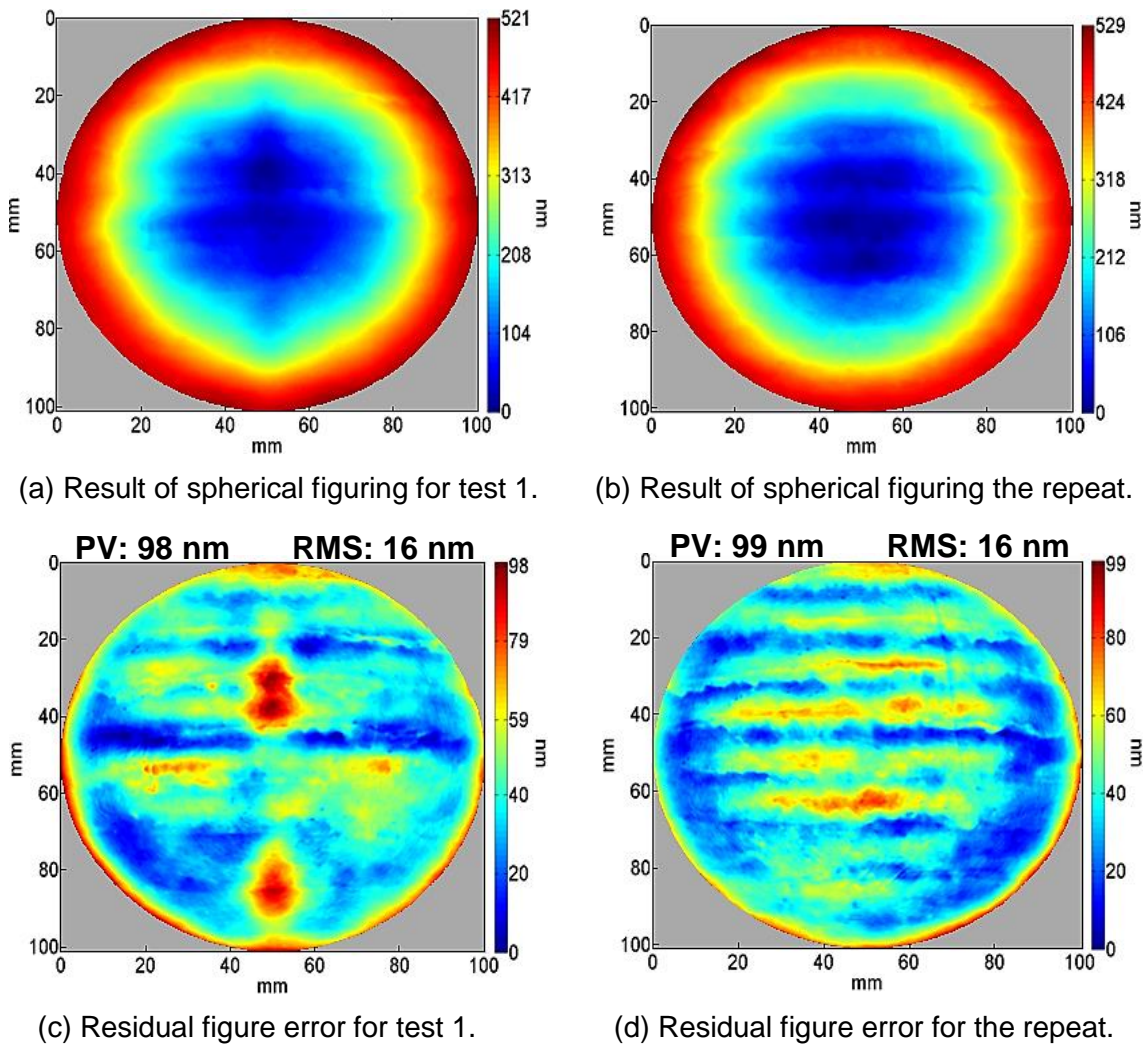
Figure 5-7 Results and residual error of spherical figuring with 2 mm wide sub-pitch after 2nd iteration.

As a correlated cause, certainly the thermal aspect has to be considered. The choice of a steeper edge extension can result into high values of run-in/run-out velocities in the boundary neighbourhood of the figuring area. Under-heating of

such peripheral zones may therefore occur, thus causing lack of material removal. The width of the edge extension function is a tuneable parameter and can be varied in order to improve the result. Alternatively, a possible improvement can be brought by the introduction of further iterations.

Table 5-1 Evaluation of figure correction experiments over 100 mm Ø areas. Operations lasting times are reported in minutes per iteration.

Evaluated aspect		Pitch: 3 mm		Pitch: 2 mm	
		Test 1	Repeat	Test 1	Repeat
Measurement time [min/it.]		30	30	30	30
Computational time [min/it.]		20	20	20	20
Torch start-up time [min/it.]		3	3	3	3
Sample loading time [min/it.]		5	5	5	5
Mean figuring time [min/it.]		6.2	6.3	6.6	6.6
Targeted % of figure error depths	Iteration 1	20	20	25	25
	Iteration 2	40	40	43	43
Convergence[10] [%]	Iteration 1	43	47	53	57
	Iteration 2	63	63	75	75
	Overall	78	79	88	89
Figure error in RMS [nm]	Initial	143	155	134	147
	After it. 1	82	82	62	64
	After it. 2	30	31	16	16

On all presented figuring outcomes a regular waviness appears across the areas (see, e.g., **Figure 5-7 (d)**). It is recognizable that such pattern matches the 12 mm wide staggering step. The reason for the observed phenomenon is ascribed to temperature variations having different effects on the loops of the tool-path. Reduction of the main staggering step was expected to trim down the amplitude of these features. As a consequence of the observed boundary

---

[10] This is defined on the basis of the convergence ratio, as reported, e.g., in [104].

issues and wavy patterns, two upgrades of the figuring procedure were introduced when scaling up the process to 150 mm diameter areas. These are discussed in the next section.

5.2.2 Figuring of 150 mm diameter areas

Following the tests described in the preceding section, upscale of the figuring procedure was undertaken. Additionally, new tool-path parameters were chosen. The staggering step was reduced to 9 mm, with a 1.5 mm wide sub-pitch in order to maintain a total of six rastering loops. As mentioned above, the aim was to reduce the residual pattern corresponding to the main pitch. For this purpose, the choice of a step value smaller than the FWHM was expected to minimise the raster-pattern print-through amplitudes.

As a first figure correction example, the 500 nm deep spherical form was used as the targeted shape. The outcome can be observed in **Figure 5-8** *(left)*. Residual RMS of 23 nm (λ/28) and 76% overall convergence are achieved after three iterations of less than seven minutes mean duration.
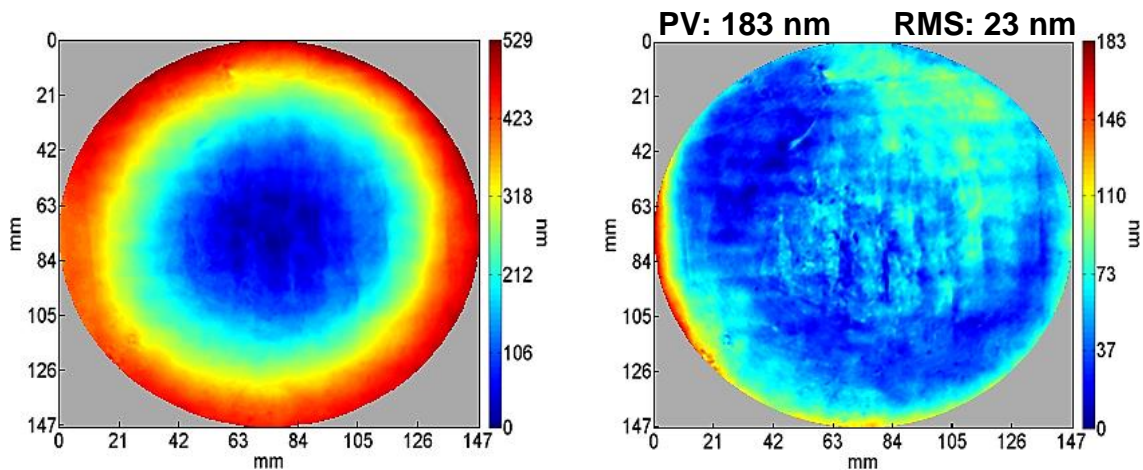
Figure 5-8 *left*: **500 nm deep spherical hollow;** *right*: **correspondent residual error.**

Finally, figuring of a flat surface was carried out. Starting from an initial figure error of 79 nm RMS, convergence was attained after three rapid processing steps. Final deviation from flatness is ~26 nm RMS (λ/24).
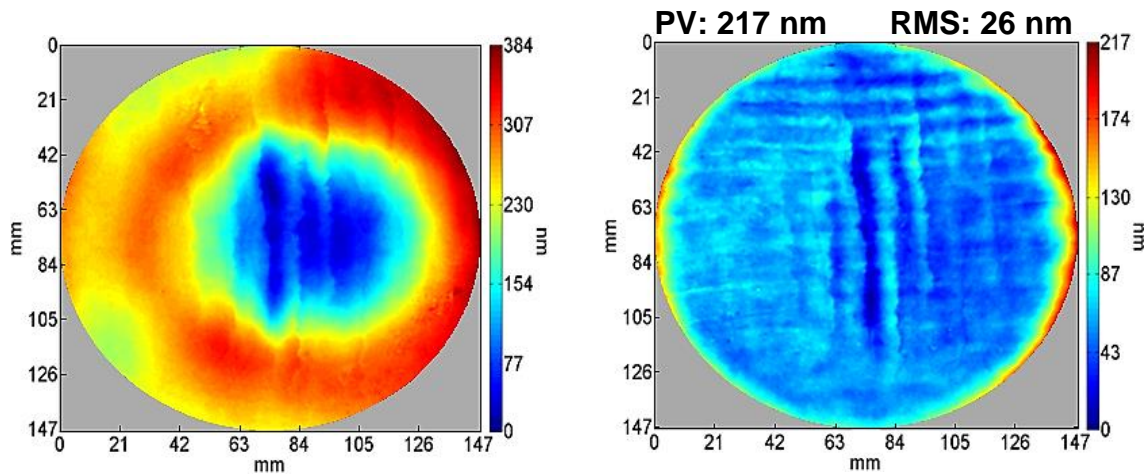
Figure 5-9 *left*: initial figure error; *right*: final flat surface.

Table 5-2 Evaluation of figure correction experiments over 150 mm Ø areas. Operations lasting times are reported in minutes per iteration.

Evaluated aspect		Spherical Hollow	Flat
Measurement time [min./iteration]		30	30
Computational time [min./iteration]		20	20
Torch start-up time [min./iteration]		3	3
Sample loading time [min./iteration]		5	5
Mean figuring time [min./iteration]		6.8	6.6
Targeted % of figure error depths	Iteration 1	25	40
	Iteration 2	60	60
	Iteration 3	40	50
Convergence [%]	Iteration 1	31	38
	Iteration 2	63	41
	Iteration 3	6	10
	Overall	76	67
Figure error in RMS [nm]	Initial	95	80
	After it. 1	66	49
	After it. 2	25	29
	After it. 3	23	26

In **Table 5-2** the data concerning single iteration steps of the two figuring processes are summarized. The time efficiency of the RAP process is confirmed by the reported etching durations. Also, a first qualitative observation of the residual figure error maps confirms that the new tool-path parameters moderate the amplitude of the staggering step print-through. A PSD analysis of residual waviness for 100 and 150 mm diameter areas is reported in section 6.2.

The third iteration was mainly introduced to reduce the edge effect. However, no substantial amelioration is visible (**Figure 5-8** and **Figure 5-9**, *right*). The residual error is still significant over few millimetres along the borders and is responsible for slightly higher RMS and PV values (see scales). Therefore, a more efficient strategy should be devised. This is discussed in section 6.3.

5.2.3 Roughness assessment

The chemical removal mechanism of plasma machining processes like RAP is known to cause surface roughening because of sub-surface defects, contamination or material grain structure (see, e.g., [10], [111]). These elements tend to cause an irregular chemical action at the lateral micro-scale. Hence, the pre-processing surface condition is a fundamental factor when evaluating post-RAP surface roughness. In particular, the final surface texture is typically influenced by the starting roughness level, as well as by the extent of micro defects (cracks) caused by previous fabrication processes like grinding or lapping [10]. Also, re-deposition of particles on surfaces after RAP processing has been observed in the whole course of research on this technology [13]. This is probably connected to the dissociated parent molecule (e.g., sulphur in SF_6) and is also considered to be a cause of roughness increase. The face-down configuration of substrates on Helios 1200 was expected to reduce the extent of this phenomenon. Additionally, as discussed in section 2.3.7, the formation of polymer residues from SF_6 or CF_4 discharges can be a reason for surface texture deterioration. The addition of oxygen to the plasma mixture is therefore auspicated in future work.

$S_q = 1.3$ nm $S_z = 8.8$ nm
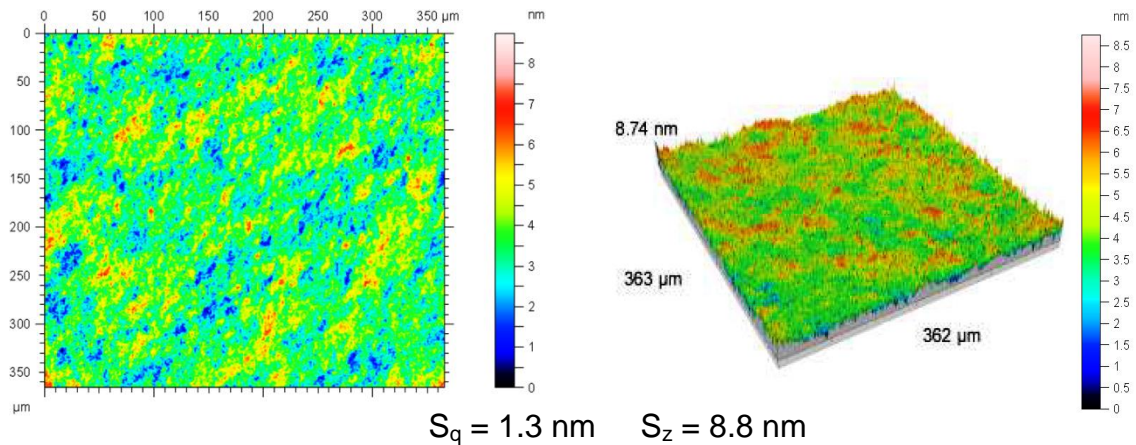
Figure 5-10 Illustrative snapshot (2D and 3D) of one of the polished fused silica surface before figuring.

In this part of the work, micro-roughness assessments were carried out only in relation to the figure correction processes over 100 mm diameter fused silica areas. In fact, for these tests, samples in pristine conditions were available. The surface roughness was investigated before and after figuring completion. Coherence probe interferometry was applied by means of a Taylor Hobson CCI 6000 using a Nikon 50X magnification lens (measurement area: 360µm x 360µm, optical resolution: 0.4 µm, see also Appendix D).

First, the roughness of the surfaces as polished was measured and the mean S_q is reported as 1.3 nm (± 0.1 nm). In **Figure 5-10**, two- and three-dimensional picture of a CCI6000 measurement taken on one of the polished fused silica before figuring is shown.

In **Figure 5-11**, the pattern followed for the measurements acquisitions is sketched. This comprised 49 snapshots spaced 10 mm from one another and arranged to cover the figuring area. The results of this investigation on the four figure corrected surfaces (section 5.2.1) are displayed in **Figure 5-12**. Hand buffing was applied for about 10 minutes after each iteration. Characteristic post-figuring roughness from this assessment ranged from ~4 to 8 nm RMS, which compares well with the data in [14]. In some zones, the S_q values were much higher than expected, particularly for the repeat figuring with 2 mm pitch (**Figure 5-12 (d)**). This is reckoned to be due to contamination from the aluminium holder, as this was observed to deteriorate when exposed to the

reactive plasma. Also, some anomalous regions were observed (e.g., **Figure 5-12 (b)**), which could be attributed to local scratches. No actual correlation of roughness to the depth of removed material appears evident from these analysis.
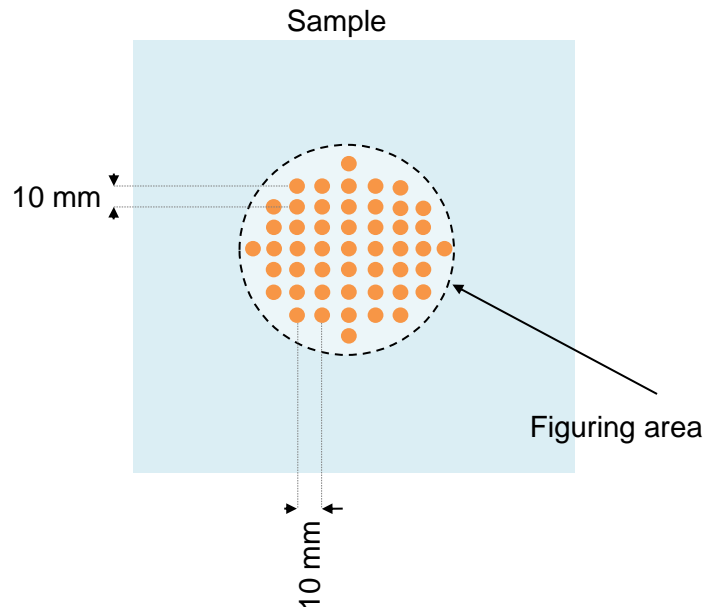
Figure 5-11 Roughness investigation pattern.

In **Figure 5-13**, two examples of roughness measurements are shown. The displayed fields correspond to the areas labelled as **(I)** and **(II)** in **Figure 5-12** and illustrate the cases of a very rough (S_q = 9.46 nm) and a relatively smooth (S_q = 2.06 nm) zone. As expected, a qualitative evaluation of the images reveals that chemical attack preferentially occurs over regions of few tens micrometres in size. In near-absence of subsurface damage, these are considered to be the areas corresponding to grain boundaries or micro-defects in the material.

On different materials like ULE the level of roughness deterioration is expected to be higher: this is ascribed to the different chemical composition of such materials that will cause differentiated etching selectivity over the process area. For instance, in ULE glass, fluorine is bound to attack either SiO_2 or TiO_2 preferentially. Also, re-deposition of the sulphur contained in SF_6 reacting with

the titanium cannot be excluded. These considerations are confirmed by the previous research as reported, e.g., in [13] and [15].

(a): 3 mm pitch – test 1.

(b): 3 mm pitch – repeat.

(c): 2 mm pitch – test 1.

(d): 2 mm pitch – repeat.
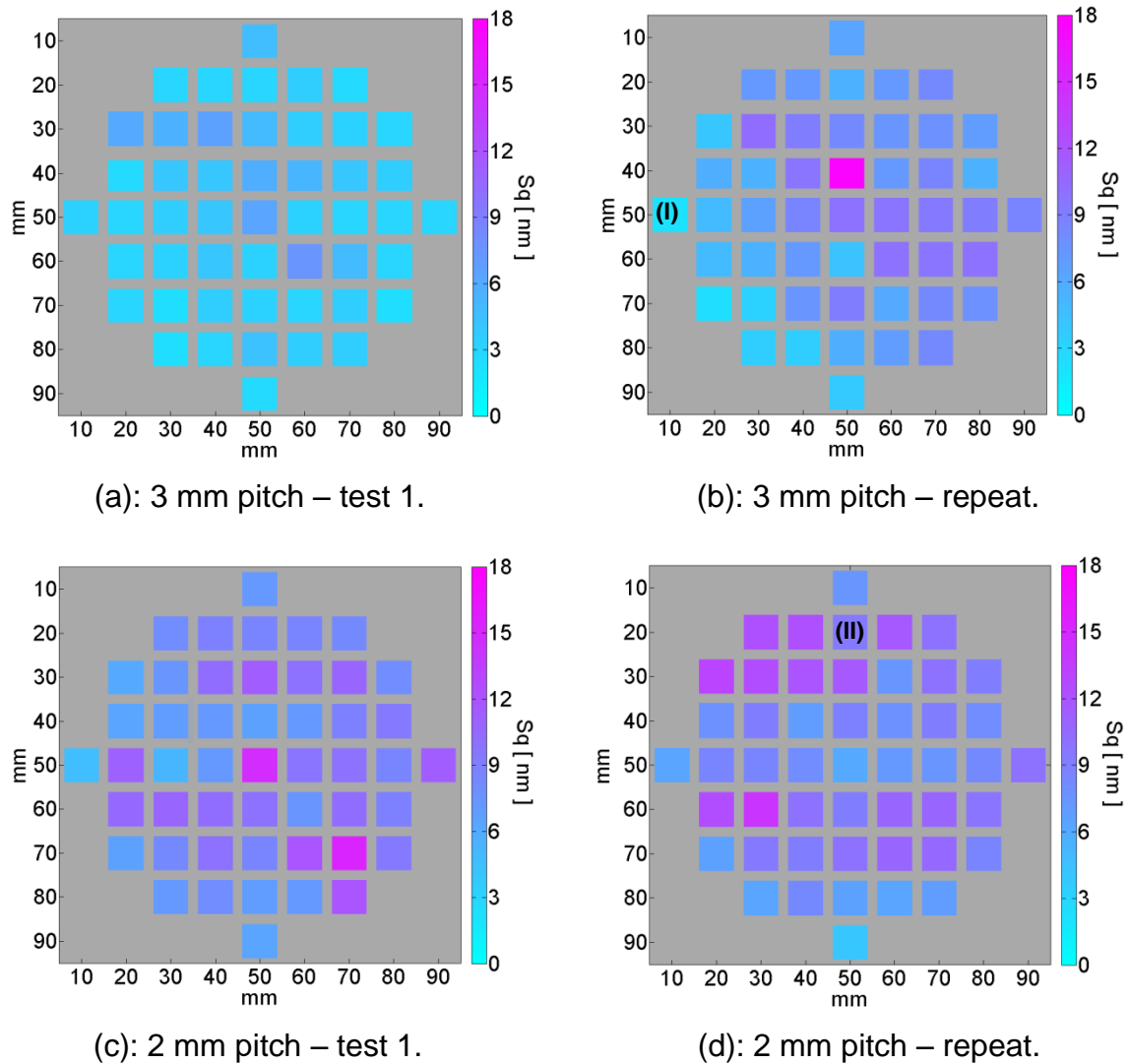
Figure 5-12 (a) and (b): RMS roughness distributions for figuring with 3 mm; (c) and (d): 2 mm pitch.

A rapid post-RAP polishing is proposed as a solution to restore the surface texture. Ideally, this would apply a near-neutral removal in the range of ~100 nm depth to smooth rough areas and remove the waviness (see also section 6.2). In case of figure error modifications due to the polisher, alternations of Reactive Atom Plasma figuring and polishing would be introduced. This type of chain has already been successfully applied, at least in one case, for PJM [111]. At the

time of writing, a "flash" polishing process by means of robotic arm is being developed at Cranfield University Precision Engineering.

$S_q = 2.1$ nm $S_z = 18.4$ nm

$S_q = 9.5$ nm $S_z = 61.2$ nm

(I)   (II)
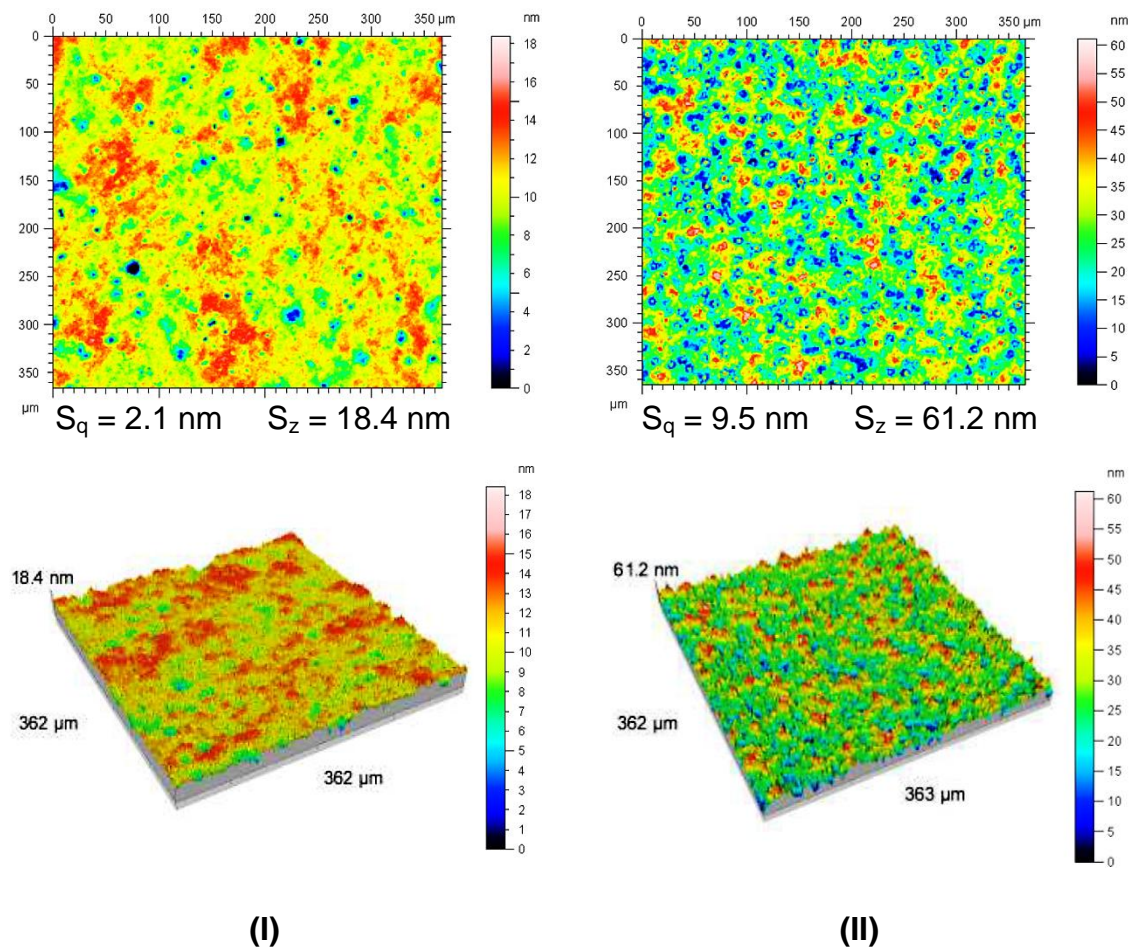
Figure 5-13 Two- and three-dimensional illustrations of snapshots taken with the CCI6000. The labelling (I) and (I) correspond to a rougher and a smoother field in Figure 5-12 (b) and (d).

5.2.4 Thermal assessments

In this section, experiments assessing the effects of surface temperature in relation to figuring processes are discussed. Two types of investigation were performed to deepen the understanding of heat effects and surface heat gradients. The substrates used in this work were the 200mm x 200mm x 27mm fused silica samples. These tests are considered an additional progress towards a temperature adapted RAP figuring.

SINUSOIDAL HOT TRENCH

In section 4.2.3, the effect of surface temperature on trenches depth was investigated for two levels of torch travel speed. However, such tests didn't fully answer the question on whether the increase of material removal due to heat would be influenced by the plasma plume speed. A complete investigation would involve a design of experiment including trenches etched at several velocities and at different values of surface temperature. In this part of the work, a more convenient approach was chosen. Just like in a figuring process, the torch velocity can be varied along its travelling direction. If such a test is performed on a preheated surface, the effects of temperature on the etching depths can be brought in relation to the speed values. In this way, a series of velocity values can be tested towards temperature effects in a single experiment. A varying velocity profile to utilise for this test was already available from the sinusoidal trench tests reported in section 5.1 (**Figure 5-1**).

In this experiment, the sample was pre-heated on a hot-plate (**Figure 4-14**). Just like for the hot trench tests discussed in section 4.2.3, the temperature was recorded with the pyrometer prior to torch traverse, and resulted as 77 ^{o}C (see also **Figure 4-14**).
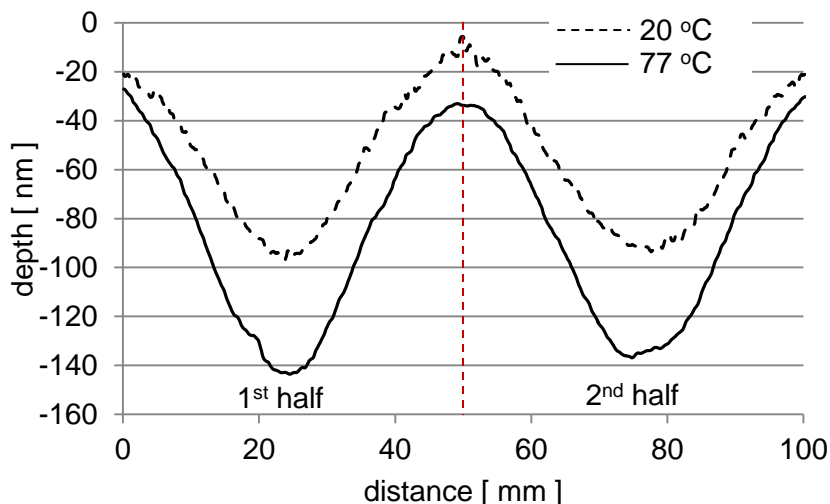
Figure 5-14 The sinusoidal trench at 77 ^{o}C (solid line) in comparison to the one etched at room temperature (dash line).

113

To assess the effect of temperature, the etch depth of the central cross-section profile of the resulting hot sinusoidal trench was compared to the one of the same trench at 20 $^{\circ}$C. The two sinusoidal profiles are plotted in **Figure 5-14**. In this comparison, the quotient of the two profiles values was subsequently computed. Obviously, the two halves of the sine patterns, and therefore of the computed quotient, essentially contain the same information. Thus, the two halves of the calculated ratio were averaged and the resulting percentile increases plotted versus the torch travel speeds. The graph showing the result is displayed in **Figure 5-15**. This reveals a non-negligible dependence of the temperature effects on the scanning speed.
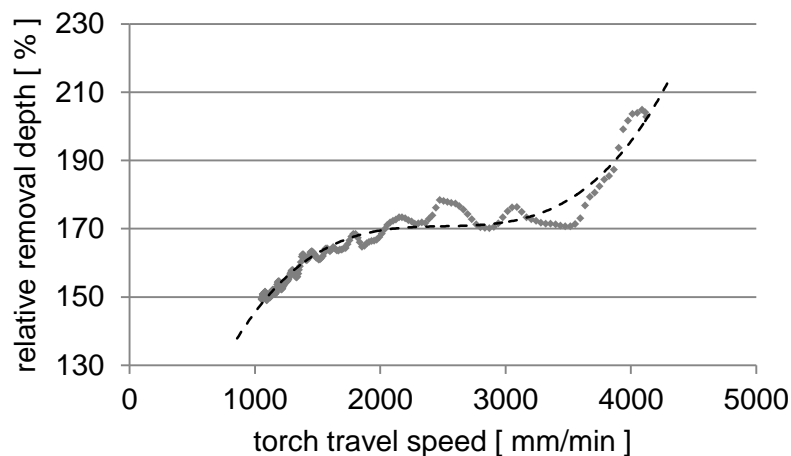
Figure 5-15 Trend of relative removal depth percentage versus torch velocity for sinusoidal trenches at 20 and 77 $^{\circ}$C.

The outcome of this last experiment opens a new perspective for the characterisation of temperature effects on etching depths utilizing sinusoidal hot trench tests. The values of the computed quotient can be exploited to derive the velocity dependent trends of the etch depths at several temperatures. In **Figure 5-16**, the dash line represents the velocity dependences of the removal depth for a substrate at a starting temperature of 20 $^{\circ}$C. The solid line is the equivalent trend at 77 $^{\circ}$C, while the red dotted lines denote hypothetical trends at different temperature values. Note that the hypothetical curves in **Figure 5-16** are introduced for illustrative purposes.
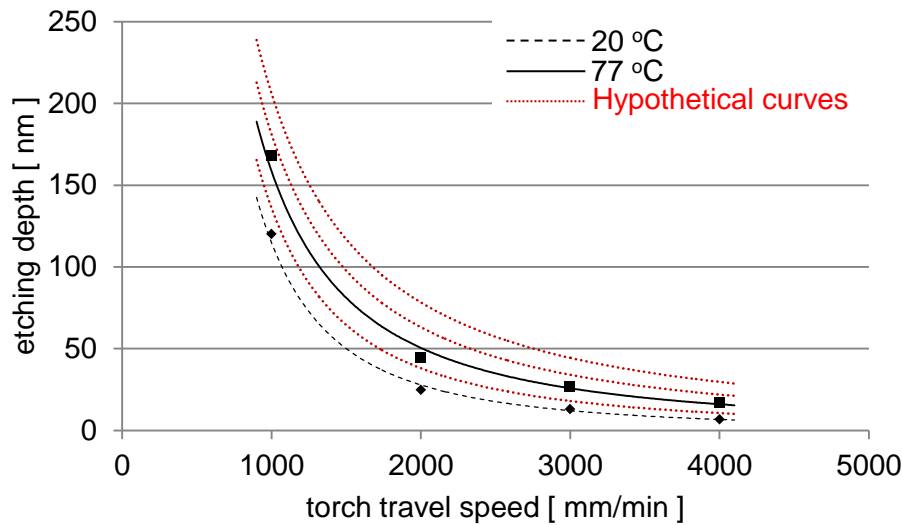
Figure 5-16 Dependencies of the etching depths on the torch travel speed for different surface temperatures: 20 °C (dash line), 77 °C (solid line) and hypothetical trends for different temperatures (red dotted lines).

Each trend can be mathematically described by a function of type av^b. Now, if the temperature effect is to be included such formulation becomes:

$$d(v) = av^b \rightarrow d(v(T)) = a(T)v^{b(T)} \qquad \textbf{(5-1)}$$

Sinusoidal hot trenches performed on surfaces at different temperatures would provide data to fill in the red-dotted curves (**Figure 5-16**). This would then allow to derive the parameters *a(T)* and *b(T)* that implicitly represent the Arrhenius aspect of the process. Finally, equation (5-1) can be exploited in a temperature adapted process to calculate the required speed values. This is further discussed in Chapter 7.

MAPPING OF SURFACE TEMPERATURE DISTRIBUTION

The next step of the thermal investigation consisted of a 2D-mapping of surface heat distributions to check the homogeneity over a whole processed area. One of the tool-path algorithms already produced for the 100 mm Ø spherical hollow figuring tests (12 mm staggering step, 3 mm pitch) was reused for the purpose of this investigation. The effects of the four reversing-loops were assessed in

sequence, by turning off the torch after a row of consecutive reversals ({1}, {1-2}, {1-2-3}, {1-2-3-4}) and mapping the surface. The sample was then systematically cooled down to room temperature after each measurements series and the process restarted for the next. Due to the lengthy cooling times, this was a one-off test utilised for a qualitative assessment of the tool-path thermal performance.

The results of this assessment are shown in **Figure 5-17**. Overall uniformity of temperature distribution can be observed, with maximal variations of ~20 ^{o}C. In particular, thermal deviations along the torch travelling direction (X-axis) are typically better than 10 ^{o}C over 100 mm. For the correct interpretation of this test, however, a delay due to the measurements acquisition time must be considered. This is responsible for the systematic Y-gradient visible over the images field in **Figure 5-17**. Therefore, only a qualitative evaluation is possible, but some valuable indications can still be derived. For instance, the type of heat distribution to be expected on low thermal conduction materials is likely to closely resemble the ones displayed in **Figure 5-17**. At the same time, one can infer that thermal gradients over the extension of the etching footprint size (~26 mm diameter) are negligible. Also, the results indicate that the number of pyrometer measurements along the X-axis for in-flight feedback can be limited to one or two for this surface size. This is further discussed in section 7.1. It would be interesting to perform similar assessments with the different sizes of staggering step and pitch adopted in the course of this project.

In conclusion, an investigation of two thermal aspects of the Reactive Atom Plasma process was carried out in this section. In particular, the relation between measured surface temperature and etching rate was explored also in relation to a new type of characterisation involving non-constant torch velocity. Moreover, the presence of thermal gradients over the process regions was qualitatively assessed. Completion of the heat effects investigation for a range of temperature values will deliver the basic tool for an in-process temperature adaptation of the figuring procedure.

T-map after 1st loop

T-map after 1st and 2nd loop

T-map after 1st, 2nd and 3rd loop

T-map at end of process
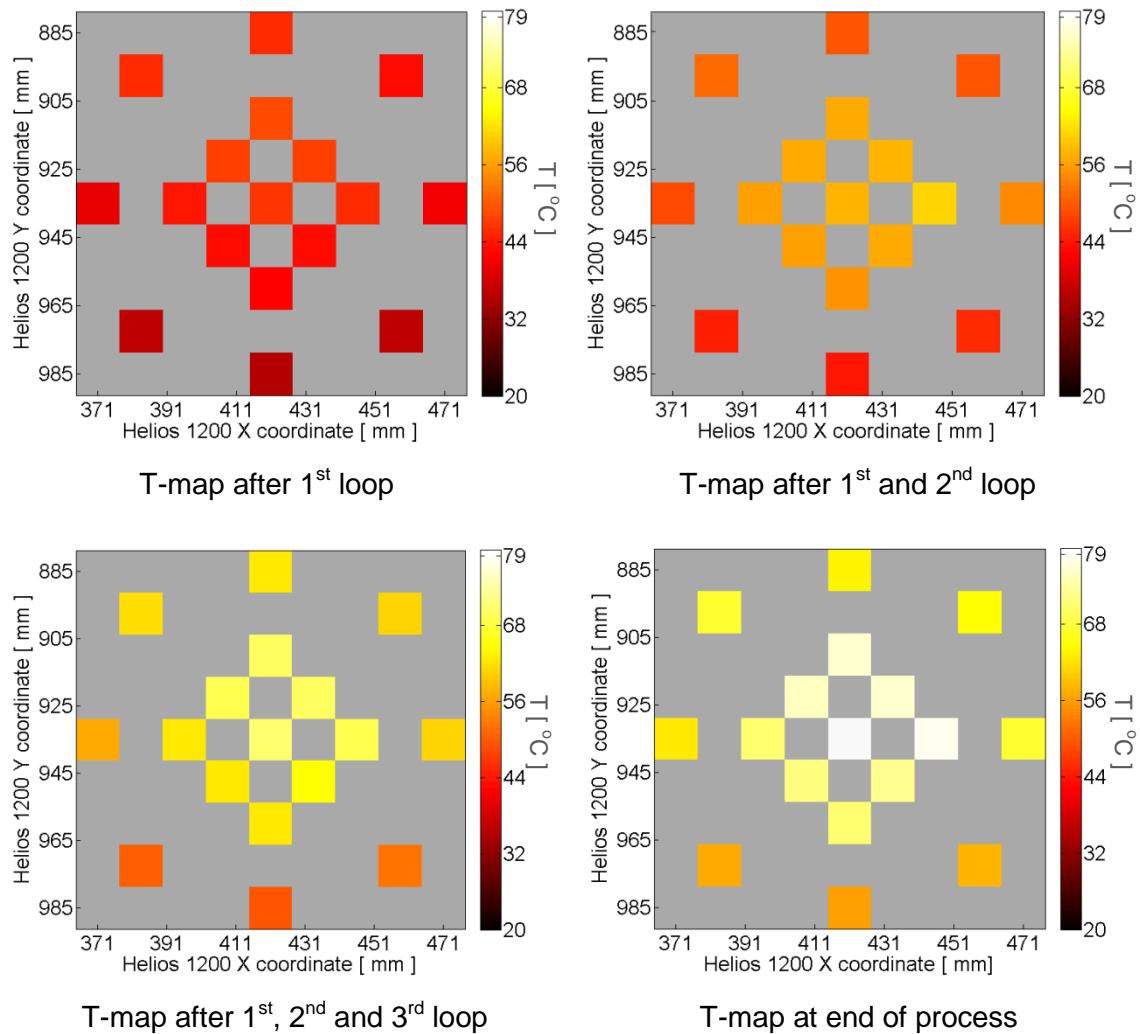
Figure 5-17 Maps of temperature distribution over the 100 mm diameter central sample area after consecutive reversals of the tool-path algorithm. The grey background represents areas with no measurements.

5.2.5 Tool-path algorithm upgrade: pseudo-randomisation.

In section 5.2.2, smaller staggering step and pitch were introduced and a net reduction of the wavy raster-scanning patterns was observed. However, a limitation has to be expected when leaving the tool-path parameters unvaried over consecutive iterations. In fact, this would repeatedly lay the same pattern over the process area. Although a complete elimination of raster tracks is unlikely to succeed, randomisation of scanning patterns has been shown to be beneficial (see section 2.5.2).

117

Based on these considerations, a pseudo-randomised method has been explored and tested in the course of this work. The terms random or pseudo-random as referred to figuring tool-paths have been used in the literature with a connotation of non-regular pattern design (section 2.5.2). Differently, in the here presented work, the name is assigned to a variation of the reversed staggered rastering tool-path. In this approach, the first iteration was to be performed adopting a larger staggering: the 9 mm step, with the matching 1.5 mm pitch, was chosen based on the results discussed in section 5.2.2. For the following iterations, the main step was reduced to 6 mm and the pitch to 1 mm to maintain six loops. This was expected to mitigate the waviness by mismatching the raster-scanning print-through over consecutive iterations.
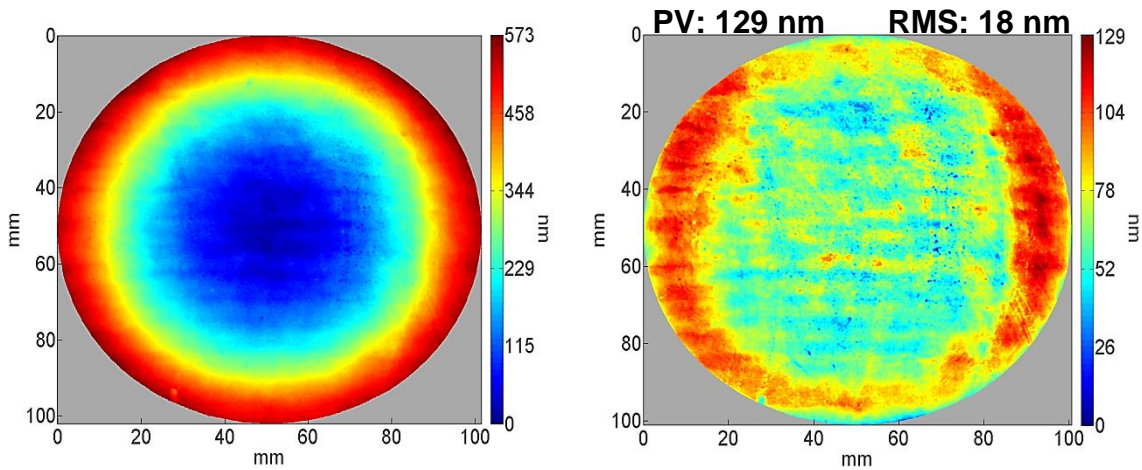
Figure 5-18 *left*: **final spherical hollow after third iteration;** *right*: **correspondent residual figure error.**

To test the method, the target shape was, once again, the 500 nm deep spherical hollow (**Figure 5-5**) and the substrate of choice was one re-polished fused silica sample. The procedure was completed within three iterations, for a mean processing time per iteration of 12 minutes and a residual figure error of 18 nm RMS (129 nm PV). The longer figuring duration was mainly due to the smaller pitch size in iteration 2 and 3.

The result of the process can be seen in **Figure 5-18**. Considering an initial deviation from the target sphere of ~169 nm RMS, an overall convergence of

89% was achieved. More details about the performance for the single iterations are listed in **Table 5-3**.

Table 5-3 Evaluation of the figure correction test over 100 mm Ø area with pseudo-randomisation. Operations lasting times are reported in minutes.

Evaluated aspect	Iteration 1	Iteration 2	Iteration 3
Figuring time [min]	9	13.5	13
Tool-path Staggering Step [mm]	9	6	6
Sub-Pitch [mm]	1.5	1	1
Targeted % of figure error depths	20	50	40
Convergence [%] (Overall: 89%)	51	31	69
Figure error in RMS [nm] (Initial: 169 nm RMS)	83	57	18

This test was utilised as a first verification for the effectiveness of the pseudo-randomisation principle and apply it to large areas (see section 5.2.6). In **Figure 5-18**, the raster-scanning tracks appear quite faint on the image, which qualitatively corroborates the methodology. The magnitude of these rippled patterns is assessed by PSD analysis in section 6.2 and is compared with the PSD plots of the figuring results presented in sections 5.2.1 and 5.2.2.

NOTE: On substrate materials like ULE, the described waviness phenomenon was expected to be more evident due to the higher etching rates. This is confirmed by the results presented in the next section.

5.2.6 Figuring of 400 mm diameter areas

The results presented in this section are considered the crowning achievement of this project and constitute a major contribution to the field of optical fabrication. In fact, for the first time, figure correction of a large surface by a

plasma etching technology has been accomplished. In this work, the effectiveness of the RAP figuring procedure was proved twice on one 405 mm diameter surface that had been re-polished between first and second figure correction cycle. In both cases, the tests were successful: the procedure devised for small areas rapidly converged to produce a λ/15 and a λ/20 (45 and 31 nm) RMS residual figure error, respectively. The large scale applicability of this fast converging strategy is particularly important as it will make RAP technology a commercially valuable figuring method on the new large optics market.
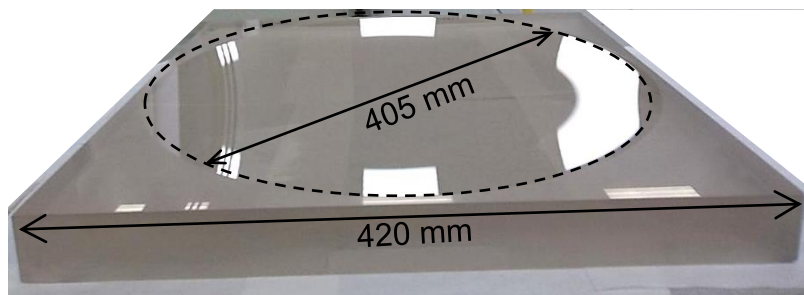
Figure 5-19 The 420x420x40 mm ULE substrate with the concave spherical mirror surface of 405 mm diameter machined in the centre of one of the 420x420 mm faces.

In **Figure 5-19**, the substrate utilised in this experimentation is shown. It is made of the same ULE type material for which the removal rates had been characterised (section 4.2.1). On one square face of this 420mm x 420mm x 40mm blank, a concave spherical geometry with 3 metres radius of curvature (ROC) was ground on the BoX machine (section 2.3.1) to ~2 μm PV form accuracy.

The grinding resulted in a 405 mm diameter aperture that was hand-polished (pitch-polishing, Optic Glyndwr Ltd.) to remove the roughness for interferometer measurements purposes only (cosmetic polishing). The reported S_q was 1.7 nm. It must be specified that, on this substrate, the polishing was not intended for subsurface damage removal. As explained in section 5.2.3, this has a major effect on the post-RAP surface texture. Hence, the final roughness cannot be considered characteristic of a RAP processed surface after fine polishing.
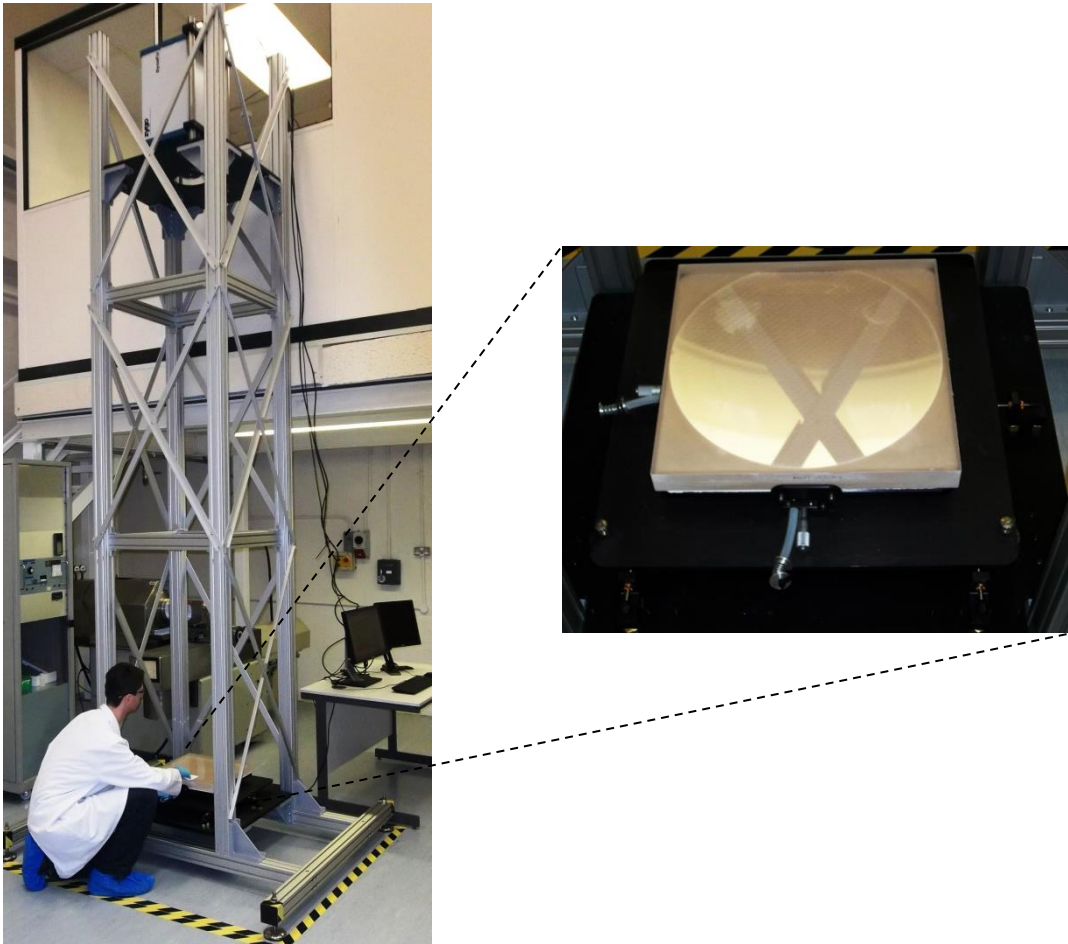
Figure 5-20 *left*: **Optical Test-tower in the laboratory of Cranfield University Precision Engineering;** *right*: **the ULE mirror on the stage of the test-tower, ready for measurement.**

The polished spherical mirror was then measured in vertical configuration on an optical test tower, purposely built within Cranfield University Precision Engineering (**Figure 5-20**). A vibration insensitive interferometer (Zygo *DynaFiz*, see Appendix D, D.3), equipped with a 4'' transmission sphere (16 nm PV), assured accurate and repeatable measurements (30-50 nm PV) over the ~3.5 metres optical testing path.

The initial figure error after focus term correction showed a near-astigmatic aberration of ~ 2.4 µm PV (2.3 µm PVr, 373 nm RMS). The high removal rates of the process on ULE material were considered suitable to prove rapid convergence. The error map can be seen in **Figure 5-21**.
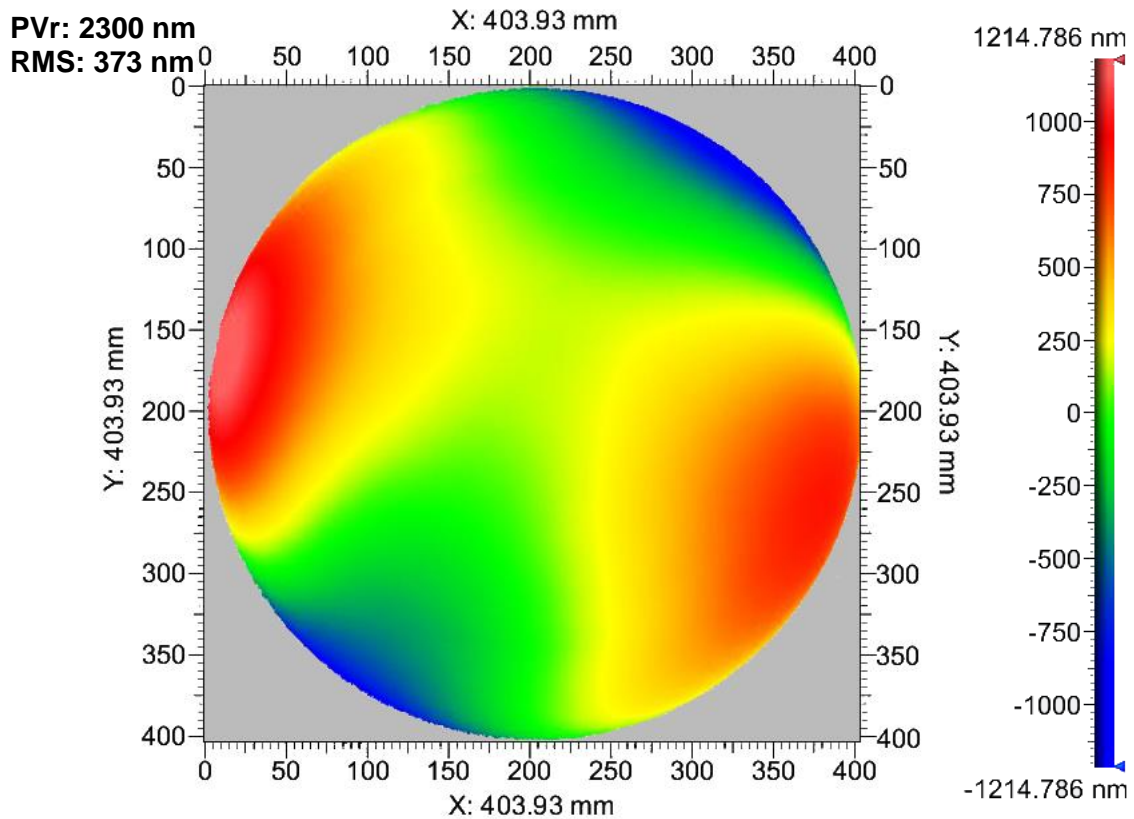
Figure 5-21 Initial figure error of the ULE mirror: near-astigmatic aberration of ~2.4 μm PV.

Prior to starting the actual surface processing, some considerations were made concerning the angle of incidence of the plasma plume onto the surface, as well as the positioning accuracy of the workpiece. Details on these pre-assessments are reported in Appendix E and Appendix F. In the first investigation, for the maximum slope that the plasma plume would traverse (edge of the clear aperture), no measurable variation of the etching footprint was observed. Conversely, positioning of a large component is an issue that requires particular attention when processing durations in the order of several hours are involved. In any precision machining system, overheating occurs due to frictions and energy dissipation from engines. On Helios 1200, additional misalignments could be introduced by the plasma heat source that will progressively cause thermal fluctuations of the inner chamber environment and, above all, expansion of the aluminium structures supporting the substrate.

If this resulted into lateral shifts of the component, additional residual errors would arise, thus slowing down the rate of convergence. In **Figure 5-22**, the hypothetical additional figure error (peak-to-valley) caused by a one-directional drift was simulated. However, solutions exist to balance non uniform dilations, like thermally compensated mounts or flexible fixtures (springs). The use of springs had already been made for 200mm x 200mm substrates and may account for the quality of the outcomes showed in the previous sections. A similar solution was indeed implemented for the mount of the 420mm x 420mm component.
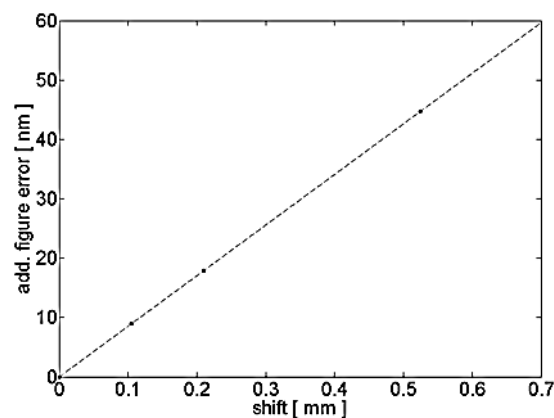
Figure 5-22 Simulated additional figure error caused by one-directional sub-millimetre shifts. Overlapping sinusoidal trenches (~100 nm max. depth) were used for the sake of this example.

Once pre-assessments were completed, the figure correction procedure was prepared. The tool-path code generator was upgraded to follow free-form geometries (Z-axis motion), while a fine tuning of the edge extension algorithm was introduce to reduce the edge effect observed in sections 5.2.1 and 5.2.2. The first figuring cycle consisted of three iterations. The initial error map was utilised for the computation of the velocity map for the first iteration. For the first iteration, a "mild" material removal was targeted. This choice aimed at confirming that the process response would be consistent with the results previously obtained on 100 and 150 mm diameter areas.
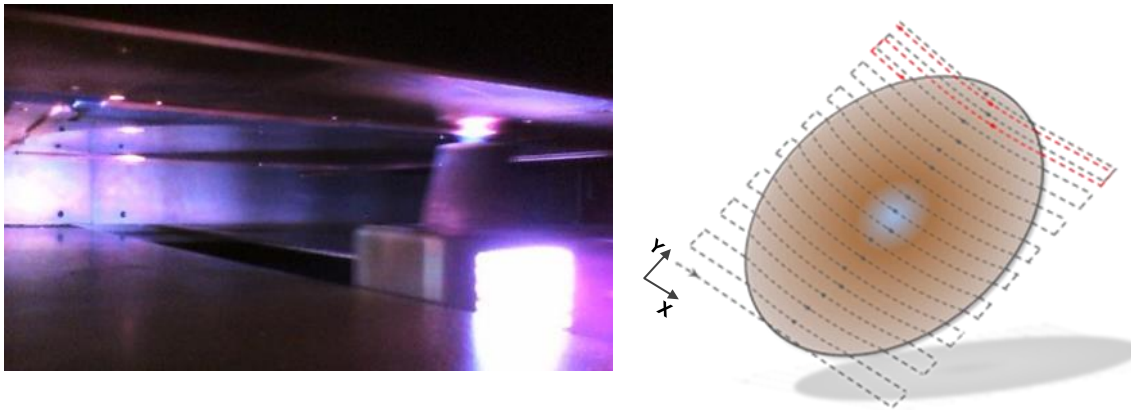
Figure 5-23 *left*: **RAP torch scanning the 420mmx420mm ULE mirror;** *right*: **Schematic of the reversed-staggered tool-path applied to the spherical mirror surface.**

For the tool-path step and pitch, the pseudo-randomised principle investigated in section 5.2.5 was applied. After this first "trial" iteration with 9 mm staggering step and 1.5 mm pitch, two further figuring steps were performed by alternating a 9 and 6 mm step, with the respective 1.5 and 1 mm pitch.

The result of this figure correction procedure can be seen in **Figure 5-24**. The residual error outcome was ~43 nm RMS (λ/15) and 280 nm PVr (450 nm PV) and was achieved after a total processing time of 2.5 hours. An overall convergence of 89% was attained after removing ~ 2 µm effective figure error depth.

The evaluation of this surface figure by the PVr concept (see section 2.3) was considered appropriate since the topography maps showed a patterned and spikey morphology. This can be mainly ascribed to the presence of subsurface damage, as well as to curly features that are interpretable as material stress (see **Figure 5-24**). This same complex morphology can also be considered a limitation to further improvement of the residual error topography.

Despite the introduction of the pseudo-randomised tool-path parameters, the residual error map still shows the raster-scanning print-through. A closer view of **Figure 5-24** shows that the pattern corresponds to the larger step. The reason can be ascribed to the high percentage targeted in the second iteration where

the 9 mm step was used. The PSD analysis in section 6.2 confirms these observations.
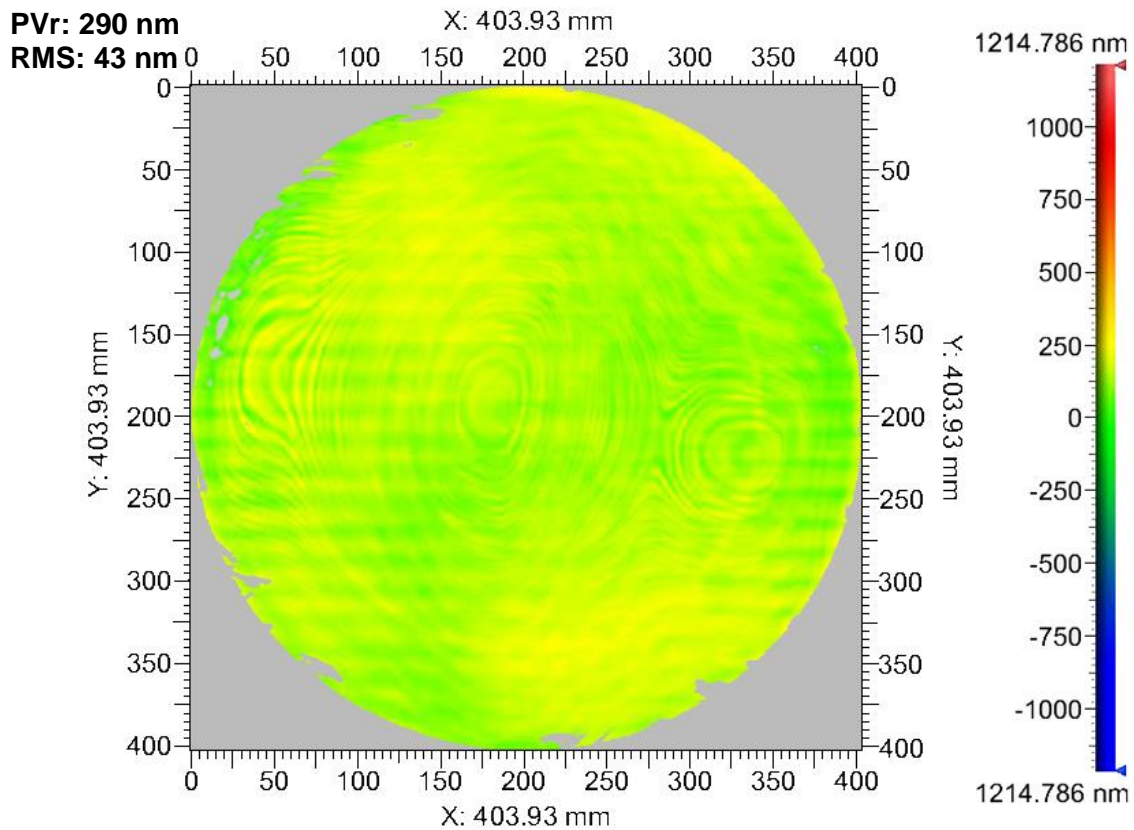
Figure 5-24 Residual figure error of the ULE mirror after first figuring.

At this stage, the reduced surface visual reflection suggested re-polishing of the process area. The surface was then hand-polished in the same manner as the first time. Restoration of roughness level and reflectivity were successful, but the reassessed figure error showed a loss of form accuracy up to ~723 nm PVr (137 nm RMS), as shown in **Figure 5-25**. Therefore, two further plasma figuring iterations were necessitated to recover the shape accuracy and these required a total processing time of 1.6 hours. Once again, the pitch sizes were alternated over the two consecutive iterations. The final residual figure error was ~31 nm RMS (230 nm PVr), which corresponds to a 92% overall process convergence after ~ 4 hours, if considering both RAP figuring cycles.

The final error map can be observed in **Figure 5-26**. In **Table 5-4**, the key data of the two figure correction cycles are summarized. Also after this figuring cycle,

raster-tracks are visible on the residual error map. The periodicity of the patterns, though, appears different when comparing **Figure 5-24** and **Figure 5-25**. In particular, the last figure error map hosts a more irregular waviness. Once again, the PSD analysis in section 6.2 identified the correspondence between tool-path patterns and mid-spatial frequencies. Yet, the introduction of the pseudo-randomization method is considered beneficial for reducing the waviness magnitude that would otherwise increase over successive iterations. For this ULE workpiece, the surface texture deterioration was considered a major factor of influence when considering waviness generation by footprint tracks.
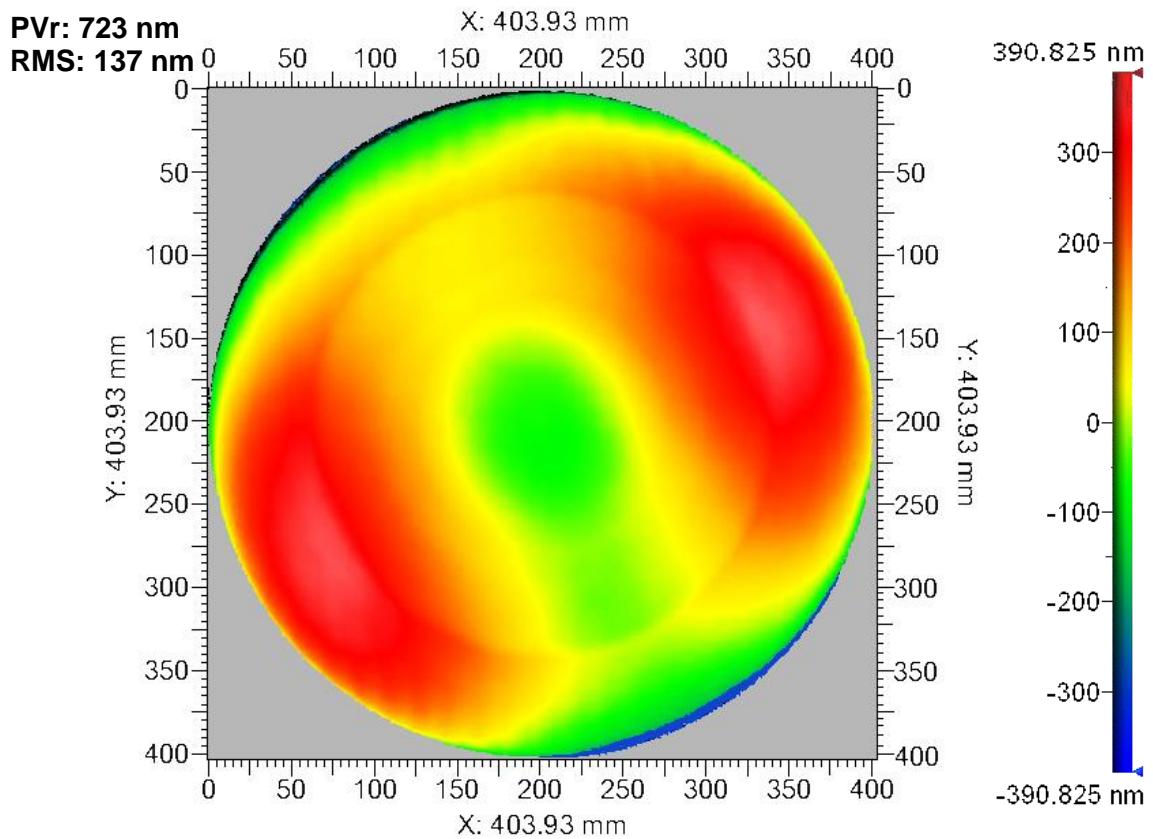
Figure 5-25 Initial figure error before second figuring.

In conclusion, the figure correction procedure designed and developed in the course of this project proved to successfully converge on a large scale optical surface. In particular, no scale dependency of the figuring capability was observed in this final part of the work. This achievement not only demonstrates

commercially valuable processing capability of ~0.4x0.4 m surfaces like laser fusion optics, but also promotes a confident approach to the meter-class figuring needed, e.g., for large telescopes mirror segments.
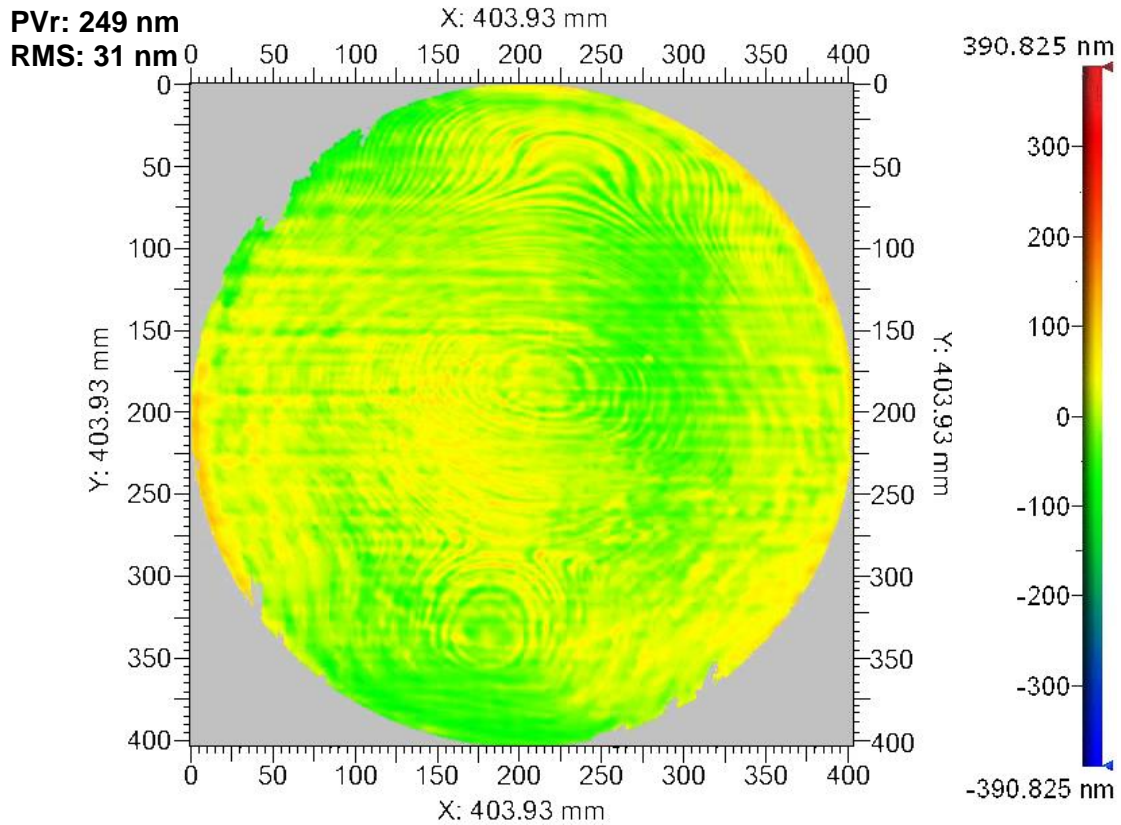
Figure 5-26 Residual figure error after second figuring.

From the presented results and the data in **Table 5-4**, it is possible to estimate the processing times required for a meter-class surface characterized by ~1 µm PV figure error. If two iterations of ~50 minutes duration each are considered, the plasma figuring procedure would be completed in about ten hours.

This short processing time fulfills the requirements for a figuring process to be incorporated into a novel optical manufacturing chain. Additionally, the time for roughness level restoration should be accounted for. The introduction of a CNC controlled "flash" polishing process would deliver a rapid surface texture finishing, while preserving the form accuracy achieved by plasma figuring.

Table 5-4 Evaluation of figure correction experiments over 400 mm Ø areas. Operations lasting times are reported in minutes per iteration.

Evaluated aspect		First figuring	Second figuring
Measurement time [min/iteration]		15	15
Computational time [min/ iteration]		20	20
Torch start-up time [min/ iteration]		3	3
Sample loading time [min/ iteration]		10	10
Mean figuring time [min/ iteration]		51	49
Targeted % of figure error depths	Iteration 1	10 Step: 9 mm Pitch: 1.5 mm	50 Step: 9 mm Pitch: 1.5 mm
	Iteration 2	50 Step: 9 mm Pitch: 1.5 mm	60 Step: 6 mm Pitch: 1 mm
	Iteration 3	50 Step: 6 mm Pitch: 1 mm	--
Convergence [%] (Over the two cycles: 92%)	Iteration 1	21	36
	Iteration 2	82	65
	Iteration 3	22	---
	Overall	89	77
Figure error in RMS [nm]	Initial	383	137
	After it. 1	304	88
	After it. 2	55	31
	After it. 3	43	---
Figure error in PVr [nm]	Initial	2408	723
	After it. 1	1880	583
	After it. 2	481	249
	After it. 3	290	-----

As mentioned above, both residual error maps after the first and second figuring cycle present a patterned morphology. This is partially due to spikiness caused

by the subsurface damage from the preceding abrasive process. However, the raster-scanning tracks of the plasma figuring can also be recognized (mid-spatial frequencies). These patterns have been investigated by means of Power Spectral Density (PSD) analysis in section 6.2.

5.3 Summary of figure correction results

In this chapter, the principal achievements of this research work have been presented and discussed. The knowledge and understanding acquired during the process characterisation, the study on non-linear dwell-time dependence and the design of the tool-path found their verification and application in the successful figure correction of optical surfaces.

A preliminary test, the sinusoidal trenches, confirmed both the validity of the non-linear dwell-time calculations and the correct estimate of the etching footprint figuring authority. The actual figure correction was then performed on areas from 100 to 400 mm diameter and the rapid figuring capability of the RAP process was proved down to 16 nm RMS using a prototype production machine.

First, a spherical hollow of 500 nm maximum depth was used as target form on four different fused silica surfaces over areas of 100 mm diameter. The effect of variation of the secondary pitch parameter was investigated in two different series of experiments, obtaining high quality surface figure correction with residual errors down to 16 nm RMS (λ/40 RMS) and confirming repeatability. The figuring procedure was then applied to 150 mm diameter fused silica areas, where a larger spherical hollow and a flat were attained on two different surfaces. Final figure error maps of, respectively, 18 and 16 nm RMS were achieved. For these tests, a smaller staggering step and a third processing iteration were introduced to reduce raster-scanning print-through and edge slope. While reduction of the rippled pattern was successful, the minor edge effect was still present. On these smaller regions, all figuring results were achieved within less than seven minutes processing time per iteration, with an overall convergence ranging from 67 to 89%.

At this stage, some thermal investigations were carried out. These were useful to confirm the temperature homogenising action of the tool-path algorithm. Also, one particular test, the sinusoidal hot trench, introduced a new type of heat effect characterisation that could be exploited for a future in-process temperature adaptation.

As part of surface quality assessment, the post-process roughness was measured through white light interferometry. This investigation was performed only on the four 100 mm diameter areas, as these were etched in pristine conditions. Each process area was mapped following a predetermined array and the S_q values were reported. Deterioration of the surface texture due to the chemical nature of the plasma process was detected. This ranged from ~2 to 14 nm S_q. A post-etching polish is proposed. Together with RAP, this would constitute a finishing process stage capable of meeting the ultra-precision optics specifications of < 20 nm RMS form accuracy and 1 nm RMS surface roughness.

Prior to scaling-up the process to a large surface, a method for waviness minimisation was introduced. A randomisation of the tool-path staggering step was induced by alternating different step sizes over consecutive iterations. An applicative example was shown by figuring the 500 nm deep sphere onto a new 100 mm diameter fused silica area. As the result appeared promising, it was decided to further utilise the method.

The figuring procedure with the new pseudo-random tool-path was subsequently applied onto a large surface. This part of the work aimed at demonstrating the rapid large scale figuring capability of the devised procedure. For this purpose, a ULE substrate of 420mm x 420mm x 40mm was utilised. On one of the 420mm x 420mm faces, this sample hosted a concave spherical geometry of 3 m ROC and 405 mm diameter clear aperture. In this way, the applicability of the process on (low-gradient) free-form surfaces could also be proved. The initial figure error presented a near-astigmatic term of ~2.3 µm PVr. Two figure correction cycles were carried out on this surface, with a polishing phase in-between. This approach aimed at showing the large scale repeatability

of the process, as well as emulating a RAP+polishing chain for optics finishing. The first cycle was completed in three iterations and a 43 nm RMS residual figure error was achieved. The texture was then recovered by hand pitch-polishing, but with a loss of form accuracy (~800 nm PV). The next figuring cycle converged to 31 nm RMS after two iterations. The mean figuring time per iteration (50 minutes) allows predicting about ten hours effective processing duration for a meter-class surface of ~1 μm PV figure error, if two iterations of 50 minutes duration each are considered.

6 Assessment of the figuring procedure performance

In this Chapter, the figure correction methodology is re-discussed in the light of the results achieved and presented in the previous sections. The rapid convergence delivered by the tool-path choice combined with the modified dwell-time calculation is assessed from a point of view of the actual material removal. In particular, in section 6.1, the correlation between depth of removal and targeted percentage is investigated by means of histograms. The next assessment concerns the analysis of the mid-spatial frequencies observed on the residual figure error maps (section 6.2). This establishes the link between scanning patterns and waviness of processed surfaces. In section 6.3, the edge effects observed for some of the figuring results are discussed in connection to actual workpiece boundaries and a correction method is proposed. Finally, the case study of E-ELT segments specifications is considered in relation to the residual error of the ULE mirror.

6.1 Process convergence

In this work, and for all figure correction results, high levels of overall process convergence (~77– 90%) have been systematically achieved. Also, every single iteration step always showed some amount, albeit in some cases small, of convergence (see summary tables of the figuring results).

In this section, a histogram analysis is carried out to investigate the relation between the targeted removal depths and the actual figure error depths removed after a single process. In **Figure 6-1**, a schematic illustrates how the histograms were generated. First, the measured effective figure error correction map was divided by the targeted figure error correction map[11]. The resulting charts of relative figure error correction factors were then plotted into histograms (bin size: 0.1).

---

[11] The maps of effective figure error correction don't necessarily represent the effective material removal depths, since such depths are actually unknown. The maps of targeted and measured figure error correction were offset so that the minimum would be zero. This explains the presence of values smaller than one in the charts of the relative depth figure error correction factors, as well as in the histograms.

Histograms are shown for each iteration step in the plots of **Figure 6-2** to **Figure 6-7**. The shadowed portions of the plots indicate the range over which ~80% of the histograms distribution is contained. The upper x-axis label reports the average etching depth attained at the locations of the corresponding relative removal factor (lower x-axis). For each plot, the average, the standard deviation and the skewness of the values distributions are reported.
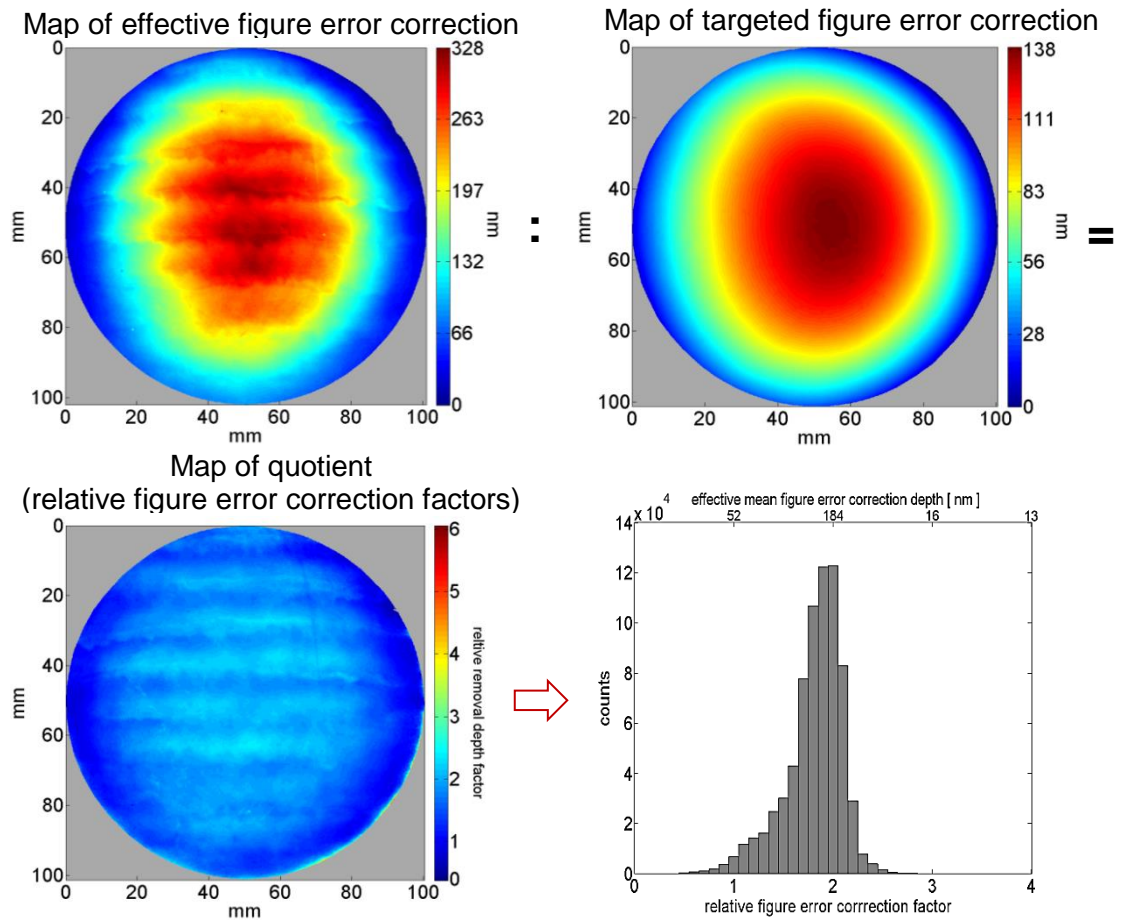
Figure 6-1 Schematic illustrating the operations leading to histogram generation. Note that targeted and effective removal maps are purposely displayed on different scales for better visualisation.

A first impression one gains from **Figure 6-1** (upper pictures) is that of a close relation between targeted and effective figure error correction maps. This is a consequence of an accurate registration of the process area position, but also and in particular of the figuring methods introduced in this work (tool-path + dwell-time calculations).

<u>100 mm Ø areas</u>: 3 mm secondary pitch.
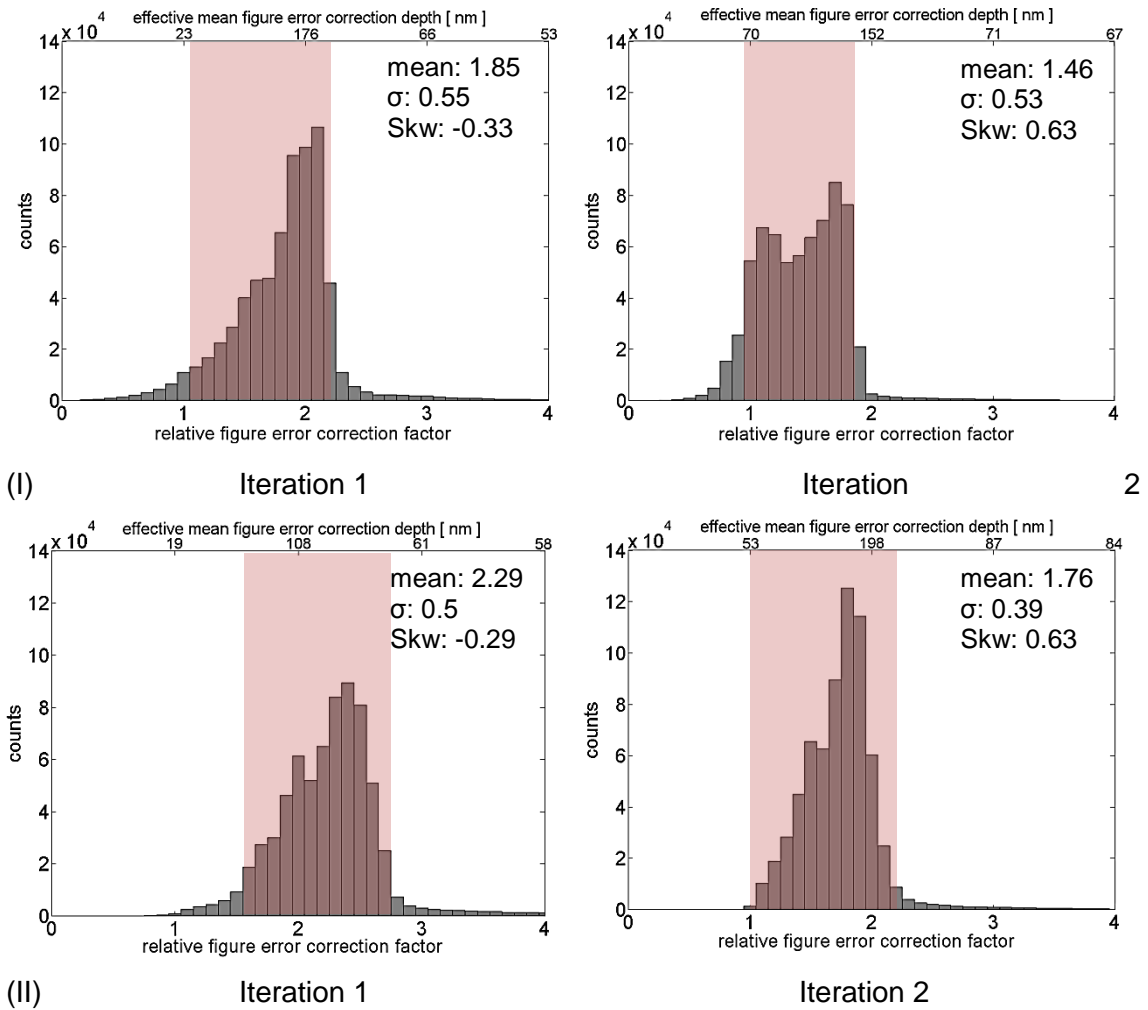
Figure 6-2 Histograms of relative figure error removal depth for single iterations: 100 mm diameter areas processed with the 3 mm secondary pitch.

However, from a more detailed observation of all histograms, it emerges that the correlation to the targeted figure error is not entirely consistent. The distributions appear to be strongly dependent on the topography of the error maps which determines the dynamics of heat transfer, hence of the etching rates. Therefore, the majority of the histograms show a non-Gaussian distribution. This point is confirmed by the skewness values. Instead, a correlation is found between effective mean figure error correction depths and histograms maxima (see upper x-axis label) and it evidences that the deeper etching is linked to a higher energy input. The distributions indicate that, due to the heat, the effective removal depth can be up to a factor ~3 larger than the

targeted one. However, it is also evident from the shadowed areas that 80% of the effective etching is more likely to be comprised between a factor 1 and 2.

<u>100 mm Ø areas</u>: 2 mm secondary pitch

(I)   Iteration 1   Iteration   2

(II)   Iteration 1   Iteration 2
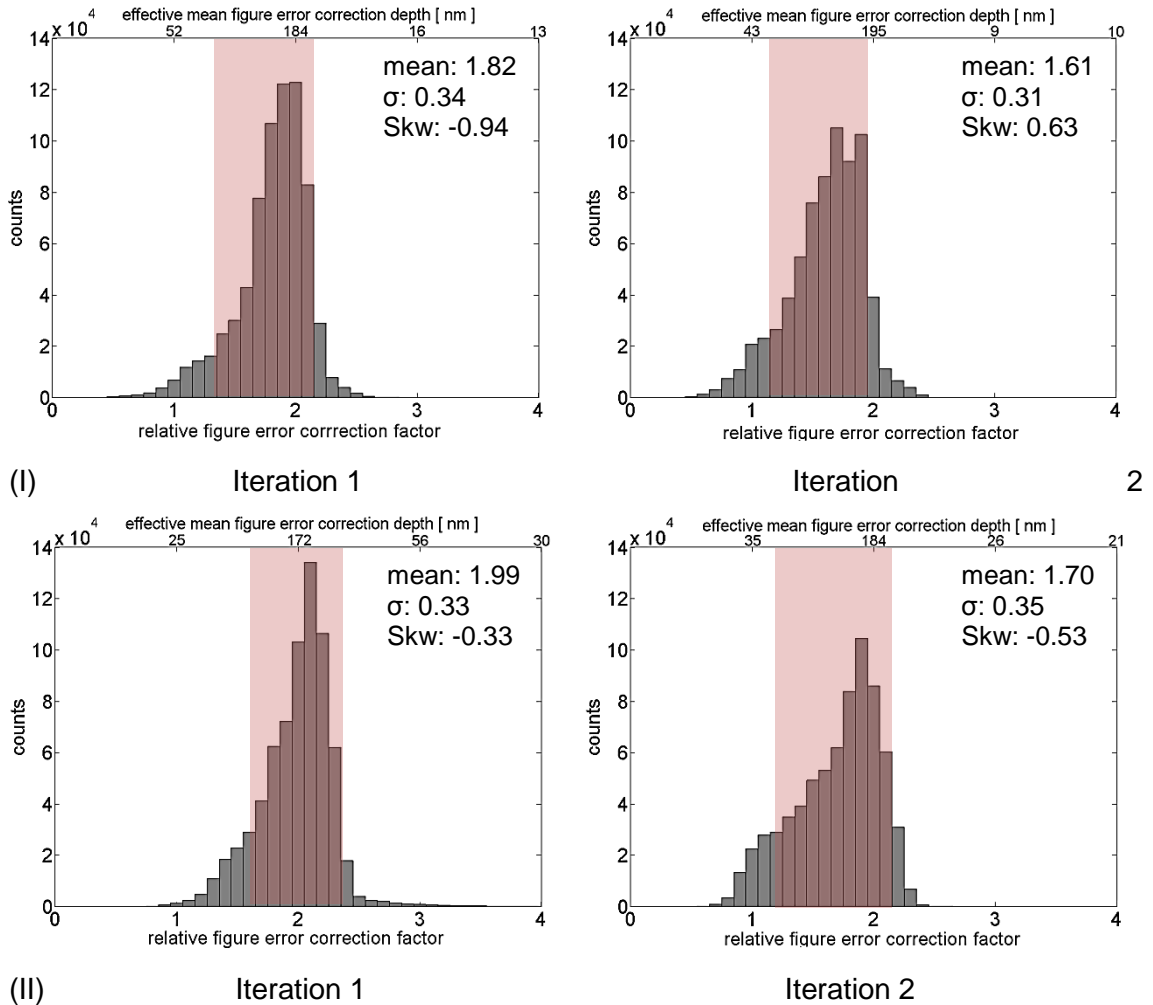
Figure 6-3 Histograms of relative figure error removal depth for single iterations: 100 mm diameter areas processed with the 2 mm secondary pitch.

In some cases, the relation between target and effective figure error correction appears more evenly distributed around a factor two, with standard deviation up to 0.5. Interestingly, the second iteration of the first 405 mm area figure correction (**Figure 6-7**) presents a very sharp histogram distribution centred over a factor ~1.9. This corresponds also to the overall largest etching depths achieved in the course of the figuring work (about 1 µm mean figure error

correction depth). Despite this being a one-off case, deep etching associated to a larger energy input is reckoned to promote a more rapid homogenisation of surface temperature distribution during the process. This, in turn, will produce more consistency of material removal.

<u>100 mm Ø areas</u>: pseudo-randomised

Iteration 1

Iteration 2
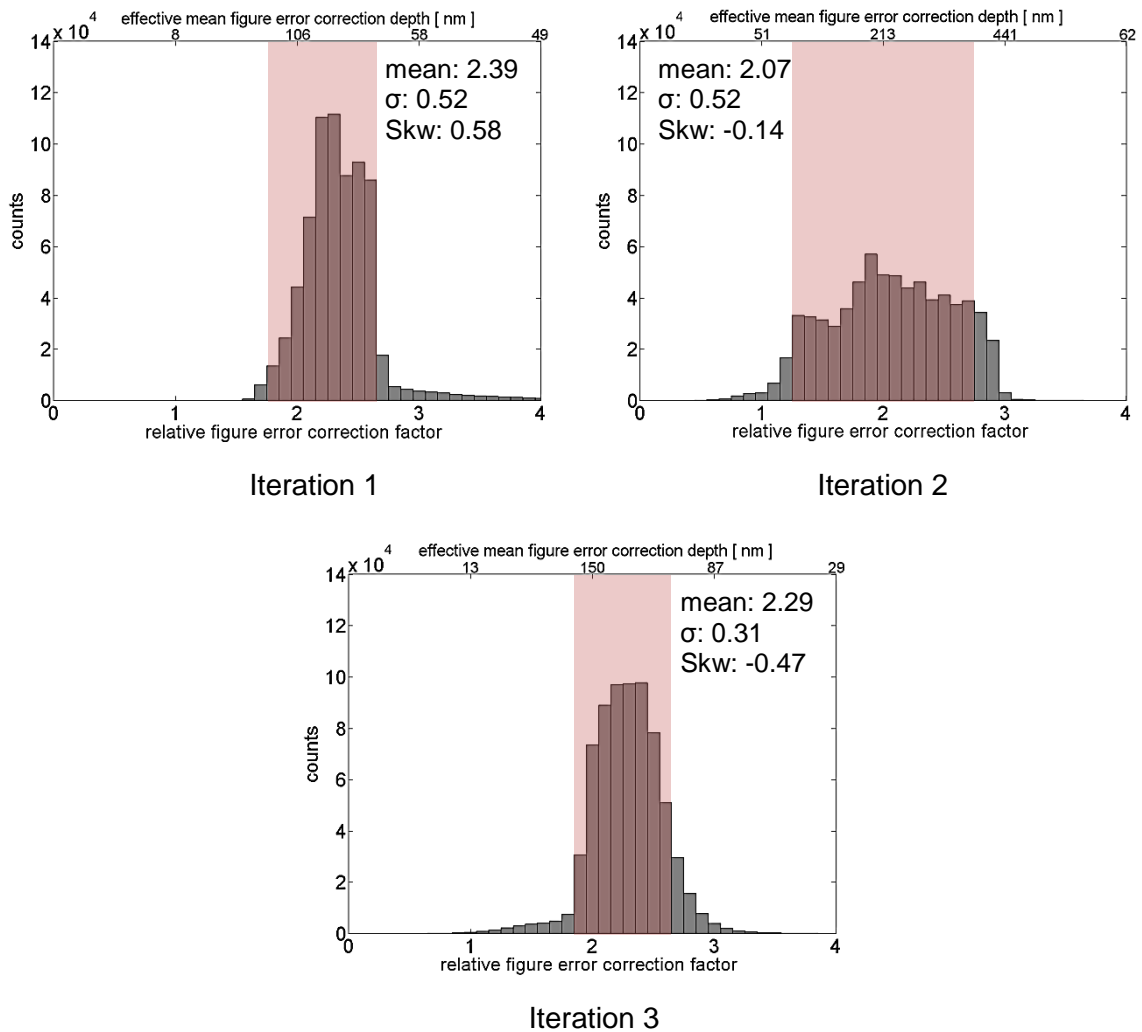
Iteration 3

Figure 6-4 Histograms of relative figure error removal depth for single iterations: 100 mm diameter areas processed with the pseudo-randomised tool-path (pitch sizes: 1.5 & 1 mm).

In this histograms investigation, a relatively narrow range of the removal depth factors distributions is evidenced. However, this applies for the reversed-staggered tool-path designed in the course of this project which promotes

homogeneity of energy transfer. To be noted is also that no correlation appears between the form of the distributions and the choice of the pitch sizes. This is to be expected since the dwell-time calculation automatically accounts for variations of the secondary pitch, which is linked to the main step by the number of reversals (typically six). Hence, reduction of the tool-path pitches always corresponds to an increase in scanning velocities, thus making the material removal independent from these parameters.

150 mm Ø area: spherical hollow.

Iteration 1   Iteration 2
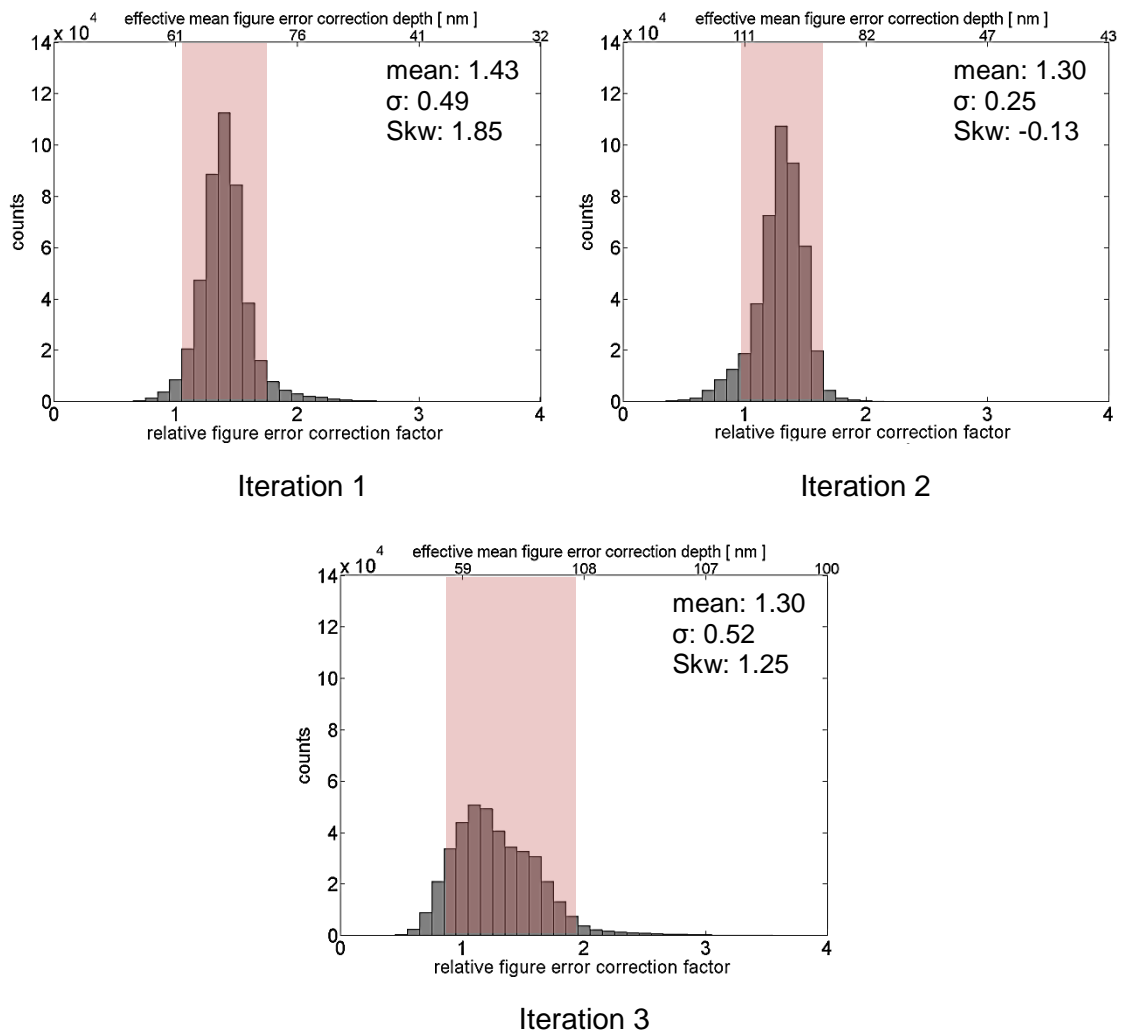
Iteration 3

Figure 6-5 Histograms of relative figure error removal depth for single iterations: spherical hollow over 150 mm diameter area.

150 mm Ø area: flat.

Iteration 1   Iteration 2
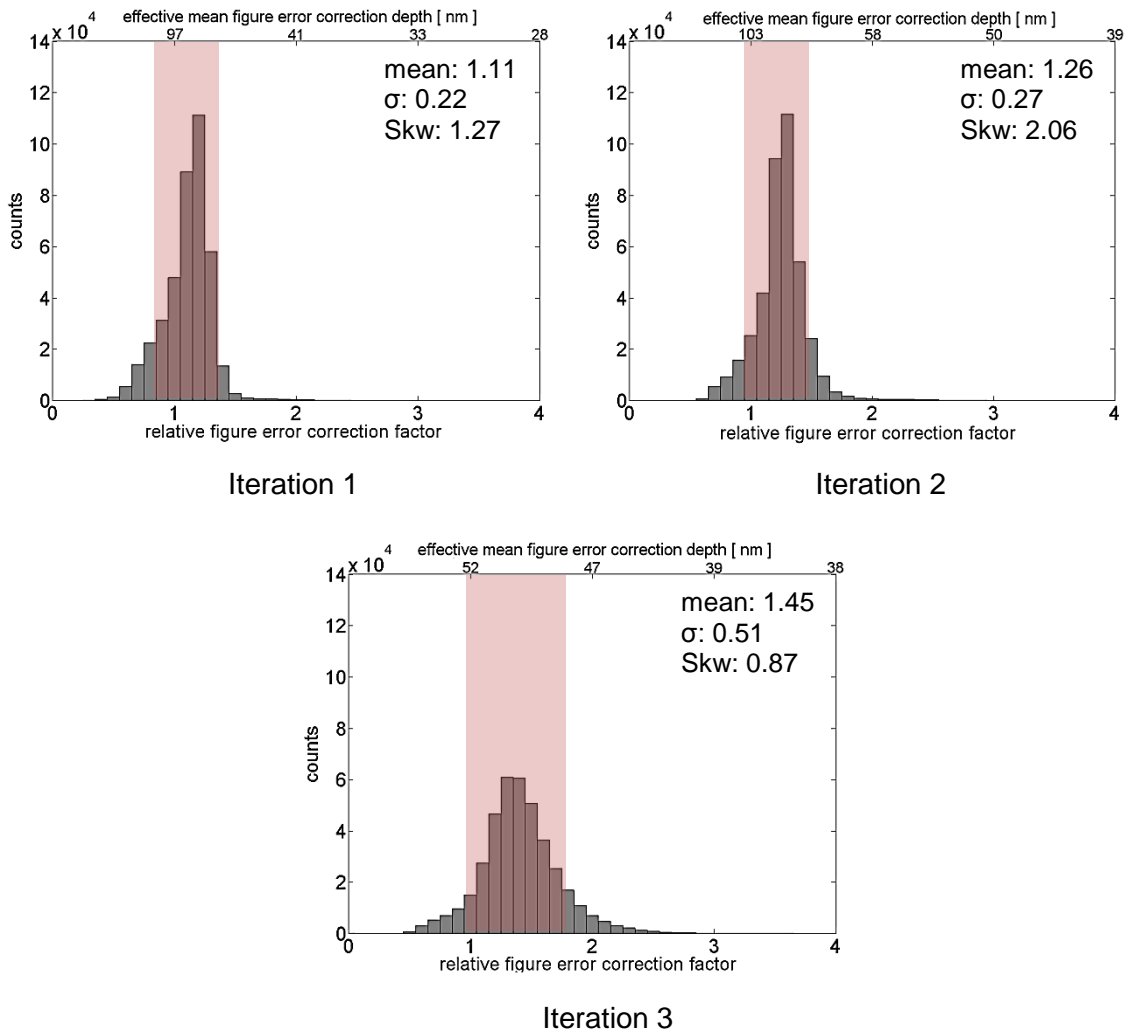
Iteration 3

Figure 6-6 Histograms of relative figure error removal depth for single iterations: flat over 150 mm diameter area.

The discussion presented in this section points out that a completely deterministic process hasn't been achieved yet. Together with the consistent convergence of the figuring procedure, though, the considerations made in this section allow indicating a "rule of thumb" for users. First, the figure correction work should be completed within two iterations to keep the processing times within the required ten hours (meter-scale). The targeted percentages to be applied on the figure error map can be split as 25–30% for the first iteration and 50–60 % for the second. This is based on the statistical assumption that the process is more likely to correct about twice the figure error as targeted.

400 mm Ø areas

(I)   Iteration 1   Iteration 2

Iteration 3

(II)   Iteration 1   Iteration 2
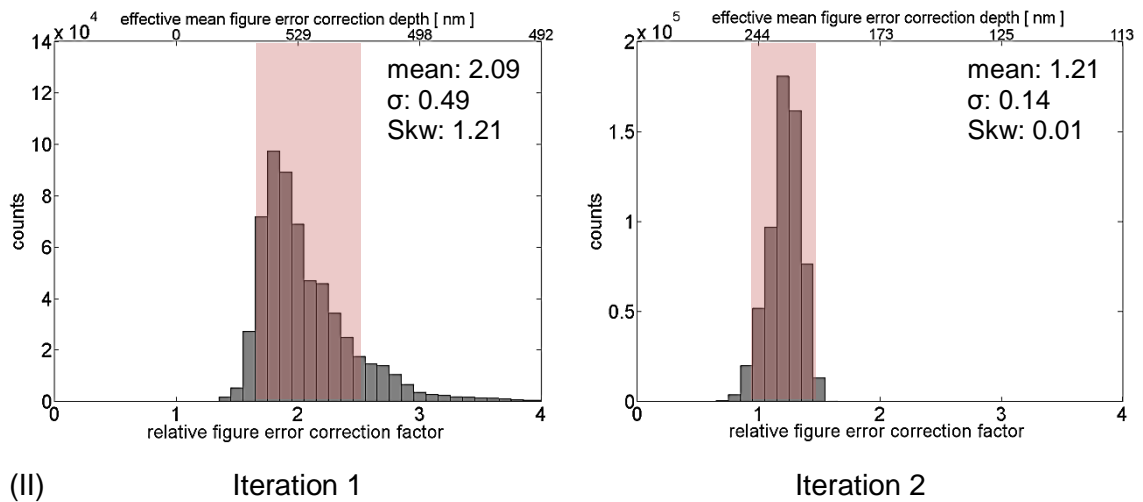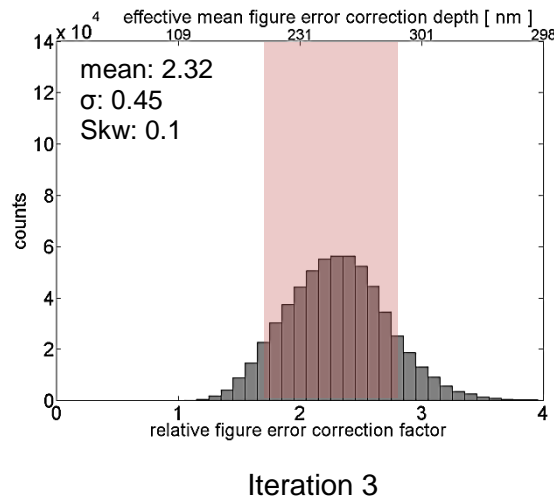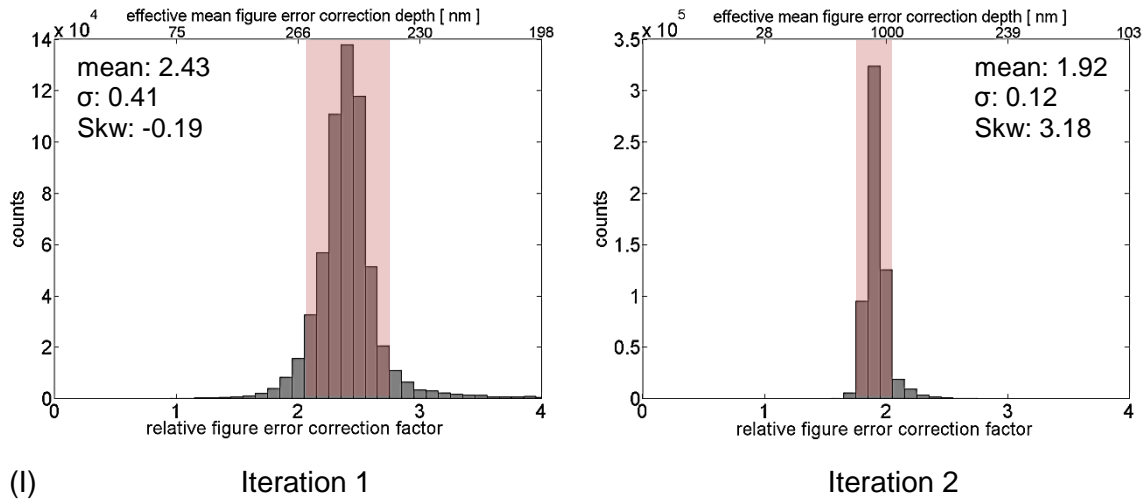
Figure 6-7 Histograms of relative figure error removal depth for single iterations: 405 mm diameter areas.

While achieving convergence, this approach would also allow a more efficient application of the pseudo-random tool-path by overlapping waviness of similar amplitude over the two iterations. Certainly, the amount of initial figure error, considered in relation to the material removal rates, will always require verifying the applicability of this method. For example, this strategy can be considered suitable for PV figure error depths up to ~1 µm for fused silica and ~2 µm for ULE. Differently, if the error map presented several micrometres of overall deviation it is suggested to adopt a more prudent scheme consisting of multiple iterations. This would avoid major deterioration of the surface and the risk of material phase transition.

6.2 Waviness and Power Spectral Density (PSD) Analysis

In this section, the waviness (mid-spatial frequencies) observed on the residual error maps of the figuring results is analysed by means of a Power Spectral Density computation. In particular, the study is carried out calculating the *average directional PSD*.

The average directional PSD is computed as the weighted average of single cross-sections PSD and is useful for evidencing peaks that match regular patterns in the surface figure error. In the Fourier transform calculations, a Hanning window was applied as an apodization function. In the graphs from **Figure 6-8 (b)** to **Figure 6-12 (b)**, the PSD plots are shown for all residual error maps of the figuring results. In all the figures, above each PSD graph, an illustrative mean cross-section is displayed. These profiles serve as illustration of the residual waviness mean amplitude in the space domain.

As mentioned in sections 5.2.1, 5.2.2 and 5.2.6, the mid-spatial frequencies visible on all residual error maps were considered due to the etching footprint raster-scanning tracks. The PSD line graphs fully confirm this hypothesis for all figuring results. As emphasized by the markers on the graphs (vertical dash lines), key peaks appear at the spatial frequencies corresponding approximately to 12, 9 and 6 mm, the input lengths of the tool-path algorithm. A comparison between the plots in **Figure 6-8** and **Figure 6-9** shows that the peaks linked to the presence of staggering patterns appear reduced when the smaller step (9

mm) was adopted, thus confirming the waviness improvement reported in section 5.2.2.

(a)

(b)
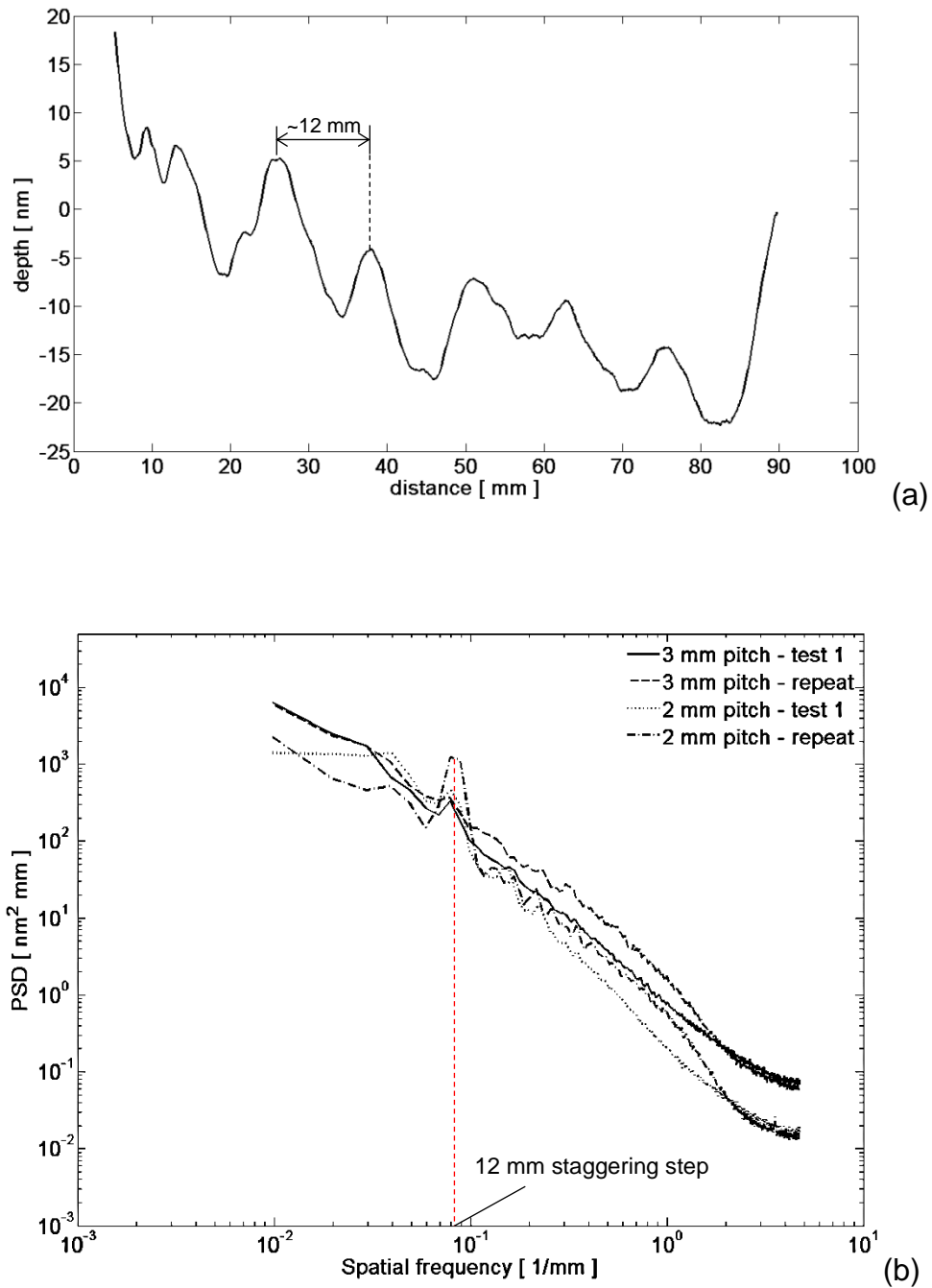
Figure 6-8 Figuring of 100 mm diameter areas (a): Illustrative example of mean cross-section (12 mm staggering step); (b): average directional PSD plots of the residual error maps Y-cross-sections.
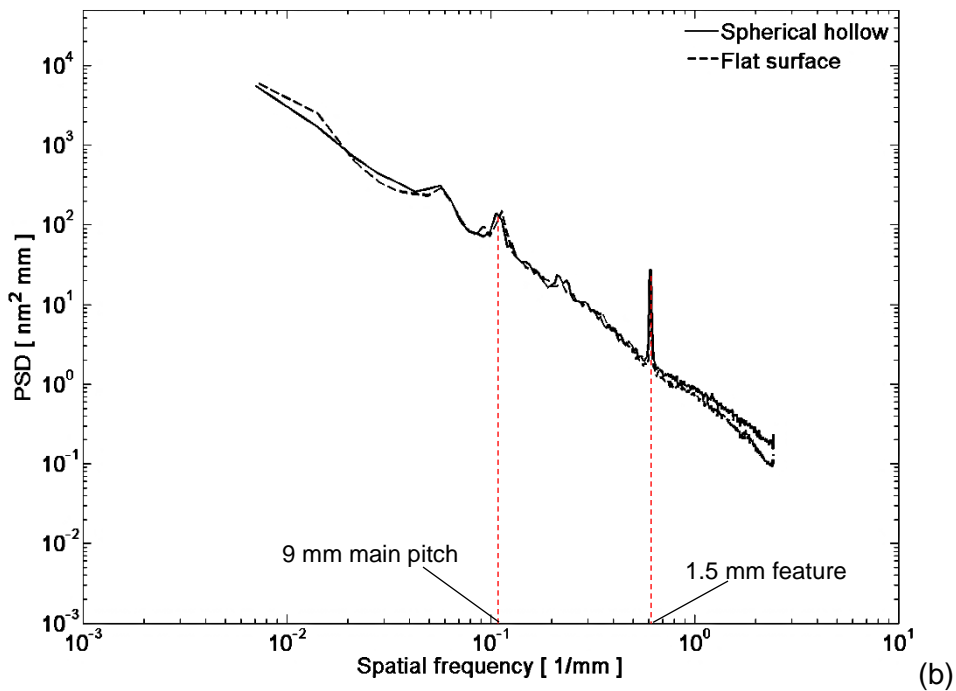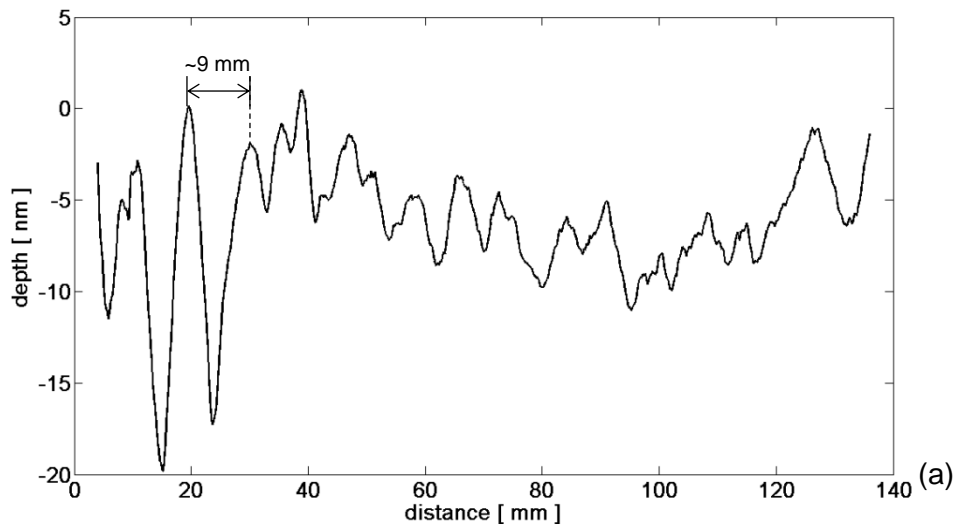
Figure 6-9 Figuring of 150 mm diameter areas: (a) Illustrative example of mean cross-section after figuring with 9 mm staggering step; (b): average directional PSD plots of the residual error maps Y-cross-sections.

However, different crests are present in the PSD plots of the 150 mm diameter areas (**Figure 6-9 (b)**), as well as where the pseudo-random tool-path was applied (**Figure 6-11 (b)** and **Figure 6-12 (b)**). Somewhat surprisingly, the waviness on the 150 mm diameter residual maps produces a peak matching the

1.5 mm secondary pitch. Since the creation of such a pattern with the current etching footprint is not expected, evidence for a different origin of the peak was sought.
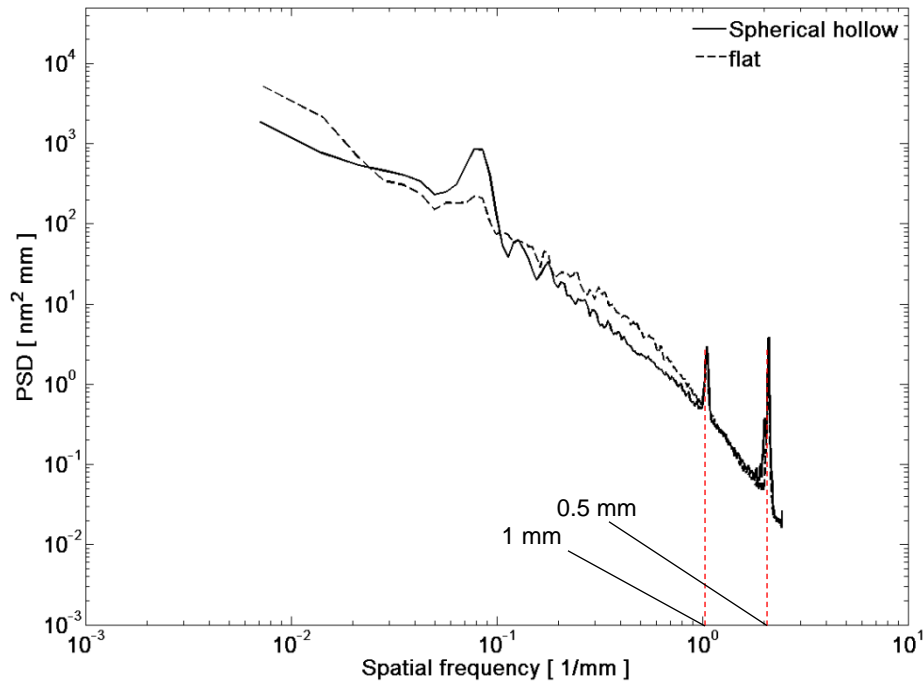
Figure 6-10 Figuring of 150 mm diameter areas: average directional PSD plots of the residual error maps X-cross-sections.

In this case, the presence of metrology artefacts was suspected. To verify this hypothesis, the PSD was computed in the perpendicular direction. In **Figure 6-10**, the resulting line graphs are shown. Here, two additional peaks appear at the spatial frequencies of 1 and 2 mm^{-1} that cannot be ascribed to the plasma process. The reason for the high frequency peaks in **Figure 6-9** and **Figure 6-10** is therefore considered linked to errors of the used instrument (Intellium H2000). In particular, such a regular pattern could be ascribed to birefringence of the optics (e.g., 150 mm diameter collimator) or defects in the detectors (cameras CCD). Also, flaws of the samples surface can be excluded, as no such patterns were observed.

Differently, the pseudo-randomised approach in the example of the 100 mm diameter fused silica area generates a PSD graph with near-absence of peaks (**Figure 6-11**). In this case, the 9 and 6 mm steps overlapped in a balanced

manner (see also **Figure 5-18**) and this created a smoothed out crest in place of a double peak.

(a)

(b)
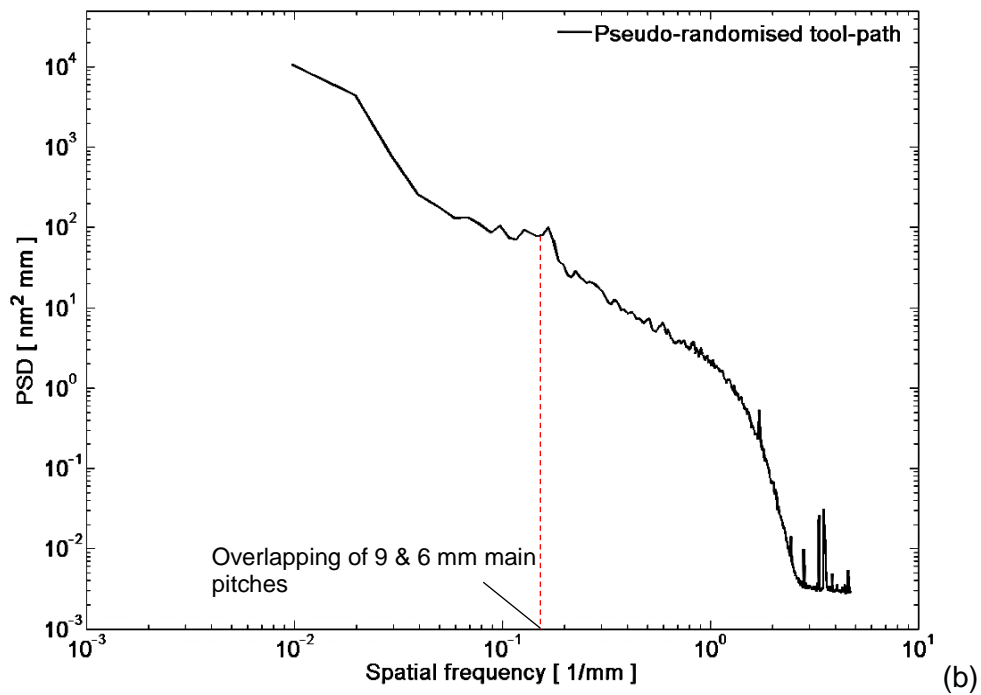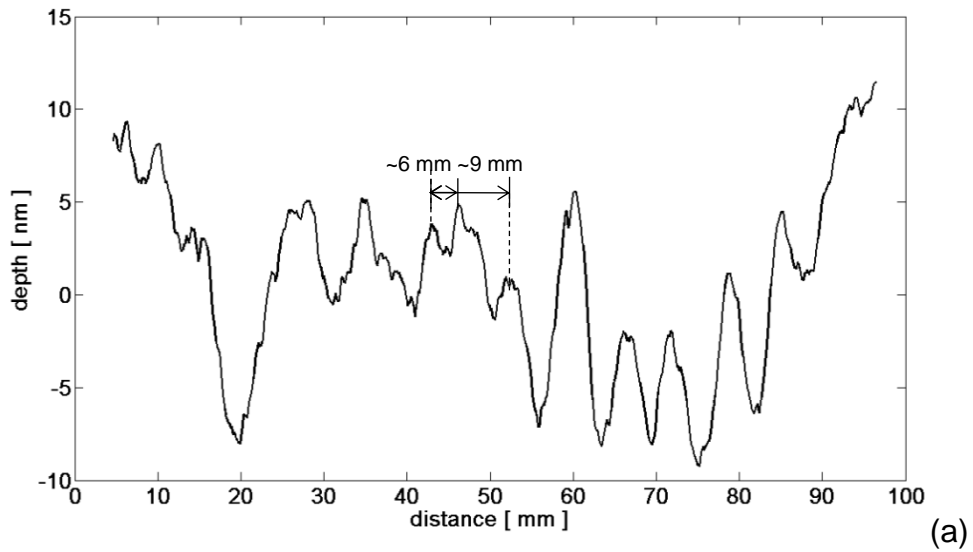
Figure 6-11 Figuring of 100 mm diameter areas with pseudo-randomised tool-path: (a) mean cross-section of the 100 mm diameter residual error maps; (b) average directional PSD plot of the residual error map Y-cross-sections.

144
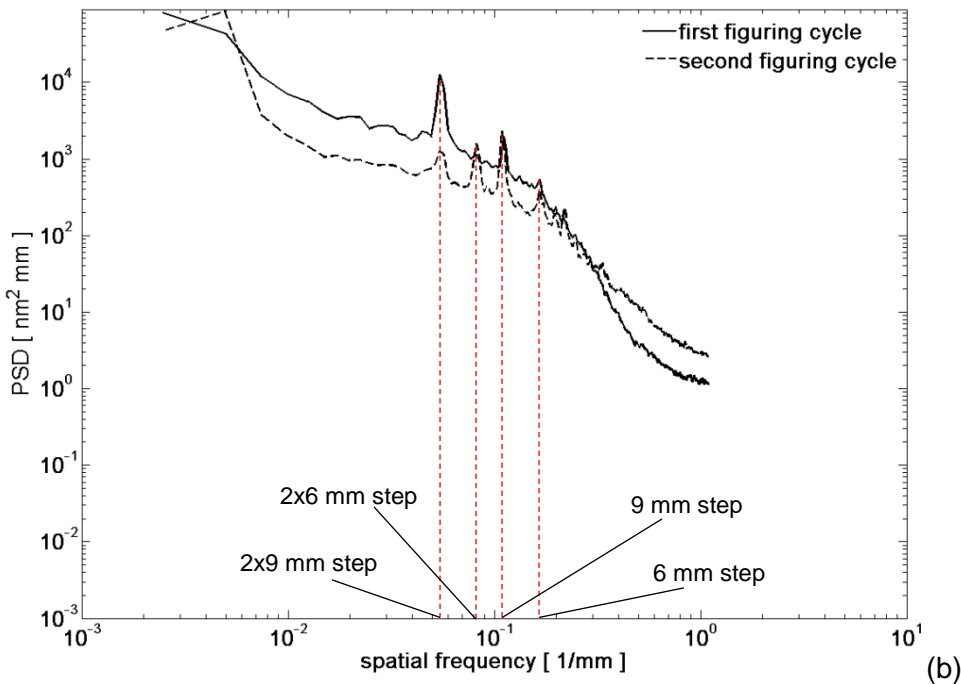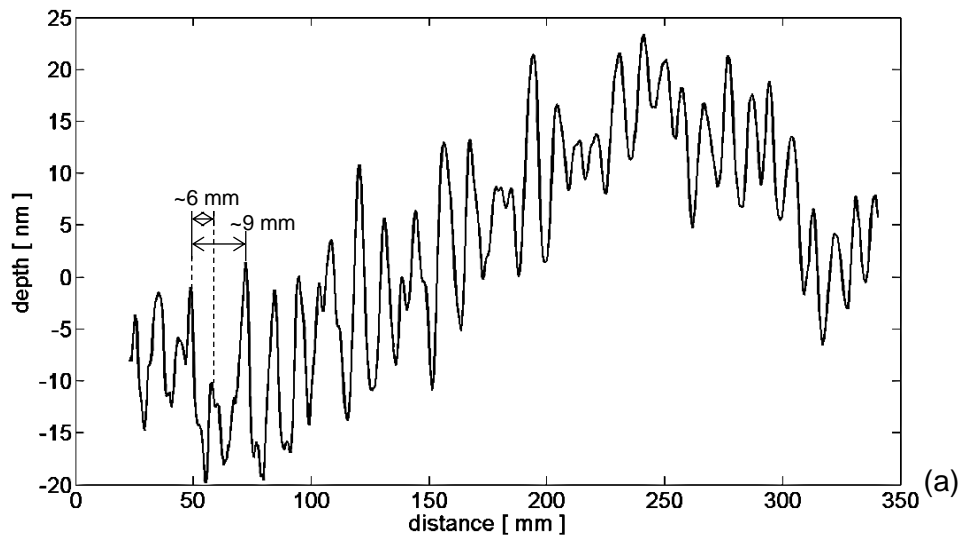
Figure 6-12 Figuring of 400 mm diameter areas: Average directional PSD plot of the residual error map Y-cross-sections for the figure correction over 400 mm diameter areas.

The reduction of peaks presence didn't fully succeed when processing the larger ULE area. A direct comparison to the results on fused silica, though, seems inappropriate, both because of the difference in material removal and because of the higher surface texture deterioration. In **Figure 6-12**, the PSD

curves of the 405 mm diameter residual maps are shown. The graph peaks reveal that the first cycle generated a predominant pattern matching the 9 mm step, as well as twice the value. This is probably due to the deep material removal in the second iteration, performed with a 9 mm staggering step. Conversely, the residual map of the second figure correction produced PSD crests matching both tool-path steps (9 and 6 mm), as well as twice their values. The sharpness of these peaks is considered a consequence of the non-balanced removal depths over the two iterations. The presence of double frequency peaks is reckoned to be linked to the superposition of the staggered pattern over consecutive loops at different temperature.

A comparison between the two curves in **Figure 6-12 (b)** shows a reduction of peaks amplitude by about one order of magnitude in the case of the second cycle. Here, the absence of an iteration with dominant etching depth allowed for a more efficient application of the pseudo-random tool-path and highlighted once more the benefit of its introduction.

The residual rippled patterns are of the order of magnitude of few tens of nanometres (see cross-sections above PSD plots). Minimisation of such features is certainly essential to comply with the specification any high precision optics. The post-RAP flash polishing, necessary for roughness restoration, is considered as a possible solution also to reduce the presence of nanometre level mid-spatial frequencies. Together with PV and RMS surface qualifiers, a post-polishing PSD assessment would then be meaningful for optics like NIF slabs to test the conformity to finishing requirements (see [64]).

A further method for waviness minimisation could consist of an approach accounting for the progressive surface temperature increase. The in-process adaptations discussed in chapter 7 are an example of such a technique. Also, on the basis of the thermal assessments conducted so far (see, e.g., **Figure 4-19** and **Figure 5-17**), an empirical compensation could be introduced. This could consist of a loop-by-loop velocities correction factor that should be inferred experimentally.

6.3 Edge Effects

As mentioned in sections 5.2.1 and 5.2.2 , the residual error maps of the small area figuring present larger values at the periphery of the measured region which increase the corresponding PV (see also **Figure 5-6**, **Figure 5-7**, **Figure 5-8** and **Figure 5-9**). This effect is related to the final forms targeted in this work that caused the heat to be concentrated in the central zone (see also **Figure 5-17**). In particular, the edge effect observed on the 100 and 150 mm diameter areas is not associated to the actual edges of the workpiece as these are not included in the metrology area. Also, when processing the entire optic surface, as a non-contact tool, the RAP plasma plume can be slickly carried across the edges. Therefore, minimal influence on the etching footprint performance should be expected. This is in contrast to well-understood limitations of contact abrasive processes where the tool overhangs the workpiece edge (section 2.3.4).

Potentially, an additional effect could be provoked by metal parts holding the component, if these are located near the chamfer. Due to the higher thermal conductivity, in fact, these could act as heat-sinks in the neighbourhood of the workpiece edge, thus affecting the behaviour of the etching distribution in the run-out/run-in phase. Further, a similar response could be due to the edge geometry itself that can influence the way heat transfer occurs at the boundaries. These points are objectives within future investigations at Cranfield.

In **Figure 6-13** and **Figure 6-14**, the edge effect is shown for the 100 and 150 mm diameter residual maps. In these graphs, the central cross-sections along the plasma plume travelling direction are plotted. As indicated by the arrows, the lines present rolled-up edges of the order of ~100-150 nm. This phenomenon is considered a consequence both of the heat stored in the centre of the process area and of the choice of the boundary extension function.

Following these considerations, prior to the work on the ULE mirror, a fine adjustment of the edge-extension algorithm was introduced to improve the figure correction performance at the outskirts of the measurement area.
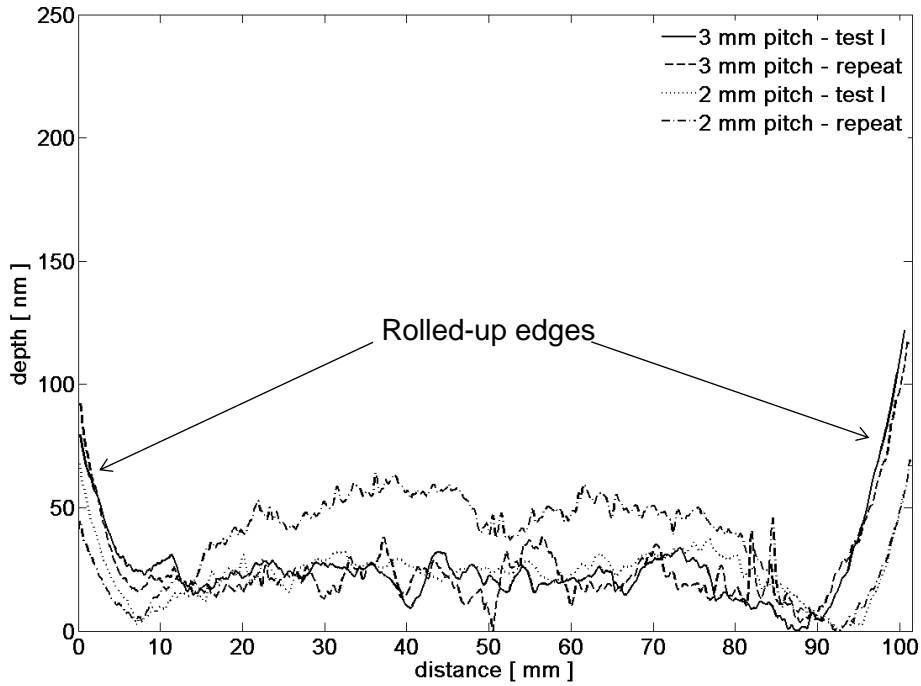
Figure 6-13 Central cross-sections of the 100 mm diameter residual figure error maps.
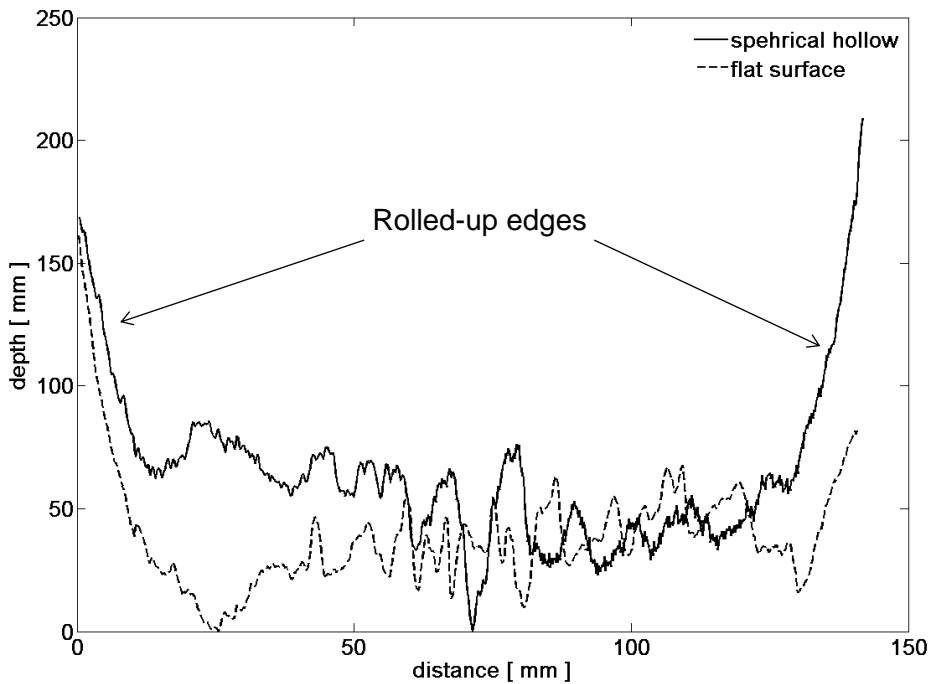
Figure 6-14 Central cross-sections of the 150 mm diameter residual figure error maps.

In **Figure 6-15**, the cross-sections of the residual maps for the two figure correction cycles on the 405 mm diameter area are shown. Despite the jagged

148

profile structure (roughness), also in this case, steep extremes with similar amplitude to the once observed on the small areas are visible. However, due to the texture spikiness, it is considered more appropriate to repeat this evaluation on a smoother surface.
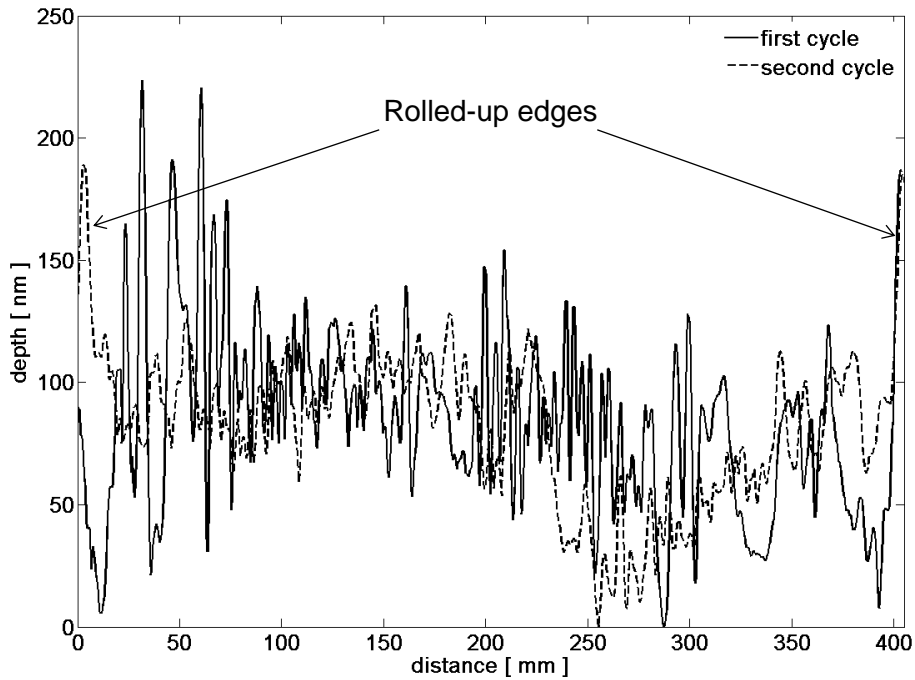
Figure 6-15 Central cross-sections of the 405 mm diameter residual figure error maps.

For the reduction of the observed rolled-up edges, the following approach can be suggested. If the edge misfigure approximately conforms to the figuring authority of the etching footprint it is theoretically possible to remove it with a single pass around the boundary by matching the position of the Gaussian to the edge slope. An example is showed in **Figure 6-16**. The edge misfigure correction can then be seen as a single trench along the limits of the measurement region (e.g., circle) and the velocity values can be inferred by non-linear deconvolution as in the case of the sinusoidal trench[12]. An edge-correction algorithm of the kind proposed in this discussion could be profitably used even for the final finishing of polished optics.

---

[12] On Helios 1200, a practical limitation can occur due to the low acceleration capability of the carrier (Y-axis).
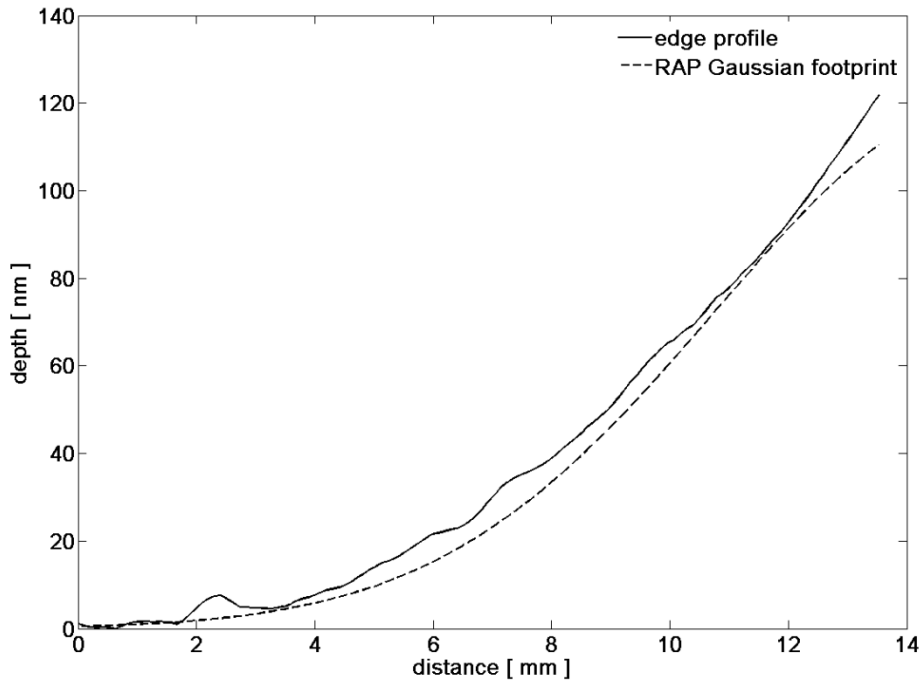
Figure 6-16 Edge correction example: rolled-up edge profile of one of the residual maps over 100 mm diameter in comparison to the Gaussian etching footprint.

A situation where the Gaussian footprint matches the edge slope after RAP figure correction is more likely to occur since the error is generated by the footprint itself. Should the edge misfigure be steeper, though, then a smaller influence function would be needed. Like in IBF or PJM, this can be attained by the use of different torch nozzles. An alternative solution could consist of a redistribution of the heat flux onto a smaller area, which would then correspond to shrinkage of the etching width. This can be obtained, for instance, by directing a laser beam in the centre of the plasma plume. The etching footprint would then relate to the superposition of the two heat sources, whereas the laser heat flux could be fine-tuned to obtain the wished shape. At the time of writing, such a technology, named Laser Assisted Plasma Processing (LAPP), is indeed under development at Cranfield University Precision Engineering [162].

6.4 Case study: E-ELT segment specifications

In this section, as an example exercise, the criteria of figure error accuracy specified for E-ELT segments are applied to the residual error map of the ULE mirror after the second figure correction cycle. Surface roughness specifications aren't investigated since no post-RAP CNC polishing was applied. This case is chosen for following reasons: ULE is one of the candidate materials for the E-ELT segments fabrication; the presence of subsurface damage makes the processed surface unsuitable for characterisation by criteria such as the ones applying to NIF slabs (e.g., RMS-gradient, PSD criteria [21]). Obviously, as an example, the exact conditions of a large hexagonal segment (e.g., support structures) cannot be realised for this case study.
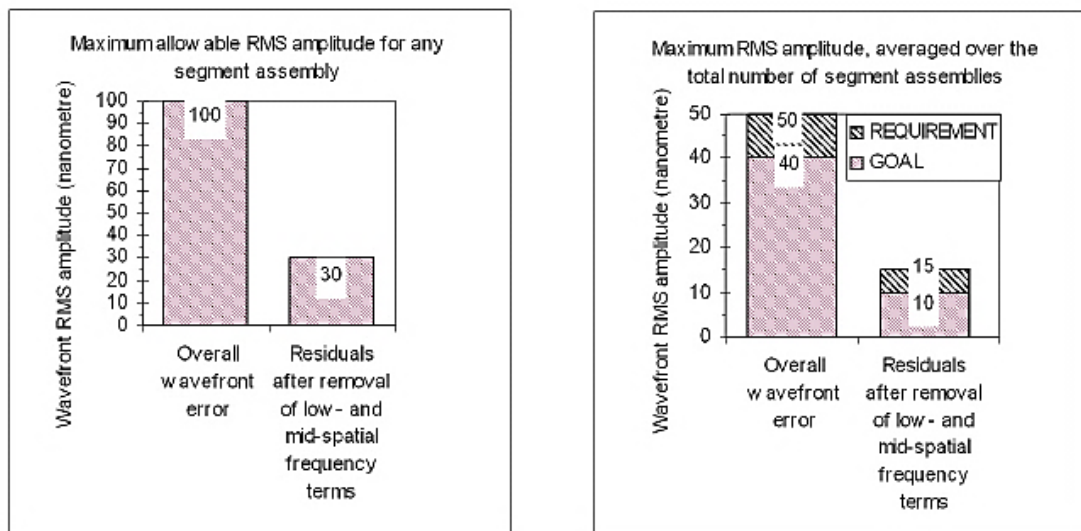
Figure 6-17 E-ELT specifications for single segment (left) and averaged over the total number of segments (right).

The E-ELT segments residual error specifications are reported in the document written for candidate suppliers [34]. In **Figure 6-17**, such requirements are illustrated for an entire assembly (left plot), as well as for the average over the number of segments (right picture). This last tighter criterion is the specification of interest, as it represents the mean allowed error for a single segment. The surface misfigure is specified after the removal of Zernike terms corresponding to power (85%), astigmatism (95%) and trefoil (85%). Additionally, details

151

concerning the tolerances on the edge roll-off are given. The requirement for the edge residual of an individual segment is 200 nm PV wavefront errors.
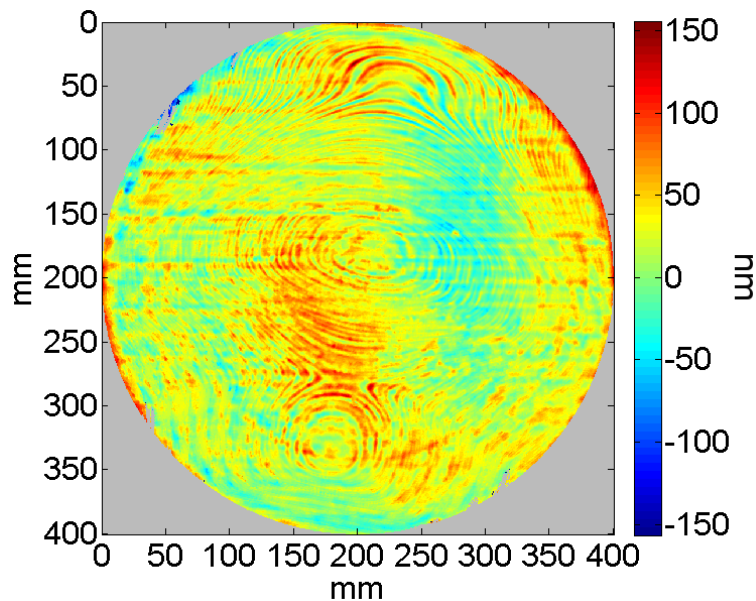
Figure 6-18 Residual figure error map of the ULE mirror at 99% clear aperture and after removal of power, astigmatism and trefoil.

All specified values are considered with respect to a *useful area*, with the edge misfigure evaluated outside such region. In [34], the extension of the useful area is specified as 10 mm to the part outer edge, which corresponds to ~99% of the entire aperture. For the case under study in this section, this threshold condition was applied.

In **Figure 6-18**, the resulting figure error map over the useful area, and after Zernikes removal, is shown. The 85% specification for the power correction couldn't be respected, as the metrology set-up didn't allow accurate focus adjustment. The residual error RMS after these corrections is ~26 nm. Evidently, this doesn't meet the requirements as reported in **Figure 6-17**. If compared with the uncorrected 31 nm RMS, though, this minimal improvement confirms once again that the residual error is not due to low spatial frequencies, but rather to waviness and micro-roughness. Indeed, a closer look at the segment specifications (**Figure 6-17 (right)**) reveals that a complete evaluation should imply the elimination of mid-spatial frequency errors. Approaches for a

minimisation of residual ripples and roughness were discussed in sections 5.2.3 and 6.2: a reassessment of the figuring performance with respect to the E-ELT criteria is therefore recommended after correction of mid- and high spatial frequencies residuals.
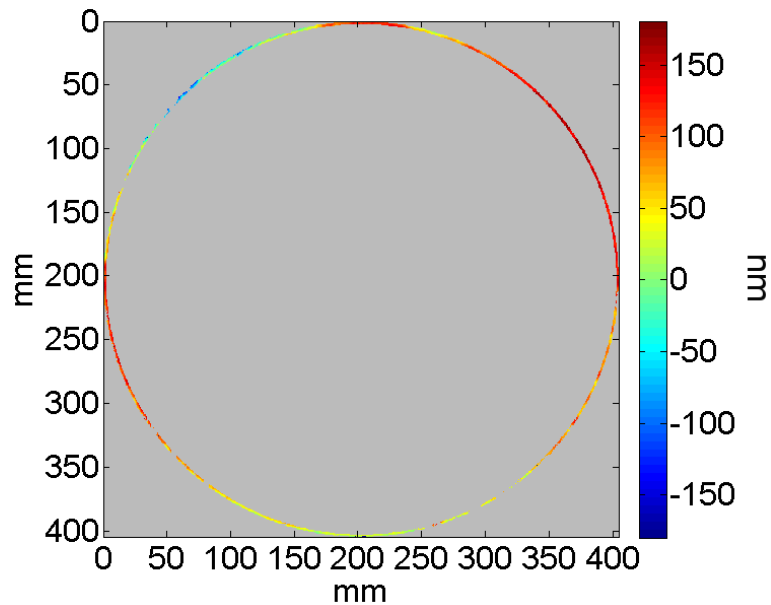
Figure 6-19 Residual edge according to the 99% useful area criterion.

In **Figure 6-19**, the residual edge misfigure outside the useful area is shown. The PV is ~300 nm and doesn't comply with the ESO segment requirement. The edges appear mainly rolled up, as expected from the considerations made in section 6.3. Following the same discussion on edge effects, the method proposed in the previous section is considered suitable for meeting such specifications. This will be object of future work.

6.5 Summary of assessment of the figuring procedure performance

In Chapter 5, the achievement of high quality figure correction results with rapid process convergence was presented. This proved the effectiveness of the RAP figuring technique for large scale ultra-precision optical surfaces. As margin for improvement is still seen, in this chapter it was decided to reanalyse such results through a more critical approach.

This time, the convergence of the process was "unfolded" by means of histograms, plotted for every single iteration step. This investigation showed that the empirical convergence factor (see section 3.1) didn't generate consistent material removal depths, but rather that these are typically correlated to the figure error morphology. From the histograms distributions, though, a range of removal depths likelihood could be recognised and a "figuring recipe" suggested. A histogram analysis of this kind can be a useful tool to assess future improvements of the RAP figuring procedure. It could also be applied to compare the convergence performances of different figuring techniques.

As conventional in surface figure analysis, the waviness on the residual error maps was investigated by means of PSD plots. In particular, a directional average PSD calculation was considered appropriate to highlight the presence of raster tracks. The observed peaks obviously matched the spatial frequencies of the tool-path step lengths; however, additional crests corresponding to half those spatial frequencies could be detected. These are considered to be caused by the overlapping of the staggered pattern during rastering loops at different temperature (see, e.g., **Figure 4-19**). The PSD analysis also confirmed that the application of the pseudo-randomised tool-path was efficient in the case of the small fused silica area, whereas the minimisation of waviness amplitude was less successful on the large ULE surface. This is a consequence of the deeper etching during one particular iteration. Also, the influence of major roughness increase due to the presence of subsurface damage is considered relevant for the PSD analysis of this surface.

Finally, the process performance at the edges of the figure correction regions was evaluated. On the residual error maps, sloped edges caused higher PV values. An assessment of central cross-sections along the tool travelling direction revealed rolled-up edges approximately matching the Gaussian etching footprint profile. Consequently, a single-pass correction approach has been proposed.

As an exercise, a case study has been considered. For this purpose, the E-ELT mirror segments specifications have been applied (within reasonable

approximation) to the final figure error of the ULE mirror. The assessment revealed that, despite being close to requirements, the residual RMS and edges PV values didn't meet such specifications. However, the flash-polishing process proposed for the reduction of waviness and roughness, and the method for edges correction are considered promising approaches for achieving the goal.

7 APPROACHES FOR IN-PROCESS TEMPERATURE ADAPTATION

In this chapter, two methods for compensation of the temperature effects on the etching rates are briefly introduced. The aim of this approach is to unravel the dwell-time – heat flux – etching rates "loop" which is at the basis of the entire process.
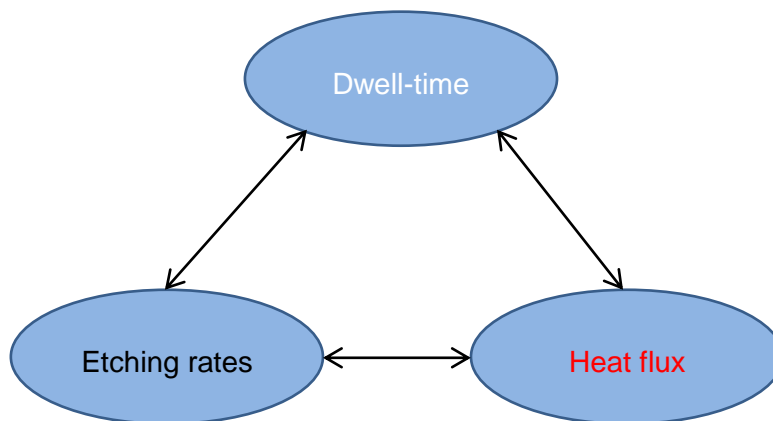
Figure 7-1 The dwell-time – temperature – etching rates "loop" of the plasma figuring process.

Such in-process temperature adaptation of the RAP figuring procedure is considered feasible and advantageous. Achieving a process closer to determinism would further reduce the figuring times and avoid the need for metrology steps after single iterations. Also, it could be beneficial for the minimisation of waviness.

7.1 Feedback mode: in-flight temperature acquisition

The principle behind this approach has been introduced in sections 4.2.3 and 5.2.4, as well as in [14]. The basic idea consists of an in-flight acquisition of the front surface temperature by means of the pyrometer prior to plasma plume traverse (**Figure 7-2**). Some results have been discussed for the case of neutral removal, where the temperature effect on the etching rates is reduced to a two-dimensional problem. Such results, however, don't constitute an actual validation of the method since the depth prediction couldn't be accurate due to the footprint wings.

Therefore, two types of test are proposed to assess this compensation technique. A first simplified case can involve a 2D-figure correction (e.g., cylindrical form): similarly to the neutral removal situation, the speed would be constant along the tool travelling direction and the temperature gradient would occur in the pitch direction. Subsequently, the verification can be extended to the actual three-dimensional figuring, for example by attempting the spherical hollow. For these suggested experiments, some implicit assumptions have been made. Firstly, the temperature gradient over the extension of the etching footprint (~26 mm radius) should be negligible in order to avoid deformations of the Gaussian shape that would significantly affect its figuring performance. Further, a stricter assumption is that the gradient along the travelling direction should be negligible.

From the investigations of section 4.2.3, an approximate etching depth increase of ~1nm/^{o}C can be inferred if one considers the linear range (20 – 80 ^{o}C) of the hot trends. This allows introducing an estimate threshold of acceptable temperature gradient and establishing how often the in-flight acquisition is required. For example, a limit of ~5 ^{o}C over the considered area could be set, as the error would mostly result below the process repeatability. With such a criterion, the 100 mm diameter areas would generally require one central snapshot by means of the pyrometer in order to compensate for the temperature effect. This appears evident from the temperature fields in **Figure 5-17**, where the temperature may result significantly lower only at the extreme peripheral regions of the circular process area (edges). For large scale surfaces, further assessments are needed to determine the most suitable strategy for multiple in-flight acquisitions.

Despite some technical limitations still to overcome (e.g., one pyrometer only, measurements on curved surfaces), prove of concept of the method is expected on areas of 100 – 200 mm diameter. This will involve completion of the heat effect characterisation (hot sinusoidal trenches) and will be object of future work. Also, in forthcoming work, the use of a thermal camera may be

considered as a replacement for the pyrometer, since this would allow monitoring of a wide field of view.
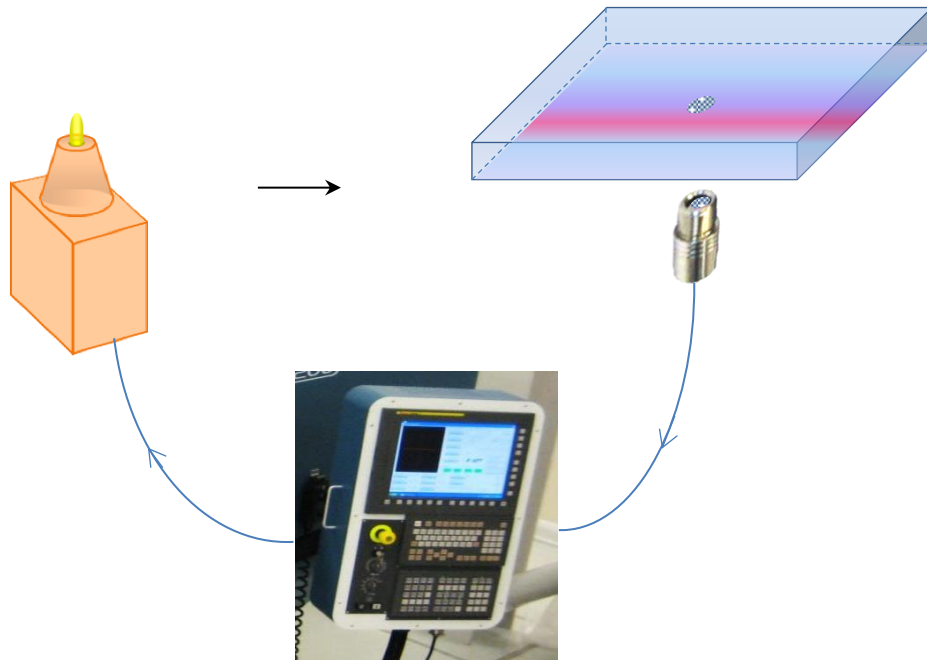
Figure 7-2 Sketch illustrating the principle of in-process adaptation by in-flight temperature acquisition.

With respect to this method, a further question may be raised concerning the temperature distribution induced by the moving heat source along the travelling direction. Simulations for PJM show that a heat tail occurs (**Figure 2-34 (*left*)**) and suggest that the etching will conform to such temperature distribution. While generally correct, this model doesn't appear relevant for the range of speeds considered for the RAP figuring procedure. Such an effect hasn't been detected for any of the results presented in this manuscript.

7.2 Feed-forward mode: heat transfer modelling

In this section, the semi-analytical model described in 2.6 is utilised to simulate the temperature distributions induced by the ICP torch plasma plume moving on a surface. For this purpose, a 200 mm diameter silicon wafer of 0.73 mm thickness was used. On the rear (unpolished) surface, five thermocouples were glued with a welding epoxy at a distance of 20 mm from each other starting

from the disk centre, and perpendicularly to the torch travelling direction. The experimental setup is sketched in **Figure 7-3**. The plasma jet was passed on the front surface at four different velocities (1000, 2000, 3000 and 4000 mm/min), by adopting the usual 1200 W forwarded power and 6 mm stand-off from the surface. Each test was repeated twice. The experimental arrangement was then rotated by 180° and the tests repeated to investigate the symmetry of the heat source distribution.
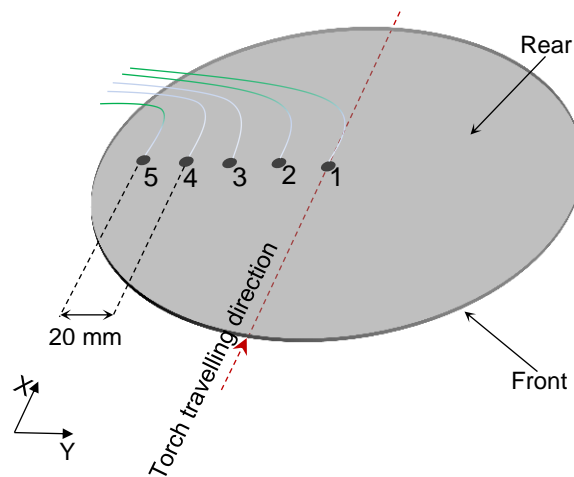
Figure 7-3 Sketch of the experimental setting for heat transfer modelling: silicon wafer of 0.73 mm thickness and 200 mm diameter with the five thermocouples glued along the direction perpendicular to the torch travelling direction.

The acquired maximum temperature values measured by each thermocouple on the back-surface were then plotted versus the sensor position in mm. This is shown in **Figure 7-4**. In **Figure 7-5**, the maximum temperature measured at the central position (sensor 1) is plotted against the correspondent velocity value.

At this point, the numerical integral solution for the Gaussian moving heat source as reported in [159] was applied after implementing a cooling term, as this appears relevant for convective heat phenomena. The integration time was taken equal to the actual travel time on the surface. Also, the Kirchhof transformation (equation (2-15)) was applied for the derivation of the actual temperatures, as the thermal conductivity of silicon is strongly temperature dependent (see also [156]).

This solution resulted accurate enough for reproducing the values of the central sensor as plotted in **Figure 7-5**. However, for other positions across the beam axis, temperature distributions were steadily overestimated. Therefore, in the formula prior or numerical integration, an empirical correction term ~1/y was introduced which accounts for a gradient along the sensors arrangement (see **Figure 7-3**). In **Figure 7-4**, the curves simulated after y-gradient correction are over-plotted to the experimental data and reasonable agreement is found.
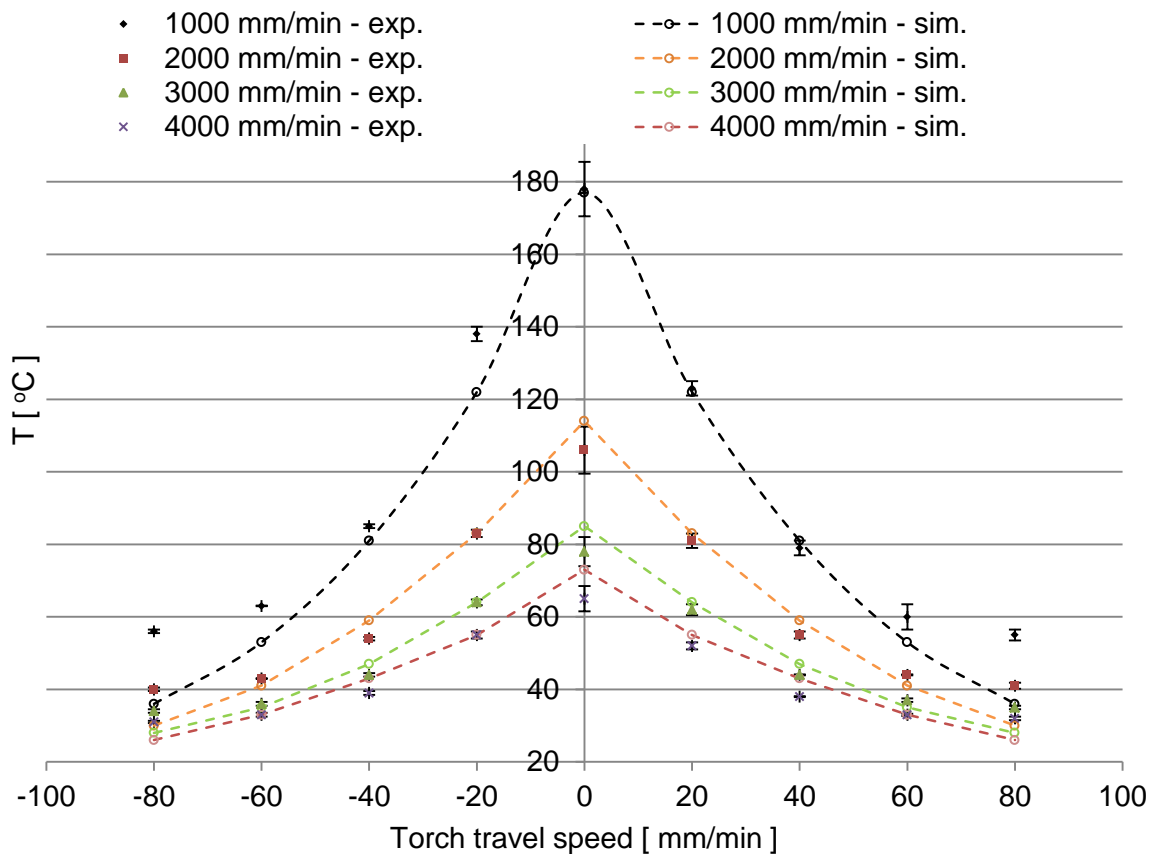
Figure 7-4 Comparison between experimental and simulated temperature distribution across the torch travelling direction for different values of travelling speed at the positions sketched in Figure 7-3.

Some larger discrepancies are still present at the points farther from the centre for the low speed tests. For this simulation, a power of ~4 W with a Gaussian distribution of 50 mm width (*P* and *R* parameters in equation (2-18)) was adopted to reproduce the experimental data.

A justification for the correction term can be based on heuristic considerations. It is possible that the model doesn't account for gas flow dynamics on the surface which may still affect regions distant from the heat source. Also, from an experimental point of view, the heat conduction property of the used thermal glue could be questioned. It is therefore suggested for these tests to be repeated utilising a different epoxy.
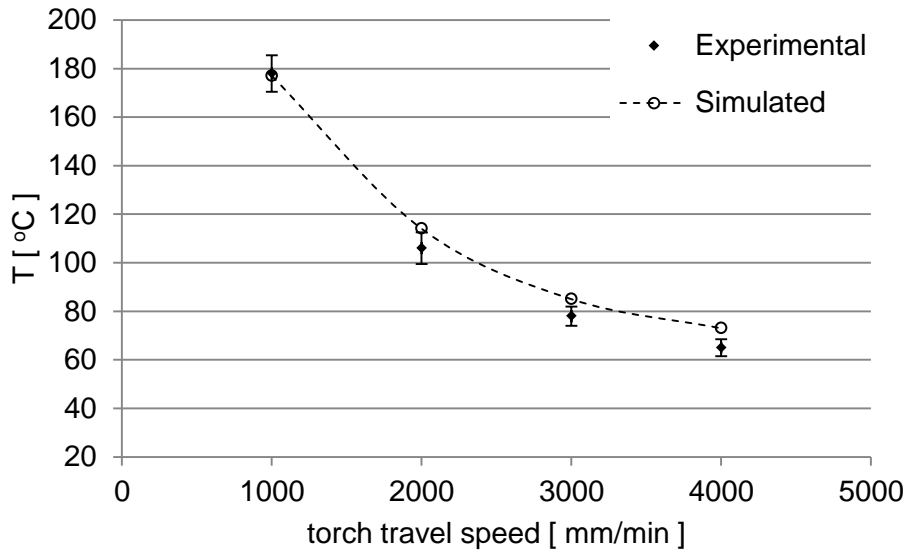
Figure 7-5 Comparison between experimental and simulated velocity dependence of the temperature increase measured at the back of the 0.73 mm thick Si-wafer at position 1 (see Figure 7-3).

The model proposed here is sufficient for predicting the 2D-temperature distribution produced by a single-pass moving heat source at constant speed. For velocity varying along the travel direction a segment-wise solution of the problem can be realised. However, simulation of an actual raster-scanning process is not directly implemented in this model and would require an upgrade to account for multiple passes shifted along the pitch direction. Such an upgrade should also involve validation on different substrate materials and verification of the model approximations.

An adaptive figuring process based on heat transfer simulations would still require the characterisation of etching rate increase with temperature. The

predicted values of local surface temperature could then be exploited to recalculate the velocities before generating the actual CNC code.

7.3 Summary of approaches for in-process temperature adaptation

In this chapter, two approaches have been proposed and discussed that can be used in future for making a figuring process adaptive to surface temperature variations. Such a technique would be very advantageous in terms of shorter processing times, reduction of unwished patterns and elimination of metrology steps.

The first method has been partially investigated in the previous chapters and implies the use of the pyrometer to provide a feedback mode based on in-flight temperature acquisitions of the front surface. This simple approach may be limited only by the arise of significant temperature gradients which would then require multiple measurement along the travel direction.

The second approach would involve simulations of heat transfer phenomena induced by a moving Gaussian source. In this work, a semi-analytical model has been considered based on the discussions of section 2.6. To validate the simulation, single pass tests were carried out on a silicon wafer at different speeds. The temperatures of the back surface were recorded by means of five thermocouples arranged in a line perpendicular to the travel direction of the torch. Comparison between experiments and prediction was successful only after implementing the cooling rate, as well as an empirical gradient correction in the calculation. This last term may rectify for limitations of the model or of the experimental setup.

For both methods, the Arrhenius trends of the material removal rates must be characterised to bring surface temperature and etching depths in relation. Only then will the dwell-time – heat – etching rates loop be unravelled.

8 SUMMARY AND DISCUSSION

The research work reported in this thesis was focussed on the development of a figure correction procedure for the RAP process. The figuring method was tested on the Helios 1200 machine. The results proved the large scale figuring capability and the rapid convergence of the process when combined with the designed procedure. Ultimately, it was demonstrated that the RAP figuring method is at least ten times faster than competing technologies like IBF. This achievement constitutes a major contribution to the field of optical fabrication and promotes the potential introduction of this plasma figuring process into an official novel rapid manufacturing chain.

The progress was initiated by a critical re-characterisation of the material removal properties of the new ICP torch on ULE and fused silica materials. In particular, anomalous steep etching features were investigated. A characterisation by trenches was considered representative of the heat transfer dynamics of the actual process (see also [14]). It was found that lack of etching selectivity can cause several tens of nanometres removal occurring sidewise with respect to the Gaussian footprint (secondary etch zone). Consequently, optimisation of the etching footprint was achieved by identifying forwarded power and stand-off from the surface as the process key parameters. The choice of 6 mm stand-off and 1200 W power minimised the presence of secondary etch zones. Also, the effect of distance from the surface was found to be in agreement with plasma jet spectroscopic analyses carried out by IOM for the PJM process.

During these experiments, unsystematic minor variations of the Gaussian footprint width were observed. However, a correlation to the torch travel speed wasn't found; conversely, a link to the surface temperature is possible (see also Appendix C). It is suggested to perform further trench tests with higher pixel resolution to assess the width parameter.

Afterwards, initial assessments of the surface temperature effects on the etching rates under optimum process conditions were carried out. These

involved the etching of trenches on preheated substrate surfaces for two levels of speed. The resulting plots demonstrated the Arrhenius nature of the process. These tests are considered a starting point for making the process adaptive to surface temperature increase.

Optimisation of the etching footprint revealed itself as a necessary, yet not sufficient condition for the development of a figuring procedure. In fact, even under optimum conditions, the elimination of the secondary etch isn't completely avoidable (except on preheated substrates). Additionally, the progressive heating of the surface during plasma processing was expected to cause divergence of an actual figure correction by influencing the removal rates.

In light of these considerations, developing a temperature adaptive process may appear, in a first instance, as a prime strategy. However, this would require extensive investigations or the Arrhenius trends, accurate surface temperature measurements and, eventually, modelling of heat transfer phenomena. Therefore, such an approach has been only partially pursued in the course of this work. Instead, further "smart" compensation methods were devised to create a converging procedure without in-process adaptation to surface temperature. The first consisted of the design of a dedicated tool-path algorithm. From the investigation of raster-scanning schemes, it was possible to identify staggered meander-type motion paths as capable of delivering homogeneity of surface temperature distribution. If reversed after shifting by a secondary pitch, such raster-patterns would produce neutral removal down to 30 nm PV over a 100 mm diameter area, thus compensating also for side etching. Consequently, this became the tool-path of choice for all figuring processes. Still, the heat effect on the removal rates needed to be contained in order to avoid over-etching. Therefore, an empirical compensation factor was introduced, where only a percentage of the figure error depth would be targeted. Implemented in an iterative figuring procedure, this approach was expected to secure rapid convergence.

The creation of tool-path algorithms still required the calculation of dwell-time/velocity maps. The footprint characterisation established the parameters of

the influence function for such computations. However, it was found that classical deconvolution based on a linear dependence of the removal depth on the dwell-time is not representative of the trends observed for ULE and fused silica. Based on the removal rates characteristic for each material, the mathematical method had to be adapted to deliver the right calculation (depth of a trench). The validity of this modified method was tested by etching a sinusoidal trench in single pass mode. The experiment was successful and a comparison with the predicted shape confirmed the correctness of the computation, as well as of the measured figuring authority of the RAP footprint (trench Gaussian width).

Experimental characterisation and observations and theoretical considerations had delivered the elements for an effective figure correction technique. Following this work, the figuring of small areas was attempted on fused silica substrates. Results were achieved over 100 and 150 mm diameter regions, with residual figure errors ranging between 16 and 31 nm RMS. In the course of these tests, the tool-path staggering step and secondary pitch were varied and their effect investigated. As expected, the choice of smaller steps produced the better results. The residual error maps also presented a waviness caused by the raster-scanning print-through. Mid-spatial frequency features due to the tool-path are a known issue of figuring processes. The use of smaller tool-path steps on the 150 mm diameter areas reduced the problem. However, an attempt of further improvement was made by introducing a pseudo-randomisation effect. To obtain such an effect, the staggering step size should be varied over subsequent iterations. One example result was attained on a fused silica area of 100 mm diameter. The ameliorations brought by modifying the tool-path parameters were later confirmed by PSD analysis.

Together with the high quality residual error maps, the significant achievement was the rapid processing time. Indeed, a maximum of three iterations of less than seven minutes duration each were required to process surfaces up to 150 mm diameter. These very promising results, though, needed to be confirmed for large scale surfaces. For this purpose, a ULE substrate of 420mm x 420mm x

40mm was prepared. One of its large square surfaces hosted a 3 m ROC concave spherical mirror, with a clear aperture of 405 mm. The figure correction was carried out following the designed procedure, and applying the pseudo-random method. A first figuring cycle composed of three iterations delivered a 43 nm RMS residual figure error, starting from a 373 nm RMS initial error map. Re-polishing of the surface to restore the texture required a second figure correction cycle, as the form accuracy had deteriorated. After two iterations, a 30 nm RMS residual error was achieved. The processing times resulted as 50 minutes per iteration. For a two-iteration process run on a meter-scale surface, this confirms the possibility of completing the figuring in about ten hours. Such an achievement makes this plasma figuring technique competitive versus state-of-the-art technologies, potentially replacing them in a novel manufacturing chain for large optics. In fact, the reported process durations for polishing or ion beam techniques are still in the range of several tens if not hundreds of hours.

In the RAP process, the chemical nature of the material removal is known to cause an increase in roughness. White light interferometry measurements of the processed fused silica surfaces revealed characteristic texture deterioration up to 7 – 8 nm S_q. Even higher values are expected on ULE. Therefore, an effective optics finishing system should associate a flash-polishing process to RAP figuring. Such process is currently in the development phase at Cranfield. The additional duration for the post-RAP polishing should then be accounted for in a complete evaluation of the finishing stage.

Finally, the figuring results were subject to detailed discussions. These involved PSD analysis of the residual error map to investigate the waviness, process convergence inspection by means of histograms and considerations on residual edge effect. As expected, the Power Spectral analysis showed the presence of peaks corresponding to the main tool-path spacing; also, it highlighted the benefits of the pseudo-randomisation method, although this wasn't fully successful in the case of the ULE mirror. In this case, the strong texture deterioration due to subsurface damage was considered a significant limitation for the reduction of mid-spatial frequency patterns. However, for residual

waviness reduction margin for improvement is still seen. A more effective application of the pseudo-randomisation should try to balance off the rippled patterns caused by single iterations. Also, the efficiency of a post-RAP polisher on mid-spatial features should be evaluated.

The histogram analysis constituted a method to investigate the effective figure error removal per iteration and its distribution with respect to the target. It also allowed defining a "recipe for figure correction". In future, improvements of the plasma figuring methods can be assessed by histograms to evaluate their closeness to determinism.

Another important evaluation concerns the performance of RAP figuring at the periphery of the metrology area. Typically, the final figure error maps showed rolled-up edges due to the heat cumulated towards the centre of the figured regions. This boundary misfigure, which is not correlated to the actual workpiece edge, was estimated in the order of ~150 nm PV. An edge corrective algorithm has been proposed where the plasma plume runs along the periphery by matching the edge slope. This method could also be utilised for minimising edge roll-off effects of polished surfaces. In case of steep edges, smaller beam footprints would be needed. Techniques for the generation of etching footprints with efficiency over a higher spatial frequency range are currently under study.

For exemplificative purposes, E-ELT segments specifications were adopted as a case study and applied to the final figure error of the ULE mirror. While requirements were not fully met by the unpolished residual map, this investigation confirmed that mid- and high spatial frequencies features were the dominant factor influencing the residuals. It was therefore suggested to reassess the surface after CNC polishing.

As a final point, heat transfer phenomena and in-process adaptation to surface temperature increase were discussed. The thermal assessments (1D and 2D) qualitatively indicated homogeneity of surface temperature, but also a stepwise temperature increase related to the tool-path reversal loops. As a first approach, a velocity correction algorithm based on in-flight temperature acquisition by means of the pyrometer was proposed. This method would require completion

of the heat effects characterisation (sinusoidal hot trenches). Proof of concept is soon expected on small (100 mm diameter) areas; scaling-up of the technique will require considering the needed frequency of sensor readings. Several benefits are seen for a temperature adapted figuring procedure. While reducing the processing times, this method is expected to minimise the residual waviness caused by the temperature increase over consecutive tool-path loops. Also, the elimination of metrology steps between iterations could be achieved if the figure error removal became more predictable.

In this PhD project, FEA modelling of RAP heat transfer phenomena wasn't carried out. Numerical simulations were developed in a parallel work. Due to disproportionate computational times, a large optics figure correction strategy based on simulations isn't considered feasible. During the concluding stage of this research, a semi-analytical model has been proposed and investigated. Despite the need for approximations and corrections made for this model, calculations can be rapidly completed. First verifications versus experimental data delivered promising results. Further studies of the RAP process heat phenomena will be object of future work.

8.1 Some cost considerations

The main achievement of this PhD work has been the one of proving that surface figuring by the RAP process is indeed much faster than with other technologies. As mentioned in the introduction to this thesis, this has significant economic implications when considering the costs involved for the finishing an ultra-precise optical surface (~ 31 nm RMS). To highlight this aspect, in this section a price comparison based on quotations by Cranfield University Precision Engineering plus two external optics manufacturers has been drafted. For this evaluation, production of a 420mm x 420mm x 40mm mirror like the one utilised in this work is taken as an example. The final figure error requirement was 31 nm RMS.

The cost of blank material was assumed as comparable for all manufacturers. Afterwards, costs have been subdivided by process (grinding, polishing and figuring). The figuring stage is, obviously, the main base for comparison. For the

external manufacturers, polishing and figure correction ought to take place simultaneously and are therefore reported as one cost unit.

Table 8-1 Costs comparison for the finishing of the 420mm x 420mm x 40mm ULE optic.

	Manufacturer		
Cost unit	CVI Melles-Griot*	Oldham Optical	CU Precision Engineering
Material	£ 4000 (fused silica – Zerodur – Clearceram)	£ 4000 (ULE)	£ 4000 (ULE)
Grinding	£ 5600	£ 1750	£ 1000 (BoX)
Polishing	£ 5600	£ 2250	£ 750 (Hand polishing)
Figuring			£ 350 (Helios 1200)
Total	£ 15200	£ 8000	£ 6100

In one case (CVI), different quotations for three materials were given without specifying single unit's costs. Therefore, an average total cost has been taken as an estimate and subsequently split as shown in **Table 8-1**. For all manufacturers, labour and metrology costs per hour are included and considered comparable. Therefore, the costs difference follows essentially from the processing time.

Tooling costs are also included. In the RAP process, such consumables are considered as follows:

- 1 bottle of 10.41 m^3 10% SF_6/Ar mixture: £ 299.00 - usage: 1 bottle every 4-6 years.
- 1 bottle of 10.41 m^3 Argon (99.999% purity): £ 17.00 - usage: 1 bottle per month.
- 1 main quartz tube (cylindrical, 110 mm length, 20 mm Ø): £ 7.50 - usage: 1 tube every three months.
- Gas detectors cartridge: three units at £ 200.00 for a 24 months lifetime each.

The costs comparison is summarised in **Table 8-1**. It is evident that Cranfield University Precision Engineering is capable of delivering a more competitive price thanks to the speed of the grinding and figuring processes. The current in-house development of a flash polisher would contribute to further cost reduction. Clearly, a significant price gap exists between the two external manufacturers. This can depend on whether the component is considered as standard or as one-off part by the company.

Further, it must be noted that the optic considered in this example has a spherical geometry which facilitate machining by sub-aperture contact processes. A raise in costs would directly follow in the case of aspherics as these are seen as a major challenge for polishing due to tool misfit. For RAP figuring, the geometry of a low gradient surface is irrelevant; hence no cost raise would be issued.

An additional financial advantage can be envisaged if the machine cost is considered. Helios 1200 costs £ 1'500'000 . The price for a large scale polishing facility is comparable, while an IBF machine with a 3 – 4 m^3 vacuum chamber can be estimated around £ 2'500'000.

In conclusion, on the basis of an actual component manufacturing, this evaluation has highlighted how the plasma figuring technique and procedure would contribute to a drastic time and costs reduction within an optics fabrication chain.

9 CONCLUSIONS AND CONTRIBUTIONS TO KNOWLEDGE

Objective I: Tool-footprint characterisation – Assessment of the etching footprint performance and identification of its suitability to figuring and any need for optimisation.

The characterisation work discussed in section 4.2.1 showed that a 6 mm stand-off distance between torch nozzle and substrate surface and 1200 W forwarded power deliver the most advantageous process conditions for the ICP torch mounted on Helios 1200. This conclusion follows from the measured enhancement of the primary near-Gaussian etching footprint as opposed to the minimisation of the secondary etch zone when adopting these optimum parameters.

Further, it was observed that the secondary etch region cannot be completely eliminated when etching a trench on a sample surface at 20 ^{o}C initial temperature. This phenomenon is considered linked to lack of etching anisotropy, chemistry evolution along the plasma plume axis, but also gas flow dynamics transporting etchant along the surface. Hence, the presence of the secondary etch removal implies that additional correction or compensation will be required when attempting neutral removal or figuring. It was concluded that this issue needed to be taken into account in the design of the tool-path algorithm. As a further conclusion, it is worth considering an improved torch design that should address gas flow dynamics and power issues in an attempt to eliminate the secondary etch region.

Objective II: Tool-path algorithm – Design of process dedicated tool motion path and development of dwell-time calculations to determine the demanded tool velocity.

Once the optimum parameters were established (with fixed etchant concentration) the dependency of the etching depth on tool scanning speed was characterised in a range between 1000 and 5000 mm/min. Such a characterisation is necessary as it delivers the input for the calculation of the

dwell-time/velocity maps utilised to drive the tool during a figuring process. This part of the investigation identified a non-linear trend of etching depth versus time. From this it follows that classical deconvolution mathematical methods need an adaptation whenever a substrate material presents non-linear etching rates. Such modified calculations were indeed introduced in this work. These were validated by the sinusoidal trenches experiments. In all these investigations, no conclusive evidence was found concerning the variation of trenches width.

For the design of the tool-path algorithm, achievement of a neutral removal over a defined area was used as a test bench. Here, the presence of the secondary etch region and the etch rate increase due to heat effects was observed to generate linear slopes when raster-scanning the surface and adopting a repositioning main step larger than 5 mm. From this observation a new kind of tool-path, named reversed staggered-rastering, was introduced and neutral removal attained down to <30 nm PV. From these results, as well as from in-flight surface temperature measurements, it was concluded that this tool motion path was capable of achieving a more uniform etch and heat distribution. Hence, it has become the tool-path of choice for the entire figuring work.

Objective III: Investigation of surface temperature effects on the etching rates and of surface temperature gradients – Consideration of an in-process adaptation to temperature variations.

The Arrhenius nature of the RAP process was investigated by means trenches etched on pre-heated fused silica substrates both at constant and varying speed. The front surface temperature was recorded, prior to torch traverse, with a pyrometer located 16 cm from the plume centre. This experimental setup didn't allow determining the actual etching temperature. From these investigations, it emerged that the etching depth can grow to more than 150% in the range between 20 and 85 ^{o}C. Further, the test with varying torch speed (sinusoidal hot trench) highlighted the fact that the percentile increase can depend on the plume velocity. It is therefore recommended to adopt this kind of

test over a broader range of temperatures for a complete characterisation of heat effects.

Surface temperature gradients were assessed for the cases of neutral removal and small scale figuring. These qualitative investigations revealed homogeneity of temperature within less than 20 ^{o}C over a 100 mm diameter area, and better than 10 ^{o}C if considering the same extension along the scanning direction. This gradient is even smaller (~5 ^{o}C) if taken over the size of the etching footprint. These results conclude that the selected tool-path does promote surface temperature homogenisation and that, thanks to this, thermal gradients are negligible and do not affect the shape of the influence function.

In light of these results, the development of a temperature adapted process is considered possible. Based on the characterisation of the heat effect on the etching rates, both feedback and a feed-forward approaches were explored as solutions in this work. The first is based on utilising the pyrometer in a closed-loop fashion and correcting the travelling speed values in-flight, while the second relies on modelling of heat transfer. Since both methods would require further extensive investigations and would add to the complexity of the final algorithms, they were not further pursued in this PhD. Therefore, conclusions on their effectiveness cannot be drawn. Instead, an error compensation method based on iterative convergence was chosen.

Objective IV: Development of a converging figuring procedure, based on the outcomes of the previous three objectives – Small scale proof of concept with particular focus on processing times, form accuracy and finish roughness.

This objective was attained by combining the newly designed tool-path and modified dwell-time calculations into an iteratively converging figuring procedure. The considerations on minimisation of temperature gradients (objective III) further supported this choice. The heat effect on the removal rates was contained through the introduction of the thermal compensation coefficient. Proof of concept was achieved in a repeatable manner on fused silica surfaces of 100 and 150 mm diameter, where residual figure errors of 16 – 31 nm RMS were obtained after a maximum of three iterations of less than 7 minutes each.

These results conclude that the introduced procedure was suitable both in terms of form accuracy and of processing time requirements, as stated in the research goal.

Residual raster tracks and rolled-up edges were still observed on the final error maps for all figuring tests described in this thesis. These are considered the consequence of heat effects. A promising solution consisting of a single pass along the surface boundary is proposed to correct the error at the edge. Since this method wasn't tested no conclusion can be drawn. A pseudo-randomisation approach, similar to one used in MRF, was chosen to minimise the raster-scanning marks and was tested on a 100 mm diameter fused silica surface. From the PSD analysis of the residual maps, it can be concluded that this method is effective at reducing residual waviness. Combined with convergence factors of ~25 and 50% over two iterations, as indicated by a histograms analysis of the residual maps, this approach provides an improvement to the designed figuring procedure. A different solution to mid-spatial frequencies could be seen in a temperature adapted process or in the use of smaller etching footprints.

Further, a white-light interferometry investigation of the 100 mm diameter areas showed that minor roughness deterioration with an average of ~7 nm RMS occurs after figuring. This result complies with the roughness level specified in the research goal. It is concluded that a "flash" post-RAP polishing process would rapidly restore the surface texture to ~1 nm RMS. The roughness increase is due to the chemical nature of the process, but also to possible re-deposition on the surface. A deeper knowledge of the composition of such contaminants by elemental analysis may help reducing the texture deterioration.

Objective V: Scaling up of the process – Demonstration of the research aim achievement.

This objective was achieved by the figure correction of the 405 mm diameter ULE surfaces. In this case, two figuring tests were carried out and proved the effectiveness of the devised figuring procedure on a large scale surface. The final topography maps presented 43 and 31 nm RMS residual error. These

results showed that a processing time of ~50 min/iteration is sufficient to correct ~1 μm PV figure error over the aforementioned area. From this, it can be concluded that a metre-sized optical surface would require 10 hours to be figured within two iterations. This last result demonstrates that the research aim has been achieved.

The major contributions to knowledge by this research are:

- Demonstrating, for the first time, fast figure correction of large optical surfaces by the RAP process. In particular, it was proved that this plasma figuring method can fulfil the process time requirements of the new large optics manufacturing chain. This production engineering result constitutes a major advance and contribution to optical fabrication.

- Study and development of a rapidly converging figuring procedure. This was achieved through the design of a novel tool-path with pseudo-randomisation upgrade, the use of adapted dwell-time calculations, as well as through the optimisation of a convergence strategy.

- Identification of etching irregularities in the footprint and optimisation of the process parameters. These investigations delivered a better understating of some aspects of the etching process and contributed to the tool-path design. They also opened new questions and perspectives in terms of torch design.

- Investigations of the effects of surface temperature on the etching rates. These tests quantified the Arrhenius nature of the process, introducing also a new type of characterisation, and laid the foundation for a temperature adapted figuring approach.

- Post-process roughness, waviness and edge effects investigations. These indicated minor surface texture deterioration and the presence of raster-scanning tracks and rolled-up edges in the residual error maps. Potential solutions were identified in a flash polishing process, as well as in the use of thinner etching footprints.

10 RECOMMENDATIONS FOR FUTURE WORK

The research work conducted during the PhD project reported in this manuscript has produced the very first large scale results of optical surface figuring by Reactive Atom Plasma on a production machine. In particular, it has been demonstrated that form accuracy of 31 nm RMS can be attained about ten times faster than competing technologies (e.g., IBF). The contribution to knowledge in the sector of optical fabrication is therefore significant. And yet, these same results open future investigation perspectives that are due both to the need, but also and in particular to the potential for further improvements.

The priority of current and future work is, once again, the upscale of the process, the ultimate target being a 1.4 meter hexagonal segment for E-ELT type telescopes. Helios 1200 has got only a 1.2 meter capability, having been designed before the final definition of segments size. Figure correction of a 1 meter diameter optical surface is therefore likely to become the first demonstration for such scale. So far, scale dependent hindrances haven't been met. Surface heat gradients, misalignments due to thermal issues or process related inconsistencies are therefore not expected even for meter-class substrates. Nevertheless, only completion of the task will allow putting aside some residual scepticism still surrounding this figuring technique.

Despite the successful optimisation of the footprint, the mechanisms behind the generation of a secondary etch region haven't been fully explained. Therefore, in future, further possible causes (e.g., plasma flow along the substrate surface or etch undercut related phenomena) should be considered and explored, together with an improved torch design.

It goes without saying that a polishing process is required to work together with the RAP. A cost-effective optical finishing system will need a synergic coordination of the two techniques, where the performance of the one will inevitably affect the other and ultimately influence the quality of the optical surface. For instance, if successful roughness level restoration can be easily

expected after polishing, it is not obvious that the figure accuracy achieved by plasma figuring will be maintained. Therefore, a finer figure correction shall reduce the number of alternations between the two processes. At the same time, the starting condition of the pre-polished surface is also bound to affect the RAP performance. Also, residual waviness and edge effect currently appear as one of the factors affecting the final figure error. Strategies for ameliorations should be implemented for both techniques to reduce production times and costs.

Increasing interest for the figure correction of silicon and SiC optical surfaces is quickly leading to an imminent application of the RAP technique on these kinds of substrates. For these materials, differences in thermal properties and etching rates with respect to glass substrates are well known. The higher thermal diffusivity of both materials is generally seen as an advantage to reduce heat effects. Silicon carbide, however, is chemically very stable and the low etching rates together with the high energy dissipation may raise some concern about the process speed for this material. Pre-heating of the substrate has been suggested, but direct application of the process is also worth attempting. The novel hybrid process called LAPP is seen as a potential solution for SiC processing, as it can input the required activation energy for an efficient etching rate.

This PhD research has not been focussed on processing of glass-ceramics like Zerodur or Clearceram. Indeed, Reactive Atom Plasma had already been shown to be rather inefficient on these kinds of materials. Should RAP become the figuring technology of preference, this will have future implications in the optics market for the choice of substrate material.

The application of RAP as a sub-aperture figuring tool would have a broader range if different sizes of influence function were available. One way of achieving this is the introduction of smaller nozzles or torches altogether. These modifications are currently being considered together with the LAPP process, both with the purpose of reshaping the etching footprint. Combined with the

strategies discussed in this thesis, the use of finer influence functions would be beneficial for the minimisation of edge roll-off and residual waviness.

In parallel to the actual plasma processing, studies on heat transfer phenomena and related simulations are still in progress. A brief discussion has been presented in this manuscript, but deepening of the topic and upgrading of models are needed. More understanding of the temperature effects and the discussed in-process adaptation could bring the process closer to determinism, thus improving its cost-effectiveness.

Some work about the use of different reactive species on different substrate materials and on the addition of oxygen to the mixture can be suggested. These would have the purpose of increasing the removal rates and reducing re-deposition traces that can sometimes still be observed after a process (e.g., on ULE).

Besides the figuring application of the technology, Reactive Atom Plasma could also be utilised as a safer alternative to acid-etching for subsurface damage reduction. Combined with the polishing, this would see the plasma method useful also in the immediate post-grinding stage.

In conclusion, the research carried out in this PhD has brought an embryonic technology to a near-commercial status. It is now imperative that efforts are focalised on pursuing its implementation into a manufacturing chain, while optimising the achieved performance.

REFERENCES

[1]   Fanara, C., Shore, P., Nicholls, J.R. (2007), *Ultra Precision Energy Beam Technology for rapid fabrication of new photonic surfaces*, IMRC Report, Part 2: Case for Support, pp. 1 – 8.

[2]   Shore, P., Parr-Burman, P. (October 2003), *Large Optics Manufacturing Study (LOMS),* Report to UK DTI.

[3]   Hallock, B., Shorey, A. and Courtney, T. (2005), "Cycle time and cost reduction in large-size optics production", in: *Optical Manufacturing and Testing VI, Proc. of SPIE,* vol. 5869, 31 July - 1 August 2005, San Diego CA, SPIE, Bellingham WA, art. no. 58690D, pp. 1 – 11.

[4]   Messner, W., Hall, C., Dumas, P., Hallock, B., Tricard, M., O'Donohue, S., Miller, S. (2007), "Manufacturing meter-scale aspheric optics", in: *Optical Manufacturing and Testing VII*, *Proc. of SPIE*, vol. 6671, 28 – 29 August 2007, San Diego CA, SPIE, Bellingham WA, art. no. 667106, pp. 1 – 8.

[5]   Hänsel, T., Frost, F., Nickel, A. and Schindler, A. (2007), "Ultra-precision surface finishing by ion beam techniques | Ultragenaue Oberflächen-endbearbeitung Mittels Ionenstrahltechniken", *Vakuum in Forschung und Praxis,* vol. 19, no. 5, pp. 24 – 30.

[6]   Gailly, P, Fleury-Frenette, K., Lecat, J.-H., Collette, J.-P., Defise, J.-M., "Ion beam figuring for precision optics", SPIE Newsroom IDx2364 (2008), available at: http://spie.org/x23641.xml?ArticleID=x23641.

[7]   Shanbhag, P. M., Feinberg, M. R., Sandri, G., Horenstein, M. N. and Bifano, T. G. (2000), "Ion-beam machining of millimeter scale optics", *Applied Optics,* vol. 39, no. 4, pp. 599 – 611.

[8]   RAPT^{TM} Industries Inc. (2011), *RAPT Industries – Rapid Damage-Free Precision Surface Engineering*, available at: http://www.raptindustries.com (accessed 13 July 2012).

[9]   Carr, J.W., RAPT Industries Inc., (2009) *Method for Atmospheric Pressure Reactive Atom Plasma Processing for Surface Modification,* US Pat. 7,591,957 B2.

[10]   Subrahmanyan, P. K. and Gardopée, G. (2008), "Reactive atom plasma (RAP™) processing of mirrors for astronomy", in: *Advanced Optical and Mechanical Technologies in Telescopes and Instrumentation, Proc. of SPIE,* vol. 7018, 23 – 28 June 2008, Marseille (F), SPIE, Bellingham WA, art. no. 701809, pp. 1 – 12.

[11]   Fanara, C., Shore, P., Nicholls, J. R., Lyford, N. and Kelley, J. (2006), "A new Reactive Atom Plasma Technology (RAPT) for Precision Machining: The Etching of ULE$^{®}$ surfaces", *Advanced Engineering Materials,* vol. 8, no. 10, pp. 933 – 939.

[12]   RAPT Industries Inc. (2010), *Cold Torch Performance* (Confidential Communication).

[13] O'Brien, W. (2011), *Characterisation and Material Removal Properties of the RAP^{TM} Process* (PhD thesis), Cranfield University, Cranfield (UK).

[14] Castelli, M., Jourdain, R., McMeeking, G., Morantz, P., Shore, P., Proscia, D. and Subrahmanyan, P. (2010), "Initial strategies for 3D RAP Processing of Optical Surfaces Based on a Temperature Adaptation Approach", in: *Proc. of the 36th MATADOR Conference*, section 18, 14 – 16 July 2010, Manchester (UK), Springer, London, pp. 569 – 572.

[15] Jourdain, R., Castelli, M., Shore, P., Subrahmanyan, P. (2010), "Process characterisation and key tasks for cost-effective 3D figuring of specular surfaces using RAP", in: *Proc. of the International Conference of the European Society for Precision Engineering and Nanotechnology*, vol. 2, 31 May – 4 June 2010, Delft (Netherlands), EUSPEN, Cranfield, pp. 185 – 188.

[16] Castelli, M., Jourdain, R., Morantz, P., Shore, P. (2012), "Reactive Atom Plasma for rapid figure correction of optical surfaces", in: *6th International Congress on Precision Machining (ICPM2011), Key Engineering Materials,* vol. 496, 13 – 15 September 2011, Liverpool (UK), Trans Tech Publications, Zürich (CH), pp. 182 – 187.

[17] Jourdain, R., Castelli, M., Shore, P., Morantz, P. (2011), "Fast 3D Figuring of Large Optical Surfaces Using Reactive Atom Plasma (RAP) Processing", in: *Proc. of the International Conference of the European Society for Precision Engineering and Nanotechnology*, vol. 2, 23 – 27 May 2011, Como (I), EUSPEN, Cranfield, pp. 406 – 408.

[18] Castelli, M., Jourdain, R., Morantz, P., Shore, P. (2012), "Rapid Optical Surface Figuring Using Reactive Atom Plasma", *Precision Engineering*, vol. 36, no. 3, pp. 467 – 476.

[19] National Ignition Facility (NIF) (2011), *NIF - National Ignition Facility & Photon Science - Bringing Star Power to Earth*, available at: https://lasers.llnl.gov/ (accessed 25 May 2011).

[20] Moses, E. I. (2010), "The National Ignition Facility and the National Ignition Campaign", *IEEE Transactions on Plasma Science,* vol. 38, no. 4, pp. 684 – 689.

[21] Campbell, J.H., Hawley-Fedder, R.A., Stolz, C.J., Menapace, J.A., Borden, M.R., Whitman, P.K., Yu, J., Runkel, M., Riley, M.O., Feit, M.D., Hackel R.P. (2004), "NIF optical materials and fabrication technologies: An overview", in: *Optical Engineering at the Lawrence Livermore National Laboratory II: The National Ignition Facility*, *Proc. of SPIE*, vol. 5341, 28 January 2004, San Jose CA, SPIE, Bellingham WA, pp. 84 – 101.

[22] BIbeau, C., Wegner, P. J., Moses, E. I ., Warner, B. E. (2006), "Generating powerful ultraviolet beams with the world largest laser", *Laser Focus World*, vol. 42, no. 6, pp. 113 – 117.

[23] CEA (2012), *Le Laser Mégajoule – Direction des Applications Militaiers*, available at: http://www-lmj.cea.fr/index-en.htm (accessed 11 June 2012).

[24] Besnard, D. (2007), "The megajoule laser program — ignition at hand", *The European Physical Journal D*, vol. 44, pp. 207 – 213.

[25] HiPER (2011)*, HiPER - Laser Science for our future...*, available at: http://www.hiper-laser.org/index.asp (accessed 23 May 2011).

[26] Rivera, A., Garoz, D., Juarez, R., Alvarez, J., González-Arrabal, R., Perlado, J. M. (2011), "Lifetime of silica final lenses subject to HiPER irradiation conditions", in: *High Power Lasers for Fusion Research, Proc. of SPIE*, vol. 7916, 25 – 27 January 2011, San Francisco CA, SPIE, Bellingham WA, art. no. 79160S, pp. 1 – 12.

[27] Stahl, H.P. (2004), "Optic Needs for Future Space Telescopes", in: *Optical Manufacturing and Testing V, Proc. of SPIE*, vol. 5180, 3 – 5 August 2003, San Diego CA, SPIE, Bellingham WA, pp. 1 – 5.

[28] Kendrick, S.E. (2009), "Monolithic versus segmented primary mirror concepts for space telescopes", in: *Optical Manufacturing and Testing VIII, Proc. of SPIE*, vol. 7426, 4 – 5 August 2009, San Diego CA, SPIE, Bellingham WA, art. no. 74260O, pp. 1 – 12.

[29] MacEwen, H. A. (2004), "Separation of functions as an approach to development of large space telescope mirrors", in: *UV/Optical/IR Space Telescopes: Innovative Technologies and Concepts, Proc. of SPIE,* vol. 5166, 3 – 5 August 2003, San Diego CA, SPIE, Bellingham WA, pp. 39 – 48.

[30] Ubertini, P., Gehrels, N., Corbett, I., De Bernardis, P., MacHado, M., Griffin, M., Hauser, M., Manchanda, R. K., Kawai, N., Zhang, S. N., Pavlinsky, M. (2012), "Future of Space Astronomy: A global Road Map for the next decades", *Advances in Space Research*, vol. 50, no. 1, pp. 1 – 55.

[31] Gilmozzi, R. (2004), "Science and technology drivers for future giant telescopes", in: *Ground-based Telescopes, Proc. of SPIE,* vol. 5489, 21 – 25 June 2004, Glasgow (UK), SPIE, Bellingham WA, no. 1, pp. 1 – 10.

[32] European Southern Observatory (ESO), "The European Extremely Large Telescope ("E-ELT") Project", available at: http://www.eso.org/sci/facilities/eelt/ (accessed 22 February 2012).

[33] Gemini Observatory, "Gemini Observatory – Exploring the Universe, Sharing its Wonders", available at: http://www.gemini.edu/ (accessed 23 February 2012).

[34] European Organisation for Astronomical Research in the Southern Observatory (2009), Specifications for the call for tenders "supply of 7 prototype segments of the 42 m diameter E-ELT primary mirror at a firm fixed price of € 5.000.000", E-SPE-ESO-300-0150(4).

[35] TMT Project, "Thirty Metre Telescope", available at: http://www.tmt.org/ (accessed 22 February 2012).

[36] Nelson, J., Sanders, G. H. (2008), "The Status of the Thirty Meter Telescope Project", in: *Ground-based and Airborne Telescopes II, Proc. of*

SPIE, vol. 7012, 23 – 28 June 2008, Marseille (F), SPIE, Bellingham WA, art. no. 70121A, pp. 1 – 18.

[37] GMTO Corporation, "Giant Magellan Telescope", available at: http://www.gmto.org/ (accessed 22 February 2012).

[38] Shectman, S., Johns, M. (2010), "GMT overview", in: *Ground-Based and Airborne Telescopes III, Proc. of SPIE,* vol. 7733, 27 June – 2 July 2010, San Diego CA, SPIE, Bellingham WA, no. 1, art. no. 77331Y, pp. 1 – 11.

[39] European Southern Observatory (ESO), "OWL – The ESO 100-m optical telescope concept", available at: http://www.eso.org/sci/facilities/eelt/owl/ (accessed 22 February 2012).

[40] Lightsey, P. A., Atkinson, C., Clampin, M., Feinberg, L.D. (2012), "James Webb Space Telescope: Large deployable cryogenic telescope in space", *Optical Engineering*, vol. 51, no. 1, art. no. 011003, pp. 1 – 19.

[41] Postman, M., Brown, T., Sembach, K., Giavalisco, M., Traub, W., Stapelfeldt, K., Calzetti, D., Oegerle, W., Rich, R. M., Stahl, H. P., Tumlinson, J., Mountain, M., Soummer, R., Hyde, T. (2010), "Science drivers and requirements for an *Advanced Technology Large Aperture Space Telescope* (ATLAST): Implications for technology development and synergies with other future facilities", in: *Space Telescopes and Instrumentation 2010: Optical, Infrared, and Millimeter Wave, Proc. of SPIE,* vol. 7731, 27 June – 2 July 2010, San Diego CA, SPIE, Bellingham WA, art. No. 77312K, pp. 1 – 12.

[42] Shore, P., Cunningham, C., Debra, D., Evans, C., Hough, J., Gilmozzi, R., Kunzmann, H., Morantz, P., Tonnellier, X. (2010), "Precision engineering for astronomy and gravity science", *CIRP Annals - Manufacturing Technology*, vol. 59, no. 2, pp. 694 – 716.

[43] Wu, B. and Kumar, A. (2009), "Extreme Ultraviolet Lithography: Towards the Next Generation of Integrated Circuits", *Optics & Photonics - focus,* [Online], vol. 7, no. 4, pp. 25 April 2010 available at: http://www.opfocus.org/index.php?topic=story&v=7&s=4.

[44] Carl Zeiss SMT AG (2011)*, Lithography: Controlled Light for Minute Circuits*, available at: www.zeiss.de (accessed 15 June 2011).

[45] Carl Zeiss SMT AG (2011)*, Lithographische Systeme - Optiken fuer EUV-Lithographie*, available at: www.zeiss.de (accessed 15 June 2011).

[46] SCHOTT AG (2011)*, Schott AG*, available at: http://www.schott.com (accessed 21 June 2011).

[47] Döhring, T., Hartmann, P., Jedamzik, R., Thomas, A., Lentes, F-T. (2006), "Properties of Zerodur Mirror Blanks for Extremely Large Telescopes", in: *2nd International Symposium on Advanced Optical Manufacturing and Testing Technologies: Large Mirrors and Telescopes, Proc. of SPIE,* vol. 6148, 2 – 5 November 2005, Xian (China), SPIE, Bellingham WA, art. no. 61480G, pp. 1 – 8.

[48] OHARA (2011), *Ohara Corporation*, available at: http://www.oharacorp.com (accessed 21 June 2011).

[49] CORNING (2011)*, Corning Glass*, available at: http://www.corning.com (accessed 21 June 2011).

[50] VanBrocklin, R.R., Mary J. Edwards, M.J., Wells, B. (2006), "Review of Corning's Capabilities for ULE[®] Mirror Blank Manufacturing for an Extremely Large Telescope", in*: Optomechanical Technologies for Astronomy, Proc. of SPIE,* vol. 6273 I, 24 – 31 May 2006, Orlando FL, SPIE, Bellingham WA, art. no. 627301, pp. 1 – 11.

[51] Johnson, J. S., Grobsky, K. and Bray, D. J. (2002), "Rapid fabrication of lightweight silicon carbide mirrors", in: *Optomechanical Design and Engineering 2002, Proc. of SPIE,* vol. 4771, 7 – 9 July 2002, Seattle WA, SPIE, Bellingham WA, pp. 243 – 253.

[52] ISO (2007), "Optics and photonics – Interferomentric measurement of optical elements and optical systems – Part 4: Interpretation and evaluation of tolerances specified in ISO 10110", ISO 14999, Part 4.

[53] ISO (2007), "Optics and photonics – Preparation of drawings for optical elements and systems - Part 5: Surface form tolerances", ISO 10110, Part 5.

[54] Malacara, D. (2007), *Optical Shop Testing* (3rd edition), John Wiley & Sons, Inc., Hoboken (NJ).

[55] ZYGO (2011), *Zygo Corporation*, available at: http://www.zygo.com (accessed 26 June 2011).

[56] Evans, C. J. (2009), "PVr – a robust amplitude parameter for optical surface specification", *Optical Engineering*, vol. 48, no. 4, art. no. 043605, pp. 1 – 4.

[57] ISO (2009), "Geometrical product specification (GPS) - Surface texture: Profile method - Terms, definitions and surface texture parameters", ISO 4287:1998 + A1:2009.

[58] ISO (2012), "Geometrical product specifications (GPS) - Surface texture: Areal - Part 2: Terms, definitions and surface texture parameters", ISO 25178-2:2012.

[59] ISO (2012), "Geometrical product specifications (GPS) - Surface texture: Areal - Part 3: Specification operators", ISO 25178-3:2012.

[60] Elson, J. M., Bennett, J. M. (1995), "Calculation of the power spectral density from surface profile data", *Applied Optics*, vol. 34, no. 1, pp. 201 – 208.

[61] Sidick, E. (2009), "Power Spectral Density Specification and Analysis of Large Optical Surfaces", in: *Modelling Aspects in Optical Metrology II*, *Proc. of SPIE*, vol. 7390, 15 – 16 June 2009, Munich (D), SPIE, Bellingham WA, art. No. 73900L, pp. 1 – 12.

[62] Walker, D.D., Beaucamp, A., Dunn, C., Evans, R., Freeman, R., Morton, R., Wei, S., Yu, G. (2008), "Active Control of Edges and Global Microstructure on Segmented Mirrors", in: *Advanced Optical and Mechanical Technologies in Telescopes and Instrumentation, Proc. of SPIE*, vol. 7018, 23 – 28 June 2008, Marseille (F), SPIE, Bellingham WA, art. no. 701812, pp. 1 – 9.

[63] Dai, Y., Shi, F., Peng, X., LI, S. (2009), "Restraint of mid-spatial frequency error in magneto-rheological finishing (MRF) process by maximum entropy method", *Science in China, Series E: Technological Sciences*, vol. 52, no. 10, pp. 3092 – 3097.

[64] Aikens, D.M., Wolfe, C.R., Lawson J.K. (1995), "Use of Power Spectral Density (PSD) functions in specifying optics for the National Ignition Facility", in: *International Conference on Optical Fabrication and Testing, Proc. of SPIE*, vol. 2576, 5 – 7 June 1995, Tokyo (Jpn), SPIE, Bellingham WA, pp. 281 – 292.

[65] Verma, Y., Chang, A. K., Berrett, J. W., Futtere, K. and Gardopee, G. J., (2006) "Rapid damage-free shaping of silicon carbide using Reactive Atom Plasma (RAP) processing", in: *Optomechanical Technologies for Astronomy, Proc. of SPIE,* vol. 6273 I, 24 – 31 May 2006, Orlando FL, SPIE, Bellingham WA, art. no. 62730B, pp. 1 – 8.

[66] Li, K. and Liao, T. W. (1996), "Surface/subsurface damage and the fracture strength of ground ceramics", *Journal of Materials Processing Technology,* vol. 57, no. 3-4, pp. 207 – 220.

[67] Bryan, J. B. (1984), "The power of deterministic thinking in machine tool accuracy", in: *First International Machine Tool Engineers Conference*, 7 – 8 November 1984,Tokyo (Jpn), pp. 1 – 16.

[68] McKeown, P., Corbett, J., Shore, P., Morantz, P. (2008), "Ultraprecision machine tools – design principles and developments", *Nanotechnology Preceptions*, vol. 4, no. 1, pp. 5 – 14.

[69] Peggs, G., May-Miller, R., Walker, D., Atadd, E., Shore, P., Smith, D. (2004), "Dimensional metrology of mirror segments for extremely-large telescopes", in: *Second Backaskog Workshop on Extremely Large Telescopes, Proc. of SPIE*, vol. 5382 (part 1), 9 – 11 September 2003, Backaskog Castle, SPIE, Bellingham WA, pp. 224 – 228.

[70] TAYLOR-HOBSON (2011), *Taylor-Hobson*, available at: http://www.taylor-hobson.com, (accessed 26 June 2011).

[71] 4D TECHOLOGY (2011), *4D Technology Corporation*, available at: http://www.4dtechnology.com (accessed 26 June 2011).

[72] ESDI (2011), *ESDI – Surface & Wavefront Metrology Beyond Compare*, available at: http://www.engsynthesis.com, (accessed 26 June 2011).

[73] QED Technologies (2011)*, QED Technologies*, available at: http://www.qedmrf.com (accessed 27 June 2011).

[74] SAFRAN – SAGEM (2012), *High-performance optics for astronomy*, available at: http://www.sagem-ds.com/spip.php?rubrique166 (accessed 10 May 2012).

[75] Geyl, R., "From VLT to GTC and the ELT's", in: *Optical Fabrication, Testing, and Metrology II, Proc. of SPIE*, vol. 5965, 13 – 15 September 2005, Jena (D), SPIE, Bellingham WA, art. no. 59650P.

[76] ZEEKO (2011)*, Zeeko Ltd. - Ultra-Precision Polishing Solutions for Optics and other Complex Surfaces*, available at: http://www.zeeko.co.uk (accessed 27 June 2011).

[77] Tonnelier, X. (2009), *Precision Grinding for Rapid Manufacturing of Large Optics* (PhD thesis), Cranfield University, Cranfield (UK).

[78] Brinksmeier, E., Mutlugünes, Y., Klocke, F., Aurich, J. C., Shore, P., Ohmori, H. (2010), "Ultra-precision grinding", *CIRP Annals - Manufacturing Technology*, vol. 59, pp. 652 – 671.

[79] Comley, P., Morantz, P., Shore, P., Tonnellier X. (2011), "Grinding metre scale mirror segments for the E-ELT ground based telescope", *CIRP Annals - Manufacturing Technology*, vol. 60, no. 1, pp. 379 – 382.

[80] FEPA-ABRASIVES (2011), *Federation of European Producers of Abrasives*, available at: http://www.fepa-abrasives.org (accessed 26 June 2011).

[81] Tonnellier, X., Morantz, P., Shore, P., Baldwin, A., Evans, R., Walker, D.D. (2007), "Subsurface damage in precision ground ULE® and Zerodur® surfaces", *Optics Express*, vol. 15, no. 9, pp. 12197 – 12205.

[82] Tonnellier, X., Shore, P., Morantz, P., Baldwin A., Walker D., Yu G., Evans R. (2008), "Sub-surface damage issues for effective fabrication of large optics", in: *Advanced Optical and Mechanical Technologies in Telescopes and Instrumentation, Proc. of SPIE,* vol. 7018, 23 – 28 June 2008, Marseille (F), SPIE, Bellingham WA, art. no. 70180F, pp. 1 – 10.

[83] Tonnellier, X., Howard, K., Morantz, P., Shore P. (2011), "Surface integrity of precision ground fused silica for high power laser applications", *Procedia Engineering*, vol. 19, pp. 357 – 362.

[84] Kaller, A. (2000), "The basic mechanism of glass polishing", *Naturwissenschaften,* vol. 87, no. 1, pp. 45 – 47.

[85] Shorey, A.B., Jacobs, S.D., Kordonski, W.I., Gans, R.F. (2001), "Experiments and observations regarding the mechanism of glass removal in magnetorheological finishing", *Applied Optics*, vol. 40, no. 1, pp. 20 – 33.

[86] DeGroote, J.E., Jacobs, S.D., Gregg, L.L., Marino, A.E., Hayes, J.C. (2001), "Quantitative characterization of optical polishing pitch", in: Optical *Manufacturing and Testing IV*, *Proc. of SPIE*, vol. 4451, 31 July – 2 August 2001, San Diego CA, SPIE, Bellingham WA, pp. 209 – 221.

[87] Wang, J., Guo, Y., Lee, Y., Xu, Q., Yang, W. (2009), "Research of optical flats in pad polishing", in: *4th International Symposium on Advanced*

Optical Manufacturing and Testing Technologies: Advanced Optical Manufacturing Technologies, Proc. of SPIE, vol. 7282, 19 – 21 November 2008, Chengdu (China), SPIE, Bellingham WA, art. no. 72820X, pp. 1 – 5.

[88] Song, C., Walker, D., Yu, G. (2011), "Misfit of rigid tools and interferometer subapertures on off-axis aspheric mirror segments", *Optical Engineering*, vol. 50, no. 7, art. no. 073401, pp. 1 – 6.

[89] Jacobs, S. D. (2004), "International innovations in optical finishing", in: *Current Developments in Lens Design and Optical Engineering V, Proc. of SPIE,* vol. 5523, 4 – 5 August 2004, Denver CO, SPIE, Bellingham WA, pp. 264 – 272.

[90] SOML (2011), *Stewart Observatory Mirror Lab*, available at: http://mirrorlab.as.arizona.edu (accessed: 27 June 2011).

[91] West, S.C., Martin, H.M., Nagel, R.H., Young, R.S., Davison, W.B., Trebisky, T.J., DeRigne, S.T., Hille, B.B. (1998), "Practical design and performance of the stressed-lap polishing tool", *Applied Optics*, vol. 33, no. 34, pp. 8094 – 8100.

[92] Martin, H.M., Allen, R.G., Burge, J.H., Kim, D.W., Kingsley, J.S., Tuell, M.T., West, S.C., Zhao, C., Zobrist, T. (2010), "Fabrication and testing of the first 8.4 m off-axis segment for the Giant Magellan Telescope", in: *Modern Technologies in Space- and Ground-Based Telescopes and Instrumentation, Proc. of SPIE*, vol. 7739, 27 June – 2 July 2010, San Diego CA, SPIE, Bellingham WA, art. no. 77390A, pp. 1 – 13.

[93] Shectman, S., Johns, M. (2010), "GMT overview", in: *Ground-Based and Airborne Telescopes III, Proc. of SPIE*, vol. 7733 (PART 1), 27 June – 2 July 2010, San Diego CA, SPIE, Bellingham WA, art. no. 77331Y, pp. 1 – 11.

[94] Walker, D. D., Brooks, D., King, A., Freeman, R. and Morton, R. (2003), "The 'Precessions' tooling for polishing and figuring flat, spherical and aspheric surfaces", *Optics Express,* vol. 11, no. 8, pp. 958 – 964.

[95] Walker, D.D., Baldwin, A., Evans, R., Freeman, R., Hamidi, S., Shore, P., Tonneller, X., Wei, S., Williams, C., Yu, G. (2007), "A quantitative comparison of three grolishing techniques for the precession[TM] process", in: *Optical Manufacturing and Testing VII, Proc. of SPIE*, vol. 6671, 28 – 29 August 2007, San Diego CA, SPIE, Bellingham WA, art. no. 66711H, pp. 1 – 9.

[96] Golini, D., Kordonski, W.I., Dumas, H. (1999), "Magnetorhelogical finishing (MRF) in commercial precision optics manufacturing", in: *Optical Manufacturing and Testing III, Proc. of SPIE*, vol. 3782, 20 – 23 July 1999, Denver CO, SPIE, Bellingham WA, pp. 80 – 91.

[97] Hu, H., Dai, Y., Peng, X., Wang, J. (2011), "Research on reducing the edge effect in magnetorheological finishing", *Applied Optics*, vol. 50, no. 9, pp. 1220 – 1226.

[98] DeGroote, J. E., Marino, A. E., Wilson, J. P., Bishop, A. L. and Lambropoulos, J. C. (2007), "Removal rate model for magnetorheological finishing of glass", *Applied Optics,* vol. 46, no. 32, pp. 7927 – 7941.

[99] Kim, D.W., Park, W.H., Kim, S-W., Burge, J.H. (2009), "Edge tool influence function library using parametric edge model for computer controlled optical surfacing", in: *Optical Manufacturing and Testing VIII, Proc. of SPIE*, vol. 7426, 4 – 5 August 2009, San Diego CA, SPIE, Bellingham WA, art. no. 74260G.

[100] Wang, W., Xu, M., Yu, G., Walker, D.D., Zhu, H. (2010), "Research on Edge Control in the Process of Polishing Using Ultra Precise Bonnet on Optical Elements", in: *5th International Symposium on Advanced Optical Manufacturing and Testing Technologies: Large Mirrors and Telescopes, Proc. of SPIE*, vol. 7654, 26 – 29 April 2010, Dalian (China), SPIE, Bellingham WA, art. no.76540N.

[101] N. Yaitskova, K. Dohlen, P. Dierickx (2003), "Diffraction in OWL: Effects of Segmentation and Segments Edge Misfigure", in: *Future Giant Telescopes*, *Proc. of SPIE,* vol. 4840, 26 – 28 August 2002, Waikoloa HI, SPIE, Bellingham WA, pp. 171 – 182.

[102] Kaufman, H.R., Robinson, R.S. (1989), "Broad-beam ion source technology and applications", *Vacuum*, vol. 39, no. 11-12, pp. 1175 – 1180.

[103] Wilson, S. R., Reicher, D. W. and McNeil, J. R. (1988), "Surface figuring using neutral ion beams", *Advances in Fabrication and Metrology for Optics and Large Optics,* vol. 966, pp. 74 – 81.

[104] Allen, L. N., Roming, H. W. (1990), "Demonstration of an ion figuring process", in: *Advanced Optical Manufacturing and Testing, Proc. of SPIE*, vol. 1333, 9 – 11 July 1990, San Diego CA, SPIE, Bellingham WA, pp. 22 – 33.

[105] Allen, L. N., Hannon, J. J., Wambach, R. W. (1992), "Final surface error correction of an off-axis aspheric petal by ion figuring", in: *Active and Adaptive Optical Components*, *Proc. of SPIE*, vol. 1543, 24 – 26 July 1991, San Diego CA, SPIE, Bellingham WA, pp. 190 – 200.

[106] Allen, L. N. (1995), "Progress in ion figuring large optics", in: *26th Annual Boulder Symposium on Laser-Induced Damage in Optical Materials, Proc. of SPIE,* vol. 2428, 24 – 26 October 1994, Boulder CO, SPIE, Bellingham WA, pp. 237 – 247.

[107] IOM (2011), *Leibniz Institut für Oberflächenmodifizierung e. V.*, available at: http://www.iom-leipzig.de (accessed 30 August 2012).

[108] Schindler, A., Haensel, T., Flamm, D., Frank, W., Boehm, G., Frost, F., Fechner, R., Bigl, F., Rauschenbach, B. (2001), "Ion beam and plasma jet etching for optical component fabrication", in: *Lithographic and Micromachining Techniques for Optical Component Fabrication, Proc. of SPIE*, vol. 4440, 29 – 30 July 2001, San Diego CA, SPIE, Bellingham WA, pp. 217 – 227.

[109] Arnold, T., Böhm, G., Fechner, R., Meister, J., Nickel, A., Frost, F., Hänsel, T., Schindler, A. (2010), "Ultra-precision surface finishing by ion beam and plasma jet techniques - status and outlook", *Nuclear Instruments and Methods in Physics Research, Section A: Accelerators, Spectrometers, Detectors and Associated Equipment*, vol. 616, no. 2 − 3, pp. 147 − 156.

[110] Frost, F., Fechner, R., Ziberi, B., Völlner, J., Flamm, D., Schindler, A. (2009), "Large area smoothing of surfaces by ion bombardment: Fundamentals and applications", *Journal of Physics Condensed Matter*, vol. 21, no. 22, art. no. 224026, pp. 1 − 20.

[111] Arnold T, Boehm G, Eichentopf I-M, Janietz M, Meister J, Schindler A (2010), "Plasma Jet Machining", *Vakuum in Forschung und Praxis*, vol. 22, no. 4, pp. 10 − 16.

[112] Schindler, A., Boehm, G., Haensel, T., Frank, W., Nickel, A., Rauschenbach, B., Bigl, F. (2001), "Precision optical asphere fabrication by Plasma Jet Chemical Etching (PJCE) and ion beam figuring", in: *Optical Manufacturing and Testing IV, Proc. of SPIE*, vol. 4451, 31 July − 2 August, San Diego CA, SPIE, Bellingham WA, pp. 242 − 248.

[113] Fähnle, O.W., Van Brug, H., Frankena, H.J., "Fluid jet polishing of optical surfaces", *Applied Optics*, vol. 37, no. 28, pp. 6771 − 6773.

[114] Kordonski, W.I., Shorey, A.B., Tricard, M. (2006), "Magnetorheological jet (MR Jet^{TM}) finishing technology", *Journal of Fluids Engineering, Transactions of the ASME*, vol. 128, no. 1, pp. 20 − 26.

[115] Shorey, A.B., Kordonski, W., Tracy, J., Tricard, M. (2007), "Developments in the finishing of domes and conformal optics", in: *Window and Dome Technologies and Materials X, Proc. of SPIE,* vol. 6545, 11 − 12 April 2007, Orlando FL, SPIE, Bellingham WA, art. no. 65450Q, pp. 1 − 9.

[116] Mori, Y., Yamauchi K., Endo, K. (1987), "Elastic Emission Machining", *Precision Engineering*, vol. 9, no. 3, pp. 123 − 128.

[117] Kanaoka, M., Liu, C., Nomura, K., Ando, M., Takino, H., Fukuda, Y., Mori, Y., Mimura, H., Yamauchi, K. (2008), "Processing efficiency of elastic emission machining for low-thermal-expansion material", *Surface and Interface Analysis*, vol. 40, no. 6-7, pp. 1002 − 1006.

[118] Yamauchi, K., Yamamura, K., Mimura, H., Sano, Y., Saito, A., Endo, K., Souvorov, A., Yabashi, M., Tamasaku, K., Ishikawa, T., Mori, Y. (2003), "Two-dimensional Submicron Focusing of Hard X-rays by Two Elliptical Mirrors Fabricated by Plasma Chemical Vaporization Machining and Elastic Emission Machining", *Japanese Journal of Applied Physics − Part 1*, vol. 42, no. 11, pp. 7129 − 7134.

[119] Boulos, M. I. (1985), "The inductively coupled R.F. (radio frequency) plasma", *Pure and Applied Chemistry*, vol. 57, no. 9, pp. 1321 − 1352.

[120] Manos, D. M. and Flamm, D. L. (1989), *Plasma etching: an introduction,* Academic Press, Boston.

[121] Tendero, C., Tixier, C., Tristant, P., Desmaison, J., Leprince, P. (2006), "Atmospheric pressure plasmas: A review", *Spectrochimica Acta - Part B Atomic Spectroscopy*, vol. 61, no. 1, pp. 2 – 30.

[122] Lieberman, M.A., Lichtenberg, A.J. (2005), "Principles of Plasma Discharges and Materials Processing", second ed., John Wiley and Sons Inc., Hoboken, New Jersey (USA).

[123] Flamm, D. L. (1990), "Mechanisms of silicon etching in fluorine- and chlorine-containing plasmas", *Pure & Appl. Chem,* vol. 62, no. 9, pp. 1709 – 1720.

[124] D'Agostino, R. and Flamm, D. L. (1981), "Plasma etching of Si and SiO_2 in SF_6-O_2 mixtures", *Journal of Applied Physics,* vol. 52, no. 1, pp. 162 – 167.

[125] Arnold, T., Schindler, A. (2008), "Mass spectrometry at a Ar/SF_6/O_2 chemically reactive plasma jet", *Physica Status Solidi (A) Applications and Materials*, vol. 205, no. 4, pp. 957 – 960.

[126] Sinke, G.C. (1966), "The Enthalpy of Dissociation of Nitrogen Trifluoride", *The Journal of Physical Chemistry*, vol. 71, no. 8, pp. 359 – 360.

[127] Roth, J.R. (1995), *Industrial Plasma Engineering*, vol. 1, Philadelphia: Institute of Physics Pub., Bristol (UK).

[128] Reed, T.B. (1961), "Induction-Coupled plasma torch", *Journal of Applied Physics*, vol. 32, no. 5, pp. 821 – 824.

[129] Eckert, H.U. (1974), "The Induction Arc: A State-of-the-Art Review", *High Temperature Science*, vol. 6, pp. 99 – 134.

[130] Bollinger, D., Gallatin, G., Samuels, J., Steinberg, G., Zarowin, C. (1990), "Rapid, non-contact optical figuring of aspheric surfaces with Plasma Assisted Chemical Etching (PACE)", in: *Advanced Optical Manufacturing and Testing*, *Proc. of SPIE*, vol. 1333, 9 – 11 July 1990, San Diego CA, SPIE, Bellingham WA, pp. 44 – 57.

[131] RAPT Industries. *Helios 1200 user manual* (Technical manual including System Specifications, User Manual, Risk Assessment, Compliance Assessment, Maintenance & Schematics).

[132] Jourdain, R., Shore, P. (2009), "Novel plasma surface figuring facility designed for effective production of large scale optical surfaces". In: *European Optical Society Conference on Manufacturing for Optical Components*, 15 – 17 June 2009, Munich (D), art. no. OC_POF10_1828.

[133] Zhang, J., Wang, B., Shen, S. (2008), "Application of atmospheric pressure plasma polishing method in machining of silicon ultra-smooth surfaces", *Frontiers of Electrical and Electronic Engineering in China*, vol. 3, No. 4, pp. 480 – 487.

[134] Jin, H.L., Wang, B., Li, N., Zhang, F.H. (2012), "Investigation of discharge characteristics and thermal effect in atmosphere pressure plasma processing", in: *Proceedings of the International Conference of the*

European Society for Precision Engineering and Nanotechnology, vol. 2, 4 – 8 June 2012, Stockholm (S), EUSPEN, Cranfield, pp. 432 – 435.

[135] Meister, J., Arnold, T. (2010), "New process simulation procedure for high-rate plasma jet machining", *Plasma Chemistry and Plasma Processing*, vol. 31, no. 1, pp. 91 – 107.

[136] Arnold, T., Böhm, G. (2012), "Application of atmospheric plasma jet machining (PJM) for effective surface figuring of SiC", *Precision Engineering*, vol. 36, no. 4, pp. 546 – 553.

[137] Yamamura, K., Shimada, S., Mori Y. (2008), "Damage-free improvement of thickness uniformity of quartz crystal wafer by plasma chemical vaporization machining", *CIRP Annals - Manufacturing Technology*, vol. 57, no. 1, pp. 567 – 570.

[138] Mori, Y., Yamauchi, K., Yamamura, K. and Sano, Y. (2000), "Development of plasma chemical vaporization machining", *Review of Scientific Instruments,* vol. 71, no. 12, pp. 4627 – 4632.

[139] Takino, H., Shibata, N., Itoh, H., Kobayashi, T., Tanaka, H., Ebi, M., Yamamura, K., Sano, Y., Mori, Y. (1998), "Computer Numerically Controlled Plasma Chemical Vaporization Machining With a Pipe Electrode for Optical Fabrication", *Applied Optics*, Vol. 37, no. 22, pp. 5198 – 5210.

[140] Takino, H., Shibata, N., Itoh, H., Kobayashi, T., Yamamura K., Sano, Y., Mori, Y. (2002), "Fabrication of optics by use of plasma chemical vaporization machining with a pipe electrode", *Applied Optics*, vol. 41, no. 19, pp. 3971 – 3977.

[141] Takino, H., Yamamura, K., Sano, Y., Mori, Y. (2012), "Shape correction of optical surfaces using plasma chemical vaporization machining with a hemispherical tip electrode", *Applied Optics*, vol. 51, no. 3, pp. 401 – 407.

[142] Drueding, T. W., Bifano, T. G. and Fawcett, S. C. (1995), "Contouring algorithm for ion figuring", *Precision Engineering,* vol. 17, pp. 10 – 21.

[143] Jiao, C., Li, S. and Xie, X. (2009), "Algorithm for ion beam figuring of low-gradient mirrors", *Applied Optics,* vol. 48, no. 21, pp. 4090 – 4096.

[144] Jansson, P. A. (ed.) (1997), *Deconvolution of Images and Spectra,* second ed, Academic Press Inc., San Diego (USA).

[145] Lucy, L. B. (1974), "An iterative technique for the rectification of observed distributions", *The Astronomical Journal,* vol. 79, no. 6, pp. 745 – 754.

[146] Richardson, W. H. (1972), "Bayesian-Based Iterative Method of Image Restoration", *Journal of the Optical Society of America,* vol. 62, no. 1, pp. 55 – 59.

[147] Jiao, C., Li, S., Xie, X., Chen, S., Wu, D., Kang, N. (2010), "Figuring algorithm for high-gradient mirrors with axis-symmetrical removal function", *Applied Optics*, vol. 49, no. 4, pp. 578 – 585.

[148] Dai, Y., Liao, W., Zhou, L., Chen, S., Xie, X. (2010), "Ion beam figuring of high-slope surfaces based on figure error compensation algorithm", *Applied Optics*, vol. 49, no. 34, pp. 6630 – 6636.

[149] Hänsel, T., Nickel, A., Schindler, A. (2008), "Ion beam figuring of strongly curved surfaces with a (x, y, z) linear three-axes system", in: *Optical Fabrication and Testing, OSA Technical Digest (CD)*, 20 – 24 October 2008, Rochester, paper no. JWD6, (available at: http://www.opticsinfobase.org/abstract.cfm?URI=OFT-2008-JWD6).

[150] Song, C., Dai, Y., Peng, X. (2010), "Model and algorithm based on accurate realization of dwell time in magnetorheological finishing", *Applied Optics*, vol. 49, no. 19, pp. 3676 – 3683.

[151] Dunn, C. R., Walker, D. D. (2008), "Pseudo-random tool paths for CNC sub-aperture polishing and other applications", *Optics Express*, vol. 16, no. 23, pp. 18942 – 18949.

[152] Aikens, D., DeGroote, J., and Youngworth, R. (2008), "Specification and control of mid-spatial frequency wavefront errors in optical systems", in: *Optical Fabrication and Testing technical digest*, *OSA*, 19 October 2008, Rochester NY, paper to keynote session.

[153] Dai, Y., Shi, F., Peng X., Li, S. (2009), "Restraint of mid-spatial frequency error in magnetorheological finishing (MRF) process by maximum entropy method", *Science in China Series E: Technological Sciences*, vol. 52, no. 10, 3092 – 3097.

[154] Hu, H., Dai, Y., Peng, X. (2010), "Restraint of tool path ripple based on surface error distribution and process parameters in deterministic finishing", *Optics Express*, vol. 18, no. 22, pp. 22973 – 22981.

[155] Carslaw, H. S., Jaeger, J. C. (1959), *Conduction of heat in solids*, second ed., Clarendon Press, Oxford.

[156] Lax, M. (1978), "Temperature rise induced by a laser beam II. The nonlinear case", *App. Physics Letters*, vol. 38, no. 8, pp. 786 – 788.

[157] Lide, D. R. (2009-2010), "CRC handbook of chemistry and physics", 9th ed., CRC Press, Boca Raton (USA).

[158] Lax, M. (1977), "Temperature rise induced by a laser beam", *Journal of Applied Physics*, vol. 48, no. 9, pp. 3919 – 3924.

[159] Cline, H. E., Anthony, T. R. (1977), "Heat treating and melting material with a scanning laser or electron beam", *Journal of Applied Physics*, vol. 48, no. 9, pp. 3895 – 3900.

[160] Smith, D. Y., Black, C. E., Homes, C. C., Shiles, E. (2007), "Optical properties of TiO 2 –SiO 2 glass over a wide spectral range", *Physica Status Solidi*, vol. 4, no. 3, pp. 838 – 842.

[161] Maeda, J. and Murata, K. (1984), "Image Restoration by an Iterative Regularized Pseudoinverse Method", *Applied Optics,* vol. 23, no. 6, pp. 857 – 861.

[162] Parkins, J., Jourdain, R., Marson, S., Shore, P., Sparkes, M., O'Neill, W. (2012), "Laser Assisted Plasma Processing: An Overview", in*: Proceedings of the International Conference of the European Society for Precision Engineering and Nanotechnology*, vol. 2, 4 – 8 June 2012, Stockholm, (S), EUSPEN, Cranfield, pp. 364 – 367.

[163] Sykora, D. M., de Groot, P. (2011), "Instantaneous measurement Fizeau interferometer with high spatial resolution", in: *Optical Manufacturing and Testing IX, Proc. of SPIE,* vol. 8126, 22 – 24 August 2011, San Diego CA, SPIE, Bellingham WA, art. no. 812610, pp. 1 – 10.

[164] Wyant, J. C. (2002), "White Light Interferometry", in: *Holography: A Tribute to Yuri Denisyuk and Emmet Leith, Proc. of SPIE,* vol. 4737, 3 – 4 April 2002, Orlando FL, SPIE, Bellingham WA, pp. 98 – 107.

APPENDICES

Appendix A Symbols and constants used in equations

A	[cm^2]	Contact area of mechanical processes
α (CTE)	[K^{-1}]	Coefficient of thermal expansion
B(x,y)	[nm s^{-1}]	Influence function
c	[m s^{-1}]	Speed of light (299792458)
c$_p$	[J Kg^{-1} K^{-1}]	Specific heat capacity
D	[cm^2 s^{-1}]	Thermal diffusivity
δ_{pe}	[m]	Skin depth
Ø	[mm]	Symbol for diameter
e	[C]	Elementary charge (1.602 · 10^{-19})
E$_a$	[J mol^{-1}]	Activation energy
E	[GPa]	Young modulus
ε	[-]	Emissivity of grey body
ε_0	[F m^{-1}]	Perimittivity of vacuum (8.854 · 10^{-12})
f$_r$	[mm step^{-1}]	Feedrate (feed per step)
	[mm rev^{-1}]	Feedrate (feed per revolution)
H	[Kg mm^{-2}]	Material hardness
I	[W m^{-2}]	Emission intensity
k	[-]	Preston coefficient
k$_B$	[J K^{-1}]	Boltzmann's constant
K	[W m^{-1} ^{o}C^{-1}]	Thermal conductivity
	[W m^{-1} K^{-1}]	

λ	[nm]	Wavelength
λ_D	[m]	Debye length
m_e	[Kg]	Electron mass ($9.11 \cdot 10^{-31}$)
μ_0	[H m^{-1}]	Magnetic permeability of vacuum ($4\pi \cdot 10^{-7}$)
μ_r	[-]	Relative magnetiv permeability
n_e	[m^{-3}]	Electron density
n_F	[mol l^{-1}]	Concentration of fluorine radicals
P	[Pa]	Pressure
Q	[W m^{-2}]	Heat flux
r(x,y)	[nm]	Removal function (figure error)
R	[J mol^{-1} K^{-1}]	Molar gas constant
ρ	[Kg mm^{-3}]	Density
S_{tool}	[-]	Tool overhanging ratio
S(r)	[m s^{-1}]	Angular speed distribution
	[rad s^{-1}]	
S_q	[nm]	$\sqrt{\frac{1}{NM}\sum_{i=1}^{N}\sum_{j=1}^{M}(Z(x_i, y_j) - \bar{Z})^2}$, Z: surface heights, $\bar{Z}$: average surface height
σ_{el}	[Ω m^{-1}]	Electric conductivity
t(x,y)	[s m^{-2}]	Dwell time
T_e	[K]	Electron temperature
v, v_w	[m s^{-1}]	Surface speed or scanning speed
	[mm min^{-1}]	

ω_{pe} [Hz]   Plasma frequency

ω_{EM} [Hz]   Frequency of electromagnetic radiation

Appendix B Methods by Van Cittert and Lucy-Richardson

<u>Van Cittert Deconvolution (self-developed):</u>

The basic method was developed by Van Cittert in 1931. A formal derivation is performed as follows: from the fundamental theorem of convolution follows that

$$\mathcal{F}[t(x,y)] = \frac{\mathcal{F}[R(x,y)]}{\mathcal{F}[B(x,y)]} \Leftrightarrow \hat{t}(k_x,k_y) = \frac{\hat{R}(k_x,k_y)}{\hat{B}(k_x,k_y)} \tag{B-1}$$

with $k_{x,y}$: spatial frequencies. To avoid the singularities that can occur for $\hat{B}(x,y)$ the function is offset as $\hat{B}'(x,y) = 1 - \hat{B}(x,y)$. A Taylor expansion delivers:

$$\frac{\hat{R}(k_x,k_y)}{1 - \hat{B}'(k_x,k_y)} = (1 + \hat{B}' + \widehat{B'}^2 + \cdots) \cdot \hat{R} \tag{B-2}$$

which in the space domain becomes

$$t(x,y) = (1 + B'(x,y) + B'(x,y)^2 + \cdots) \otimes R(x,y) \tag{B-3}$$

It can be shown that the polynomial in equation (B-3) is rewritable as

$$t_{i+1}(x,y) = R(x,y) + [1 - B(x,y)] \otimes t_i(x,y) \tag{B-4}$$

where the "zero" iteration step t_0 is take equal to *R(x,y)*. Intuitively, an interpretation of equation (B-4) is that a given measured dataset (*R*) can already be considered as an approximation of the sought object (in figuring, the dwell time). Now, if the data are "blurred" (e.g., by a Gaussian filter *B*), the difference between original and blurred information must be related to the error of the result to be obtained. This error estimate could be exploited as rectification term for the first "smart guess" t_0, thus producing a new approximation for the result. Repeating this procedure over and over, a progressive improvement is aimed for. Analytical convergence of the method is given by the fact that it is derived from an inverse filter-like expression. However, one must note that the Taylor expansion implicitly imposes that $|1 - \hat{B}| < 1$.

Van Cittert's method is often considered a starting point from which more efficient algorithms have been developed. A simple improvement (for convergence) consists of multiplying the term in squared brackets of equation (B-4)by a so-called *relaxation factor*. Several other examples are given in [144] (e.g., Jansson's method). In the context of this project an alternative solution was attempted. This is reported by Jansson to achieve high rate of convergence and deal with noise. This version was originally developed by Maeda and Murata (1984) [161] and consists of substituting the relaxation factor by a convolution with a relaxation function. This can be some kind of smoothing filter; following Maeda & Murata again, the current code uses the Gaussian beam function itself for this purpose.

$$[R(x,y) - B(x,y) \otimes t(x,y)] \rightarrow B(x,y) \otimes [R(x,y) - B(x,y) \otimes t(x,y)] \qquad \textbf{(B-5)}$$

The reader might note that equation (B-5) doesn't represent a linear deconvolution method. It is also clear that the method doesn't automatically contain any constraint on the solution. The result can therefore show, for example, negative dwell times. Such outsider values can be easily suppressed. The implementation of a positivity constraint has been introduced in the actual code.

Lucy-Richardson method:

This algorithm was developed independently by W.H. Richardson (1972) [146] and L.B. Lucy (1974) [145], both working on images reconstruction. Their derivation followed from observing that image data (including noise) can be considered as Poisson-distributed about their mean value[13]. The analogues of a figuring process consist of regarding the figure error map and the dwell time as randomized distributions [143]. Following Jiao et al. [143], the search for the "best" dwell time distribution is equivalent to maximizing the *posterior probability function* P(t|R). This last expression is called the *conditional probability* of t

---

[13] A statistic approach is not surprising when treating, e.g., data counts and noise; the same argumentations for the derivation of Lucy-Richardson's algorithm apply for Gaussian distributions.

being the solution, given R. With help of the *Bayesian theorem* in the 1D case follows:

$$P(t|R) = \frac{P(R|t) \cdot P(t)}{P(R)} \tag{B-6}$$

with P(R|t) corresponding to the beam function. Finding the "most probable" solution of equation (B-6) is equivalent to maximizing following log-likelihood function

$$\iint R(x,y) \cdot \ln[(B \otimes t)(x,y)] - (B \otimes t)(x,y)dxdy \tag{B-7}$$

Derivation with respect to *t* and equalising to zero delivers:

$$\frac{B(-x,-y)}{\iint B(-x,-y)dxdy} \otimes \frac{R(x,y)}{B(x,y) \otimes t(x,y)} = 1 \tag{B-8}$$

Through a multiplicative algorithm, following iterative form can be derived:

$$t_{k+1}(x,y) = t_k(x,y) \cdot \frac{B(-x,-y)}{\iint B(-x,-y)dxdy} \otimes \frac{R(x,y)}{B(x,y) \otimes t_k(x,y)} \tag{B-9}$$

Equation (B-9) represents the standard form of the Lucy-Richardson deconvolution algorithm. Once again, as first iteration step, t_0 is usually taken equal *R*. This non-linear method is one of the most used techniques in image recovery, as well as figuring processes. The main advantage, together with noise containment, consists of positivity self-constraint. It is in fact easy to recognize that, if the input functions *B(x,y)* and *R(x,y)* are positive, the resulting dwell time is bound to be positive too[14]. Convergence of the Lucy-Richardson algorithm is discussed by Jansson in [144]. In this discussion, it is argued that if the maximum likelihood condition is satisfied then the iteration will deliver $t_{k+1} = t_k$.

---

[14]This property applies also to other multiplicative algorithms like the Gold's method.

Performance of the deconvolution algorithms:

In **Figure B-1**, the performance of the described deconvolution algorithms is exemplified. An arbitrary figure error map (with edge extension) is deconvoluted both using Lucy-Richardson and Van Cittert methods. For the function $B(x,y)$, the normalised RAP etching footprint is taken. From the resulting (pseudo-) dwell time maps, the error maps are reconstructed by convolution with $B(x,y)$. The residuals, calculated as difference between measured and reconstructed error map, show similar performances of the two deconvolution codes.

(a)

(b)

(c)
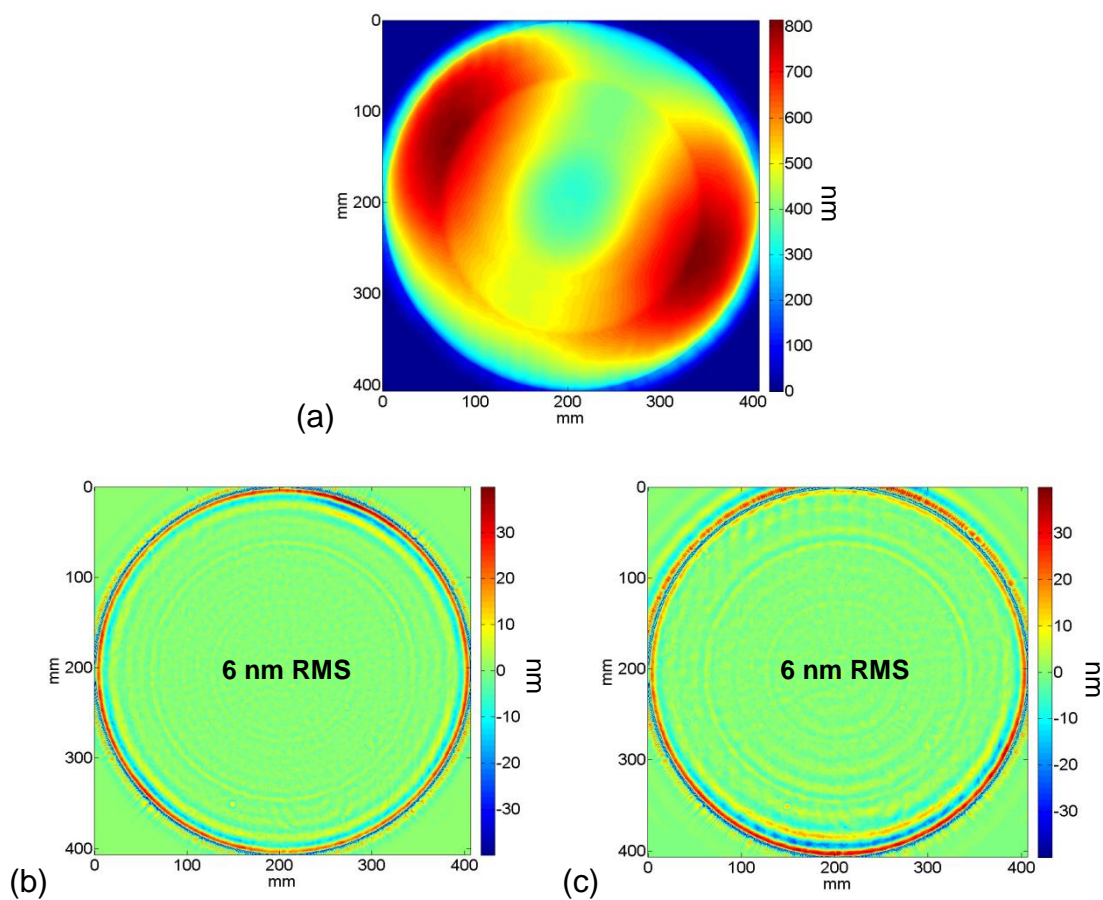
Figure B-1 (a): edge extended figure error; (b): residual with Lucy-Richardson algorithm; (c): residual with Van Cittert algorithm.

In **Figure B-1**, some larger values are present at the edges and are probably due to the slope of the figure error at the boundary. In this work, with the use of ten numerical iterations (default), it was ascertained that the residuals were within a few nanometres RMS.

Appendix C Evaluation of trench data
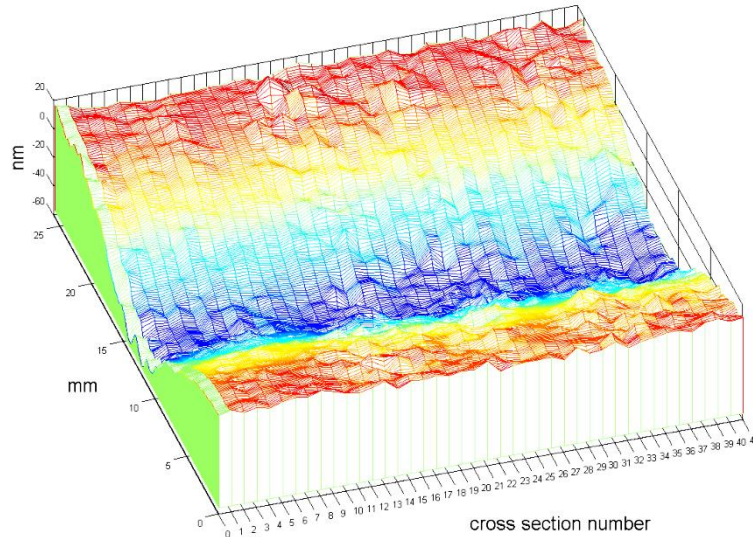
Figure C-1 Illustration showing a trench divided into a series of cross-sections, where each cross-section results from averaging 20 pixels of the original dataset.

As illustrated in **Figure C-1**, the evaluation of trenches parameters, like etching depth and profile width, was performed by "slicing" single trenches into a series of cross-sections, where each cross section resulted from averaging 20 pixels (~2 mm) of the original data set. A Gaussian curve fit was then performed for each single cross-section and depth and width parameters derived. The values were subsequently averaged the errors estimated by considering the standard deviations. From those parameters, the volumetric material removal rates were also derived. The results for ULE and fused silica materials are reported in **Table C-1** and **Table C-2**.

This method accounts for the scattering of values within a single measurement, which are mainly due to surface asperities and detector noise. Also, every trench was etched either horizontally or vertically with respect to the interferometer field of view. Yet, misalignments are still possible at pixel or sub-pixel level, which may cause errors in the evaluation of the trench parameters.

The described data analysis method, though, eliminates this source of error by evaluating a trench cross section by cross section.

Table C-1Trenches parameters for ULE.

ULE			
V [mm/min]	depth [nm]	sigma [mm]	MRR [mm^3/min]
1000	206.6 ± 4.5	7.40 ± 0.12	2.71 ± 0.07
1500	97 ± 1.8	6.71 ± 0.14	1.73 ± 0.05
2000	57.4 ± 2.5	6.56 ± 0.23	1.33 ± 0.07
2500	35.3 ± 2.6	6.38 ± 0.46	0.9962 ± 0.1
3000	25.6 ± 1.2	6.43 ± 0.35	0.88 ± 0.06
4000	14.1 ± 1.7	6.49 ± 0.79	0.67 ± 0.11

Table C-2 Trenches parameters for fused silica.

FUSED SILICA			
V [mm/min]	depth [nm]	sigma [mm]	MRR [mm^3/min]
1000	120.5 ± 2.9	6.00 ± 0.25	1.28 ± 0.06
1500	42.5 ± 1.8	6.34 ± 0.27	0.72 ± 0.04
2000	24.7 ± 3.9	6.20 ± 0.74	0.54 ± 0.11
2500	13.9 ± 1	6.35 ± 0.38	0.39 ± 0.03
3000*	14.2 ± 1.3	7.27 ± 0.45	0.55 ± 0.06
4000*	8.1 ± 0.8	7.28 ± 0.51	0.42 ± 0.05

*: Theses trenches present a very shallow profile and single pass etching would produce groove depths near the limit of the interferometer noise (~3 nm). Therefore, to improve the signal to noise ratio, each trench was etched through multiple passes (two and four times respectively), and waiting for the sample to cool in-between.

<u>HOT TRENCHES</u>

The same analysis method was also utilised for the evaluation of hot trenches data. The values are reported in **Table C-3.**

Table C-3 Hot trenches parameters (material: fused silica).

3000 mm/min			
T [^{o}C]	depth [nm]	sigma [mm]	MRR [mm^3 / min]
21	14.2± 1.3	7.27 ± 0.45	0.55 ± 0.06
53	19.9 ± 2.9	6.98 ± 1.92	0.74 ± 0.23
79	21.8 ± 3.2	7.61 ± 1.34	0.88 ± 0.2
102	37.6 ± 3	7.70 ± 0.43	1.54 ± 0.15
1000 mm/min			
T [^{o}C]	depth [nm]	sigma [mm]	MRR [mm^3 / min]
21	120.00 ± 2.9	6.00 ± 0.25	1.28 ± 0.12
51	149.40 ± 2.9	6.62 ± 0.19	1.75 ± 0.12
86	193.14 ± 3	7.47 ± 0.06	2.56 ± 0.1

Appendix D Metrology

D.1 Twyman-Green interferometer FST10 by Fisba Optik

In **Figure D-1,** the interferometer utilised for the surface measurements over 100 mm diameter areas is shown. This was set on a tip-tilt triangular stage (three precision screws), sitting on a vibrations isolating table. A He-Ne laser at λ = 632.8 nm constitutes the coherent light source and the resolution with the 100 mm diameter collimator is 0.1 mm/pixel. This interferometer configuration corresponds to a classical Twyman-Green design and is based on the data acquisition principle of phase-shift interferometry (see, e.g., [54]). In particular, for all topography maps generated with this instrument, a so-called 5-frames algorithm was consistently applied. As reported, e.g., by Malacara [54], this kind of algorithm is efficient at reducing phase-shift errors, as well as fringes residual print-through due to detector non-linearities. Also, averaging of multiple interferograms assured repeatability down to 10 nm PV (**Figure D-2**). During the entire course of the experimental work with this instrument, nanometre level repeatability and accuracy were also guaranteed by systematically recalibrating the interferometer before every measurement.
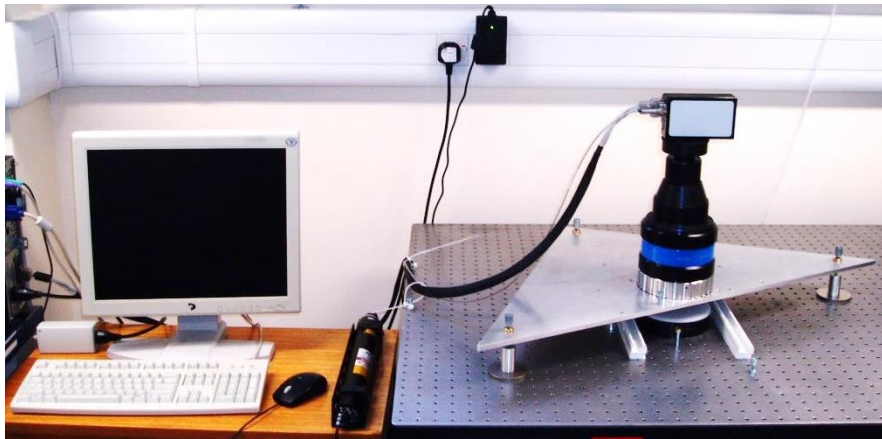
Figure D-1 Twyman-Green interferometer by Fisba Optik and setup utilised for the 100 mm diameter areas measurements.

The calibration was carried out with a λ/8 PV (~80 nm) 4'' ISO standard flat that was constantly kept in the same position underneath the collimator. Such a

calibration compensated also for errors due to collimator defects and effects of thermal fluctuations in the metrology room.
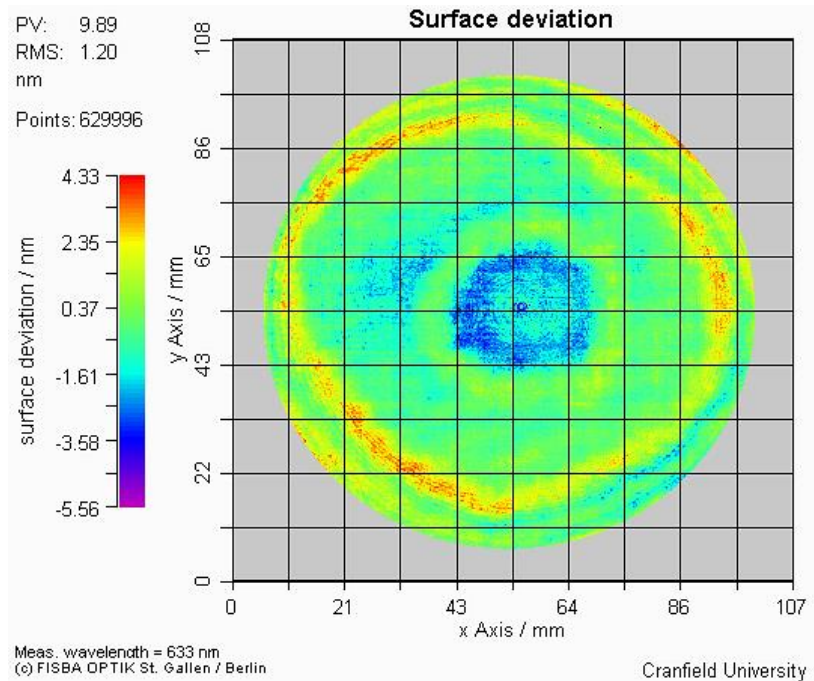
Figure D-2 Repetability of the FST10 over the 100 mm diameter area: ~10 nm PV and ~1 nm RMS.
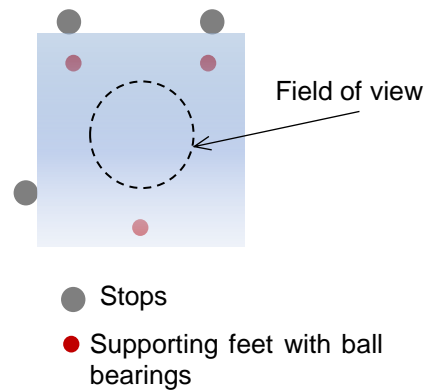

Figure D-3 Kinematic mount for the 200mm x 200mm samples.

In **Figure D-3**, the sketch illustrates the kinematic mount for the 200mm x 200mm samples. The sample sits on three ball-bearings attached on top of three supports, while the horizontal repositioning is assured from measurement to measurement by three cylindrical stops. Supports and stops are firmly bolted

in the table plate (see also **Figure D-1**). This setup was designed to allow sliding the sample between stage and calibration flat without moving this last item.

In **Figure D-4**, an example of live fringes of this interferometer is shown. Long term stability of the fringes was systematically checked during measurements to improve the acquisition.
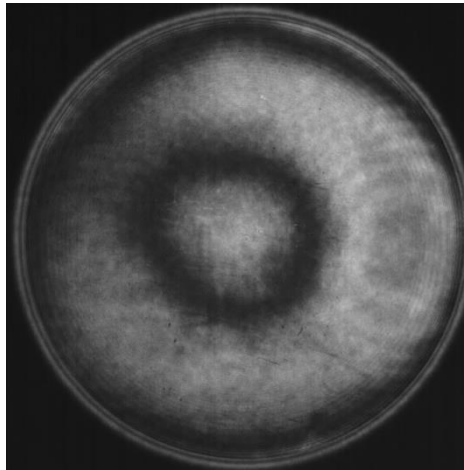
Figure D-4 Fringes from the interferometer live camera image for one of the spherical hollows figured with a 3 mm pitch (correspondent error map: Figure 5-6 (b)).

The images in **Figure D-5** summarize the software options applied for the acquisition of the surface topography map data by means of this interferometer. The systematic data acquisition procedure described in this appendix is fundamental for the evaluation of trenches data.

For such a characterisation, in fact, interferograms acquired before and after plasma etching need to be compared to measure grooves of few tens nanometres depth.
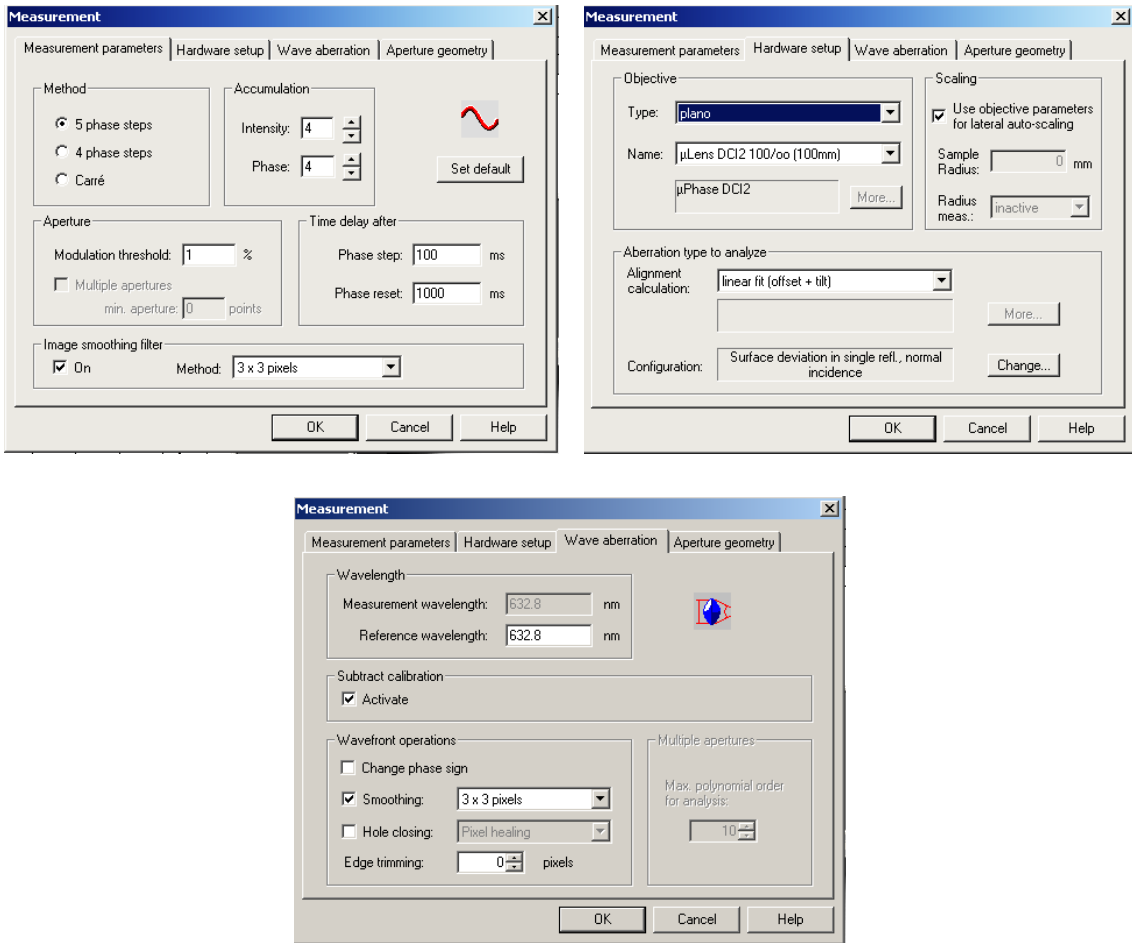
Figure D-5 Menu interfaces of the interferometer software (µPhase 4.9) showing the acquisition options selected for all measurements performed with this instrument.

D.2 Intellium H2000 interferometer by ESDI
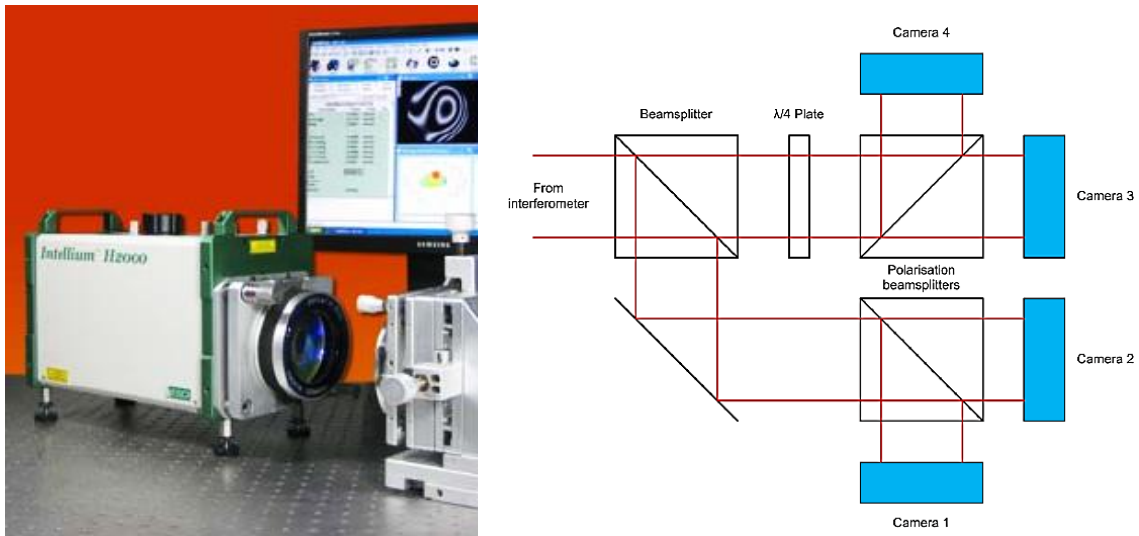
Figure D-6 *left*: **Intellium** *H2000* **vibration insensitive interferometer by ESDI (source: [72]);** *right*: **sketch of the principle of simultaneous phase shifting by polarization optics (source:** *Basic Optical Testing* **– Lecture by J. Mitchel).**

The Intellium *H2000* Fizeau interferometer (**Figure D-6**) is an example of vibration insensitive technology based on instantaneous phase-shifting by polarisation methods. In **Figure D-6 (***right***)**, a schematic of the working principle is shown. The laser beam (usually He-Ne at 632.8 nm) is polarised and redirected by prisms and beam splitters so that the four cameras simultaneously receive four phase-shifted fringes maps. The cameras are set in a cemented structure that maintains their precise relative positions. The extremely short needed exposure times (microseconds) allow "freezing" the effects of vibrations and air turbulence.

This device was available only for a short period during this PhD project. In combination with a 150 mm diameter collimator, it was utilised for the measurement of the areas of equivalent size (resolution: 0.2 mm/pixel). For these measurements, the transmission flat had a reported form accuracy of ~42 nm PV.

The acquisitions took place by averaging 32 short exposure frames and applying single frame quality control. This was based on criteria set on

modulation transfer function, error map histogram distribution and intensity threshold. The control method was introduced because of repeatability issues encountered during tests on the instrument (fringes print-through). Additionally, two further expedients had to be adopted to attain repeatability better than 30 nm PV. The sample surface was brought ~7 mm from the collimator and a jet of air by a fan was directed in the gap between substrate and entrance pupil. This had the purpose of provoking fringes fluctuations, thus averaging the errors observed in previous tests. The origin of such errors has been investigated in cooperation with ESDI, but is not to be reported in this manuscript.

D.3 Spatial carrier interferometer DynaFiz by Zygo and optical test tower

The measurements of the 3 m ROC ULE mirror were carried out with a Zygo *DynaFiz* interferometer [55] mounted on top of a test-tower. The light source is a He-Ne laser at λ = 632.8 nm. The *DynaFiz* is a Fizeau-type interferometer with vibration insensitive technology based on the spatial carrier fringes method (**Figure D-8**). Extensive and detailed descriptions of this technique and its numerous variants can be found in the literature (see, e.g., [54]).
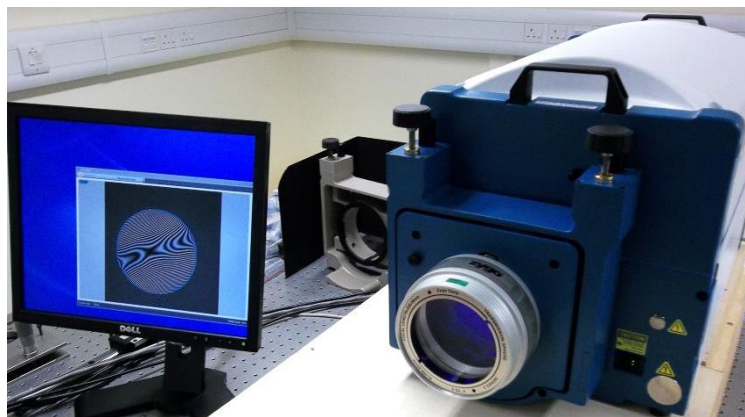
Figure D-7 Zygo *DynaFiz* vibration insensitive interferometer based on the spatial carrier method.

In this method, a large amount of tilt is introduced which produced numerous narrow fringes. The intensities of these fringes on neighbouring pixels correspond to a near-constant phase difference (for local low gradients) which allows calculating such phase directly. In this way, one image only is, in principle, sufficient to generate the final interferogram. This allows acquisitions with very short exposure time (microseconds), which makes the technology vibration and turbulence insensitive since the response time is smaller than the relaxation time of environmental disturbances.

Despite the advantage of such method, some limitations had to be considered and, when possible, compensated by the manufacturer. For instance, surface with high local slopes (e.g., steps) cannot be measured, as the fringe/pixel density would overcome the Nyquist limit [163].
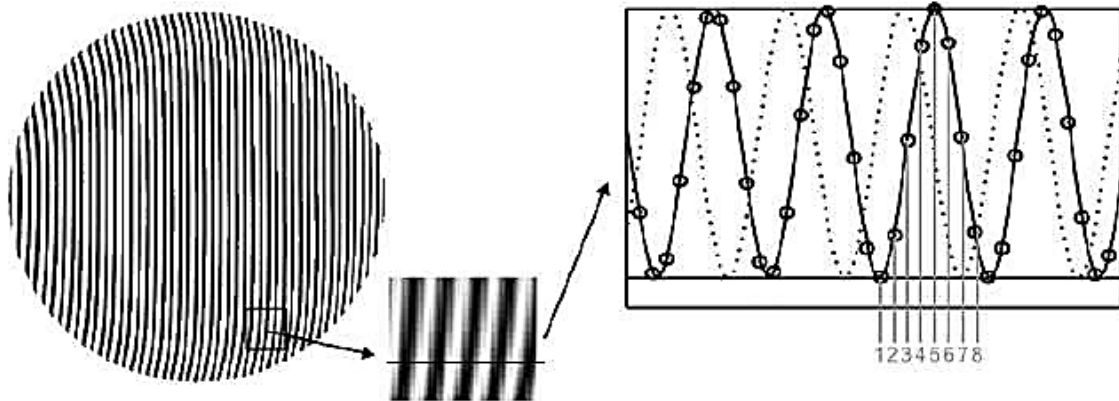
Figure D-8 Illustration of the spatial carrier finges method (source: [54]).

A further simple issue consists of introducing the "right amount" of tilt, which is limited by the maximum allowed fringes density [163]. For *DynaFiz*, software developers have therefore embedded an interface of real-time generated artificial fringes. Here, the tilt effect is removed to help the user setting the test surface at the optimum inclination by minimising the number of synthetic fringes.

Another problem is the arise of additional optical aberrations (coma, astigmatism) at the high angle of incidence introduced with the tilt. The measurement procedure includes, therefore, an error compensation technique. Four acquisitions are carried out by introducing the carrier tilt in the four directions along the diagonals of the field of view (45°). Averaging the four measurements, the aberrations induced by the tilt can be characterised and compensated for a single test surface. This procedure needs to be applied only once for each new surface under test.

For the measurements of the spherical mirror, the device was provided with an f/3.3 transmission sphere (form accuracy: 16 nm PV, 12.5 nm PVr) which allowed a resolution of 0.46 mm/pixel at 1.73X magnification. The repeatability of the system was assured to ~28 nm PV by averaging 64 short exposure frames[15], with an interval of one second between subsequent acquisitions

---

[15] The exposure time is determined by the camera shutter, set at 5% by default. According to the instrument specifications, this corresponds to <1 milliseconds for 1200x1200 pixels. The

(**Figure D-9**). This waiting time was introduced to compensate for air turbulence effects. Post-RAP surfaces, which showed a rough texture, required the use of a tolerant acquisition mode. This option lowered the acquisition acceptance threshold at each data point from 100% to 65%.
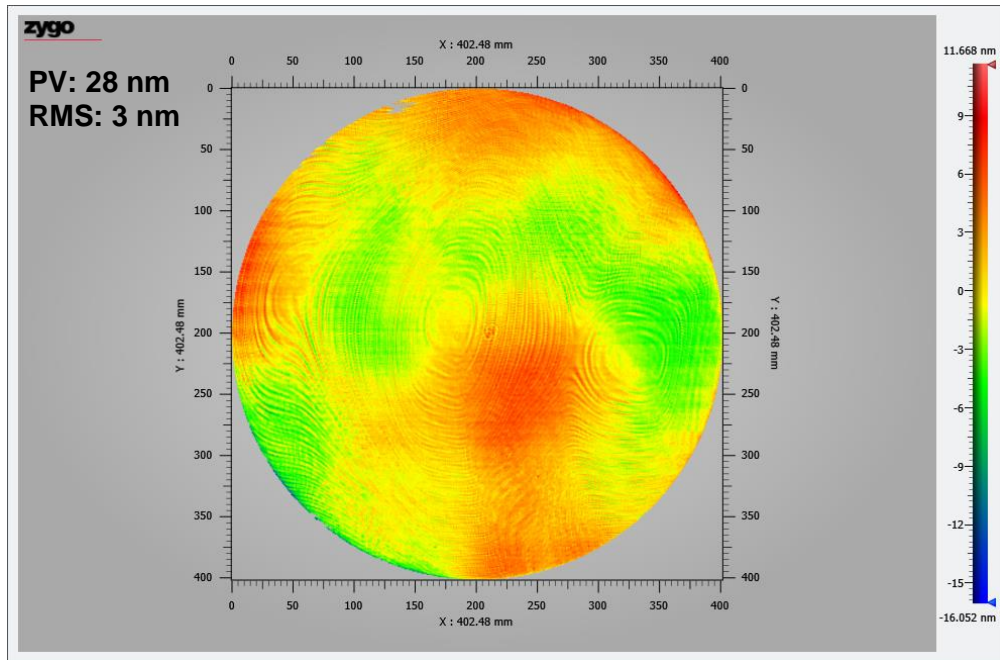

Figure D-9 Repeatability over a 400 mm diameter area of the *DynaFiz* mounted on the optical test tower.

The software options utilised for the data pre-processing are illustrated by the images on the following pages. Here, the interfaces for data handling are shown as set for the polished (**Figure D-10**), as well as for the rougher post-RAP surfaces (**Figure D-11** to **Figure D-15**).

---

measurements of the ULE mirror included 881x881 pixels, thus making the exposure time <2 milliseconds.
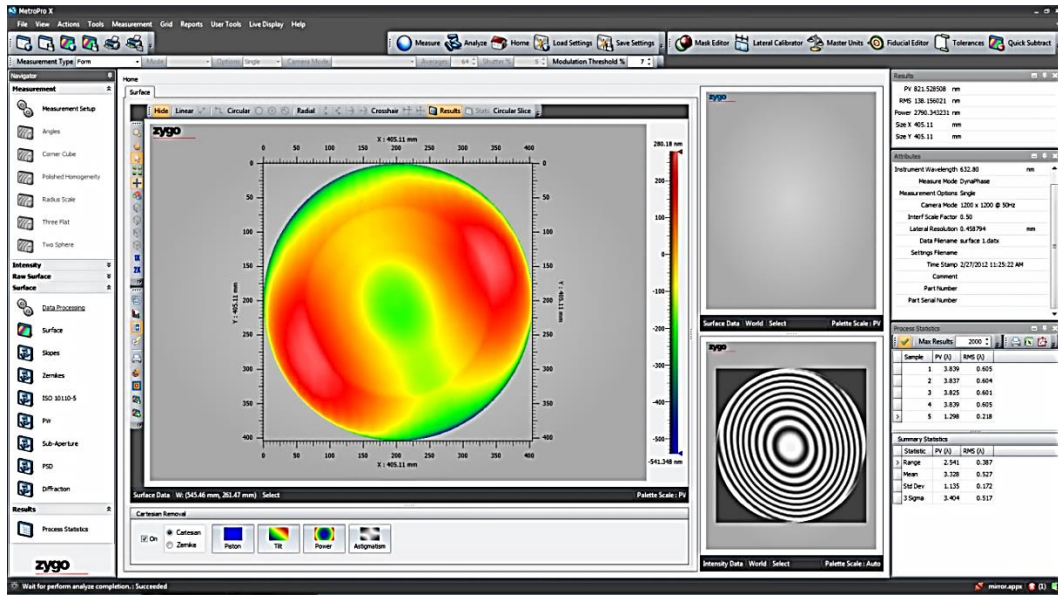
Figure D-10 Template for polished surface: no further data manipulation occurred except for the subtraction of piston, tilt and focus term.
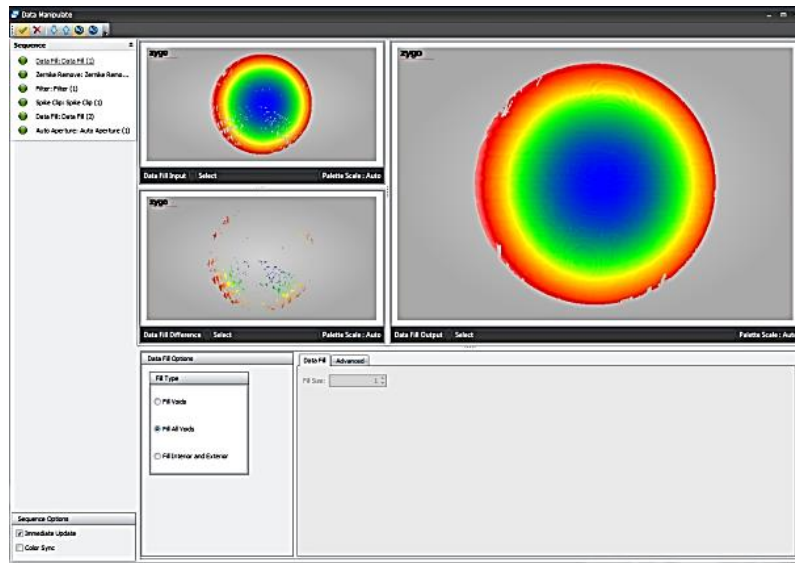
Figure D-11 Data fill.
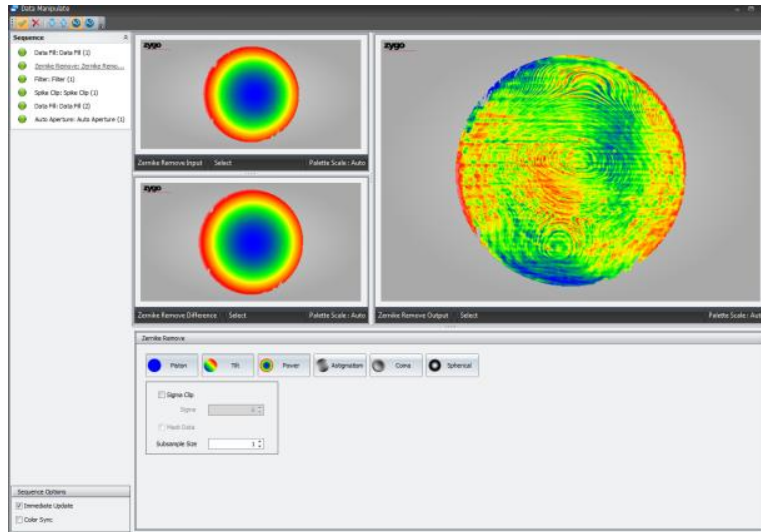
Figure D-12 Zernike polynomials removal (piston, tilt, focus).
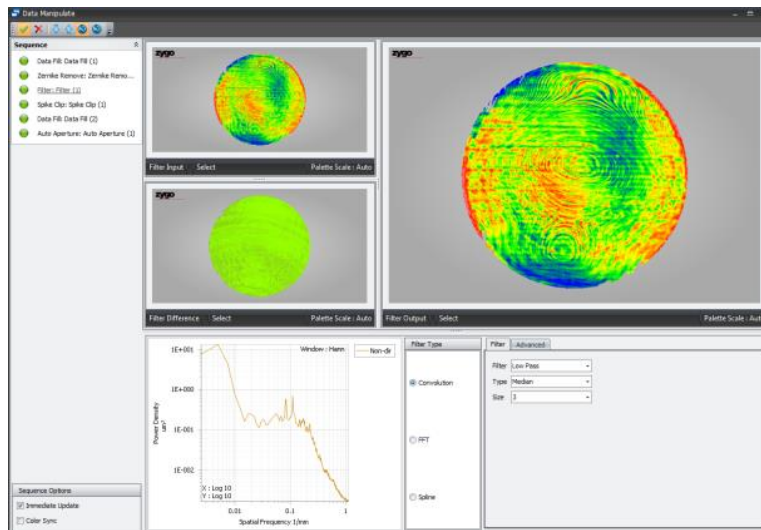
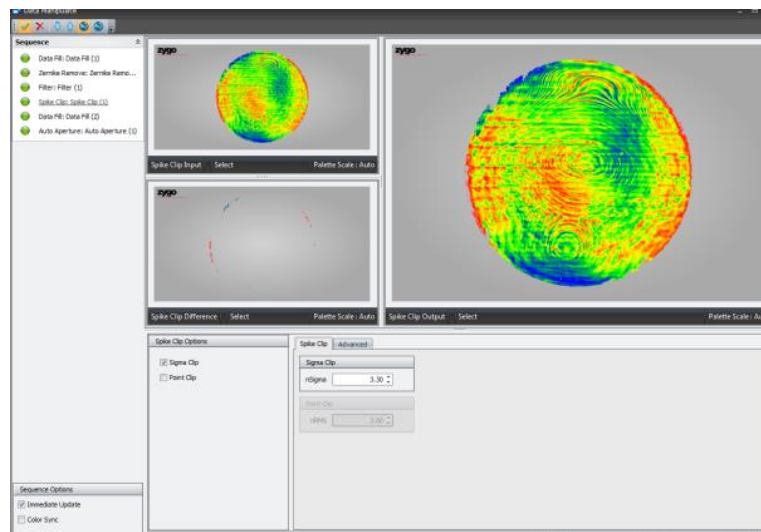**Figure D-13 Median Filter (3X3 pixels)**
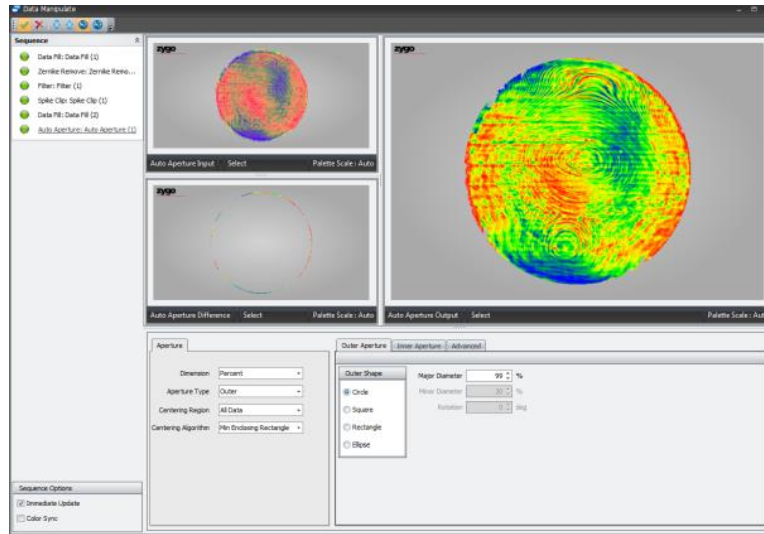

Figure D-14 Spikes clip (sigma: 3.30)

Figure D-15 Auto aperture (99%).

In **Figure D-16**, 2- and 3D technical drawings of the optical test tower designed by Dr. R. Jourdain are shown. This structure is designed for the measurement of optics with ROC up to 4 m.
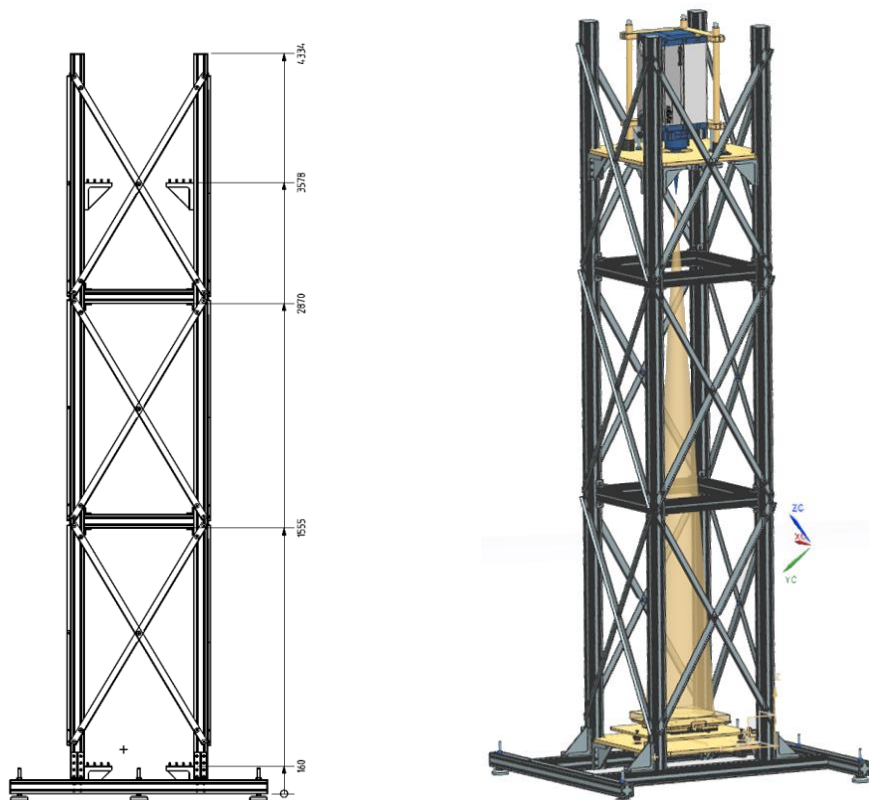
Figure D-16 The optical test tower designed and built by the Precision Engineering Institute at Cranfield University (*source*: R. Jourdain): technical drawing (*left*) and 3D view (*right*).

The optic sits on a stage (see also **Figure 5-20**) that allows for a three-point tip-tilt adjustment by precision screws. These can also be used to tune the piston. The stage is aligned with the interferometer field of view and lateral shifts are controlled in the vertical and horizontal directions by micrometre screws. While on the stage, the substrate is not in direct contact with the plate, but lies on a soft mat. This has the purpose of avoiding damage of the glass, as well as minimising distortion due to sag.

During the repeatability assessments, the solidity of the construction allowed observing high fringes stability, both in terms of oscillatory movements (vibrations) and of lateral drift.

D.4 White-light interferometer CCI6000 by Taylor-Hobson

For the roughness measurements carried out in this project, the white-light (or Coherence Correlation) interferometer CCI6000 by Taylor Hobson was used in combination with a 50X magnification lens (Nikon). This has a field of view of 366x366 µm. A picture of the device and a sketch of the working principle are shown in **Figure D-17**.
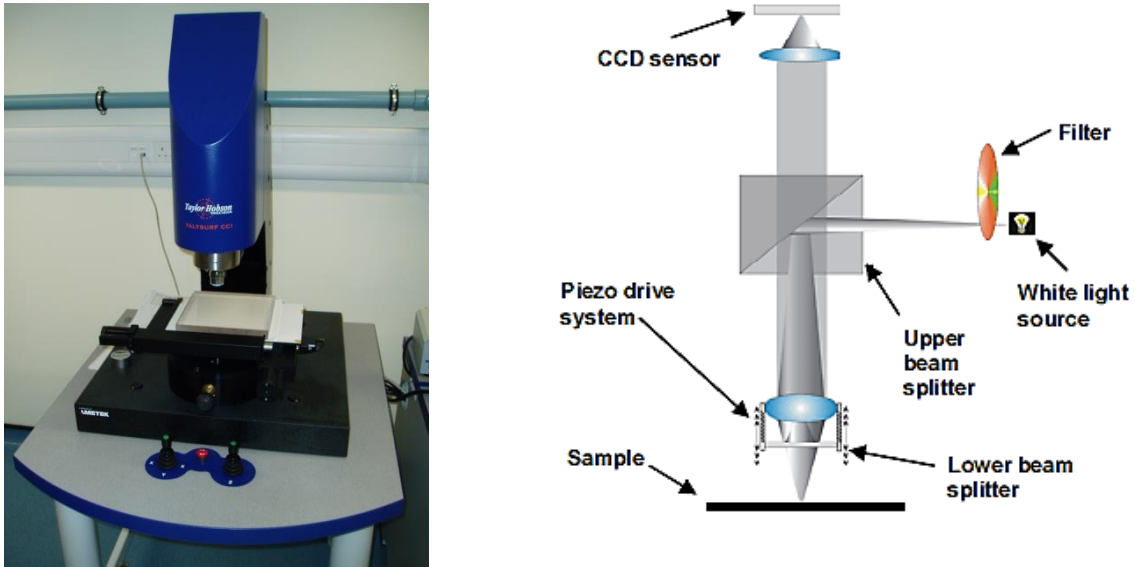

Figure D-17 *left*: **The CCI6000 by Taylor-Hobson;** *right*: **sketch of a typical white-light interferometer (source: CCI6000 Helpfile).**

White-light interferometry is a well-established method for measuring highly sloped surface features and areal roughness parameters. Monochromatic phase-shifting interferometers suffer of a limitation for step measurements that cannot be higher than $\lambda/4$ (~158 nm) [164]. Therefore, a broadband light source with small coherence length can be used to overcome such restriction (see, e.g., **Figure D-18**), as interference will occur only when the optical path differences are tightly matched. Fringes generation takes place by interference of light from the test surface with light from a reference mounted on a PZT driving element. This allows scanning a pre-set range of heights.
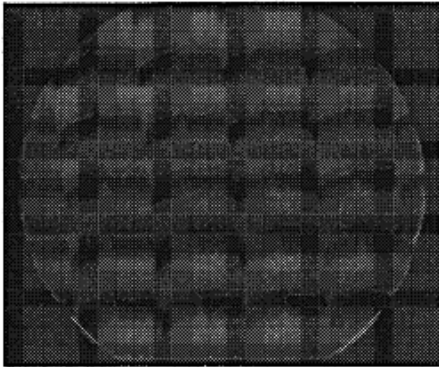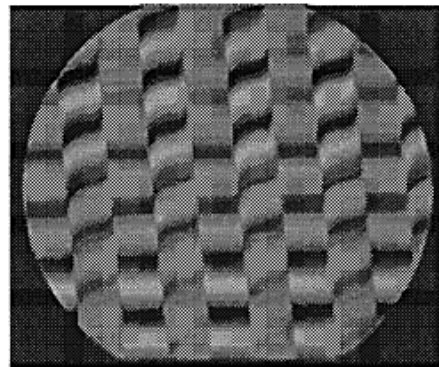
Figure D-18 Benefit of white light interferometry (source: [164]).

The CCI6000 was calibrated prior to every measurement series reported in section 5.2.3. This procedure included vertical, lateral and flatness calibration by means of ISO standard artefacts. Also, the roughness of one same surface (SiC standard flat) was assessed before every acquisition series to confirm the response consistency of the instrument. Also, for the measurement of each 366μm x366μm region, two consecutive acquisitions were performed and averaged. This had the purpose of reducing errors due to vibrations or air turbulence.

In this work, the acquisition and processing of the CCI6000 data took place according to the options specified in **Figure-D-19** to **Figure D-22**. In **Figure-D-19**, the interface of the CCI6000 control software is shown, with the activated option for smooth surfaces. This implies an automatic Gaussian filtering (3 pixels width) of the data to eliminate unrealistic peaks and pits due to noise. The Talymap Gold data analysis software interface is shown in **Figure D-20**. In the left window, the operators applied on each dataset are listed.
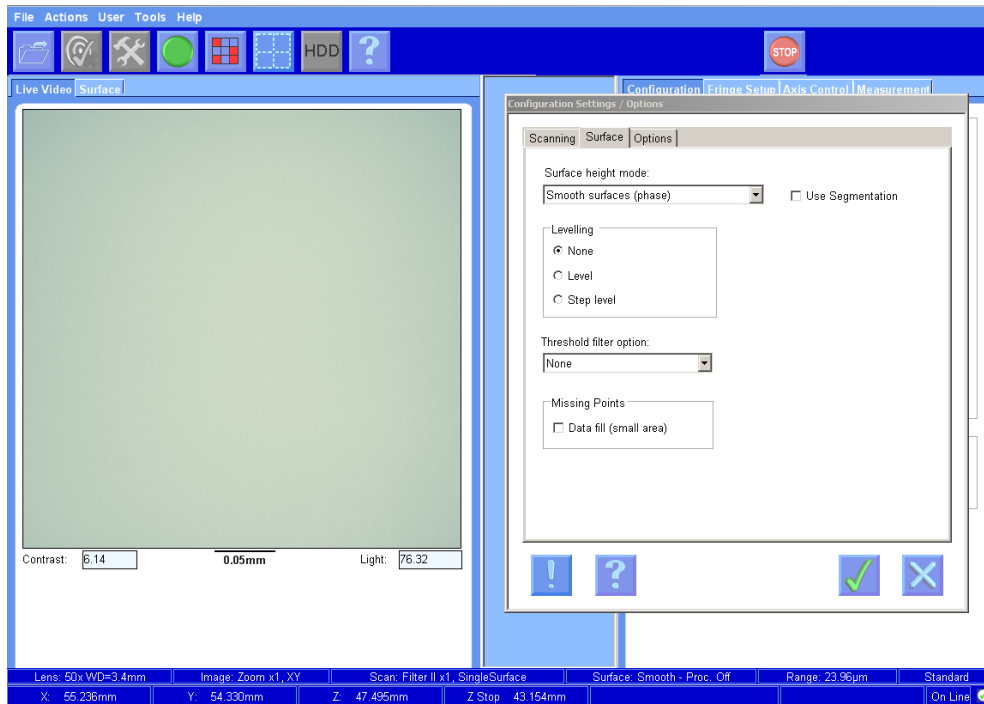
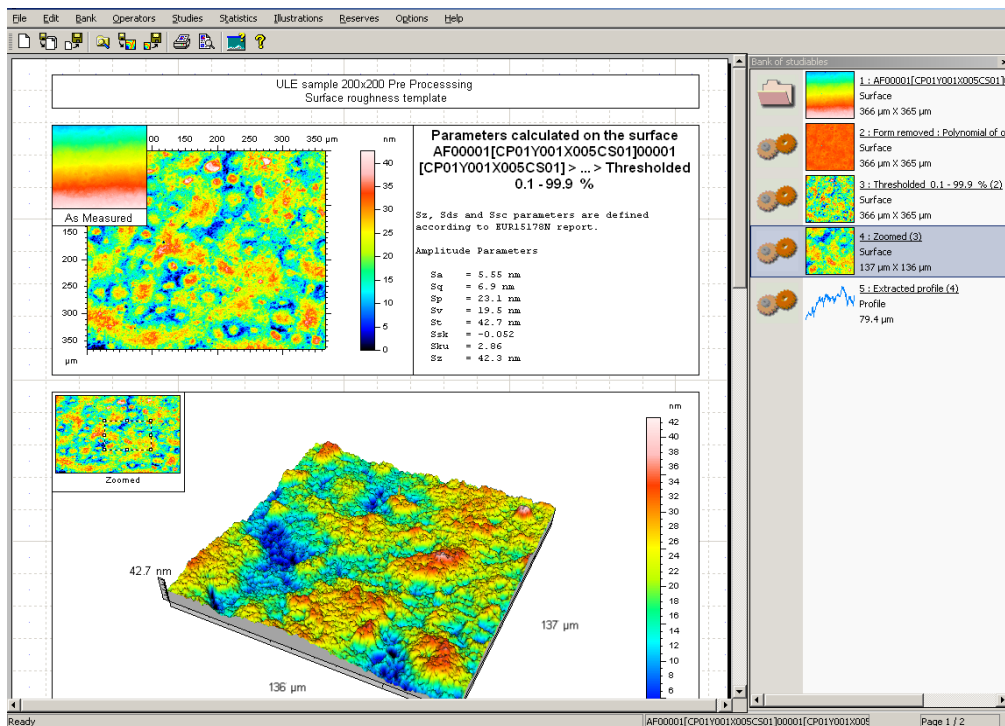**Figure-D-19 Interface of the CCI6000 control software: the acquisition option set for smooth surfaces.**

Figure D-20 The data processing software Talymap Gold: in the left window, the applied data processing oprator are listed; their details are given in Figure D-21 and Figure D-22.

Relevant data processing operations are the form removal (3rd degree polynomial) and the threshold filtering by 0.1% of the so-called Abbott curve. These data manipulations had the aim of removing the tilt, but also unwished artefacts caused e.g., by dust particles. Details on these operations are illustrated in **Figure D-21** and **Figure D-22**.

NOTE: The data processing template reported in this appendix was agreed in a private communication with Taylor-Hobson [70]. In particular, no cut-off filtering is applied for this low roughness level. Filters are not defied by ISO standards for roughness below 6 nm S_a (or R_a). In this way, the cut-off length becomes the entire field of view. This procedure is considered suitable for nanometer level roughness of glass surfaces.
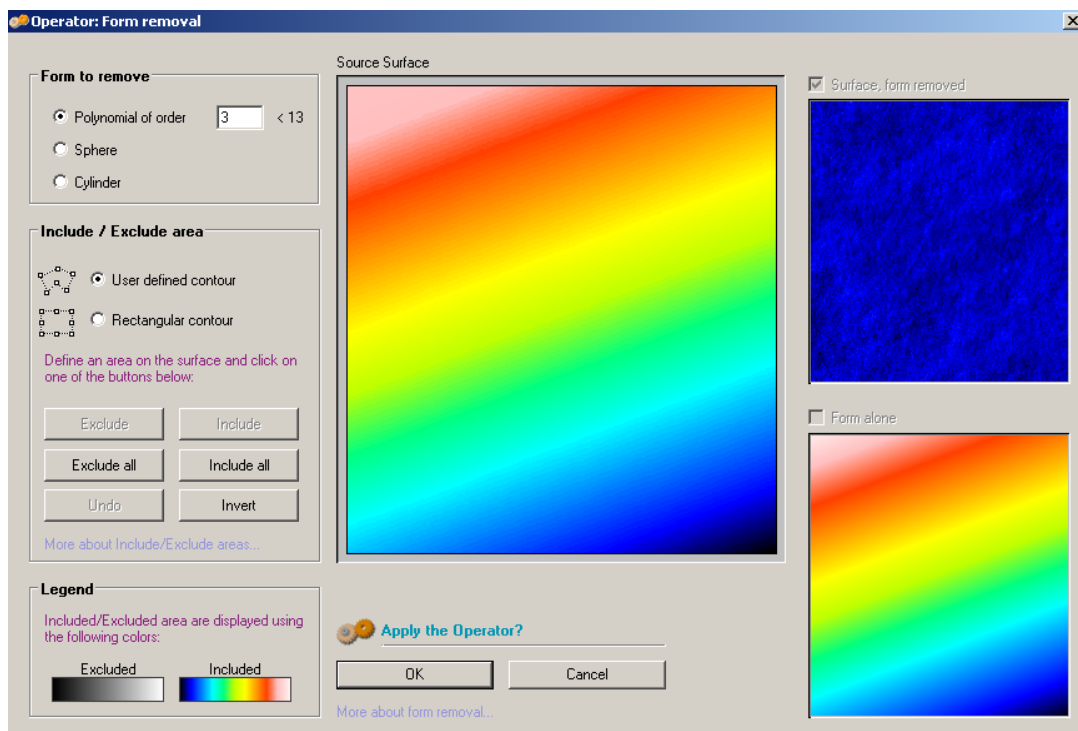

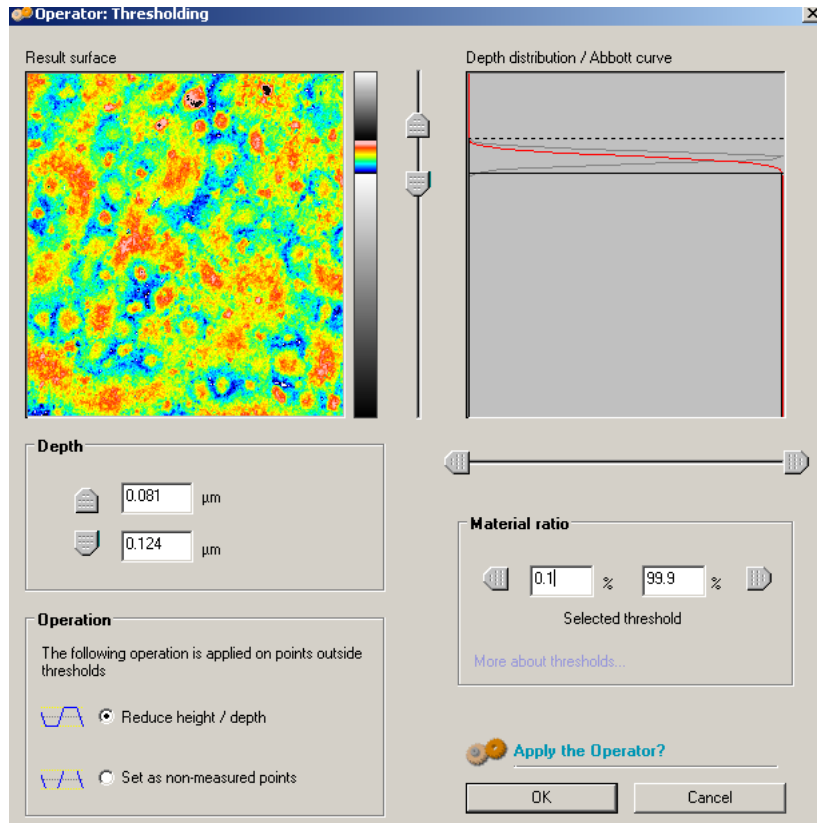**Figure D-21 Form removed from the raw data prior to parameters evaluation.**

Figure D-22 Data threshold by 0.1% of the so-called Abbott-Firestone curve, the *cumulative probability density function* **of the surface heights.**

D.5 Instrumentation for surface temperature measurements

To assess the temperature field of optical surfaces, two types of equipment were available for the work presented in this manuscript: thermocouples and a pyrometer.

Thermocouples represent a simple thermometric technique based on the principle of the Seeback effect. This consists of a voltage surge caused by heat affecting the two different metal types of which the tip of thermocouples is made. The difference in electrostatic potential is generated by charges migration from the higher to the lower temperature conductor. This tension variation can then be converted into temperatures. The simplicity in the use of thermocouples is often made problematic by environmental disturbances (e.g., electromagnetic). Also, pristine wiring insulation should be assured. More importantly, as an invasive measurement instrument, thermocouples need intimate contact with the measurement zone. The definition of such area is mostly determined by the size of the sensors head, as well as by the technique adopted to improve contact. In the context of this project, thermocouples of type K were used and their output logged by means of a USB Pico TC-08 (Omega). Their calibration should be granted by manufacturers. Thermal contact with surfaces was provided by means of a thermally conducting paste by Omega or by welding resin. These thermocouples are not considered suitable for measurements in the neighbourhood of a plasma plume and were therefore utilised for acquisitions on the substrates rear surface only.

For front surface temperature acquisitions, the Helios 1200 machine is equipped with a pyrometer positioned along the X-axis and aligned with the nozzle centre. Nozzle and pyrometer are kept ~16 cm apart. In the original torch design, the pyrometer was located in closest proximity to the nozzle and pointing at angle towards the surface portion stricken by the plasma plume. This configuration couldn't be maintained due to electromagnetic disturbances between torch and pyrometer that prevented correct function of the system.

A pyrometer is a sensor that acquires and analyses thermal radiation, typically emitted by objects in the infrared range of the spectrum. The measurement

principle is based on the assumption of grey-body radiation intensity for materials like glass and glass-ceramics. Grey-body emission is expressed as follows:

$$I = \varepsilon\sigma T^4$$

with σ: Stefan-Boltzmann constant, ε: substrate emissivity. The pyrometer outputs a temperature value averaged over the reading spot size.

The available instrument is an IN 530-N model by IMPAC; the experimental parameters are:

- Temperature range: -40 – 700 ^{o}C.

- Calibrated for: 0 – 500 ^{o}C.

- Spectral range: 8 – 14 µm.

- Uncertainty: ~ 1 ^{o}C.

- Response time: ~ 200 ms.

- Tuneable emissivity.

- Sensor head temperature compensated.

Measurement spot size: dependent on distance (head with 10:1 field of view → ~5.5 mm Ø for a distance of 6 mm).

The spectral range matches one of the silica main absorption lines [160], which confirms the suitability of the instrument for the two materials utilised in this work. The emissivity can be adjusted according to the type of material (> 90% for glasses and glass-ceramics). For the work presented in this thesis, a calibration versus a black spot (black body) was performed in the range 20 – 100 ^{o}C and is shown in **Figure D-23**. This is range of temperature expected on RAP processed surfaces away from the plasma plume.
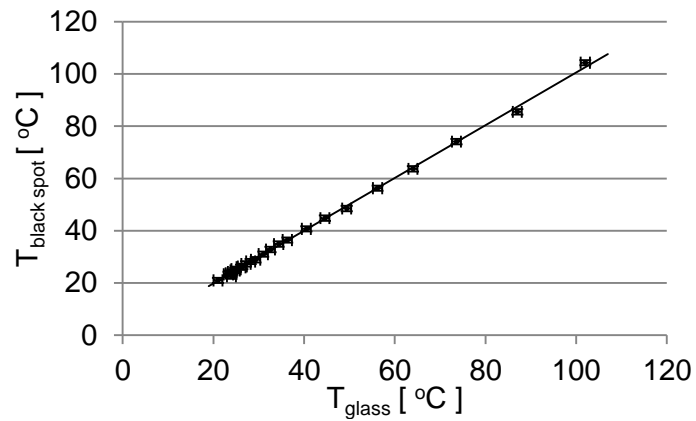
Figure D-23 Calibration of the pyrometer: temperature values measured on a black spot and on the nearby area of a fused silica surface by rapidly shifting the pyrometer from one zone to the other.

NOTE: The surface roughness is known to influence the accuracy of infrared measurements because of radiation scattering due to local asperities. This factor has been neglected for the acquisitions performed in this work, as surfaces still presented roughness at nanometre level. This point, though, shall be object of future investigations.

Appendix E Matching metrology and machine coordinate systems

As mentioned in section 5.2.6 (**Figure 5-22**), the accuracy of the information about the position of the workpiece with respect to the tool, but also to the interferometer field of view can significantly influence the result of surface machining processes (e.g., grinding, diamond turning, polishing). Figuring processes are no exception to this principle. Some systems are provided with CMM arms that help registering the workpiece to be machined (e.g., BoX grinding machine, MRF machines). Helios 1200 is not equipped with this kind of embedded metrology, but has a camera with crosshair locator (**Figure E-4**) which is mounted ~100 mm on the left-hand side of the torch. This camera faces upwards and can be utilised to envision the edges and corners of a substrate. Accuracy comparable to the one of the machine motion system can be assumed (~10 μm), although some arbitrariness due to the visual nature of the method is present.

For the figure correction work described in this thesis, two methods to locate the area of interest have been adopted. For the 100 and 150 mm diameter regions, the interferometer field of view was smaller than the sample area (200mm x 200mm). Perfect centring of the collimator over the surface wasn't possible and location of the figuring area by the camera system would have therefore been inadequate. Therefore, a so-called fiducial method was introduced to identify the process region. Conversely, the ULE mirror had been machined with micrometre accuracy in the centre of the square substrate surface and the interferometer was capable of measuring the entire clear aperture. Therefore, in this case the camera crosshair method was considered sufficient for registering the part. Details about the two methods are described in the following subsections.

METHOD I: FIDUCIALS

In **Figure E-1**, the sketch illustrates how a 200mm x 200mm sample is typically positioned on the holder with respect to the machine coordinate system. In the sketch, the area to be figure corrected is highlighted. Through the camera

crosshair, the corner of the sample can be identified; hence the surface centre point can be defined in terms of machine coordinates. The fiducial method utilised in this work is based on the etching of a one-second spot at this coordinate point (**Figure E-2**).
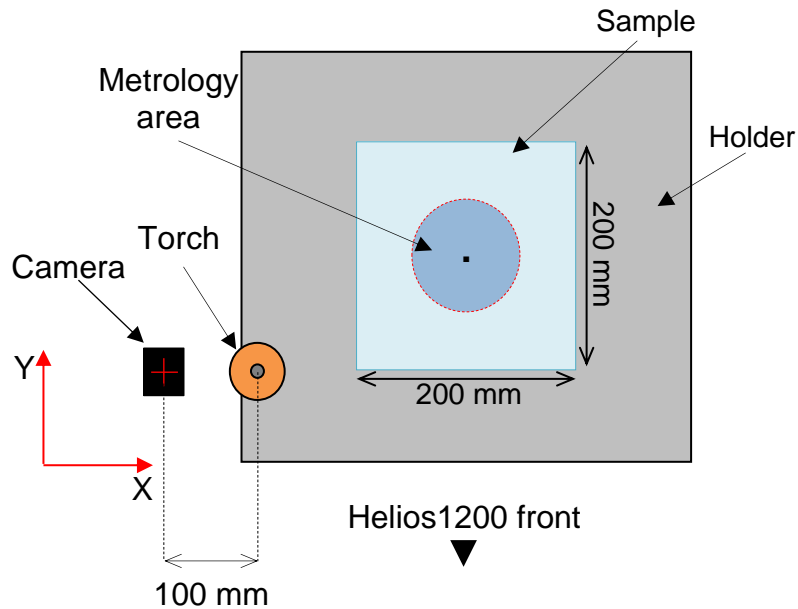

Figure E-1 Sketch illustrating a 200mm x 200mm sample located on the holder with respect to the Helios 1200 coordinate system.

Measurement of the area before and after etching enables to relate the spot centre to the midpoint of the interferometer field of view. In order to establish the coordinate's values with sub-pixel resolution, a Gaussian curve is fitted to the central X- and Y-cross-sections (**Figure E-3**). This procedure results in the definition of a shift transformation [ΔX, ΔY] to be accounted for when generating a tool-path algorithm CNC code.

This method is considered suitable for small fields of view, where possible rotations of the workpiece by tiny angles in the X-Y plane would produce non-significant misalignments. For larger apertures, the etching of two or more spots near the boundaries of the field of view is suggested. This would enable to account for shifts and rotations, while improving the accuracy of the method.
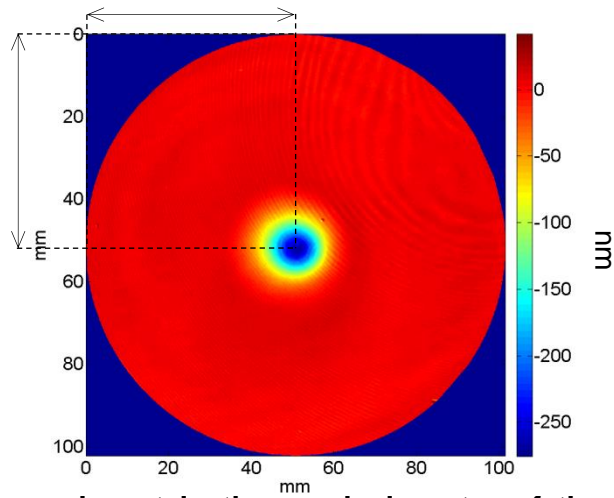
Figure E-2 One-second spot in the nominal centre of the measurement area (material: ULE).
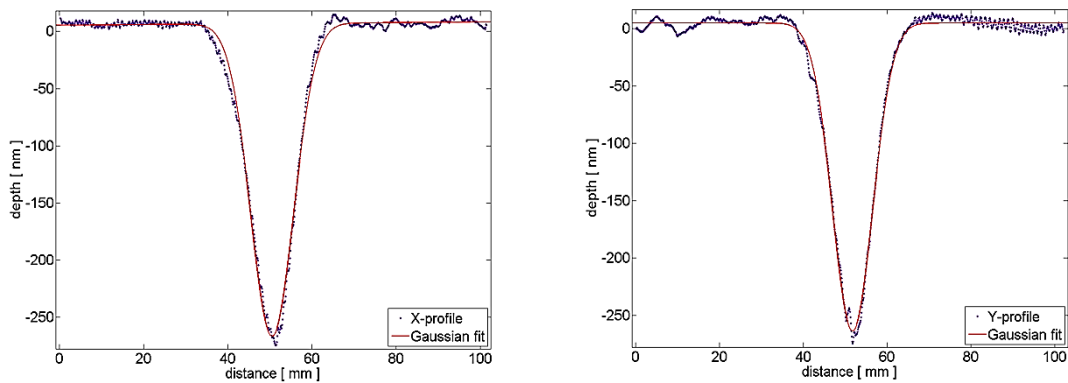

Figure E-3 Gaussian curve fits of the X- (right) and Y- (left) cross sections of the one-second spot etched in the nominal centre of the metrology area (material: ULE).

This method was utilised to determine the position for the figure correction of the 100 and 150 mm diameter areas. Note that, in all cases, the one second spot was etched on a spare 200mm x 200mm surface (ULE or fused silica). This was measured and positioned in exactly the same conditions as the surfaces to be figured.

METHOD II: TORCH CAMERA SYSTEM

In this method, the sole use of the torch camera is sufficient. As specified above, this is the standard positioning method for Helios 1200 and is applicable every time the field of view can be identified with respect to the workpiece area.

For the figure correction work on the ULE mirror, one of the substrate corners was utilised as reference and its coordinate were checked with the camera crosshair. This allowed establishing the offset. Additionally, the locator was "run" along the edges of the workpiece to investigate the alignment with respect to the machine X- and Y-axis.
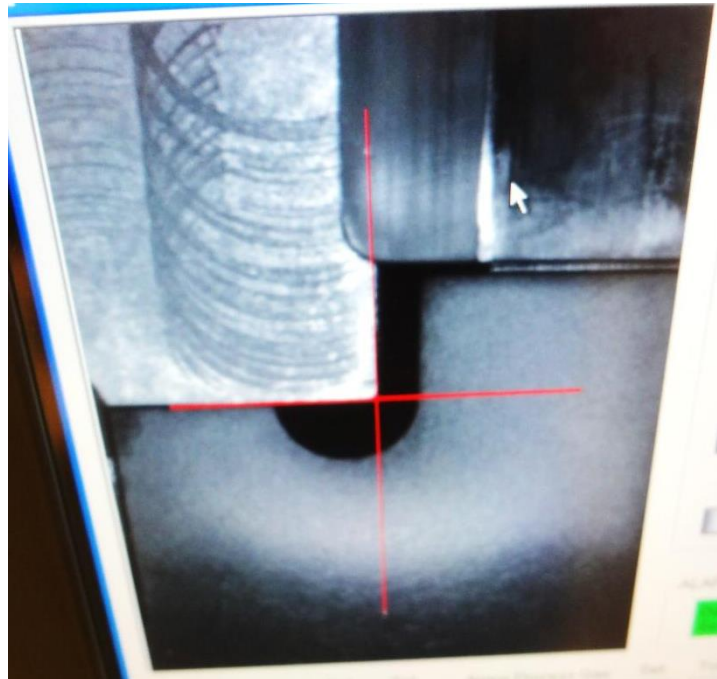

Figure E-4 Field of view of the camera system located 100 mm on the lefthand side of the ICP torch. The photograph of the RAP interface software illustrates the red crosshair positioned on a corner.

The so applied method relies on the straightness and squareness of the workpiece edges. For this ULE substrate, the squareness was measured on a CMM during the grinding phase. This resulted within ~90 µm, thus allowing the use of the camera system on Helios 1200.

Appendix F Effect of angle of incidence

If an energy beam doesn't strike the process surface perpendicularly a deformation of the removal function is to be expected. For instance, the footprint of ion beam processes will undergo an elliptical elongation, as well as a change in the removal depth that will depend on the angle of incidence (**Figure F-1**). As mentioned in section 5.2.6, the effect on a plasma jet may involve additional alterations due inevitable variations of to the gas flow dynamics. The influence of the angle of incidence, though, would be expected on high gradient surfaces. In order to verify the suitability of the etching footprint for the 3 m ROC surface processed in this work, a spot test was carried out. The principle is sketched in **Figure F-2**.
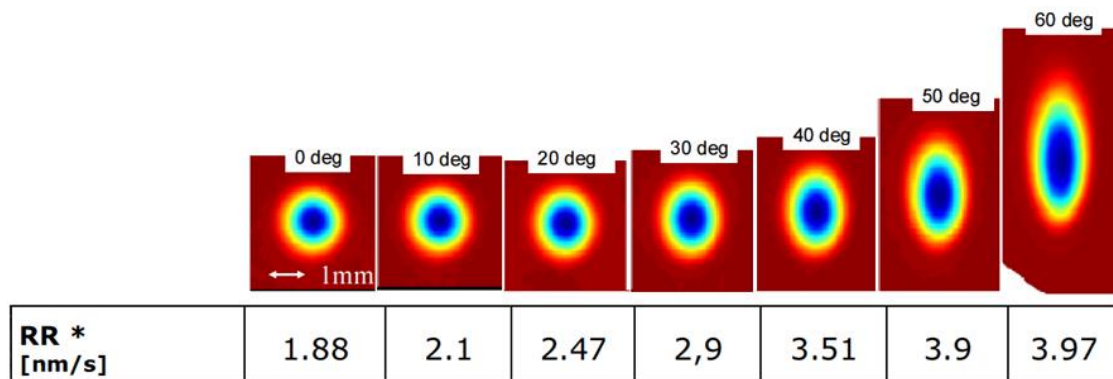

RR * [nm/s]	1.88	2.1	2.47	2,9	3.51	3.9	3.97

Figure F-1 Illustrative image of the effect of angle of incidence for an ion beam source of 1.2 mm FWHM (source: [149]).

The region of maximum slope on the edge of the clear aperture of ULE mirror corresponds to an angle of incidence of ~3.5^o, taken between the torch axis and the normal to the surface. These processing conditions were reproduced by positioning a ULE substrate (200mm x 200mm x 25mm) at 3.5^o angle inclination and etching a one-second spot.

The footprint etched on the tilted sample was then compared with a one-second spot processed without slope. The results can be seen in **Figure F-3**. From this figure, and considering the reported values for the FWHM of the cross-sections, it is trivial to infer that no relevant effect due to the incidence angle occurs for this low gradient surface.
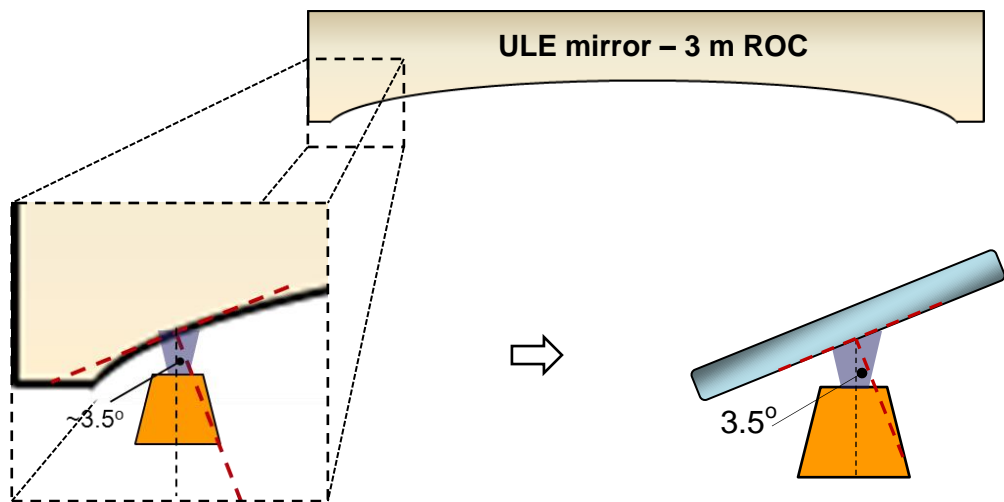
Figure F-2 Sketch illustrating the equivalence of a spot test on an inclined sample and the incidence of the plasma plume onto the region of maximum slope of the 3 m ROC ULE mirror.
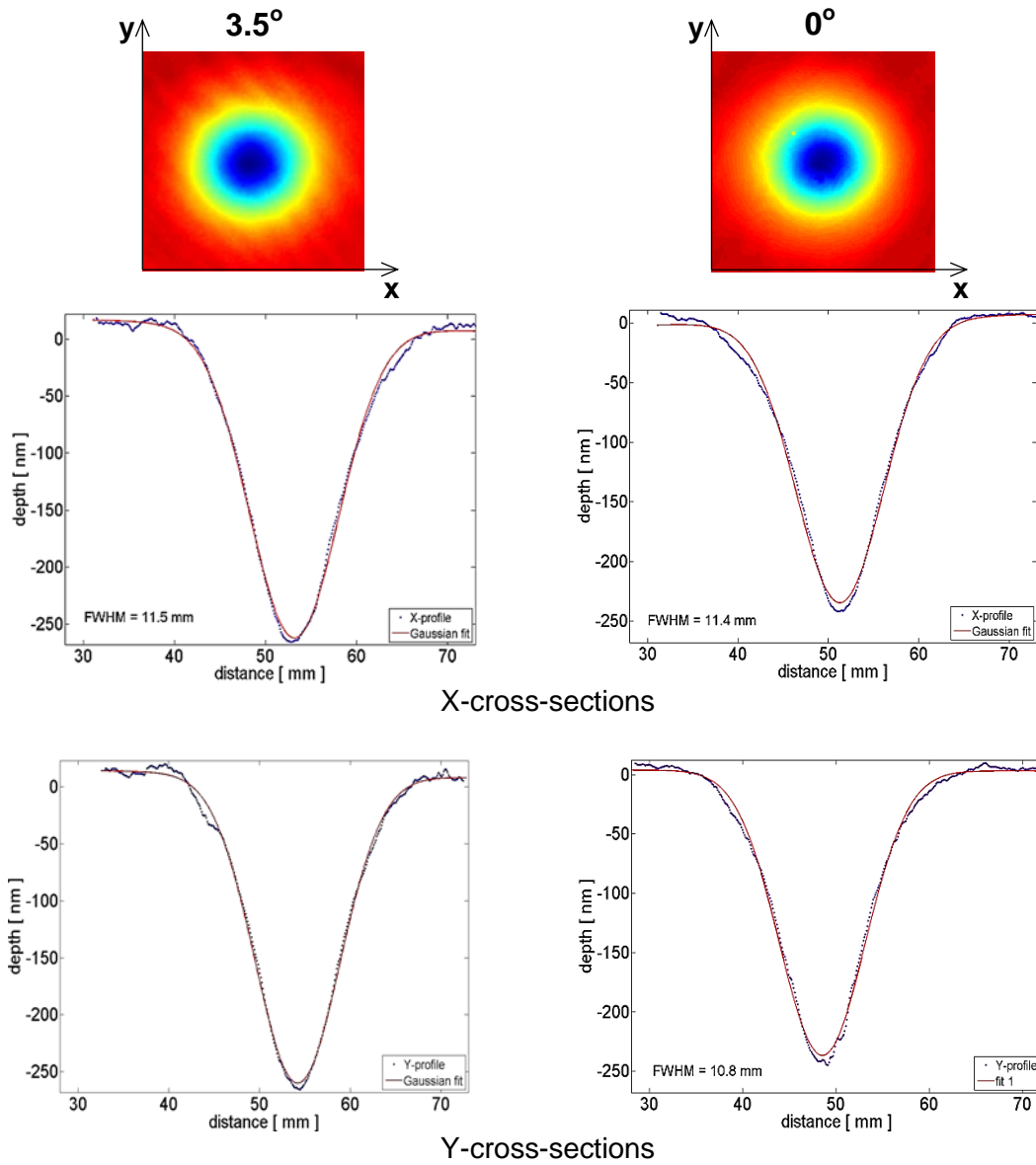
Figure F-3 Comparison between a one-second spot etched with an angle of incidence of 3.5° and a one-second spot processed with no slope. The plots show the central x- and y-cross-sections with respective Gaussian fits; the FWHM values are reported on the graphs.